

https://dspace.org/

Seismic shear wave borehole tormography and the application of the curvelet transform to reflection seismic data

Von Ketelhodt, Julius Karl

2019-05
https://hdl.handle.net/10539/29588

Downloaded from a DSpace repository. https://dspace.org/

SEISMIC SHEAR WAVE BOREHOLE TOMOGRAPHY AND THE APPLICATION OF THE CURVELET TRANSFORM TO REFLECTION SEISMIC DATA

JULIUS KARL FREIHERR VON KETELHODT

A thesis submitted in fulfilment of the requirements for the degree of

DOCTOR OF PHILOSOPHY (GEOPHYSICS)

In the

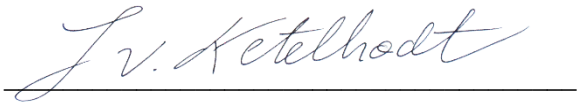
SCHOOL OF GEOSCIENCES

UNIVERSITY OF THE WITWATERSRAND

MAY 2019

DECLARATION

I declare that this thesis is my own, unaided work. It is being submitted for the Degree of Doctor of Philosophy at the University of the Witwatersrand, Johannesburg. It has not been submitted before for any degree or examination at any other University.



Julius Karl Freiherr von Ketelhodt
Student number: 475098

Signed on the
23rd day of May 2019, Split, Croatia

THESIS SUMMARY

Title:	Seismic shear wave borehole tomography and the application of the curvelet transform to reflection seismic data
Author:	Julius Karl Freiherr von Ketelhodt
Supervisors:	Prof. Musa Manzi
	Prof. Raymond Durrheim
School:	Geosciences
University:	University of the Witwatersrand
Degree:	Doctor of Philosophy by thesis (Geophysics)

ABSTRACT

This thesis is comprised of two parts. In the first part, I show the application of seismic S-wave cross-borehole tomography in different geological environments and find optimal processing and interpretation flows adapted to different exploration questions. In general, S-wave tomographic imaging offers many additional parameter estimates and interpretational insight compared to P-wave tomography on its own. In the first case study, I show that prior to the construction of a large infrastructural project, cross-borehole P- and S-wave tomography can be effectively used to derive elastic parameters, and detect a large weak zone in highly weathered and karstic limestone. In the second case study, I used S-wave tomography, in conjunction with MASW and SCPT measurements, to improve an earthquake velocity model, by increasing the reliability of the near-surface S-wave velocity, and detecting zones of variable surface wave amplification. These two case studies were complemented with S-wave measurements in an overconsolidated clay environment, were different processing and interpretational capabilities of S-wave tomography were developed. One of the disadvantages of interpreting S-wave velocities, is the lower measurement accuracy of the S-wave traveltimes compared to P-wave traveltimes. To overcome this limitation, I propose a new method, whereby the less accurate S-wave traveltimes are structurally coupled to the more accurate P-wave traveltimes. This joint-inversion approach resulted in more accurate S-wave tomographic images, enhancing the interpretational capabilities. Further, I show that anisotropy plays an important role when interpreting S-wave data. Measurements with two directional sources produced differently polarised S-waves, which travelled at different velocities. The measurements show that S-wave anisotropy is far more severe compared to P-wave anisotropy, especially in a near-surface environment, and could be a reason for the reduction in accuracy, if an isotropic approach is taken. Parameters for a vertically transversely isotropic (VTI) medium were estimated by jointly inverting P- and S-wave traveltimes, which markedly improved the data fit and resolution of the tomographic images.

The second part of the thesis shows the benefit of enhancing legacy seismic data from the Kalahari-Karoo Basin, Botswana. The curvelet transform is employed to reduce noise, thereby enhancing the interpretational capabilities of the post-stack reflection seismic sections. I show that the reflection seismic method, and in particular re-utilising legacy data, is an invaluable tool to prospect for coalbed methane resources in Botswana.

ACKNOWLEDGEMENTS

I would like to express my appreciation to the following individuals and organisations. Without their collaboration, assistance and guidance this thesis would not have been possible.

a) My supervisors Prof. Musa Manzi and Prof. Raymond Durrheim from the University of the Witwatersrand who provided me with funding, invaluable advice, and who have read and improved all of my manuscripts, proposals and this thesis. Thank you for your continuous support.
b) Geotomographie GmbH, specifically Dr Thomas Fechner, who funded some of the data acquisition and provided invaluable advice concerning borehole tomography
c) Julius Marschollek, Ralf Hermanns, Hocine Yousfi and Michele Scaroni who all helped tremendously acquiring the seismic data for tomographic analysis
d) Devendran Arumugam and Dr Ooi from MMC-Gamuda, who enabled the publication of the tomography survey in Kuala Lumpur
e) Dr Ralf Trabitzsch from the Umweltforschungszentrum (UFZ) in Germany, who granted me access to the SAFIRA research facility in Zeitz, Germany and thereby enabled seismic measurements for tomographic analysis, and who provided valuable experiences and information from his years working there
f) Prof. Ari Tryggvason from Uppsala University for his thoughtful comments on the topic of joint-inversions
g) Dr Bing Zhou from the Petroleum Institute, Abu Dhabi for making his anisotropic inversion code available to me and for providing comments regarding seismic anisotropy parameter estimation
h) The National Research Foundation and the Thuthuka Research Fund of South Africa who provided financial assistance
i) The Seismic Research Centre of the University of the Witwatersrand for providing software.
j) The EAGE for providing partial funding to attend the 80th EAGE Conference and Exhibition in Copenhagen, Denmark.
k) The constructive criticism of several anonymous reviewers and editors, which improved the quality of the individual publications and manuscripts currently still under review
l) My wife Tanja, who has continuously supported me.

LIST OF PUBLICATIONS

This thesis is based on the following publications, which are subsequently referred to by their Roman numerals

I **von Ketelhodt, J.K.**, Fechner, T., Manzi, M.S.D, Durrheim, R.J. 2017. Elastic Parameters from Compressional and Shear Wave Tomographic Survey: A Case Study from Kuala Lumpur, Malaysia. Journal of Environmental and Engineering Geophysics, 22(4), 427–434.

II Noorlandt R., Kruiver, P.P, de Kleine, M.P.E, Karaoulis, M., de Lange, G., Di Matteo, A., **von Ketelhodt, J.K.**, Ruigrok, E., Edwards, B., Rodriguez-Marek, A., Bommer, J.J., van Elk, J., Doornhof, D. 2018. Characterisation of ground motion recording stations in the Groningen gas field. Journal of Seismology, 22, 605–623.

III **von Ketelhodt, J.K.**, Fechner, T., Manzi, M.S.D, Durrheim, R.J. 2018. Joint-Inversion of Cross-Borehole P-waves, horizontally and vertically polarised S-waves: Tomographic data for hydrogeophysical site characterisation. Near Surface Geophysics, 16, 529–542.

IV **von Ketelhodt, J.K.**, Manzi, M.S.D, Durrheim, R.J., Fechner, T. 2019. Seismic VTI Parameter Inversion from P- and S-wave Cross-Borehole Measurements in an Aquifer Environment. Geophysics, (accepted for publication on 14.2.2019).

V **von Ketelhodt, J.K.**, Manzi, M.S.D, Durrheim, R.J. 2019. Post-Stack Denoising of Legacy Reflection Seismic Data: Implications for Coalbed Methane Exploration, Kalahari Karoo Basin, Botswana. Exploration Geophysics, (major revision submitted 14.1.2019, first submitted 7.8.2018).

Further publications were made during my PhD studies, which do not form part of this thesis

VI **von Ketelhodt, J.K.**, Fechner, T., Tweeton, D.R., Manzi, M.S.D, Durrheim, R.J. 2017. Anisotropy Parameters from Shear and Compressional Wave Borehole Tomographic Measurements. *12th Annual AfricaArray Workshop*, 27 June - 1 July 2017, Johannesburg, South Africa.

VII **von Ketelhodt, J.K.**, Fechner, T., Manzi, M.S.D, Durrheim, R.J. 2017. Multi - Component Anisotropic Seismic Borehole Tomography. *Extended Abstract, 15th SAGA Biennial Conference & Exhibition*, 10-13 September 2017, Cape Town, South Africa.

VIII **von Ketelhodt, J.K.**, Manzi, M.S.D, Durrheim, R.J. Fechner, T., 2018. Joint-Inversion of Borehole Tomographic Data. Extended Abstract, *80th EAGE Conference & Exhibition*, 11-14 June 2018, Copenhagen, Denmark.

IX **von Ketelhodt, J.K.**, Manzi, M.S.D, Durrheim, R.J. Fechner, T., 2019. Inversion for seismic anisotropy parameters from P- and S-wave Cross-Borehole Measurements. Abstract, *79th Conference of the Deutsche Geophysikalische Gesellschaft*, 4-8 March 2019, Braunschweig, Germany.

TABLE OF CONTENTS

1. INTRODUCTION 16
   1.1 Structure of the Thesis 17
2. GEOPHYSICAL THEORY 20
   2.1 Seismic Tomography 20
      2.1.1 SIRT algorithm 23
      2.1.2 LSQR algorithm 24
      2.1.3 Joint-inversion 26
   2.2 S-wave Velocities for Geotechnical Site Characterisation 27
   2.3 Seismic Anisotropy 29
   2.4 Acquisition of Seismic Data for Tomographic Analysis 37
   2.5 Curvelet Transform 41
3. PUBLICATION I: ELASTIC PARAMETERS FROM COMPRESSIONAL AND SHEAR WAVE TOMOGRAPHIC SURVEY: A CASE STUDY FROM KUALA LUMPUR, MALAYSIA 44
   3.1 Introduction 44
   3.2 Methodology 46
   3.3 Data Processing and Analysis 46
   3.4 Results and Discussion 48
   3.5 Conclusion 53
4. PUBLICATION II: CHARACTERISATION OF GROUND MOTION RECORDING STATIONS IN THE GRONINGEN GAS FIELD 54
   4.1 Introduction 54
   4.2 Methods and Setup 56
      4.2.1 Overview 56
      4.2.2 SCPT 58
      4.2.3 MASW and microtremor array method 61
      4.2.4 Cross-hole tomography 70
      4.2.5 Seismic interferometry at vertical seismic arrays 71
   4.3 Integration of Various Methods 71
   4.4 Discussion 74
      4.4.1 Performance of techniques and sampling scales 74
      4.4.2 Comparison to other types of V_S estimates and derived analyses 75
   4.5 Conclusions 78

5. PUBLICATION III: JOINT-INVERSION OF CROSS-BOREHOLE P-WAVES, HORIZONTALLY AND VERTICALLY POLARISED S-WAVES: TOMOGRAPHIC DATA FOR HYDROGEOPHYSICAL SITE CHARACTERISATION 80
5.1 Introduction 80
5.2 Geology of the SAFIRA Site 81
5.3 Data Acquisition 82
5.4 Tomographic Inversion 85
5.4.1 Separate inversion 85
5.4.2 Joint-inversion 87
5.5 Results 89
5.5.1 Separate inversion 89
5.5.2 Joint-inversion 91
5.5.3 Resolution and data accuracy 93
5.6 Discussion 93
5.6.1 Elastic properties 93
5.6.2 Estimation of anisotropic effects 95
5.7 Conclusion 97
6. PUBLICATION IV: SEISMIC VTI PARAMETER INVERSION FROM P- AND S-WAVE CROSS-BOREHOLE MEASUREMENTS IN AN AQUIFER ENVIRONMENT 98
6.1 Abstract 98
6.2 Introduction 98
6.3 Tomographic Inversion Theory 100
6.3.1 VTI model 100
6.3.2 First order traveltime perturbation equation 101
6.3.3 Joint-inversion for anisotropy parameters 103
6.3.4 Constraints 104
6.3.5 Iterative inversion scheme 106
6.4 Synthetic Verification 106
6.5 Application to the SAFIRA Site 108
6.5.1 The SAFIRA dataset 108
6.5.2 Polarization analysis 110
6.5.3 Estimation of anisotropy 116
6.5.4 Inversion for anisotropy parameters 118
6.6 Resolution 121
6.7 Discussion 124
6.8 Conclusions 127

7. PUBLICATION V: POST-STACK DENOISING OF LEGACY REFLECTION SEISMIC DATA: IMPLICATIONS FOR COALBED METHANE EXPLORATION, KALAHARI KAROO BASIN, BOTSWANA 128
7.1 Abstract 128
7.2 Introduction 128
7.3 Geological Setting 131
7.4 Legacy Seismic Data 132
7.5 Curvelet Denoising 135
7.6 Application to Legacy Coalbed Methane Dataset 143
7.7 Discussion 150
7.8 Conclusion 151
8. CONCLUSIONS AND OUTLOOK 153
8.1 Conclusions 153
8.2 Outlook 153
9. REFERENCES 156
10. APPENDIX 169
10.1 Joint-Inversion – Matlab Code Instructions 169
10.2 Inversion for Anisotropy Parameters – Matlab Code Instructions 169
10.3 Curvelet Denoising – Matlab Code Instructions 169

TABLE OF FIGURES

Figure 2.1: Principle of cross-borehole seismic traveltime tomography 20
Figure 2.2: Principle of discretisation in seismic tomography 21
Figure 2.3: Relationship between the Shear modulus and the shear strain 27
Figure 2.4: Example of a seismic anisotropic rock. 30
Figure 2.5: Difference between wavefront velocity and raypath velocity in anisotropic media 32
Figure 2.6: Forward modelling of anisotropy parameters 34
Figure 2.7: Forward modelling of SV-wavefront anisotropy effects 35
Figure 2.8: Anisotropy effect for crosshole measurements compared to surface reflection survey 36
Figure 2.9: Borehole sources for generating P- and S-waves in boreholes 38
Figure 2.10: Impulse generator, horizontal source and vertical source 38
Figure 2.11: Borehole receivers used for tomography 39
Figure 2.12: Typical S-wave acquisition sequence 40
Figure 2.13: Curvelets of different scales and angular directions 42
Figure 2.14: Denoising procedure using curvelet thresholding 43
Figure 3.1: Examples shot gathers 48
Figure 3.2: Tomographic inversions for P-wave and the S-wave traveltimes 49
Figure 3.3: Elastic Parameters 50
Figure 3.4: Density zonation and Shear Modulus 52
Figure 4.1: Location of recording stations in the Groningen field in the north of the Netherlands 55
Figure 4.2: Schematic illustration of offset SCPT setup 59
Figure 4.3: CPT and SCPT data for station BLOP 60
Figure 4.4: OSCPT result for SCPT19 and SCPT25 for station BLOP 61
Figure 4.5: Survey setup for MASW and microtremor array 62
Figure 4.6: Sorting and pre-processing of MASW data 63
Figure 4.7: Schematic representation of CMPcc binning 64
Figure 4.8: MASW result for station BWIR 65
Figure 4.9: CMPcc result for station BWIR 66
Figure 4.10: Dispersion curves determined with the ESAC method 67
Figure 4.11: Comparison of dispersion plots for station BKAN 69
Figure 4.12: V_S and V_P images from cross-hole tomography for station BUHZ 70
Figure 4.13: V_S profiles for station BWSE from different measurement techniques 72
Figure 4.14: Example of SCPT profile on MASW for station BWSE 73
Figure 4.15: V_S profiles at selected B stations 74
Figure 4.16: V_S profiles at selected G stations 76
Figure 4.17: Comparison for selected B stations of empirical amplification 77

Figure 4.18: Comparison for selected G stations of FAS spectral ratio 78
Figure 5.1: Overview of the borehole locations at the SAFIRA research facility in Germany 82
Figure 5.2: Example of a raw receiver gather for tomographic slice plane B29-B51 83
Figure 5.3: SV-, SH- and P-wave traveltimes of the SAFIRA research site 85
Figure 5.4: Individually inverted P-, SH- and SV-wave tomograms 90
Figure 5.5: Jointly inverted P-, SH- and SV-wave tomograms 92
Figure 5.6: Ratio of the jointly inverted P-wave to S-wave velocities 94
Figure 5.7: Receiver gathers at a depth of 22 m 95
Figure 5.8: Ratio of the jointly inverted SV- and SH-wave tomograms 96
Figure 6.1: Synthetic anisotropic models 108
Figure 6.2: Overview of boreholes employed for the seismic acquisition 109
Figure 6.3: Example hodogram analysis 111
Figure 6.4: P-wave polarization of the crosshole data subset 113
Figure 6.5: S-wave polarization for boreholes B27 and B51 114
Figure 6.6: S-wave polarization for boreholes B44 and B45 115
Figure 6.7: Receiver gather at a depth of 22 m 117
Figure 6.8: Straight ray velocities plotted as a function of the ray path angle 118
Figure 6.9: Joint-inversion for VTI parameters for tomographic Plane 1 120
Figure 6.10: Joint-inversion for VTI parameters for tomographic Plane 2 121
Figure 6.11: Coarse checkerboard VTI-model with approximately 3×3 m cell sizes 122
Figure 6.12: Fine checkerboard VTI-model with approximately 1.5×1.5 m cell sizes 123
Figure 6.13: The absolute error estimated for the VTI parameters 124
Figure 6.14: SV-wave velocity as a function of the raypath angle for different Vp/Vs ratios 125
Figure 7.1: The distribution of the Kalahari Karoo Basin in Botswana 129
Figure 7.2: Stratigraphy of the Central Kalahari Karoo Basin 132
Figure 7.3: A curvelet in the spatial and frequency domain 136
Figure 7.4: Example of a seismic image and its deconstruction into multi-scale curvelets 137
Figure 7.5: The Marmousi2 model 138
Figure 7.6: Marmousi2 with added broadband white noise 139
Figure 7.7: Marmousi2 with added self-similar noise 140
Figure 7.8: The frequency-wavenumber domains corresponding to Fig. 7.6 141
Figure 7.9: The frequency-wavenumber domains corresponding to Fig. 7.7 142
Figure 7.10: The inverse curvelet transform applied to different scales and angular wedges 143
Figure 7.11: Curvelet denoising applied to the CBM Botswana dataset 144
Figure 7.12: Improvements to interpretation after curvelet denoising 145
Figure 7.13: Curvelet denoising applied to the original data of Line 2 146
Figure 7.14: Instantaneous phase computed for CBM Botswana subsets 148

Figure 7.15: Stacked and denoised seismic sections and interpretation 149

TABLE OF TABLES

Table 4.1: Summary of survey setup for the four different shear-wave methods 58
Table 7.1: Data acquisition parameters of the 2D CBM Botswana dataset 133
Table 7.2: Processing steps applied to L1-L3 reflection seismic data 135

LIST OF ABBREVIATIONS

1D	One-Dimensional
2D	Two-Dimensional
3D	Three-Dimensional
AFs	Amplification Functions
ART	Algebraic Reconstruction Technique
CMPcc	Common Midpoint cross-correlation
CPT	Cone Penetration Test
FAS	Fourier Amplitude Spectra
FWI	Full Waveform Inversion
HTI	Horizontally Transversely Isotropic
MASW	Multichannel Analysis of Surface Waves
OSCPT	Offset Seismic Cone Penetration Test
PVC	PolyVinyl Chloride
RMS	Root-Mean-Squared
S/B	Surface-to-Borehole
SAFIRA	SAnierungs-Forschung In Regional kontaminierten Aquiferen, i.e. research on remedial measures in regionally contaminated aquifers, research facility in Zeitz, Germany
SCPT	Seismic Cone Penetration Test
SH-wave	Horizontally polarised shear wave
SIRT	Simultaneous Iterative Reconstruction Technique
SPT	Standard Penetration Test
SV-wave	Vertically polarised shear wave
Tcm	Trillion cubic meters
TFs	Transfer Functions
TTI	Transverse Isotropy with a tilted axis of symmetry
VSP	Vertical Seismic Profiling
VTI	Vertically Transversely Isotropic

1. INTRODUCTION

Geophysical surveys provide cost-effective means for the exploration of geological structures. Seismic traveltime tomography in particular is a high-resolution method commonly applied to various fields. Seismic data for tomographic analysis has been acquired for geotechnical site characterisation (Yamamoto et al., 1994; Angioni et al., 2003; Rumpf and Tronicke 2014), hydrogeological studies (Fechner, 1998; Paasche et al., 2006; Doetsch et al., 2010), mining exploration (Seebold et al., 1999), the monitoring of radioactive nuclear waste (Wong et al., 1983; Marelli et al., 2010), and reservoir characterisation (Macrides et al., 1988; Zhang et al., 2012). Commonly only the P-wave is interpreted in such surveys (Paasche et al., 2011). In this thesis, I evaluate S-wave tomography in different geological settings and find optimal processing and interpretation flows adapted to different exploration questions. In general, I show that jointly measuring and interpreting P- and S-waves offers many new insights compared to P-wave data on their own.

Firstly, S-wave measurements for tomographic analysis are advantageous for geotechnical applications, as they do not suffer from sampling biases as is the case with direct push technologies, such as the Standard Penetration Test (SPT) or the Cone Penetration Test (CPT) (Andrus and Stokoe, 2000; Clayton et al., 2012). In addition, the S-wave velocity is a mechanical soil property and directly related to the small-strain Shear modulus (Mayne, 2001). Jointly interpreting both the P- and S-wave data enables the determination of additional elastic parameters such as Poisson's ratio, Young's modulus and the Bulk modulus, which, as shown by Dietrich and Tronicke (2009), can aid the geological interpretation.

Secondly, different directional seismic sources can be employed while maintaining the same acquisition geometry. Thus, a jointly measured dataset consisting of different traveltimes (P- and S-wave traveltimes) can be acquired. These traveltimes enable the estimation of the P- and S-wave velocity, by jointly inverting the different datasets. Often a direct parameter coupling or a structural coupling is emplaced (Gallardo and Meju, 2003, 2004; Moorkamp et al., 2011). Such a joint inversion ensures that the error is minimised taking all data into consideration and that the resulting tomographic images are compatible. Generating and interpreting only P-wave data does not offer this capability.

Finally, when employing directional sources in an anisotropic environment, different S-wave modes are generated, such as a horizontally polarised S-wave (SH-wave) and a vertically polarised S-wave (SV-wave) (Ku and Mayne, 2014; Mackens et al., 2017). Recording these different S-wave mode traveltimes, enables an anisotropy parameters estimation. Zhou et al. (2008) describe such an anisotropy parameter estimation, which they realise with an inversion based on the traveltime perturbation equation.

The second part of the thesis focuses on the application of the curvelet transform to reflection seismic data. The curvelet transform is a multi-resolution transform and was originally designed to denoise images (Starck et al. 2002; Candès and Guo 2002; Candès and Donoho 2004). Recently, the curvelet transform has been successfully applied to reflection seismic data for denoising purposes (Hennenfent and Herrmann, 2006; Neelamani et al., 2008; Shan et al., 2009; Górszczyk et al., 2014, Naghizadeh and Sacchi, 2018). I show that legacy reflection seismic data can be cost-effectively denoised and enhanced by manipulating the data in the curvelet domain.

This thesis complements the work of the Seismic Research Centre at the University of the Witwatersrand. Over the last 10 years the seismology research group has worked with 2 and 3D reflection seismic data from the Witwatersrand Basin, the Bushveld Complex and the Orange Basin, with geological and geophysical logs, conducted laboratory rock physics and generated synthetic seismograms. This thesis expands the research group's know-how for near-surface studies, both in terms of techniques, notably joint-inversion of P- and S-waves, the estimation of anisotropy and the application of the curvelet transform, and in terms of the type of data, notably crosshole and coalbed methane reflection data from the Kalahari-Karoo Basin.

1.1 Structure of the Thesis

The thesis is based on five papers and organised as follows.

Chapter 2 serves as an overview of the geophysical theory addressed in the subsequent publications. First, the theory of seismic tomography, with the different inversion algorithms, is covered. Then the advantages of generating and interpreting S-waves in conjunction with P-waves for geotechnical site characterisation is discussed, prior to introducing the concept of seismic anisotropy. Further, the acquisition of seismic data for tomographic analysis is described, with the different equipment shown. Finally, the curvelet transform and its ability to denoise seismic data is introduced.

Chapter 3, **Paper I** shows the application of a co-located P- and S-wave tomography survey in Kuala Lumpur to delineate a large zone of weakness for a geotechnical site characterisation of a large-scale infrastructural project. Conducting such a co-located survey showed a better interpretation capability than a P- or S-wave tomogram on its own. Elastic parameters, i.e. P- to S-wave velocity ratio, Poisson's ratio, bulk modulus, Young's modulus and the shear modulus were derived from the P- and S-wave tomography data. This enhanced the interpretation, as areas with limited traveltime accuracy and thus, an increase in tomographic error, could be identified, and the extent of a large cavity could be estimated more reliably.

As the papers first author, I lead the data acquisition, processed and interpreted the data and wrote the paper. The second author, Thomas Fechner, had the original idea of acquiring and interpreting co-located P- and S-wave tomography data. The third and fourth author, my PhD supervisors Musa Manzi and Raymond Durrheim, read the manuscripts and provided thoughtful comments.

Chapter 4, **Paper II** describes different measurements conducted to derive the S-wave velocity in the area of the onshore Groningen gas field in the Netherlands up to a depth of 30 m. These measurements include offset seismic cone penetration tests (OSCPT), multichannel analysis of surface waves (MASW), microtremor array, cross-borehole tomography and suspension P-S logging. Specifically, MASW, OSCPT and tomography measurements revealed considerable lateral S-wave velocity variations of the unconsolidated sediments. The measured S-wave profiles were used to update the velocity model in the Groningen gas field and will be useful for a better seismic hazard and risk analysis in the future.

The primary authors of the paper, Rik Noorlandt, Pauline Kruiver, Marco de Kleine, Marios Karaoulis and Ger de Lange of Deltares were responsible for the geophysical project management, data integration and wrote the majority of the paper. I contributed by leading the tomography data acquisition, analysing the data and writing of the tomography section in the paper. Other co-authors contributed for data acquisition and analysis, or were project partners.

Chapter 5, **Paper III** discusses seismic cross-borehole measurements in a near-surface aquifer environment at the SAFIRA research facility in Zeitz, Germany. Two different directional sources were employed, a horizontal and vertical source, and the data were recorded with a tri-axial multi-level receiver array. The two different directional sources produced P-waves, horizontally polarised S-waves and vertically polarised S-waves. A joint-inversion utilising cross-gradient constraints improved the S-wave tomograms and enabled a better interpretation than the individually inverted tomograms on their own.

As first author, my contribution to the paper was the following. I had the original idea of testing with two directional sources to acquire data for tomographic analysis in an overconsolidated environment. I initiated a search for a suitable test site, conceptualised the survey and lead the data acquisition on-site. I further had the idea of jointly interpreting the data, wrote the inversion code, analysed the data and wrote the paper. The second author, Thomas Fechner, had the idea of manufacturing the equipment that was used, supported me with the survey conceptualisation, helped with the data acquisition, partially funded the project and read and improved the manuscripts. The third and fourth author, my supervisors Musa Manzi and Raymond Durrheim, read the manuscripts and provided thoughtful comments.

Chapter 6, **Paper IV** discusses the same seismic dataset for tomographic analysis of **Paper III**. However, in this paper, anisotropy effects are examined in more detail. First, a polarisation analysis is conducted, which revealed an anisotropy zone that can be approximated by a vertically transversely isotropic (VTI) medium. Then, a joint-inversion for VTI anisotropy parameters is proposed utilising cross-gradient constraints to stabilise the inversion. Finally, an inversion for the anisotropy parameters is conducted, which shows considerable (10% to 15%) S-wave anisotropy. In comparison the P-wave anisotropy is negligible, leading to the interpretation that S-wave anisotropy is far more severe in a near-surface environment compared to P-wave anisotropy.

The author contributions for this paper are similar to the ones for Paper III, since the same dataset was used. As first author, I had the idea of deriving anisotropy parameters by inverting the traveltimes, wrote the joint-inversion code, analysed the data and wrote the paper. The second and third author were my supervisors Musa Manzi and Raymond Durrheim, who read and improved the manuscripts. Fourth author, Thomas Fechner, had the same contribution as for Paper III.

Chapter 7, **Paper V** shows the application of the curvelet transform to enhance legacy seismic data from the Kalahari-Karoo Basin, Botswana. Since the discovery of coalbed methane (CBM) resources, these seismic data, initially acquired in the 1980s, became relevant again. The paper describes an effective procedure to denoise legacy post-stack reflection seismic data, by operating in the curvelet domain and manipulating the curvelet coefficients by different thresholding techniques.

My contribution as first author was the following. I wrote the code for denoising the data, processed the data and wrote the paper. The second author, Musa Manzi, had the original idea of applying the curvelet transform to data from the Kalahari-Karoo Basin and read and improved the manuscripts. Third author, Raymond Durrheim, also read and improved the manuscripts.

Chapter 8 concludes the findings and provides an outlook for future research.

2. GEOPHYSICAL THEORY

2.1 Seismic Tomography

Computerised tomography has its origin in medical imaging, where for example X-Ray or ultrasound sources and receivers are closely placed around a patient to produce detailed images used for diagnoses (e.g. Kak, 1979). The geophysical community caught on to the new opportunities provided by tomographic imaging, both in the exploration and global geophysical spheres. For example, tomographic imaging based on seismic traveltimes from earthquake sources proved highly successful in imaging the circulation of material in the mantle (van der Hilst et al., 1997), subduction slabs (van der Hilst et al., 1991; Pavlis et al., 2012), and mantle plumes (Zhao, 2004). The first application of tomographic imaging in an exploration seismological setting was conducted by Bois et al. in 1972 between two reservoir wells. Since then, cross-borehole seismic tomography has evolved to a commonly applied high-resolution method.

The principle of seismic tomography is to estimate physical property distributions by using a number of different projections. These projections are usually the traveltimes along a raypath, but can also be amplitudes (Quan and Harris, 1997), or more recently the full seismic waveform (Lüth et al., 2014). Figure 2.1 shows the principle of tomography by sampling a medium in between two vertical boreholes. The lines show the projections, in this context they are the raypaths of the seismic waves. From the traveltime inversion a physical property, such as seismic slowness, can be estimated.

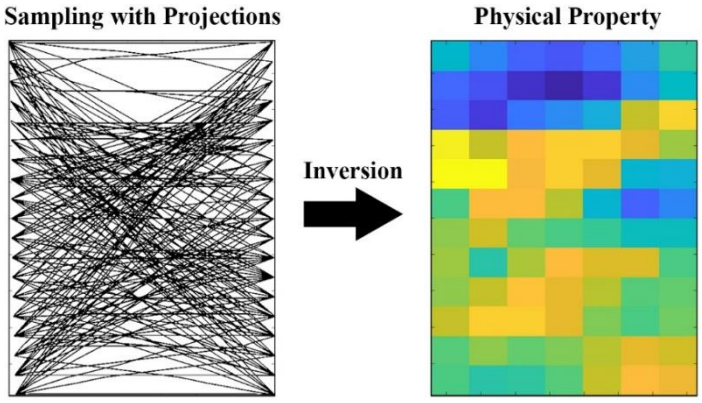


Figure 2.1: Principle of cross-borehole seismic traveltime tomography. The lines show the sampling of the medium and are the raypaths, i.e. the projections. From a traveltime inversion a physical property distribution, for example a 2D P-wave slowness distribution, can be estimated.

Seismic tomography is a subset of inverse theory, whereby a function, i.e. the physical property, is reconstructed from its line or plane integrals (Natterer, 1986). In other words, the measured projections are the Radon Transform (Rf) of a physical property function (f) summed along a line (L)

$$Rf(L) = \int_L f(x)|dx|. \tag{2.1}$$

The challenge is to find the physical property (*f*), from the measurements (*Rf*), through the inverse Radon Transform, for which there are many different approaches. These can be categorised into transform methods, such as filtered backprojection and Fourier techniques, and series expansion methods, such as the Simultaneous Iterative Reconstruction Technique (SIRT) algorithm and least-squares methods (Stewart, 1991).

Most of these methods, discretise the medium into many different cells, with the medium property assumed constant in each cell. Generally in seismic tomography, we have to sum the model property in a given cell with the distance the ray has travelled in that particular cell. This principle of discretisation and summation for a single raypath is shown in Figure 2.2.

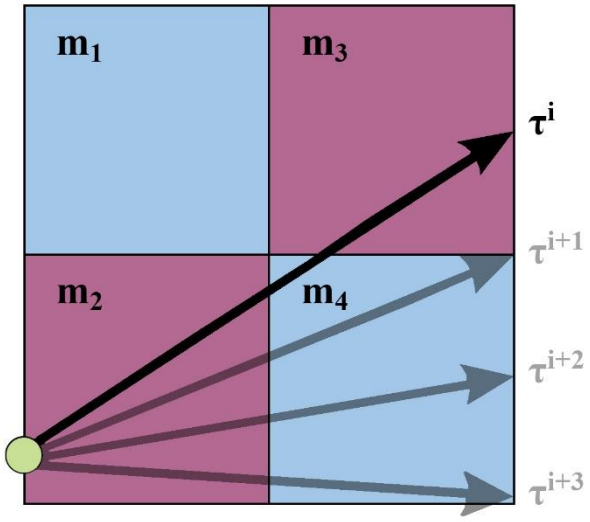


Figure 2.2: Principle of discretisation in seismic tomography. A raypath passes through cells m_2, m_3 and m_4. The traveltime (τ^i) is a sum of all model cell properties and the raypath segment distances of x_2, x_3 and x_4 (modified from Vesnaver and Böhm, 2000).

The raypath associated with the traveltime (τ^i) in Figure 2.2, passes through cells m_2, m_3 and m_4. Thus, the traveltime (τ^i) is given by

$$\tau^i = x_2^i m_2 + x_3^i m_3 + x_4^i m_4, \tag{2.2}$$

with the model slowness (m_j) and raypath segments (x_j), that correspond to the i^{th} raypath. The raypath segments, i.e. lengths of the ray in each cell, are simply the traveltime derivatives (or Jacobian matrix) with respect to the slowness model

$$x_j^i = \frac{\partial \tau_j^i}{\partial m_i}. \tag{2.3}$$

Thus, for many raypaths, equation 2.2 can be expressed in matrix form as

$$\boldsymbol{\tau} = \frac{\partial \tau}{\partial m} m = \mathbf{J}\mathbf{m}, \tag{2.4}$$

with the Jacobian matrix (**J**), the discretised slowness model (**m**), and the observed traveltimes ($\boldsymbol{\tau}$).

Equation 2.4 is non-linear, in that the raypaths (x_j^i) are dependent on the slowness model ($\mathbf{m}_k$) and need to be updated after the computation of a new model ($\mathbf{m}_{k+1}$), at iteration $k + 1$. Therefore, equation 2.4 is iteratively solved, starting with a first guessed model (e.g. the average velocity for all traveltimes with straight, linear raypaths). Subsequent raytracing provides calculated traveltimes, which are then subtracted from the observed traveltimes, forming a traveltime residual. Thus, the slowness model is updated by solving for a model perturbation ($\Delta\mathbf{m}$) that fits the traveltime residual ($\Delta\boldsymbol{\tau}$)

$$\mathbf{J}\Delta\mathbf{m} = \Delta\boldsymbol{\tau}. \tag{2.5}$$

The model (**m**) is then updated by adding the perturbation ($\Delta\mathbf{m}$)

$$\mathbf{m}_{k+1} = \mathbf{m}_k + \Delta\mathbf{m}_k. \tag{2.6}$$

Further iterations are computed, starting with a raytracing through this updated model ($\mathbf{m}_{k+1}$).

Because, a raypath generally only passes through a very limited number of model cells, the Jacobian (**J**) has the following features. Firstly, **J** consists mainly of zeros (in general approximately 1% are non-zero). Secondly, the matrix is usually large. Even for a relatively small traveltime inversion, we have at least 1,000 traveltimes and 10 x 20 model cells. The Jacobian (**J**) would then have 200,000 (mostly zero) entries. Thirdly, the matrix is ill-conditioned, with condition numbers as large as 10^5 not uncommon (Scales et al., 1988). Finally, even though the matrix has generally more rows than columns (i.e. more traveltimes to fit than model cells), it is generally still an under-determined or mixed-determined problem that needs to be solved. For that reason, no single solution exists to equation 2.5 and it is usually not possible, to simply compute the generalised inverse ($\mathbf{J}^{-g}$) and solve for the model perturbations ($\Delta\mathbf{m}$) with

$$\Delta\mathbf{m} = \mathbf{J}^{-g}\Delta\boldsymbol{\tau}. \tag{2.7}$$

Since there is no unique model to fit all the observations ($\boldsymbol{\tau}$), equation 2.5 is generally solved in a least-squares sense and an objective function is defined that is subsequently minimised. There are different methods to achieve this. In this thesis, I used two different approaches. Firstly, I solve equation 2.5 by using the software GeotomCG, which employs the Simultaneous Iterative Reconstruction Technique (SIRT) algorithm. I used this algorithm in Chapter 3 and 4, for example to invert P- and S-wave

traveltimes and estimate P- and S-wave velocities in a karstic environment in Kuala Lumpur and to obtain elastic properties prior to construction of a Mass Rapid Transit station. Secondly, equation 2.5 can be solved with an LSQR algorithm, which I used in Chapter 5 to perform a joint-inversion for P- and S-wave traveltimes to estimate the velocities at the SAFIRA site, and in Chapter 6 to estimate anisotropy parameters, also at the SAFIRA site.

2.1.1 SIRT algorithm

The SIRT algorithm is based on the Kaczmarz method (1937) of solving simultaneous equations and first proposed by Dines and Lytle (1979), and summarised by Stewart (1991). Mathematically, equation 2.5 is solved, expressed as

$$\Delta\tau^i = \sum_j \mathrm{x}_j^i \, \Delta\mathrm{m}_j^i, \tag{2.8}$$

with the traveltime residuals ($\Delta\tau^i$), the model slowness (m_j^i) and raypath segments (x_j^i), subject to the constraint that the model perturbations should be as small as possible, i.e.

$$\min \sum_j \left(\Delta\mathrm{m}_j^i\right)^2. \tag{2.9}$$

Using a Lagrange multiplier (λ), an objective function (K) is formulated for equation 2.8 with constraint 2.9 as (Al-Yahya, 1985, p. 135)

$$K = \sum_j \left[\left(\Delta\mathrm{m}_j^i\right)^2 - \lambda \mathrm{x}_j^i \Delta\mathrm{m}_j^i\right] + \lambda\Delta\tau^i. \tag{2.10}$$

This objective function (equation 2.10) needs to be minimised. Thus, the derivative with respect to the model parameter ($\partial K / \partial \Delta m_j^i$) should be zero, i.e.

$$\frac{\partial K}{\partial \Delta\mathrm{m}_j^i} = 2\Delta\mathrm{m}_j^i - \lambda \mathrm{x}_j^i = 0, \tag{2.11}$$

$$\Delta\mathrm{m}_j^i = \frac{\lambda \mathrm{x}_j^i}{2}. \tag{2.12}$$

When substituting equation 2.12 into 2.8, we can solve for the Lagrange multiplier (λ)

$$\lambda = \frac{2\Delta\tau^i}{\sum_j \mathrm{x}_j^{i\,2}}. \tag{2.13}$$

With the known Lagrange multiplier (equation 2.13), the model perturbation (equation 2.12) is stated as

$$\Delta m_j^i = \frac{\Delta\tau^i \mathrm{x}_j^i}{\sum_j \mathrm{x}_j^{i\,2}}. \tag{2.14}$$

This equation can be understood as the multiplication of two factors. Factor one is given by $\Delta\tau^i / \sum \mathrm{x}_j^i$ and is the total slowness error. Factor two is given by $\mathrm{x}_j^i / \sum \mathrm{x}_j^i$ and is the proportion of the i$^{\mathrm{th}}$ ray in a

particular j[th] cell. Thus, the product of these two factors is the (smallest possible) slowness error that is proportionally assigned to the cell (Stewart, 1991). This is essentially the algebraic reconstruction technique (ART), whereby the model (Δm_j^i) is continuously updated, raypath by raypath.

A better approach is to update the perturbation contributions only at the end, after all perturbation contributions are determined. This is how the SIRT algorithm works. In other words, the j[th] cell slowness (m_j) is updated simultaneously using all of the slowness errors that are computed for the raypaths that intersect that j[th] cell, such that

$$\Delta m_j = \frac{1}{N}\sum_{i=1}^{N} \Delta m_j^i, \tag{2.15}$$

with the number of raypaths (N) that intersect cell m_j.

This model slowness perturbation (Δm, equation 2.15), is added to the previous slowness model (m) by using equation 2.6. Subsequently, a raytracing algorithm, in case of GeotomCG a raytracing algorithm of Um and Thurber (1987), is employed, which finds new raypath segments. The process of finding a new slowness perturbation (equations 2.14 and 2.15) is then repeated. The stopping criteria is usually limited by the number of iterations (e.g. 20 raytracing and SIRT iterations).

2.1.2 LSQR algorithm

For the SIRT algorithm the objective function (equation 2.10) was defined with the constraint of minimising the model perturbation update. Alternatively, an objective function can be defined directly from the fundamental tomographic equation 2.5 by minimising a residual error (**r**) of the form (Scales et al., 1988)

$$\| \mathbf{r} \|_p = \| \Delta\boldsymbol{\tau} - \mathbf{J}\Delta\mathbf{m} \|_p , \quad p \geq 1. \tag{2.16}$$

Generally, for the sake of simplicity, the least-squares version of equation 2.16 is chosen, although some publications show that the choice of an $\ell 1$ norm, or an $\ell 2$ norm with the removal of outliers, i.e. $1 \leq p \leq 2$, may be better, since outliers effect the least-squares $\ell 2$ norm more (Nolet, 1987, p. 14). Nonetheless, the least-squares version of equation 2.16 is given by

$$\| \mathbf{r} \|_2 = \| \Delta\boldsymbol{\tau} - \mathbf{J}\Delta\mathbf{m} \|_2, \tag{2.17}$$

$$\mathbf{r}^T\mathbf{r} = (\Delta\boldsymbol{\tau} - \mathbf{J}\Delta\mathbf{m})^T(\Delta\boldsymbol{\tau} - \mathbf{J}\Delta\mathbf{m}), \tag{2.18}$$

$$\mathbf{r}^T\mathbf{r} = (\Delta\boldsymbol{\tau}^T - \Delta\mathbf{m}^T\mathbf{J}^T)(\Delta\boldsymbol{\tau} - \mathbf{J}\Delta\mathbf{m}), \tag{2.19}$$

$$\mathbf{r}^T\mathbf{r} = \Delta m^T J^T J\Delta m - \Delta m^T J^T \Delta\tau - \Delta\tau^T J\Delta m + \Delta\tau^T\Delta\tau, \tag{2.20}$$

$$\mathbf{r}^T\mathbf{r} = 2\left(\frac{1}{2}\Delta\mathbf{m}^T\mathbf{J}^T\mathbf{J}\Delta\mathbf{m} - \Delta\mathbf{m}^T\mathbf{J}^T\Delta\boldsymbol{\tau}\right) + \Delta\boldsymbol{\tau}^T\Delta\boldsymbol{\tau}. \tag{2.21}$$

Minimising $\mathbf{r}^T\mathbf{r}$ resembles the minimisation of the quadratic form in matrix notation, where the problem

$$\min\left(\frac{1}{2}\mathbf{x}^T\mathbf{A}\mathbf{x} - \mathbf{x}^T\mathbf{b}\right) \Leftrightarrow \mathbf{A}\mathbf{x} = \mathbf{b}. \tag{2.22}$$

Therefore, when finding the minimum of $\mathbf{r}^T\mathbf{r}$ (equation 2.21), the least-squares version of equation 2.5 emerges as

$$\Delta\mathbf{m} = (\mathbf{J}^T\mathbf{J})^{-1}\mathbf{J}^T\Delta\boldsymbol{\tau}. \tag{2.23}$$

The problem with this least-squares version is its sensitivity to noise. For that reason the objective function is defined with an additional Tikhonov regularisation term ($\boldsymbol{\Gamma}$), such that

$$\| \mathbf{r} \|_2 = \| \Delta\boldsymbol{\tau} - \mathbf{J}\Delta\mathbf{m} \|_2 + \| \boldsymbol{\Gamma}\Delta\mathbf{m} \|_2 \tag{2.24}$$

and the least-squares version then given by

$$\Delta\mathbf{m} = (\mathbf{J}^T\mathbf{J} + \boldsymbol{\Gamma}^T\boldsymbol{\Gamma})^{-1}\mathbf{J}^T\Delta\boldsymbol{\tau}. \tag{2.25}$$

These least-squares equations (equations 2.23 and 2.25) can be solved with an LSQR algorithm (Paige and Saunders, 1982), which is a variant of the conjugate gradient algorithm (Nolet, 1987). The LSQR algorithm is better, both in terms of error and convergence (Nolet, 1984; Nolet, 1985), than the SIRT algorithm, and employs a factorisation of the matrix product $\mathbf{J}^T\mathbf{J}$ (or $\mathbf{J}^T\mathbf{J} + \boldsymbol{\Gamma}^T\boldsymbol{\Gamma}$) into an orthogonal matrix ($\mathbf{Q}$) and an upper triangular matrix ($\mathbf{R}$), i.e. QR-factorisation. Finding the inverse of this factored matrix $(\mathbf{QR})^{-1}$ is then straightforward, since the inverse of an orthogonal matrix is equivalent to its transpose, i.e. $\mathbf{Q}^{-1} = \mathbf{Q}^T$, and the inverse of an upper triangular matrix can be found easily by back substitution. Algorithmically, LSQR is iterative and has a stopping criteria based on convergence criteria, the residual or the number of iterations.

Equivalent to the SIRT algorithm, the slowness perturbation update $\Delta\mathbf{m}$ is added to the known slowness model $\mathbf{m}$ (equation 2.6). This process is repeated by starting with the next curved raytracing iteration through this new slowness model, until all curved raytracing iterations are performed and the resulting computed traveltimes are similar enough, e.g. root-mean-square error, to the observed traveltimes.

2.1.3 Joint-inversion

Previously, the model consisted only of a single parameter, e.g. P-wave slowness or S-wave slowness. When interpreting P- and S-wave traveltimes, recorded with the same acquisition geometry, then two model parameters, P-wave slowness and S-wave slowness, can be estimated by jointly inverting the P- and S-wave traveltimes. The simplest version of such a joint-inversion would be to expand the Jacobian matrix to accommodate both P- and S-wave raypath lengths, as well as the traveltime residual vector $\Delta\tau$ for both P- and S-wave traveltime residuals (Tryggvason et al., 2002; Moorkamp et al., 2011). Then the inversion result produces a model perturbation vector $\Delta\mathbf{m}$ for both the P- and S-wave velocity. Thus, the Jacobian ($\mathbf{J}$), model perturbation vector ($\Delta\mathbf{m}$) and residual traveltime vector ($\Delta\boldsymbol{\tau}$) are then given by

$$\mathbf{J} = \begin{pmatrix} \mathbf{J}_P & 0 \\ 0 & \mathbf{J}_S \end{pmatrix}, \tag{2.26}$$

$$\Delta\mathbf{m} = \begin{pmatrix} \Delta\mathbf{m}_P \\ \Delta\mathbf{m}_S \end{pmatrix}, \tag{2.27}$$

$$\Delta\boldsymbol{\tau} = \begin{pmatrix} \Delta\boldsymbol{\tau}_P \\ \Delta\boldsymbol{\tau}_S \end{pmatrix}, \tag{2.28}$$

with the subscripts P and S denoting P-wave and S-wave data. Everything else remains the same, such as the objective function and the solution using an LSQR algorithm.

The problem with this simple approach is the following. Firstly, the S-wave travels at a far lower velocity than the P-wave. Depending on the velocity ratio (v_P/v_S) the difference in traveltime is a factor of approximately 2 (consolidated rock, see Chapter 3) to 10 (near-surface soft sediments, see Chapter 4 and 5). Thus, when minimising the residual error, largely the S-wave traveltimes are fitted to a better S-wave slowness model. The P-wave traveltimes are only poorly fitted, since they play a small or even negligible role towards the error. Thus, an accurate S-wave slowness model is obtained, but a poor P-wave slowness model. For this reason, I introduced a factor that compensates for this resolution difference. This factor (β) is defined as the difference in standard deviation between the P- and S-wave traveltimes. Hence, the Jacobian and regularisation ($\boldsymbol{\Gamma}$) are expressed as

$$\mathbf{J} = \begin{pmatrix} \beta\mathbf{J}_P & 0 \\ 0 & \mathbf{J}_S \end{pmatrix}, \tag{2.29}$$

$$\boldsymbol{\Gamma} = \begin{pmatrix} \beta\boldsymbol{\Gamma}_P & 0 \\ 0 & \boldsymbol{\Gamma}_S \end{pmatrix}. \tag{2.30}$$

Such a joint-inversion approach was chosen in Chapter 5 and Chapter 6, with an additional structural constraint, i.e. cross-gradient constraints, to ensure good agreement between the resulting models.

2.2 S-wave Velocities for Geotechnical Site Characterisation

Usually P-waves are used more frequently for high-resolution cross-borehole seismic surveys for tomographic analysis than S-waves (Paasche et al., 2014). However, estimating the S-wave velocity has many advantages for geotechnical site characterization (Andrus and Stokoe, 2000; Clayton et al., 2012). Firstly, the S-wave velocity can be obtained in areas that are otherwise difficult to sample by drilling. Secondly, S-wave velocity measurements do not suffer from sampling biases as is the case with direct push technologies, such as the Standard Penetration Test (SPT) or the Cone Penetration Test (CPT). Thirdly, the S-wave velocity is a mechanical soil property and directly related to the small-strain Shear modulus (G_0), expressed by the relationship

$$G_0 = \rho v_S^2, \tag{2.31}$$

with the bulk density (ρ) and the elastic shear wave velocity (v_S) that is generated at very small strain amplitudes of less than $10^{-4}\%$ (Sully and Campanella, 1995). The relationship between the Shear modulus (G) and the shear strain (γ_S) is shown below in Figure 2.3. The Shear modulus increases with a decrease in the shear strain, which depends on the amplitude of a seismic vibration (A) and the S-wave velocity (v_S).

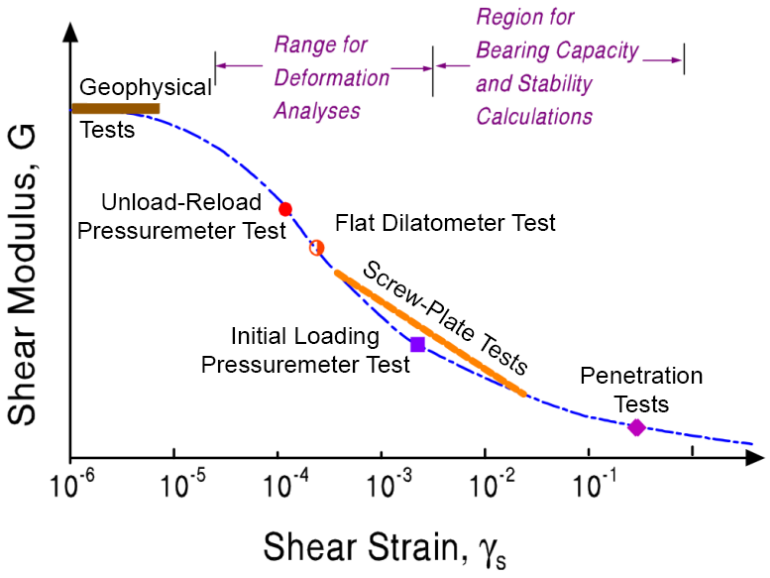


Figure 2.3: Relationship between the Shear modulus (G) and the shear strain (γ_S), modified after Mayne (2001) is shown. Note the inverse relationship between G and γ_S and the flattening out of G for very small γ_S. This flattening out is referred to as the maximum Shear modulus G_0. The Shear modulus axis is linear and magnitudes of G are dependent on the material.

This Shear modulus increases steadily for smaller shear strains, with the relationship flattening out for very small shear strains. This area is denoted as the maximum Shear modulus (G_{max}), or also denoted G_0. Even though the Shear modulus does not approach an asymptote, but instead continuously increases with smaller shear strains (Cox, 1856), this flattening out is practically considered as the upper stiffness

limit of the soil and is therefore an important parameter in geotechnical engineering (Clayton et al., 2012). For example it is used to determine the deflection of shallow and deep foundations, retaining walls and embankments (Mayne, 2001). It is also used to evaluate the liquefaction resistance of soils in earthquake prone environments (Andrus and Stokoe, 2000; Tokimatsu and Uchida, 1990). Importantly, G_0 applies to both drained and undrained environments, as the pore water pressure does not take effect at these small strains (Mayne, 2001).

Further elastic parameters can be calculated if both the P- and S-wave velocities are known. Among them are Poisson's ratio (ν), Young's modulus (E_0), the bulk modulus (K), and the ratio between the P-wave and S-wave velocity (v_P/v_S). These elastic parameters can be determined by

$$\nu = \frac{v_P^2 - 2v_S^2}{2(v_P^2 - v_S^2)}, \tag{2.32}$$

$$E_0 = 2G_0\,(1 + \nu), \tag{2.33}$$

$$K = \frac{E_0}{3 - 6\nu}, \tag{2.34}$$

with the P-wave velocity (v_P), the S-wave velocity (v_S), and the small strain shear stiffness (G_0).

The S-wave velocity of an earth material can be determined by a number of different seismic methods. Principally, they can be divided into surface and borehole methods. Among the surface methods it is possible to determine the S-wave velocity using refraction seismic or analysing surface waves, e.g. using the Continuous Surface Wave (CSW) or the Multichannel Analysis of Surface Waves (MASW) methods (Clayton et al., 2012). Borehole methods include the Downhole Test (DHT) and the Crosshole Test (CHT). In addition, S-wave velocities are often measured in conjunction with a direct-push system such as the seismic cone penetration testing (SCPT). Chapter 4 discusses different methods to estimate the S-wave velocity, which is then used to improve the characterisation of ground motion recording stations at the microtremor and earthquake-prone Groningen reservoir in the Netherlands. However, all of these methods, with the exception of refraction seismic S-wave surveys, obtain a 1D S-wave velocity measurement along a profile or depth interval.

Of the above methods, crosshole testing is similar to the S-wave tomography method that I used in Chapters 3, 4, 5 and 6. For a CHT at least two cased boreholes are required to lower an S-wave source in one borehole and a receiver in the other to an equal elevation. Subsequently, S-waves are generated at the source, which travel through the medium before being recorded at the receiver. The arrival time of the S-wave is picked, usually by either the crossover method (Tanimoto and Kurzeme, 1973; Mackens et al., 2017), or by the cross correlation method (Lee and Santamarina, 2004), in the case that three co-

linear boreholes with two in-line receivers are available. This arrival time is then used in conjunction with the distance between the boreholes to determine the S-wave velocity, see ASTM D4428 (2000) for a standardised procedure used in industry.

There are several limitations for the CHT (Clayton et al., 2012). First, straight ray paths between the source and receiver are assumed. Thus, the obtained S-wave velocities are averaged values in heterogeneous environments with lateral S-wave velocity variations. In addition, the S-wave raypath may lie somewhere else altogether, e.g. along stiffer horizontal layers. Secondly, picking of S-wave arrivals can be challenging and at times prone to error. This is often the case, since each depth interval displays only a single measurement. The S-wave traveltime trends can thus be difficult to detect. Thirdly, the inter-borehole material is sampled for only horizontal raypaths. Consequently, the obtained S-wave velocities rely on only a few 1D measurements.

To overcome these limitations of the CHT, I used the S-wave tomography method to estimate S-wave velocities. In addition, the usage of different directional sources, produced S-waves with different polarisations, which travelled at different velocities in an anisotropic environment.

2.3 Seismic Anisotropy

In an anisotropic medium, waves travelling in different directions possess different velocities. In other words, the seismic velocity is angle dependent (Thomsen, 2002). The seismic velocity refers to both P- and S-waves, and for all frequencies. The angle sometimes refers to the azimuthal angle, when the medium is also called a horizontally transversely isotropic (HTI) medium, with a horizontal symmetry axis. At other times the angle refers to only the polar angle, when the medium is also referred to as a vertically transversely isotropic (VTI) medium, with a vertical symmetry axis. The terms *VTI medium* and *polar anisotropic medium* are subsequently used interchangeably. Of course, the layering doesn't need be horizontal (as is the case for a VTI-medium) or the fractures don't need to be vertical (as is the case for an HTI-medium). This is especially the case for metamorphic rocks or tilted sedimentary layers. In such a case, the material is described as a transversely isotropic medium with a tilted symmetry axis (TTI-medium). In more complicated scenarios, the velocity can be a function of both the azimuthal and polar angle, when we speak of an orthorhombic medium or, in the case of non-orthogonal orientations in the horizontal plane, of a monoclinic medium.

An example of a seismically anisotropic rock is shown in Figure 2.4. The horizontal layering of the sandstone likely causes the velocity to be dependent on the polar angle (VTI medium). In addition, the joints most likely cause an azimuthal dependency as well, resulting in either orthorhombic or monoclinic anisotropy. Anisotropy is the texture or fabric of the rock, which can range from the microscopic, e.g.

the arrangement of crystals, to the macroscopic, such as large fracture systems or layering. Anisotropy is therefore distinct from heterogeneity, which is dependent on the position (Thomsen, 2002).

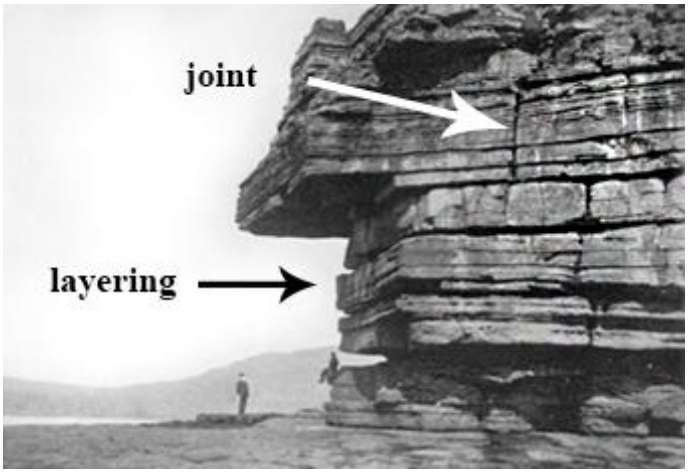


Figure 2.4: Example of a (most likely) seismic anisotropic rock. Here, Muckross Head, Ireland, is shown with the layering of the sandstone and joints causing probably either an orthorhombic or monoclinic symmetry (modified from Thomsen, 2002).

Analysing cross-borehole seismic data makes it possible to examine if the material can be approximated by a VTI medium, since the raypaths associated with the traveltimes range from horizontal to sub-vertical. Therefore, the subsequent focus lies on estimating VTI parameters. In most cases it is only an approximation to describe the material as a VTI medium. Yet, this approximation is often better than the assumption of isotropy and helps to derive additional, albeit simplified, parameters and to improve the tomography processing and inversion.

The stress-strain relationship is useful to examine seismic anisotropy mathematically, with the elastic full tensor description given by

$$\sigma_{ij} = \sum_{k,l=1}^{3} c_{ijkl}\, \varepsilon_{kl}, \tag{2.35}$$

where the stress (σ) is related to the strain (ε) by the fourth order elastic tensor (c_{ijkl}). This fourth rank tensor is quite difficult to handle and therefore a simplification was made by Voigt (1910, p. 560) to convert the tensor into a 6x6 matrix (C_{ij}). This mapping was possible due to the symmetrical nature of the tensor (c_{ijkl}). The stress-strain relationship is then expressed as

$$\sigma_{ij} = C_{ij}\varepsilon_{ij}. \tag{2.36}$$

In the simplest case of isotropy the matrix C_{ij} assumes the form

$$C_{ij} = \begin{bmatrix} C_{33} & (C_{33}-2C_{44}) & (C_{33}-2C_{44}) & 0 & 0 & 0 \\ 0 & C_{33} & (C_{33}-2C_{44}) & 0 & 0 & 0 \\ 0 & 0 & C_{33} & 0 & 0 & 0 \\ 0 & 0 & 0 & C_{44} & 0 & 0 \\ 0 & 0 & 0 & 0 & C_{44} & 0 \\ 0 & 0 & 0 & 0 & 0 & C_{44} \end{bmatrix}. \quad (2.37)$$

The two independent elastic tensor components C_{33} and C_{44} are related to the Lamé parameters (λ and μ) and to the bulk modulus (K) by

$$C_{33} = \lambda + 2\mu = K + \frac{4}{3}\mu, \quad (2.38)$$

$$C_{44} = \mu. \quad (2.39)$$

Subsequently, the isotropic P- and S-wave velocities can be determined, with

$$v_P = \sqrt{\frac{C_{33}}{\rho}} = \sqrt{\frac{\lambda + 2\mu}{\rho}}, \quad (2.40)$$

$$v_S = \sqrt{\frac{C_{44}}{\rho}} = \sqrt{\frac{\mu}{\rho}}. \quad (2.41)$$

For sedimentary rocks the simplest assumption is that they are layered. To describe such material as a VTI medium is usually a good first approximation. For this special case, the elastic modulus matrix then has five independent components

$$C_{ij} = \begin{bmatrix} C_{11} & (C_{11}-2C_{66}) & C_{13} & 0 & 0 & 0 \\ 0 & C_{11} & C_{13} & 0 & 0 & 0 \\ 0 & 0 & C_{33} & 0 & 0 & 0 \\ 0 & 0 & 0 & C_{44} & 0 & 0 \\ 0 & 0 & 0 & 0 & C_{44} & 0 \\ 0 & 0 & 0 & 0 & 0 & C_{66} \end{bmatrix}. \quad (2.42)$$

This elastic modulus matrix is used to solve the wave equation, which yields three independent solutions for the phase velocities of the three types of waves, which are the quasi P-wave, quasi SH-wave and quasi SV-wave (Daley and Hron, 1977)

$$v_{qP}^2(\theta) = \frac{1}{2}[C_{33} + C_{44} + (C_{11} - C_{33})\sin^2\theta + D(\theta)], \quad (2.43)$$

$$v_{qSV}^2(\theta) = \frac{1}{2}\left[C_{33} + C_{44} + (C_{11} - C_{33})\sin^2\theta - D(\theta)\right], \tag{2.44}$$

$$v_{qSH}^2(\theta) = C_{66}\sin^2\theta + C_{44}\cos^2\theta, \tag{2.45}$$

with $D(\theta)$ being the quadratic combination

$$\begin{aligned} D(\theta) \equiv \{&(C_{33} + C_{44})^2 + 2[2(C_{13} + C_{44})^2 - (C_{33} - C_{44})(C_{11} + C_{33} - 2C_{44})]\sin^2\theta \\ &+ [(C_{11} + C_{33} - 2C_{44})^2 - 4(C_{13} + C_{44})^2]\sin^4\theta\}^{\frac{1}{2}}. \end{aligned} \tag{2.46}$$

They are called quasi P-waves, because the P-wave polarisation no longer has the same direction as the raypath or propagation direction. Similarly, for the quasi SH- and SV-wave, the polarisation is no longer perpendicular to the raypath, i.e. to the direction of propagation. They are different, as the velocity of the wavefront, the P-wave polarisation direction, is no longer the same as the velocity of the raypath, as shown in Figure 2.5.

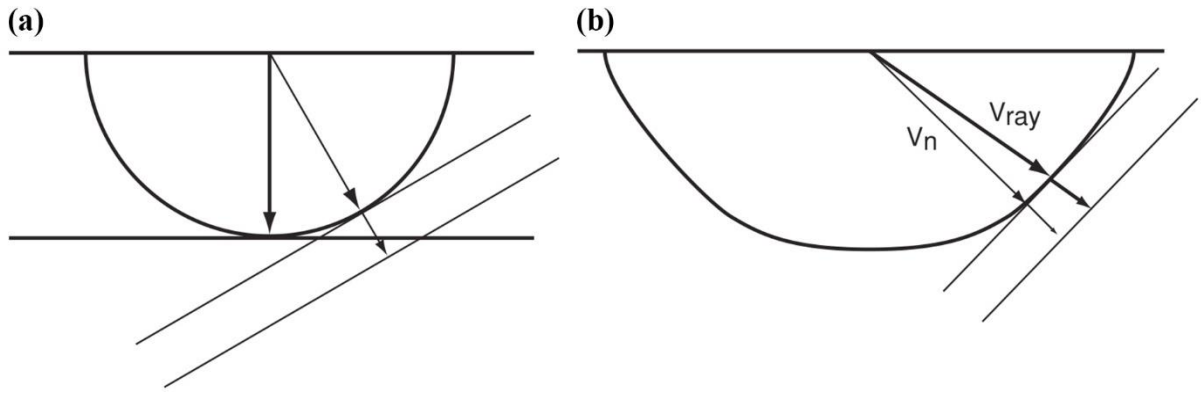


Figure 2.5: The velocity of the wavefront (Vn) is different from the velocity of the raypath (Vray) for an anisotropic medium (b). For an isotropic medium (a), the two velocities are the same. (Helbig and Thomsen, 2005).

Due to the long quadratic term (D in equation 2.46), these solutions tend to be difficult to handle and non-intuitive. Therefore, Thomsen (1986) introduced the VTI parameters ε, δ^* and γ that would simplify the above equations with

$$\varepsilon = \frac{C_{11} - C_{33}}{2C_{33}}, \tag{2.47}$$

$$\delta^* = \frac{1}{2C_{33}^2}[2(C_{13} - C_{44})^2 - (C_{33} - C_{44})(C_{11} + C_{33} - 2C_{44})], \tag{2.48}$$

$$\gamma = \frac{C_{66} - C_{44}}{2C_{44}}. \tag{2.49}$$

With the vertical P- and S-wave velocities

$$v_{P0} = \sqrt{\frac{C_{33}}{\rho}}, \tag{2.50}$$

$$v_{S0} = \sqrt{\frac{C_{44}}{\rho}}, \tag{2.51}$$

the equations of Daley and Hron (1977), i.e. equations 2.43 to 2.45, can then be re-writtten in terms of Thomsen's (1986) anisotropy parameters

$$v_{qP}^2(\theta) = v_{P0}^2[1 + \varepsilon \sin^2\theta + D^*(\theta)], \tag{2.52}$$

$$v_{qSV}^2(\theta) = v_{S0}^2\left[1 + \frac{v_{P0}^2}{v_{S0}^2}\varepsilon \sin^2\theta - \frac{v_{P0}^2}{v_{S0}^2}D^*(\theta)\right], \tag{2.53}$$

$$v_{qSH}^2(\theta) = v_{S0}^2[1 + 2\gamma \sin^2\theta]. \tag{2.54}$$

Once again, a term D^* complicates the above equations 2.52 to 2.54, given by

$$D^*(\theta) \equiv \frac{1}{2}\left(1 - \frac{v_{S0}^2}{v_{P0}^2}\right)\left\{\left[1 + \frac{4\delta^*}{(1 - v_{S0}^2/v_{P0}^2)}\sin^2\theta\cos^2\theta + \frac{4\left(1 - v_{S0}^2/v_{P0}^2 + \varepsilon\right)\varepsilon}{(1 - v_{S0}^2/v_{P0}^2)^2}\sin^4\theta\right]^{1/2} - 1\right\}. \tag{2.55}$$

For this reason, the assumption of weak anisotropy is made by Thomsen (1986), after which a Taylor expansion of equation 2.55 gives

$$D^*(\theta) \approx \frac{\delta^*}{1 - v_{S0}^2/v_{P0}^2}\sin^2\theta\cos^2\theta + \varepsilon \sin^4\theta. \tag{2.56}$$

With the introduction of the anisotropy parameter δ,

$$\delta = \frac{1}{2}\left[\varepsilon + \frac{\delta^*}{1 - v_{S0}^2/v_{P0}^2}\right], \tag{2.57}$$

the above angle dependent velocity equations 2.52 to 2.54 are simplified to

$$v_P(\theta) \approx v_{P0}[\,1 + \delta\sin^2\theta\cos^2\theta + \varepsilon \sin^4\theta\,], \tag{2.58}$$

$$v_{SV}(\theta) \approx v_{S0}\left[1 + \left(\frac{V_{P0}}{V_{S0}}\right)^2 (\varepsilon - \delta)\sin^2\theta\cos^2\theta\right], \tag{2.59}$$

$$v_{SH}(\theta) \approx v_{S0}[\,1 + \gamma\sin^2\theta\,]. \tag{2.60}$$

Note, that for the assumption of weak anisotropy the wavefront and raypath velocities are similar. Therefore, the q, for "quasi", was omitted.

The seismic velocity is now dependent on the polar angle (θ). Figure 2.6 shows an example of how the phase velocity changes for different angles. The anisotropy parameters were measured in Wills Point shale and determined as $\varepsilon = 0.215$, $\delta = 0.315$, $\gamma = 0.280$, with vertical P-wave and S-wave velocities of $v_{P0} = 1058\ m/s$ and $v_{S0} = 387\ m/s$ (Robertson and Corrigan, 1983). We can see that the P-wave and S-wave velocities can be highly influenced in an anisotropic environment.

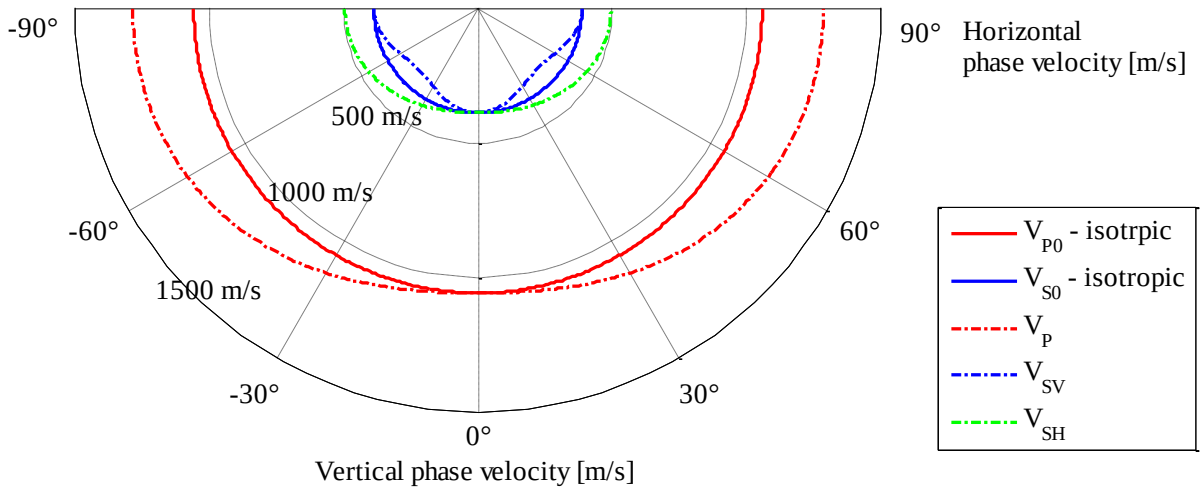


Figure 2.6: Re-produced forward modelling of anisotropy parameters by measuring angle dependent P- and S-wave phase velocities in Wills Point shale (Robertson and Corrigan, 1983). The VTI parameters are $v_{P0} = 1058\ m/s$, $v_{S0} = 387\ m/s$, $\varepsilon = 0.215$, $\delta = 0.315$ and $\gamma = 0.280$.

The P-wavefront is spherical if ε = δ = 0, in which case we have the isotropic case. The P-wavefront is elliptical if ε = δ, with the short and long axes of the ellipse given by v_{P0} and v_{P90}. If ε ≠ δ, then the wavefront is no longer elliptical. In that case, δ would approximate an ellipse fitted to the near-vertical directions and ε would approximate an ellipse fitted to the near-horizontal directions. The short and long axes of the ellipse are then still given by v_{P0} and v_{P90}. Laboratory measurements have shown that it is common that ε ≠ δ (Wang, 2002), and therefore, the ellipticity assumption should not be, or only very carefully, applied.

The SV-wavefront is the same for the vertical and horizontal directions. For all angles in between, the parameters ε, δ and v_{P0}/v_{S0} ratio determine the divergence of the wavefront from the isotropic spherical case. Since the velocity ratio is squared, it is expected that in the near-surface environment, where high v_{P0}/v_{S0} ratios of 5 or higher are common, even small anisotropy is likely to have a large influence on the SV-wavefront. This is shown in the forward computation for small amounts of SV-wave anisotropy in Figure 2.7.

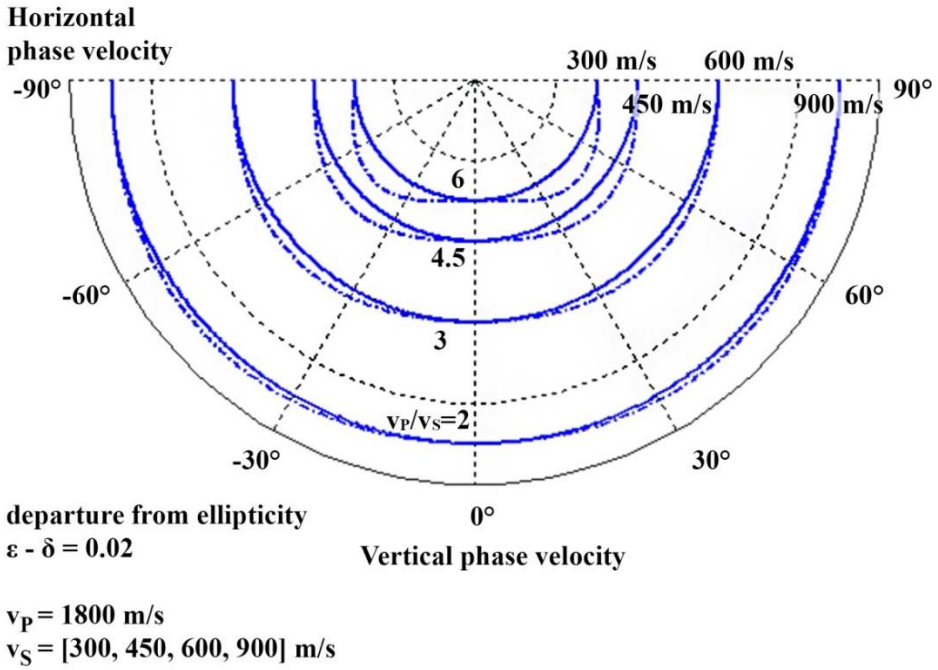


Figure 2.7: Forward modelling of SV-wavefront anisotropy effects for varying v_{P0}/v_{S0} ratios. The P-wave velocity was kept constant at 1800 m/s, as well as the small departure from ellipticity (ε – δ) at 0.02. The isotropic wavefront is shown by the semi-circular solid blue line and the anisotropic wavefront is shown by the dashed line. We can see that for high v_P/v_S ratios the wavefront departs substantially from the isotropic circular reference, even for such minor anisotropy.

The SH-wavefront is slightly simpler than the P- and SV-wavefronts. Only the anisotropy parameter γ determines the SH-wavefront shape, i.e. the SH-wavefront is always elliptical (as long as the assumption of a VTI medium is valid). It is important to note, that $\gamma > 0$. Otherwise the stiffness matrix is no longer positive definite. For solid sedimentary rocks, the anisotropy parameters γ (governing the SH-wave anisotropy) and ε (largely governing the P-wave anisotropy) are usually linearly correlated (Wang, 2002). If this relationship also holds for unconsolidated rocks and soil as found in the near-surface is not reported.

As seen in Figure 2.6, differently polarised S-waves will travel with variable velocities in an anisotropic medium. In geotechnical publications (e.g. Ku and Mayne, 2014) often three different types of polarised S-waves are discussed. Firstly, there is a horizontally polarised S-wave travelling horizontally, denoted

v_{SHH}. Secondly, there is a vertically polarised S-wave travelling horizontally, denoted v_{SHV}. Both of these S-wave modes are generated by directional sources in a cross-borehole setup. And thirdly, a horizontally polarised S-wave travelling vertically downwards exists, which is denoted v_{SVH}. This S-wave polarisation is generally produced when conducting a Downhole survey. By looking at equations 2.58 to 2.60 again, we see that these three S-wave polarisation definitions are in fact just two, since the v_{SVH} wave type is simply v_{SV0}, i.e. $v_{SV}(0°)$.

Furthermore, Figure 2.6 suggests that a VTI medium affects cross-borehole measurements, with horizontal and sub-vertical raypaths, to a far greater extent than surface seismic reflection measurements. This is illustrated in Figure 2.8 and was confirmed by Carrion et al. (1992), who showed with tomography forward modelling that even weak structurally-induced anisotropy can produce visible artefacts in P-wave tomograms, significantly distort the result and introduce X-shaped artefacts into the tomogram. Such distortions in the P-wave tomograms have also been reported in field measurements (e.g. Pratt and Chapman, 1992). For S-waves the anisotropy plays an even more pronounced role, since the S-wave polarisation is always dependent on the fast and slow anisotropy directions, regardless of the strength of the anisotropy. Therefore, anisotropy should be considered when interpreting seismic data for tomographic analysis and anisotropy parameters incorporated into the inversion. Publication IV, addresses the anisotropy of the measurements conducted at the SAFIRA site, by estimating the VTI parameters v_{P0}, v_{S0}, ε, δ and γ through a joint inversion.

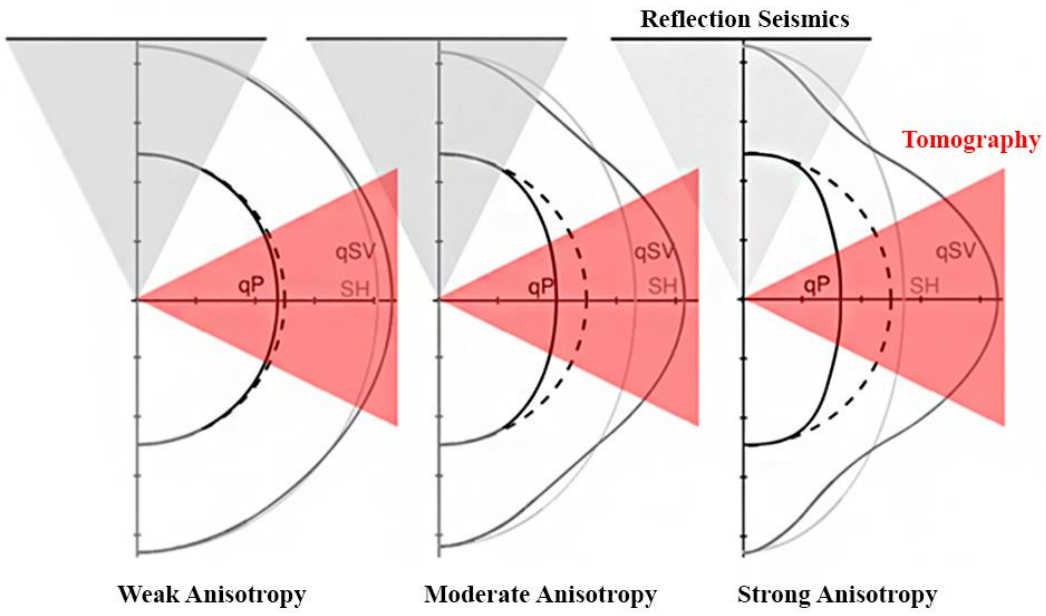


Figure 2.8: Cross-borehole measurements, with the angular domain highlighted in red, are severely more affected by anisotropy compared to surface seismic reflection surveys, with the angular domain highlighted in grey. The slowness (qP, qSV, qSH) as a function of polar angle illustrates this (modified after Helbig and Thomsen, 2005).

2.4 Acquisition of Seismic Data for Tomographic Analysis

Borehole sources and receivers can be used to acquire P- and S-wave data for tomographic analysis. In this thesis cross-borehole data acquisition was conducted with equipment from Geotomographie GmbH. Geotomographie produces a number of different borehole sources and receivers. Among the sources are a P-wave sparker source of the type SBS42, horizontal sources BIS-SH and BIS-SH-DS, and a vertical source BIS-SV. These sources are electrically powered by either a 5000 V (sparker SBS42 and horizontal source BIS-SH) or an 800 V impulse generator (SH source BIS-SH-DS and vertical source BIS-SV), denoted IPG5000 and IPG800 respectively. Figure 2.9 shows the 5000 V generator and the two sources that can be connected. Figure 2.10 shows the smaller 800 V generator with the two directional sources that can be connected.

The horizontal sources BIS-SH and BIS-SH-DS are similar in their construction. A number of electromagnetic coils are placed adjacent to a copper plate. The copper plate and the coils are repulsed when an electrical current flows. This causes the plate to strike the side of the borehole wall. This sideways mechanical impact produces both a horizontally polarised S-wave and a P-wave. The sources are coupled to the borehole wall by a pneumatic clamping device in the form of an air bladder and function in both water filled and dry boreholes.

The vertical source BIS-SV also functions with electromagnetic coils and a pneumatically clamping air bladder. In this case the coils are repulsed vertically, which produces a vertical shearing motion on the side of the borehole. Due to this shearing motion on the side of the borehole, less compressional energy is transferred horizontally into the material compared to the horizontal source, i.e. the P-wave content of this source is lower for a cross-borehole setup. The source also functions in both dry and water filled boreholes.

The sparker type SBS42 has two electrodes in a water filled chamber. When the energy from the impulse generator is released, a spark discharges through the water chamber. Thereby the water is vaporised, which rapidly expands and collapses, producing predominantly P-waves. Therefore, the sparker source functions only in water filled boreholes and needs no direct coupling to the borehole wall.

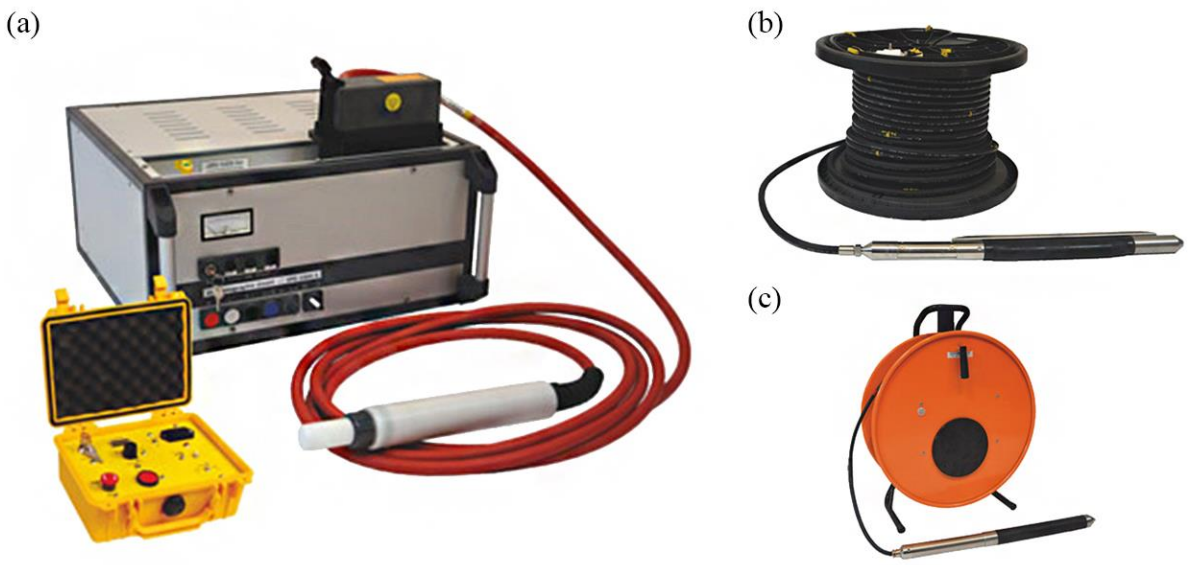


Figure 2.9: P- and S-wave generating equipment using the 5000 V generator IPG5000 (a). Triggering occurs remotely, using the yellow remote control unit. The horizontal source BIS-SH (b) generates both P- and S-waves, and the sparker source SBS42 (c) generates high-amplitude P-waves. (photos provided by Geotomographie GmbH)

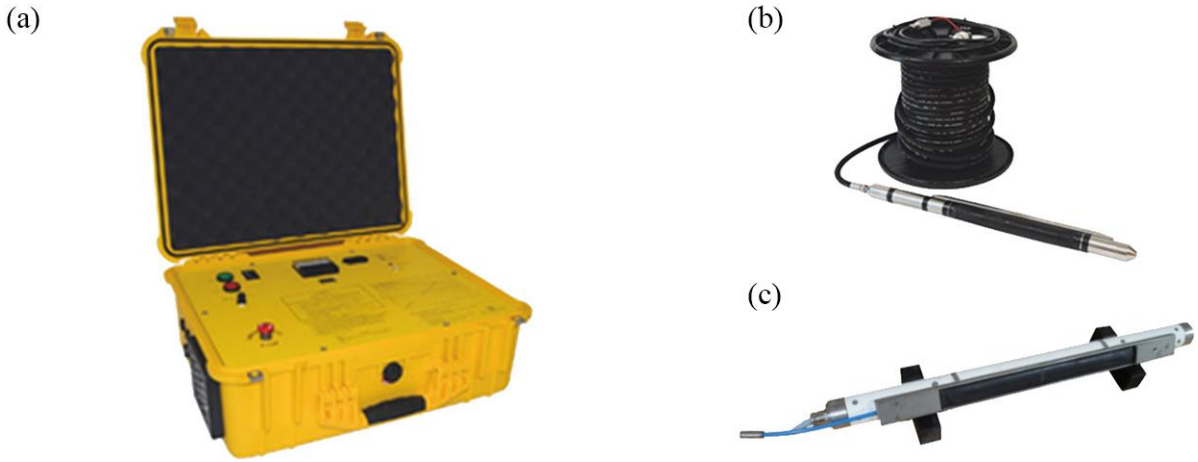


Figure 2.10: 800 V impulse generator IPG800 (a), which powers the horizontal source BIS-SH-DS (b) and vertical source BIS-SV (c) (photos provided by Geotomographie GmbH).

A hydrophone string type BHC4, usually consisting of 24 Channels spaced at 1 m intervals, was used for P-wave tomography data collection and a multi-station tri-axial receiver array (MBAS), consisting of up to 10 stations spaced at 1 m intervals, was used to record both P- and S-wave data. The hydrophone is connected to a seismograph on surface, while the multi-station receiver array has digitisation units installed next to the tri-axial sensors to digitise the signal prior to sending it up the borehole and to the connected computer software. The two versions of receiver equipment are displayed in Figure 2.11.

(a) (b)



Figure 2.11: Receivers used for tomography are shown, which includes the multi-station (7 depicted) tri-axial receiver array (a) and a hydrophone string with 24 receivers (b) (photos provided by Geotomographie GmbH).

Before conducting a tomographic survey, the boreholes were prepared. Generally, the boreholes had an inner diameter of at least 75 mm, were cased with a polyvinyl chloride (PVC) pipe and grouted with a cement bentonite mixture. For high resolution tomography the distance between the two boreholes should be known for all shot and receiver positions. Therefore, a borehole verticality survey was performed to measure the X, Y and Z coordinates of the boreholes with depth.

The data acquisition sequence was generally the following for an S-wave tomography survey. The source, either one of the horizontal sources BIS-SH or BIS-SH-DS, or the vertical source BIS-SV was lowered in one of the two available boreholes to the lowest shooting position, connected to the impulse generator on surface and pneumatically clamped to the borehole wall. In case a horizontal source was employed, the source was aligned perpendicular (in a 90° or -90° angle) to the receiver borehole. The multi-station receiver array was lowered in the other borehole to the lowest desired position, aligned in such a way that one of the two horizontal receivers is facing the source borehole, pneumatically clamped to the borehole wall and connected to a computer. For each depth the horizontal source was shot perpendicular to the receiver borehole, to emit S-waves of high amplitudes. Once sufficient data quality was achieved, this perpendicular shooting configuration was reversed for each depth to reverse the polarity of the first arriving S-wave. Originally, it was expected that this orientation from surface would also align the sources and receivers at depth. Later polarisation analysis showed that this was not the case, see Chapter 6: Publication IV. Thus, the receivers had to be virtually aligned prior to further processing by an axial rotation.

Surveys employing the vertical source were conducted in a similar manner to the horizontal source acquisition, shooting up and down instead of shooting perpendicular to the receiver borehole. Subsequently, the source was moved upwards to the next depth position until data were collected for all depths. Usually the shot and receiver interval was 1 m. If the MBAS receiver array needed to be shifted

by a spread upwards, then the shooting for the lower spread would end a number of positions above the spread. Shooting for the subsequent, higher, spread would start at a lower position than the lowest receiver. This ensured that sufficient data coverage was achieved in the depth were the two spreads met. This is illustrated in Figure 2.12. The acquisition sequence for conducting P-wave tomography using the sparker as a source and BHC4 hydrophone string as receivers was analogous to the S-wave acquisition sequence described above.

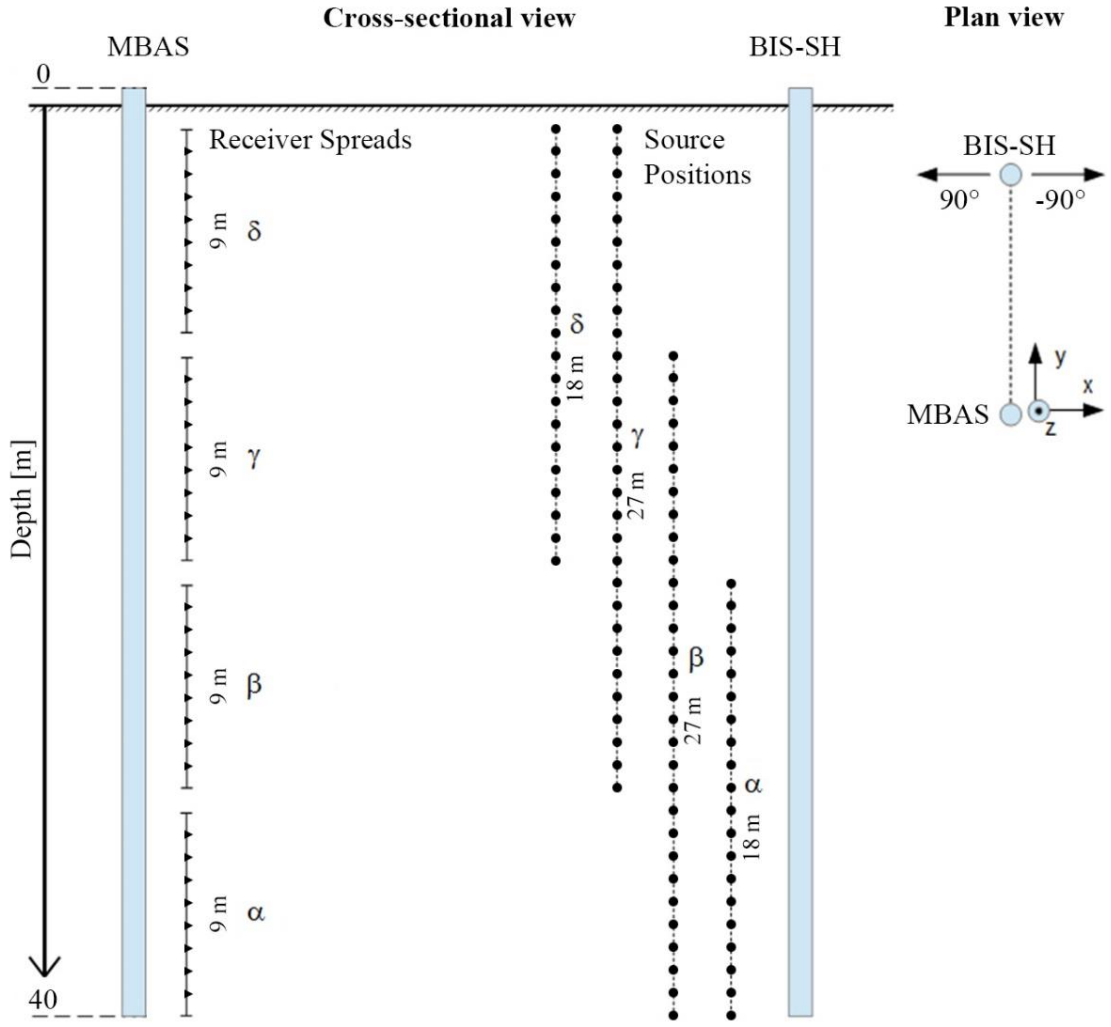


Figure 2.12: Typical S-wave acquisition sequence using the BIS-SH and a 10 station MBAS receiver array. Here the seismic data is gathered for depths of 40 m to 1 m for a total of 4 receiver spreads. The receiver and shot spreads are shown in a cross-sectional view, whereby the Greek letters associate the receiver with the shot spreads. The plan view shows the shooting direction of the BIS-SH, either shooting in a 90° or -90° angle to the receiver borehole, and the receiver orientation of the X-, Y- and Z-channel.

2.5 Curvelet Transform

The curvelet transform is a mathematical multi-scale and multi-directional transform to sparsely represent two or more-dimensional data, and originating in image denoising applications (Candès and Guo, 2002; Starck et al., 2002; Candès and Donoho, 2004). Mathematically, the construction of curvelets is given by Candès et al. (2005). First, curvelets are constructed using two windows, namely a radial window $W(r)$ and an angular window $V(t)$. These two windows obey the admissibility condition, in that

$$\sum_{j=-\infty}^{\infty} W^2\left(2^j r\right) = 1\,, \qquad r \in \left(\frac{3}{4}, \frac{3}{2}\right), \tag{2.61}$$

$$\sum_{l=-\infty}^{\infty} V^2(t-l) = 1\,, \qquad r \in \left(-\frac{1}{2}, \frac{1}{2}\right). \tag{2.62}$$

Further, these two windows are then used to define a frequency window U_j in the Fourier domain

$$U_j(r,\theta) = 2^{-3j/4} W\left(2^{-j} r\right) V\left(\frac{2\lfloor j/2 \rfloor \theta}{2\pi}\right), \tag{2.63}$$

with $\lfloor j/2 \rfloor$ meaning the integer part of $j/2$. This frequency window U_j is therefore an angular wedge, limited radially by the window W and angularly by the window V. The inverse Fourier transform of $U_j(\omega) = \widehat{\varphi_j}(\omega)$ then yields a so-called "mother" curvelet φ_j. This mother wavelet of scale 2^{-j} is rotated and translated to derive all other curvelets of that scale. The rotations involve angles from $\theta_l = 2\pi \cdot 2^{-\lfloor j/2 \rfloor} \cdot l$, with $l = 0, 1, \ldots$, such that $0 \le \theta_l \le 2\pi$. Thus, the angular spacing between adjacent curvelets is scale dependent (at low scales, relatively few angular wedges are defined, and at high scales many angular wedges are defined). The translations (k) involve all sequences of the n-dimensional space (in the 2D case: $k = (k_1, k_2) \in \mathbb{Z}^2$). With these rotations (l) and translations (k), curvelets of scale 2^{-j}, can then be derived from the "mother" curvelet in 2D with

$$\varphi_{j,l,k}(x) = \varphi_j\left(\mathrm{R}_{\theta_l}(x - x_k^{(j,l)})\right), \tag{2.64}$$

with the standard rotation matrix R_{θ_l} by θ_l radians.

Thus, a curvelet coefficient (c) is then defined as the inner product between a function $f \in \mathrm{L}^2(\mathbb{R}^2)$ and a curvelet $\varphi_{j,l,k}$

$$c(j,l,k) \equiv \langle f, \varphi_{j,l,k} \rangle = \int_{\mathbb{R}^2} f(x) \overline{\varphi_{j,l,k}(x)} dx. \tag{2.65}$$

The curvelet transform is a tight frame, in that any function $f \in L^2(\mathbb{R}^2)$, can be represented as a combination of curvelets. An example of different curvelets in the spatial and frequency domain is shown in Figure 2.13. The curvelets possess different scales and angular directions, stemming from their construction in the frequency space (Figure 2.13 c).

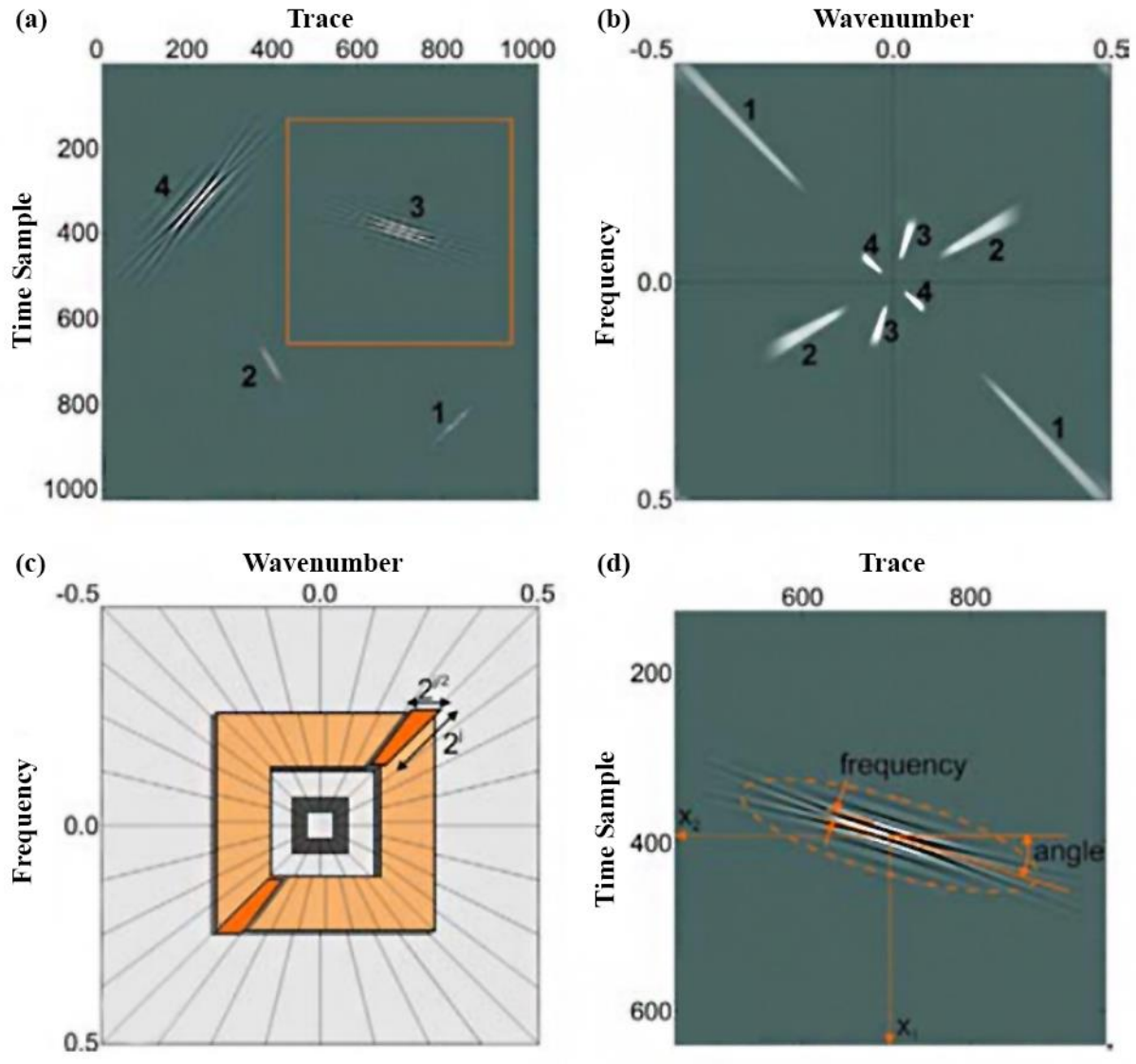


Figure 2.13: Curvelets of different scales and angular directions are shown in the spatial (a) and Fourier domain (b). The construction of the curvelets takes place in the Fourier domain, which is partitioned into angularly and radially constrained windows (c). Curvelets of scale 1 are at the centre, and the highlighted curvelet (d) is of scale 4. (modified after Górszczyk et al., 2014).

Curvelets have an anisotropic geometrical design that distinguishes them from wavelets. They follow the parabolic scaling relation, in that a curvelet at scale 2^{-j}, is constrained by an envelope of length, also called ridge, $2^{-j/2}$ and a width of 2^{-j}. Thus, for finer scales, the curvelets become more and more

anisotropic or needle-like in their design. This feature makes them ideal to sparsely represent objects, which are characterised by both smooth and edge-like boundaries, such as seismic wavefronts. For this reason the curvelet transform has been successfully applied to reflection seismic data for denoising applications (Hennenfent and Herrmann, 2006; Neelamani et al., 2008; Shan et al., 2009; Górszczyk et al., 2014; Naghizadeh and Sacchi, 2018).

This denoising procedure is usually applied in the following way. Take the curvelet transform of a seismic image, threshold the curvelet coefficients, and finally perform the inverse curvelet transform. This procedure is outlined in Figure 2.14. In Chapter 7, Publication V, a similar curvelet denoising procedure is applied to enhance reflection seismic data from the Kalahari-Karoo Basin, Botswana.

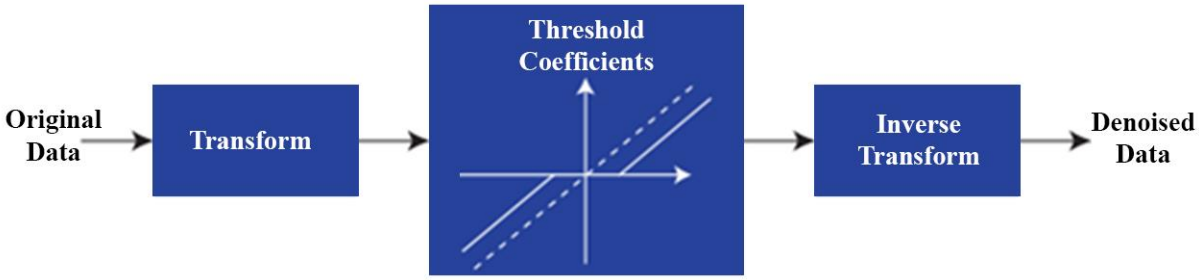


Figure 2.14: Denoising procedure using curvelet thresholding (modified after Hennenfent and Hermann, 2006).

3. PUBLICATION I: ELASTIC PARAMETERS FROM COMPRESSIONAL AND SHEAR WAVE TOMOGRAPHIC SURVEY: A CASE STUDY FROM KUALA LUMPUR, MALAYSIA

An integrated P- and S-wave cross-borehole tomographic survey was performed in the city center of Kuala Lumpur, Malaysia with the aim of exploring a karstic limestone area near an area that previously encountered cavities. Horizontally polarized shear waves were generated with two opposing, perpendicular strike directions and recorded with a multi-level, three-component receiver array. This allowed a high quality picking of the traveltimes, whereby the wave train reverses at the time of the S-wave arrival. In addition, high quality sparker generated P-waves were recorded. The P- and S-wave traveltimes were used to invert for two co-located tomograms. These tomograms enabled a better interpretation capability than a P- or S-wave tomogram on its own. The tomograms enabled the calculation of the elastic parameters, i.e., P- to S-wave velocity (Vp/Vs) ratio, Poisson's ratio, bulk modulus, Young's modulus and the shear modulus, on a 2D surface between the boreholes. This further aided the interpretation, as areas with limited traveltime accuracy and thus, an increase in tomographic error, could be easily identified, and the extent of a large cavity could be estimated. The interpretation of the tomograms was constrained by two additional boreholes, which provided more confidence on the delineation and location of cavities at depths. The survey shows the benefit of co-locating P- and S-wave tomography surveys.

3.1 Introduction

Kuala Lumpur, Malaysia has been undergoing continuous expansion and development in the past several years. As a measure to cope with the increase in traffic, a new Mass Rapid Transit (MRT) line is planned, whereby a tunnel boring machine will be employed. Such tunnel boring machines can have difficulty operating in karstic environments as found in Kuala Lumpur, particularly with varying bulk densities of the material. The construction of a tunnel in a geological environment that is not adequately explored and understood can be costly. For example, the construction of the Milwaukee Sewage Tunnel between 1984 and 1993 did not take the extent of the karstic environment into account, which led to remedial grouting and linings, costing an additional 50 million dollars above the initial estimate (Day, 2004). Therefore, exploring the geology beforehand in a karstic environment is highly advisable, and this motivated the MRT construction company to commission a co-located cross-borehole P- and S-wave tomographic survey in the centre of Kuala Lumpur. The survey was conducted in a particularly karstic area with the presence of cavities already identified by exploration drilling.

High-resolution tomographic investigations between two or more boreholes are routinely conducted, whereby traveltimes of horizontal and sub-vertical raypaths are used to image detailed structures in 2D or less frequently in 3D. These tomographic surveys often employ compressional waves for the

exploration of geological structures, as P-waves are easier to generate and record compared to S-waves. For example, the recommendations given by the American Soil Testing Materials Committee (ASTM D4428, 2000) for crosshole seismic testing are to use three-component geophones at each receiver position and to ensure good coupling of both source and receivers to the borehole wall. Furthermore, the orientation of the horizontally polarizing S-wave source is an important parameter to generate consistent S-waves. For a better S-wave traveltime determination, it is recommended to reverse the shooting direction of the S-wave source and thereby change the polarity of the S-wave arrival (Tanimoto and Kurzeme, 1973; Sully and Campanella, 1995). In contrast, P-wave tomographic surveys are often easier to conduct, for example with a sparker source and a hydrophone string, where no direct coupling or alignment of the source or receivers is necessary (e.g. Mackens et al., 2014). In addition, the traveltime picking of P-waves is usually easier and more accurate compared to picking S-wave traveltimes (Dietrich and Tronicke, 2009). For these reasons, few S-wave surveys have been conducted to date (Paasche et al., 2014).

Despite the challenges, S-wave tomographic surveys have a number of potential advantages over conventional P-wave tomographic surveys, such as the high near surface mapping resolution due to the lower S-wave velocities. Furthermore, the joint acquisition and interpretation of seismic P- and S-wave tomographic data enables a more detailed description of the subsurface in terms of elastic soil or rock parameters. These can now be calculated for a 2D plane in between the boreholes and with higher resolution compared to conventional crosshole or downhole testing surveys. Such a combined tomographic survey was performed by Angioni et al. (2003) to derive elastic parameters for geotechnical analysis of a bridge foundation. Even though they faced a challenging data acquisition, i.e. relatively few, unaligned receivers, and only simple straight ray tracing inversions were used, the combination of the two P- and S-wave tomograms provided useful in the derivation for engineering properties. Similarly, Dietrich and Tronicke (2009) show that these elastic soil parameters, i.e., the small strain shear modulus, Poisson's ratio, Young's modulus, bulk modulus, and the P- to S-wave velocity ratio are useful in a joint interpretation. The small strain shear modulus, in particular, is an important elastic parameter for larger building projects. The foundation and construction design is largely dependent on the small strain shear modulus, since this influences the force transfer between the structures and the soil.

Based on the general lack of studies aimed at combining P- and S-wave tomographic data for engineering analyses, we conduct such a survey on a portion of the planned MRT tunnel in Kuala Lumpur. Our work shows that the co-located measurements facilitate the computation of elastic parameters which helped in the geological interpretation, identifying karstic areas and estimating the degree of reliability of the tomograms.

3.2 Methodology

The tomographic measurements exploring for cavities employed P waves and horizontally polarized S-waves between two 40 m deep, near-vertical boreholes, spaced 20 m apart on surface. The site is underlain by extensive limestone bedrock, known as the Kuala Lumpur Limestone Formation, which is highly weathered and karstic (Tan, 2006). Previous geotechnical excavations have shown an undulating rockhead, solution channels, large-scale cave systems and overhangs (Boon et al., 2017). An approximately 13.5 m thick Quaternary alluvium covers the limestone, with the area being saturated almost to the surface.

The experimental design was similar to other high resolution P-wave tomographic surveys (e.g. Yamamoto et al., 1994; Fechner et al., 2015) and S-wave tomographic surveys (e.g. Angioni et al., 2003; Daley et al., 2004). For both P- and S-wave measurements, the source and receiver spacing was 1 m and source excitation was carried out above and below the spread, to ensure a high degree of overlap between neighbouring receiver spreads and a dense sampling of the inter-borehole material. To generate and record the P-wave seismic signals, a Geotomographie sparker source was used in conjunction with a 24-channel hydrophone string. The P-wave signal was sampled at 32 kHz. S-wave signals were generated with a horizontally polarizing S-wave source and recorded with a seven-station three-component receiver array, sampled at 16 kHz. Both the sparker and horizontally polarizing S-wave source were powered by a 5 kV impulse generator. This electrical energy is transmitted by cable to the borehole source. For the P-wave source, a spark discharges through a water chamber, whereby the water is vaporized, which rapidly expands and collapses, producing predominantly seismic compressional waves. For the horizontally polarizing S-wave source a number of electromagnetic coils are placed adjacent to a copper plate. The copper plate and the coils are repelled when the electrical current flows, causing the plate to strike the side of the borehole wall. This sideways mechanical impact produces predominantly horizontally-polarized S-waves. The sources are pneumatically coupled to the borehole wall by an air bladder and the S-wave source and receivers were aligned from surface by a rotationally stiff hose. Four to eightfold vertical stacking ensured a high signal-to-noise ratio, despite operating in an urban environment, with traffic, construction and electrical noise in proximity.

3.3 Data Processing and Analysis

The P-wave data were of good quality enabling accurate traveltime picking. The S-wave data were enhanced by applying a 1 kHz low pass Butterworth filter. An example of a P- and S-wave shot gather is displayed in Figure 3.1a and b with visualizations in variable density mode. The P-wave and S-wave arrivals are clearly visible. An example of picking the traveltimes is shown in variable amplitude mode for the P-wave (Figure 3.1c) and for the S-wave (Figure 3.1d). The S-wave traveltimes were picked on the horizontal crossline channels. Therefore, the trace reversal for the two opposing shots at 90° and 270° to the receiver borehole is visible and aided in the S-wave traveltime picking process.

Subsequently, all traveltimes were analysed for their plausibility and re-picked if necessary. In total, approximately 1,400 P-wave and 650 S-wave traveltimes were picked. The traveltime error is estimated at approximately 0.5 ms for the S-wave picks and at 0.1 ms for the P-wave picks. A higher degree of uncertainty in the P-wave traveltime picks exists for receivers close to the surface at depths of approximately 2 to 8 m. This higher degree of uncertainty is caused by a lower signal-to-noise ratio for these near-surface receivers.

In addition to the acquired P- and S-wave tomographic data, the borehole deviation was measured with a borehole tool that measures both tilt and azimuth. From those two angles the X, Y and Z coordinates were determined and the deviation of the borehole was calculated. Both boreholes begin vertical, but after a depth of approximately 20 to 25 m they diverge from the vertical position by as much as 0.5 m. This divergence from vertical causes the boreholes to no longer have the same separation as on the surface. The velocity determination is crucially dependent on the distance between the boreholes, therefore it was important to consider the borehole deviation in the tomography calculation. Subsequently, both P- and S-wave 2D tomograms were determined with the program GeotomCG on a three dimensional grid, similar to the one used by Polymenakos and Tweeton (2015), with cell sizes of 1 x 1 x 1.2 m (inline length, crossline length and vertical height). GeotomCG, derived from the US Bureau of Mines tomography program 3DTOM (Jackson and Tweeton, 1996), uses a variation of the SIRT (simultaneous iterative reconstruction technique) algorithm, developed by Lytle et al. (1978) and Peterson et al. (1985). The raypaths are calculated for each iteration with either a straight-ray or a curved-ray tracing algorithm, similar to the curved-ray algorithm by Um and Thurber (1987). The inversion requires a starting model, which was assumed to be homogeneous. This starting model was then improved by selecting only the horizontal ray paths and performing a two-iteration straight-ray inversion. This improved, horizontal model was then used as the starting model for a ten-iteration curved-ray inversion with all traveltimes of a wave type. The P-wave velocities were constrained by an upper limit of 7,000 m/s, since the seismic P-wave velocity in intact limestone is approximately 4,000 to 6,000 m/s (Birch, 1966; Sheriff and Geldart, 1995, p. 111). However, the presence of weathered or fractured limestone in our study area is likely characterized by relatively lower seismic velocities. The goodness of fit was estimated with the root-mean-square error (P-wave: 0.79 ms; S-wave: 0.67 ms).

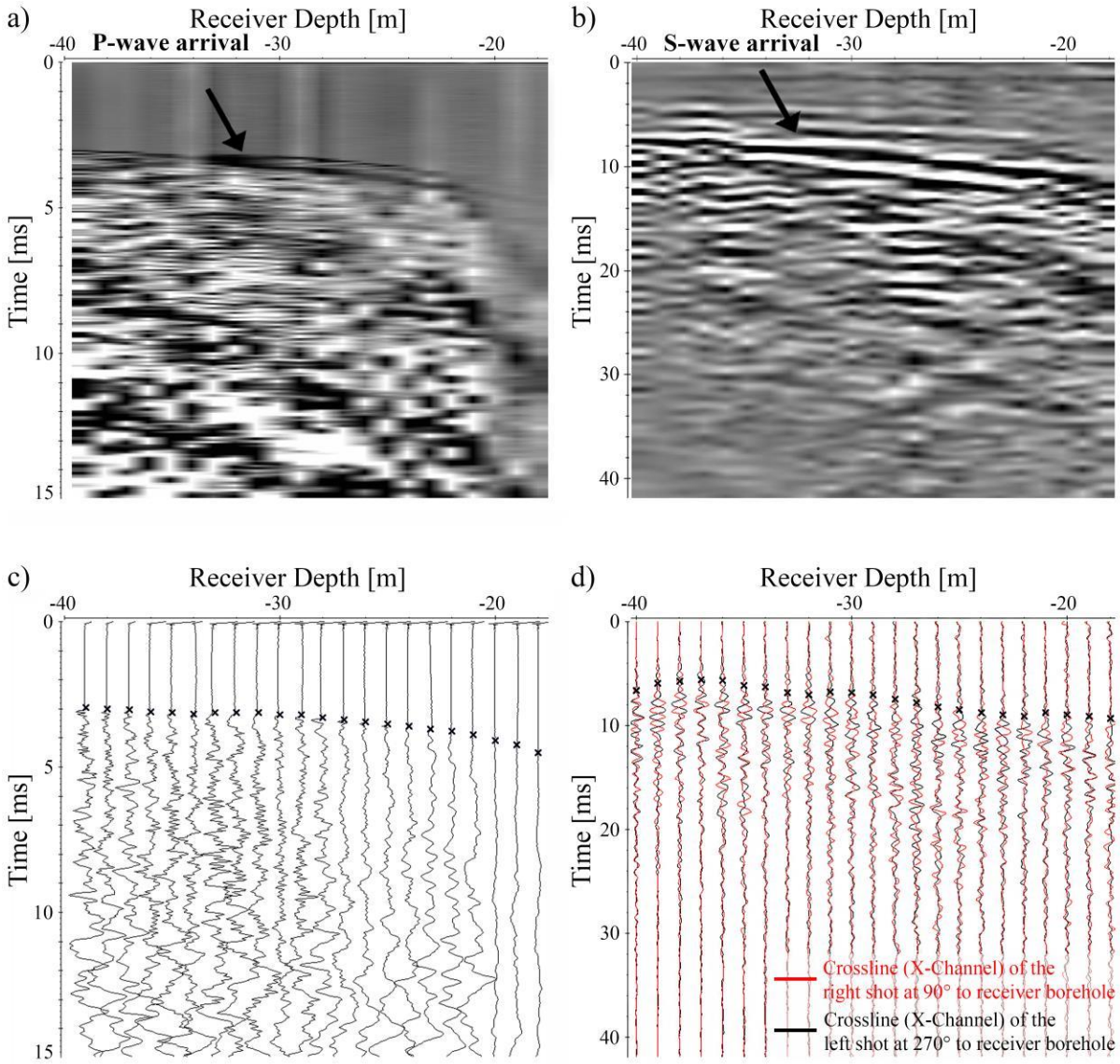


Figure 3.1: Examples of the shot gathers shown in variable density mode for the P-wave source (a) and the S-wave source (b), both at 36 m depth. The traveltime picking is shown, whereby the data are displayed in variable amplitude mode for the P-wave (c) and the S-wave (d). The traveltime picks are shown by the black crosses.

3.4 Results and Discussion

The P- and S-wave tomograms are displayed in Figure 3.2 with the borehole logs of BH1 and BH2 shown on the sides of the tomograms. Both tomograms show three zones which are also observed in the borehole logs. The upper 15 m are characterized by low P-wave velocities (~ 1,500 m/s) of the saturated alluvium. Below the alluvium, where the karstic limestone starts, both the P-wave and S-wave velocity seem to increase sharply (P-wave: 5,800 m/s and S-wave: 2,750 m/s) at the bedrock boundary. Between the elevations of about 12 to 19 m a large low velocity zone (P-wave: 2,700 to 3,600 m/s; S-wave: 1,000 to 2,000 m/s) is observed near BH2, which extends laterally almost to BH1. This area is likely to be a

large, partially infilled, cavity, as observed in the borehole log of BH2 (see Figure 3.2). Below this low velocity zone, the velocity increases from 5,000 to 6,500 m/s for the P-wave and from 2,300 to 3,800 m/s for the S-wave. However, both tomograms suggest that the limestone is not homogenous and that a number of smaller cavities or heterogeneities (3 to 6 m in extent) might exist at those depths as well. Especially, the S-wave tomogram shows more inhomogeneities than the P-wave tomogram, with S-wave velocities in the range of 2,000 to 3,800 m/s and P-wave velocities ranging only from 5,000 to 6,500 m/s. In relative terms, the range from minimum to maximum S-wave velocity therefore constitutes a 90% increase, whereas the P-wave constitutes only an increase of 30%. Following the tomographic surveys, two further boreholes, BH3 and BH4, were drilled to verify the results, with BH3 confirming the presence of the cavity as interpreted in the tomograms. A good correlation between both the P-wave and S-wave tomograms and the borehole logs has further provided more confidence in our interpretation.

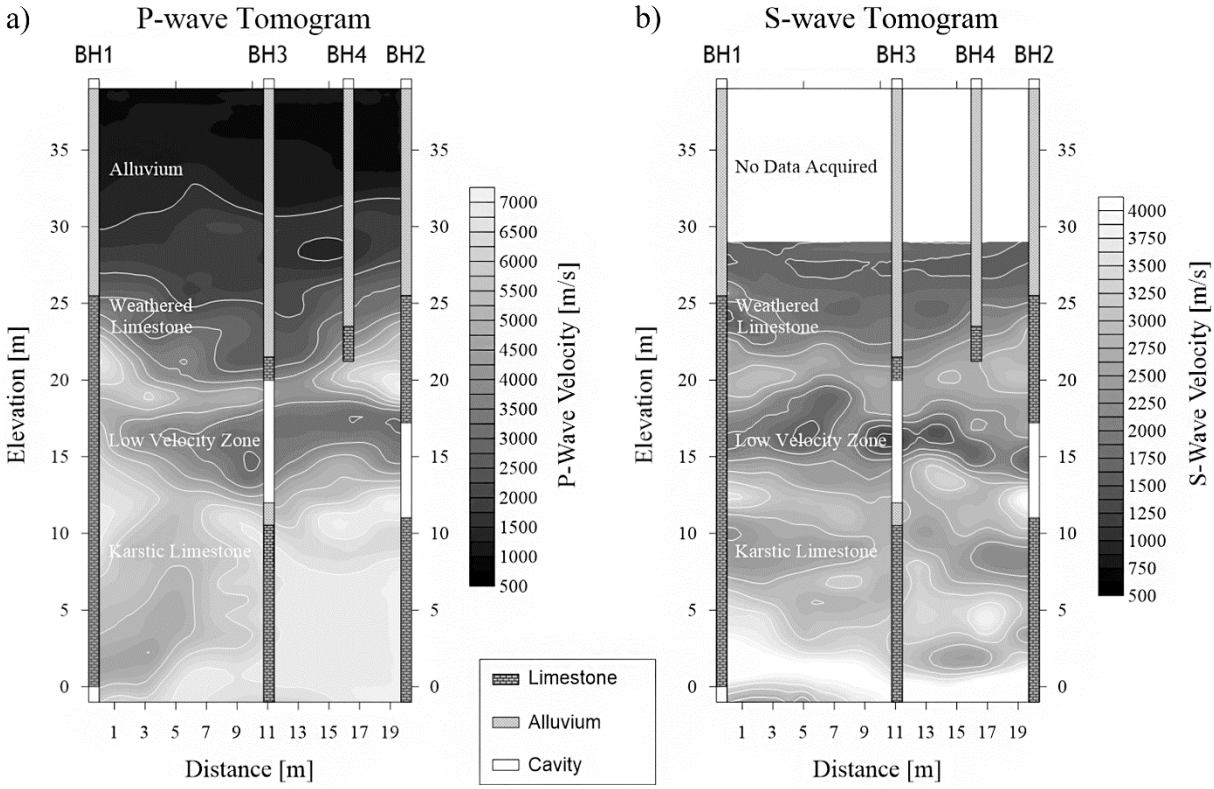


Figure 3.2: Tomographic inversions for the P-wave (a) and the S-wave traveltimes (b), showing a good correlation with the boreholes.

Once the P- and S-wave velocities have been established and a reliability exists in the tomograms, it is now possible to calculate the elastic moduli on a 2D plane between the boreholes. These moduli, i.e., the P-wave to S-wave velocity ratio, Poisson's ratio, bulk modulus and Young's modulus are displayed in Figure 3.3. In addition the shear modulus was determined by utilizing the S-wave velocities in conjunction with estimated density values, shown in Figure 3.4. To estimate densities, we applied a similar approach to Paasche et al. (2006), whereby the tomograms were partitioned into three distinct

zones using k-means clustering of the P- and S-wave velocities (Figure 3.4a). These zones (Figure 3.4b) are interpreted to consist of 1) alluvium with a density of 1,500 kg/m3; 2) moderately weathered limestone with a density of 1,900 kg/m^3 (e.g., Dubois et al., 2014); and 3) intact limestone with a density of 2,500 kg/m^3 (e.g., Bourbie et al., 1987).

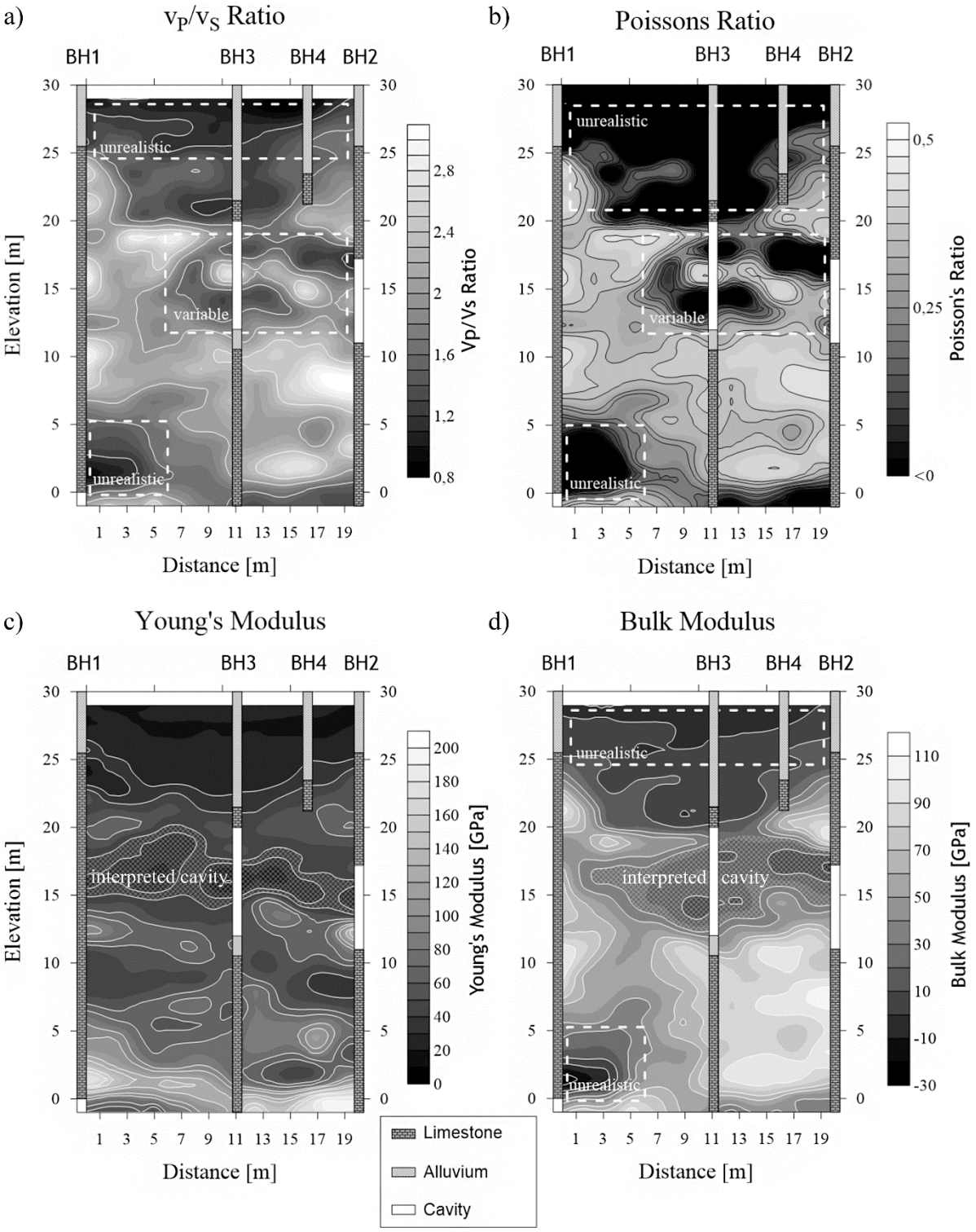


Figure 3.3: Elastic Parameters: (a) Vp/Vs Ratio, (b) bulk modulus, (c) Young's Modulus, and (d) shear modulus.

The elastic parameters are helpful at visualizing the subsurface structures and can also be useful in identifying areas that are prone to error. For example, the P-wave to S-wave velocity ratio (see Fig 3(a)) indicates very low values between 0.9 and 1.4. Such low Vp/Vs ratios are unexpected and could be due to incorrectly determined traveltime picks and a low ray coverage in that area. Another explanation is that the elastic bulk and shear moduli are distributed differently in the subsurface. Thus, 3D effects could come into consideration, whereby the first arriving P- and S-waves would not travel along the same path. Mufti (1995) has shown that these 3D effects can have significant effects on tomographic imaging. Considering, that the S-wave does not travel through cavities, but would rather travel around them, may be the reason for differing P-wave and S-wave travel paths. This in turn is most likely responsible for the highly varying Vp/Vs ratios and unrealistic Poisson's ratios. Thus, the high variabilities in these two ratios could indicate the presence of a large cavity.

The bulk modulus ranges from unrealistic negative values to approximately 100 GPa. The structure of the bulk modulus closely resembles the P-wave distribution. Young's modulus and the shear modulus on the other hand resemble more the S-wave velocity distribution, with Young's modulus ranging from 10 to 100 GPa in most areas and the Shear modulus ranging mostly from 5 to about 50 GPa.

The elastic parameters are a weighted combination of the P- and S-wave velocities and can therefore be used for the interpretation of geological structures. Thus, the elastic parameters were used to determine the size of the low velocity zone, which is interpreted as a cavity. The cavity has the dimension of approximately 16.5 to 19 m in length by 6 to 7 m in height based on the elastic parameter interfaces. Variations in the interpreted cavity shape could give an indication in terms of the uncertainty in its size and position. By comparing the interpreted cavity to the borehole log of BH3, it is clear that the P-wave tomogram and bulk modulus correlate better than the S-wave tomogram and its derived elastic shear modulus. Nonetheless, the Vp/Vs ratio, and similarly Poisson's ratio show a high variability where BH3 intersected the cavity.

To further enhance the interpretation and estimate the usefulness of the tomograms, the elastic parameters can also be used to determine the earthquake vulnerability of the future tunnel, since Wang and Munfakh (2001) show that earthquake resilience is dependent on the surrounding material stiffness. Another benefit is that the elastic parameters can improve the prediction of the penetration rate of the tunnel boring machine (TBM). If elastic parameters would be collected in a larger scale or in problematic environments, these could play an important role in the economic and time planning of the construction project, since Ghasemi et al. (2014) show that the penetration rate of a TBM can be accurately modelled using compressive strength, rock brittleness, distance between planes of weakness and the orientation of discontinuities in the rock mass. It is therefore likely, that the elastic parameters can aid the modelling of the TBM penetration rate.

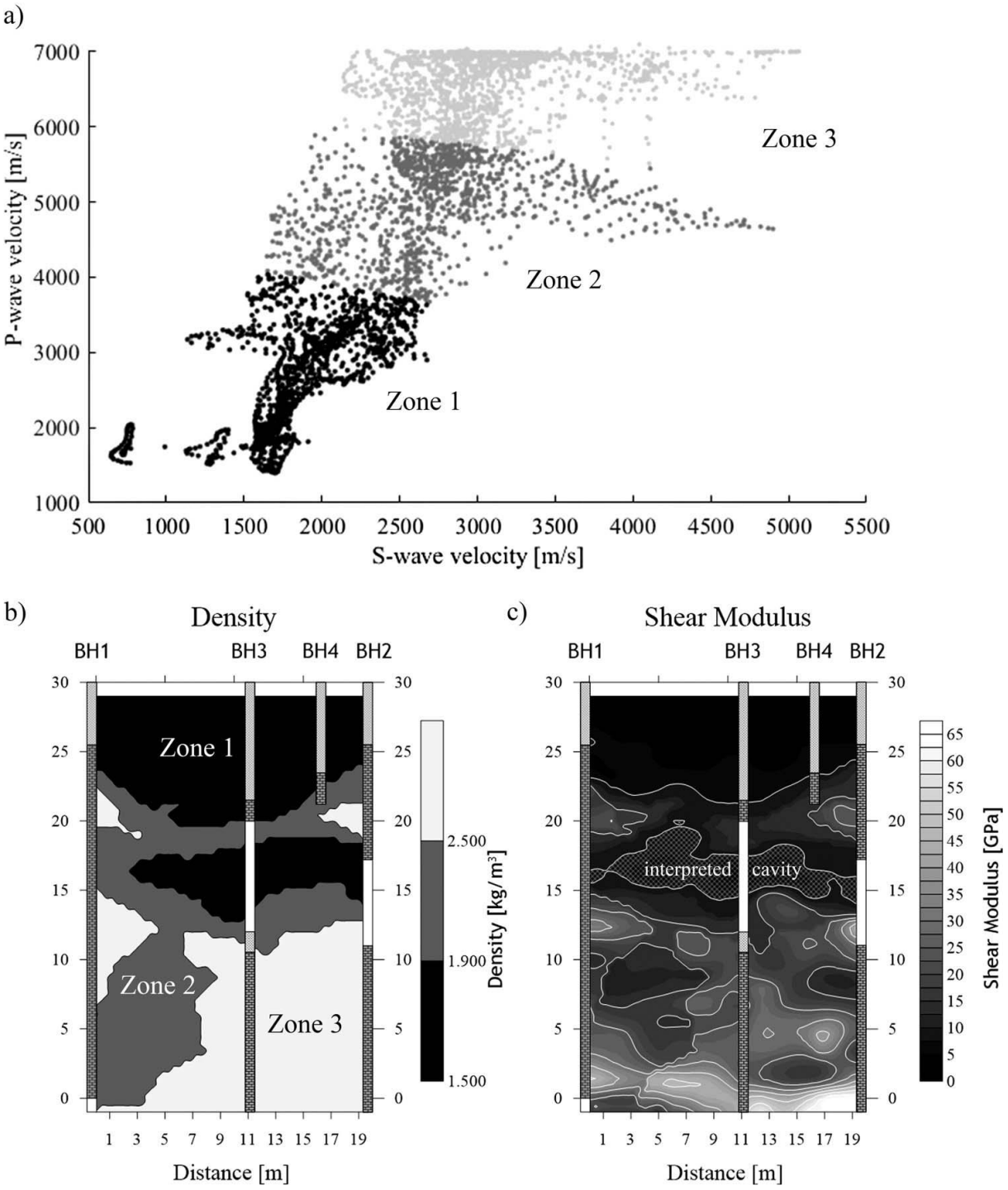


Figure 3.4: Density zonation and Shear Modulus: (a) k-means clustering to partition the tomograms into three zones, (b) the assignment of density values to three zones, and (c) calculated shear modulus.

3.5 Conclusion

P- and S-wave tomography measurements were carried out between two near-vertical boreholes to a depth of about 40 m at a site in the city center of Kuala Lumpur, Malaysia. Despite carrying out the survey in an urban environment, high quality data were acquired over a distance of approximately 20 m. The S-wave and P-wave traveltimes were independently picked and tomograms calculated which show similar structures. The two tomograms were used to determine elastic parameters which helped in the geological interpretation, identifying karstic areas and estimating the degree of reliability of the tomograms. A low velocity zone is visible in both tomograms, which was interpreted as a cavity with the dimension of about 16.5 to 19 m horizontally by 6 to 7 m vertically. Two boreholes were subsequently drilled, which correlate well with the interpretation. The survey shows the potential of routinely carrying out P- and S wave tomography surveys in karstic, hard rock environments to enhance the geological interpretation, with the added benefit of deriving small strain elastic parameters.

4. PUBLICATION II: CHARACTERISATION OF GROUND MOTION RECORDING STATIONS IN THE GRONINGEN GAS FIELD

The seismic hazard and risk analysis for the onshore Groningen gas field requires information about local soil properties, in particular shear-wave velocity (V_S). A fieldwork campaign was conducted at 18 surface accelerograph stations of the monitoring network. The subsurface in the region consists of unconsolidated sediments and is heterogeneous in composition and properties. A range of different methods was applied to acquire in situ Vs values to a target depth of at least 30 m. The techniques include seismic cone penetration tests (SCPT) with varying source offsets, multichannel analysis of surface waves (MASW) on Rayleigh waves with different processing approaches, microtremor array, cross-hole tomography and suspension P-S logging. The offset SCPT, cross-hole tomography and common midpoint cross-correlation (CMPcc) processing of MASW data all revealed lateral variations on length scales of several to tens of metres in this geological setting. SCPTs resulted in very detailed V_S profiles with depth, but represent point measurements in a heterogeneous environment. The MASW results represent V_S information on a larger spatial scale and smooth some of the heterogeneity encountered at the sites. The combination of MASW and SCPT proved to be a powerful and cost-effective approach in determining representative Vs profiles at the accelerograph station sites. The measured V_S profiles correspond well with the modelled profiles and they significantly enhance the ground motion model derivation. The similarity between the theoretical transfer function from the V_S profile and the observed amplification from vertical array stations is also excellent.

4.1 Introduction

Induced earthquakes due to gas production in the Groningen field in the northern Netherlands has prompted the development of seismic hazard and loss estimation models in order to allow risk-informed decision-making with regard to mitigation options. A key element of the seismic hazard and risk models for the Groningen field is a ground motion prediction model to estimate surface motions due to each possible earthquake scenario. The ground motion model for the Groningen field is comprised of predictive equations for spectral accelerations and peak ground velocity at a reference rock horizon (located at about 800 m depth) and non-linear frequency-dependent amplification functions reflecting the dynamic response of the overlying soil layers (Bommer et al., 2017).

The ground motion model derivation has benefited from a database of recordings of ground motions obtained from accelerograph and borehole geophone networks installed in the Groningen field. The location of the stations is shown in Figure 4.1. The first stage of the model building process is to deconvolve the recorded surface motions to the reference rock horizon. The uncertainty in this process is greatly reduced by the accurate characterisation of dynamic properties of the soil column, particularly in the uppermost tens of metres that exert the strongest influence on the site response. Although an

excellent velocity model of the Groningen field has been constructed using measurements at depths from below about 50 m, the near-surface portion of the profiles are inferred from lithological profiles with shear-wave velocities (V_S) assigned based on available seismic CPT measurements (Kruiver et al., 2017a). To refine the profiles at the locations of the ground motion recording stations, in situ Vs measurements were made using a variety of borehole and non-invasive techniques. Challenges encountered in this work include the fact that in several cases it was not possible to perform the measurements in very close proximity to the location of the recording stations. The paper describes how these tests were conducted and the procedures followed to reconcile the different measurements to construct the final profile for each station.

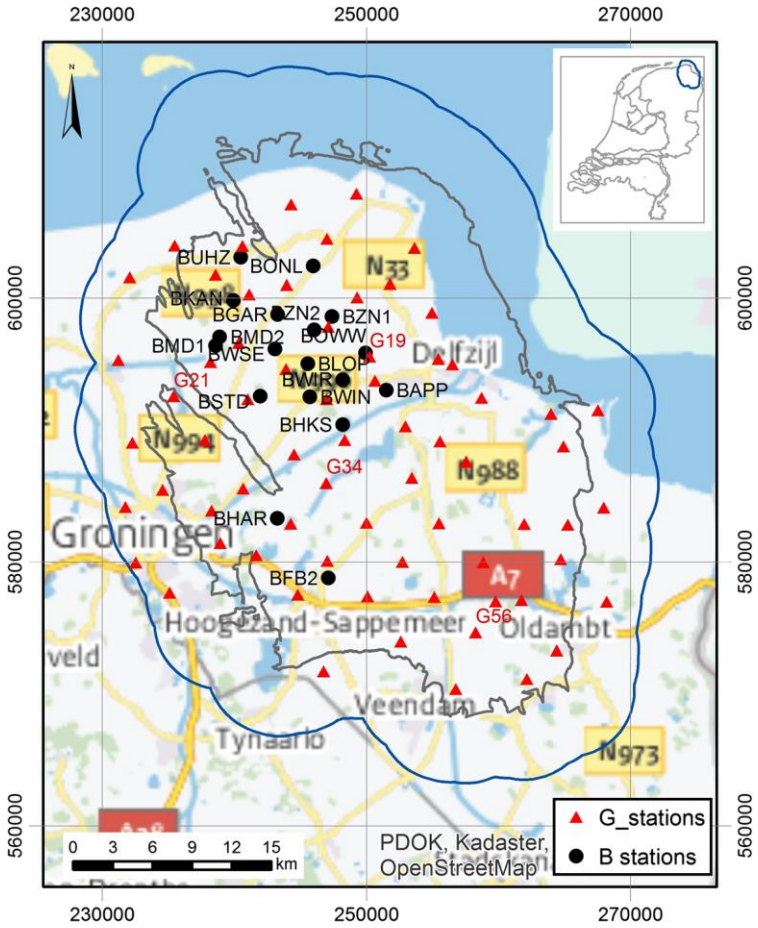


Figure 4.1: Location of recording stations in the Groningen field in the north of the Netherlands: 18 surface stations and 68 vertical array stations. Labels are shown for all 18 surface stations (coded B) characterised in this study and for the vertical array stations (coded G) from the examples in this paper (Figs. 16 and 18). Grid coordinates refer to the Dutch Ordnance System. The inset shows the location of the gas field in the northern part of the Netherlands.

The measured near-surface profiles also served to demonstrate that the geologically-derived V_S profiles provide a very good approximation to the field conditions. Empirical transfer functions at the recording

stations obtained from inversions of the surface recordings (Edwards et al., 2013) agree remarkably well with those calculated using the measured V_S profiles (Bommer et al., 2017). These comparisons not only confirm the reliability of the inferred velocity profiles for the whole field but also vindicate the assumption of 1D vertical wave propagation implicit in the site response analyses.

No direct V_S measurements have been made at the borehole stations, but interval velocities have been calculated from recordings at these locations and these also show excellent agreement with the inferred profiles for the same locations. The theoretical transfer functions for these profiles, calculated at the surface and 200 m depth, are similar to the surface-to-borehole spectral ratios of earthquake records.

4.2 Methods and Setup

4.2.1 Overview

The shallow subsurface in the Groningen region is of heterogeneous composition as a result of the relatively recent formation. Although site amplification as a result of induced earthquake is present in Groningen to larger depths, the maximum depth of investigation was limited to 30 m. This depth of investigation is not related to V_{S30} (time-averaged V_S over the top 30 m), but forms a good balance between fieldwork effort and added value of detailed V_S profiles to this depth. The geological setting is described in detail in Kruiver et al. (2017b) and references therein and summarised in this section. The sedimentary infill is influenced by two recent ice ages and by sea level fluctuations. The Elsterian glaciation produced deep subglacial features known as ‘tunnel valleys’, which were filled with sands and clays of the Peelo Formation. These tunnel valleys were buried by younger sediments. The second glaciation (Drenthe Substage of the Saalian glacial) produced the till sheet that is present in part of the region. The ridge-and-valley topography is still present in the relatively flat landscape. The region was not covered by ice sheets during the last ice-age (Weichselian). During that period, a widespread superficial blanket of eolian sand (the so-called cover sand) that formed in many places marks the top of the Pleistocene deposits. The northern part of the Netherlands borders the North Sea. During interglacial periods with relatively high sea levels, a large part of Groningen formed the coastal plain of this sea. The most recent Holocene deposits typically consist of stacked vertical sequences of tidal clays and sands that are often thinly bedded and are intermittent with peat layers. The Holocene sediment thickness varies from ~20 m in the northern part to being absent in the southern part of the region. Due to the presence of various intersection channel systems, namely the Pleistocene tunnel valleys and Holocene tidal channels, the subsurface is very heterogeneous. From the very large number of borings and from the geology, we can infer that infilled channels are present. It is, however, impossible to know the exact location of all individual channels.

In order to characterise the subsoil below the recording stations and considering the level of heterogeneity to be expected, the V_S measurements were to be located as close to the stations as possible. The stations are generally located in barns of farms in the rural areas and in public buildings (e.g. town halls) and houses in villages. Therefore, it was not always possible to locate all measurements in close vicinity of the stations. The distance between the station and the test site varied between 40 and 600 m, with an average distance of 150 m.

Four different V_S techniques were applied at the station locations. This section provides a short description of acquisition and processing for each of the methods. The survey setup is summarised in Table 4.1. Although the methods are routinely used in site characterisations (e.g. Garofaloetal. 2016a, b), we have implemented several adjustments to either improve the acquisition or the processing and interpretation of results. Suspension P-S logging (Ohya et al., 1984; Ogura et al., 1989) was applied unsuccessfully during this survey campaign, probably due to the combination of the borehole construction, grouting and the local geological setting. Therefore, these data were not further processed and interpreted.

Table 4.1: Summary of survey setup for the four different shear-wave methods

	SCPT	**MASW**	**Microtremor or array**	**Cross-hole tomography**	**Suspension P-S logging**
Source	Wooden beam and sledgehammer at 1.1, 5, 10, 15 and 20 m from SCPT truck	Accelerated weight drop 'Impacter'	Ambient noise	Borehole source of type BIS-SH	Hammer source in tool
Receivers	3-component accelerometer in SCPT cone	96 to 120 planted vertical 4.5 Hz geophones	Planted geophones of MASW array	3-component geophone string of 7 units with spacing of 1.0 m	Two 3-component hydrophone receivers in tool separated by acoustic damping tubes
Remark	Vertical sample interval max 1.0 m and coinciding with stratigraphical transitions	T-shaped array with geophone spacing of 2.0 or 3.0 m (4.5 Hz) and 4.0 m (1 Hz)	Recording of 70-80 x 3-2 s (120 x 1-6 s at one site)	L-shaped array of 3 boreholes with the source the corner of the L and the receivers in borehole at 10 (short leg of L) or 25 m (long leg of L). Boreholes are lined with blind liners	In one of the boreholes for cross-hole tomography
Depth of investigation	20 – 30 m	15 – 50 m	10 – 50 m	30 m	30 m
Lateral averaging	~ 2 m	Up to ~ 200 m		~ 1 m	~ 1 m
Vertical resolution	High, except shallow part	Medium, decreasing with depth	Medium, decreasing with depth	High	High

4.2.2 SCPT

Seismic cone penetration tests consist of a normal CPT with a geophone or accelerometer contained in the cone. The cone is penetrated into the soils and stopped at defined depth intervals for a V_S measurement. Shear waves were generated at the surface by striking a 10 kg sledgehammer on opposite sides of 2.5 m hardwood beams. Typically, the cone penetration is stopped every 1.0 m and the source is located ~1 m from the entry point at the surface (Butcher et al., 2005). In the Groningen case, alternations between peat, clay and sand occur at irregular intervals that are often smaller than 50 cm. In order to correctly sample the V_S of for each individual stratigraphy, the depth intervals at which the cone was stopped were determined by a normal CPT that preceded the SCPT. For example, when an 80 cm thick peat layer was present between 1.7 and 2.5 m on top on of sand, a V_S measurement was performed at 1.7 and 2.5 m instead of at 2.0 and 3.0 m. In this way, the peat V_S was not contaminated

by the much stiffer sand below it. Sources at offsets of 5, 10, 15 and 20 m were added to the standard 1.1 m source to gain insight in short-spaced lateral variations in V_S (Figure 4.2). This is referred to as offset SCPT (OSCPT). Coupling of the wooden beams to the ground was increased by sand bags. At each source location, three shots were performed and stacked at each depth, both from the left and right sides of the beam. The maximum target depth of SCPTs was 30 m, but in some cases the measurement was terminated earlier (e.g. at ~20 m) when the cone could not be penetrated further upon reaching the maximum capacity of the truck.

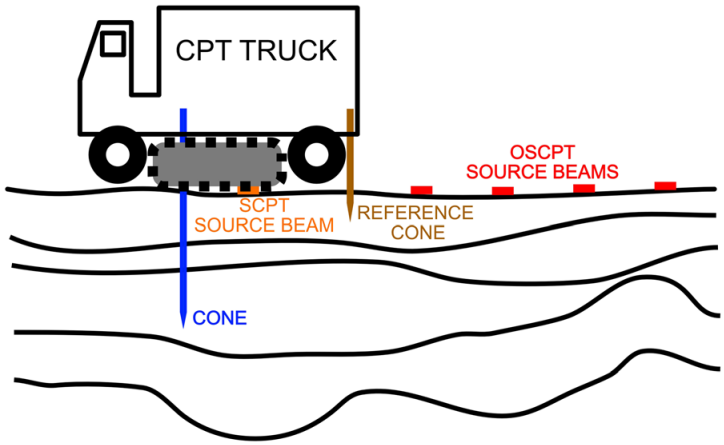


Figure 4.2: Schematic illustration of offset SCPT setup (not to scale).

SCPT data were processed using the BCE SC3-RAV 2015 seismic data analysis software (Version 15.0.1-June 2015). This software allows semi-automatic interval time picking using cross-correlation of the wave trains of subsequent test depths. The algorithm uses a simple ray tracing principle based on a horizontal stratigraphy model to determine the travel path length to calculate the interval shear-wave velocities. The left and right shots from the shear-wave source were processed separately. The traces for the OSCPT had to be hand-picked due to the lower signal-to-noise ratio for the larger offsets. The model subsurface from the OSCPT data was discretised using a grid of nodes, with a node distance of 0.5 m. For each of the nodes, the optimum V_S was determined by minimising the misfit defined as the root-mean-square (RMS) between the modelled travel times and the measured travel times. The 'fast marching method' (Sethian, 1999) was used to calculate the modelled travel times of seismic waves from source to receivers. For the optimisation, the Fresnel ray-path approach (Watanabe et al., 1999) was used. An example of CPT soundings and SCPT V_S profiles for station BLOP is given in Figure 4.3. The distance between the (S)CPTs is ~80 m. The CPT soundings show transitions at 8 – 9 m (Naaldwijk clay to Boxtel sand and Drente-Gieten clayey sand), 11.5 – 12 m (Drente-Gieten clayey sand to Peelo fine sand) and 15.5–16.5 m (Peelo fine sand to Peelo medium sand). The transitions in two nearby (S)CPTs do not occur at the exactly same depth, illustrating the heterogeneity of the geology. The transition between Holocene and Pleistocene Formations at 8 – 9 m depth can be clearly observed as a jump in the SCPT V_S profiles. The effect of the transition between different lithoclasses within the Peelo

Formation at 15 – 16 m depth is rather subtle. The OCPTs images (Figure 4.4) are much smoother than an individual SCPT V_S profile. Figure 4 consistently shows the Holocene/Pleistocene V_S transition and the Boxtel/Drente-Gieten Formations on top of the Peelo Formation. The Boxtel Formation can be cemented very locally, giving rise to relatively high V_S values. The OSCPT images show that even on very short (~ metre) spatial scales the values of V_S and the transition depths vary.

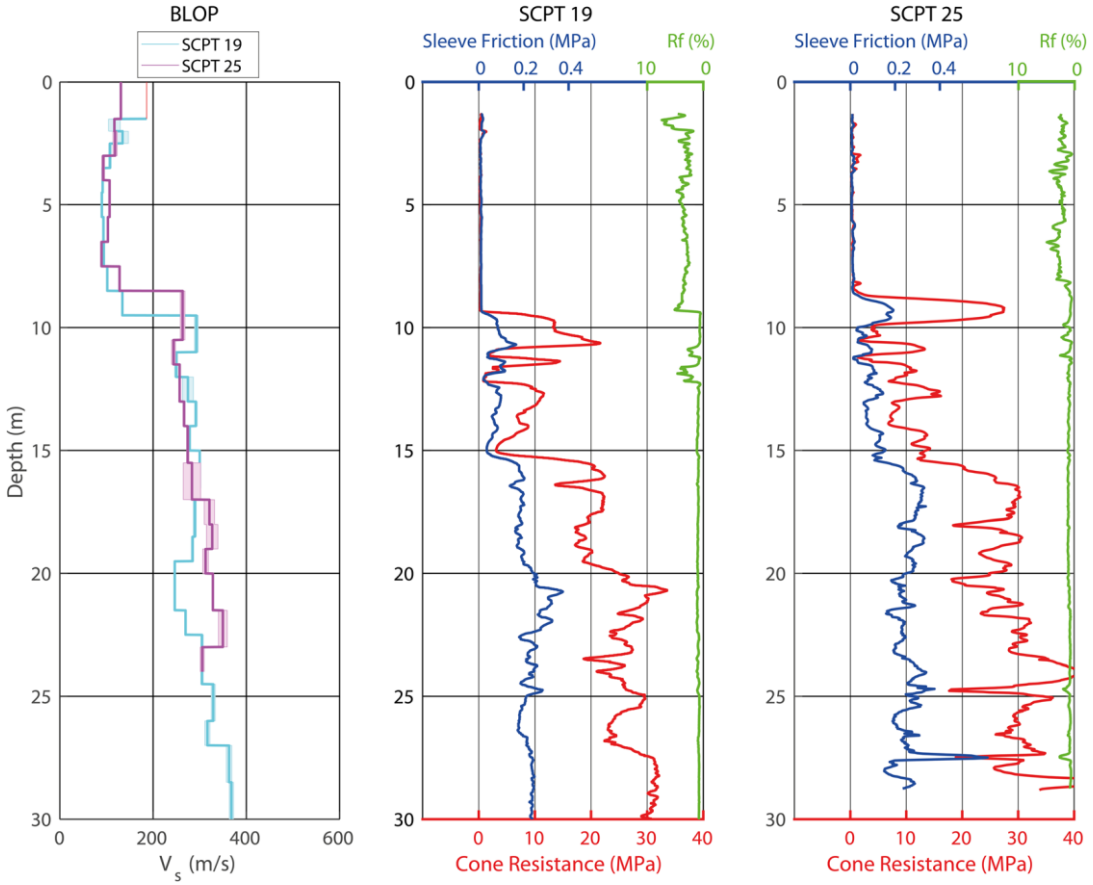


Figure 4.3: CPT and SCPT data for station BLOP. Left: V_S profiles of SCPT 19 (blue) and SCPT 25 (purple). The shaded band indicates the results from the left and the right blow. Middle and right: CPT soundings of SCPT 19 and SCPT 25, with cone resistance in red, sleeve friction in dark blue and friction ratio Rf in green.

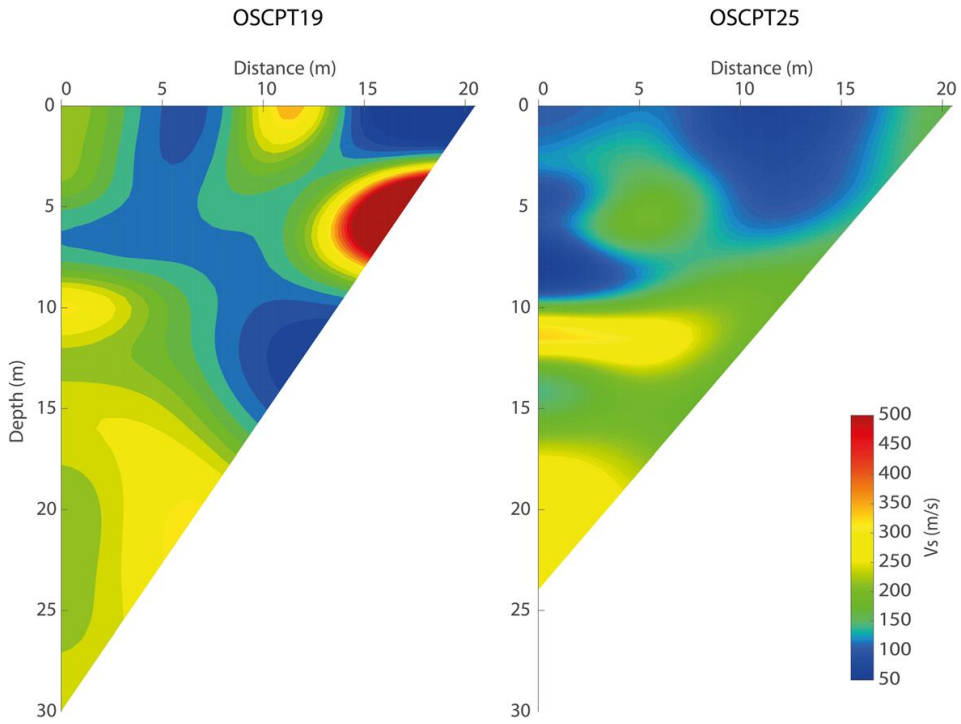


Figure 4.4: OSCPT result for SCPT19 (left) and SCPT25 (right) for station BLOP.

4.2.3 MASW and microtremor array method

The MASW method uses the dispersive behaviour of surface waves, i.e. the fact that the different frequencies of the wave signal travel with different speeds, to derive V_S profiles with depth (Park et al. 1999). The dispersion of a wave can be determined using multiple receivers that record the passage of a surface wave. The surface wave itself can be actively generated for the analysis, for example with a hammer blow or weight drop, or can be of ambient origin, like traffic or ocean noise. If active source and ambient noise recordings contain different frequency ranges, they might be combined to increase the depth range and resolution. However, while the prominent source direction is known in an active acquisition, in ambient noise acquisition it is unknown beforehand. Therefore, we acquired the seismic data using T-shaped arrays, with different sets of geophones, as visualised in Figure 4.5 and summarised in Table 4.1. The main line consisted of 96 4.5-Hz geophones (72 in the first locations). To obtain lower frequency content 12 1-Hz geophones were placed parallel to the main line. Perpendicular to the main line 24 4.5-Hz geophones were placed for directionality analysis. For the active data acquisition an accelerated weight drop source (‘Impacter’) was used, at the shot locations indicated in Figure 4.5.

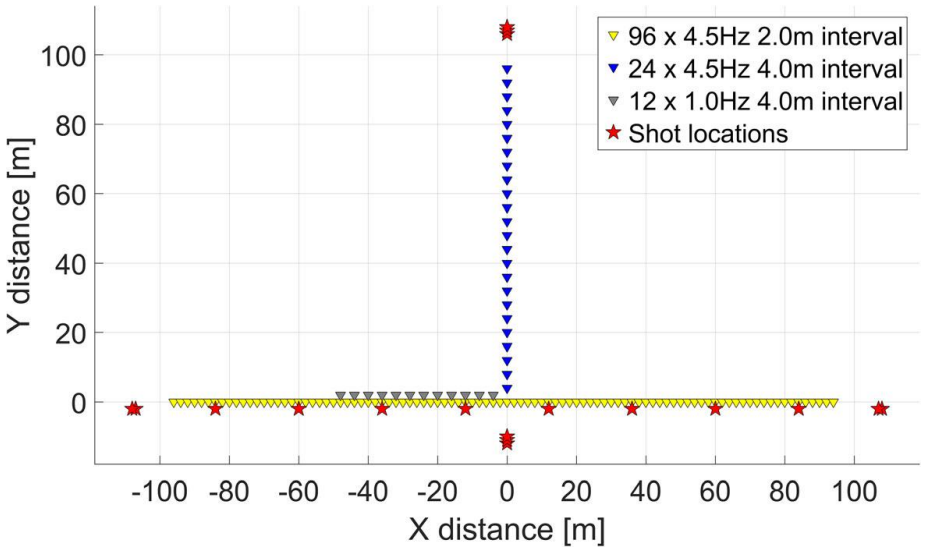


Figure 4.5: Survey setup for MASW and microtremor array with planted geophones. Triangles represent geophone locations, and stars represent shot locations.

Our analysis of MASW and microtremor array data is based on records of Rayleigh waves. Generally, the lowest frequency of both microtremor array and MASW data is 2 to 4 Hz and the maximum usable wavelength under the assumption of a homogeneous medium ranges between ~40 and 200 m. Given the heterogeneous and layered subsurface of the Groningen region, with low V_S layers and V_S values decreasing at certain depths, the theoretical wavelength at a certain frequency does not represent the true penetration depth. Although wavelengths of about 200 m were observed, the inversion of the data showed that typical penetration depth was in the order of 10 to 50 m.

The dispersion analysis of the MASW data was done in two ways, making use of the different source locations. The first method focuses on getting the highest resolution dispersion plot for the whole line, while the second method focuses on determining multiple (lower resolution) dispersion plots along the array to detect heterogeneity within the array. The basic idea behind the methods is sketched in Figure 4.6. The static array was used in two ways to combine multiple shot locations. In the method sketched in the top row, the geophones are sorted on source-receiver offset to get a densely-sampled virtual record. This is referred to as an offset gather. For the main line the sampling was improved from 96 channels at 2 m interval to 192 channels at 1 m interval by shifting the source by 1 m. In this way, the spatial sampling interval is halved and the amount of data is doubled. This procedure was possible because the Impacter (accelerated weight drop) produced a repeatable signal.

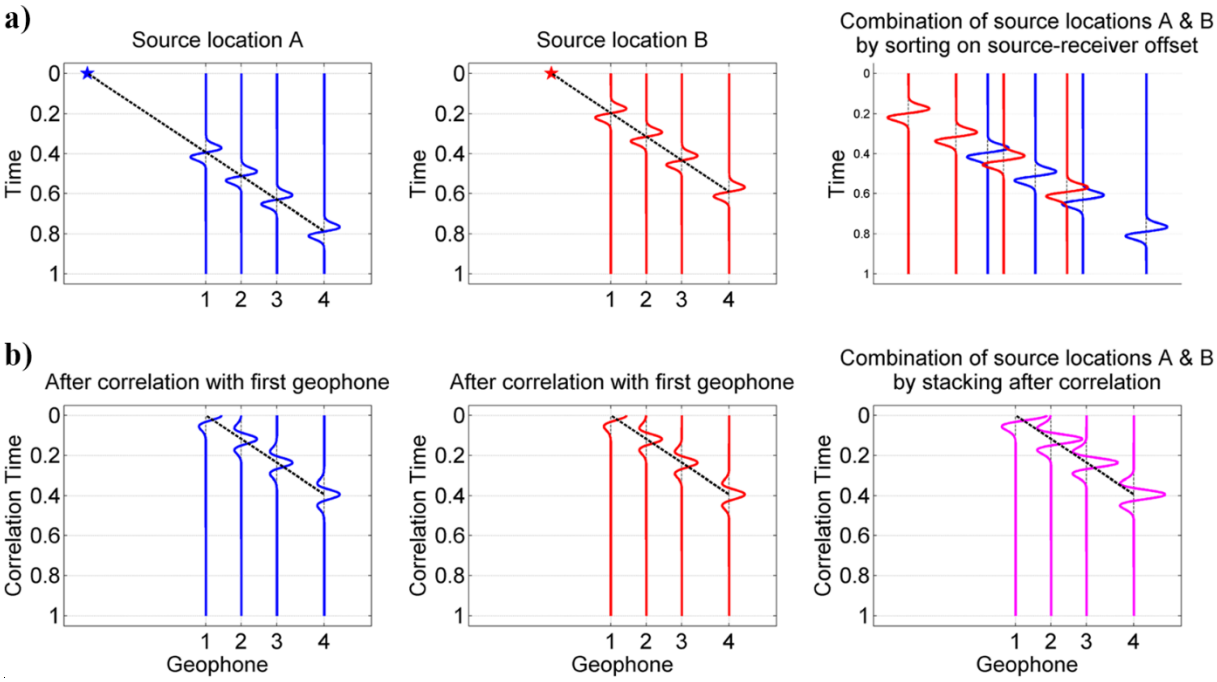


Figure 4.6: Sorting and pre-processing of MASW data to obtain offset gathers (a) and geophone correlation gathers (b) to prepare for CMPcc binning.

The second method focuses on determining heterogeneity and is sketched in the bottom row of Figure 4.6. The influence of the source-receiver offset is removed by correlating the recordings from different receivers, for subsequent sources, and stacking these correlations over the sources. Virtual records along the array are generated using different correlation pairs. The dispersion behaviour of the virtual records is determined using the common midpoint cross-correlation approach (CMPcc) approach (Hayashi and Suzuki, 2004). Although 96 geophones can be combined to form a maximum of 4560 correlation pairs, approximately one third of the combinations were used. This is to ensure equal numbers of pairs in each CMPcc bin (Figure 4.7). For visualisation purposes, the array has been reduced to 24 geophones in this figure, but the same principle applies to the 96 geophones of our array. Correlations are binned based on the midpoint of the geophone pairs being correlated. The different offsets between the correlation pairs within a bin are used to determine the dispersion for each bin. A minimum number of correlation pairs within a bin is required to estimate the dispersion with sufficient confidence. Therefore, the first and last bins cannot be used for dispersion plotting because they contain an insufficient number of pairs spanning too limited an offset. This applies to the first two and last three bins in Figure 4.7. Correlation pairs with too large an offset were excluded as well, because the purpose of the CMPcc analysis was to investigate heterogeneity. This procedure ensures that each bin contains the same number of correlation pairs. Therefore, changes in dispersion can be attributed to differences of ground properties, rather than to resolution differences between the bins. Our CMPcc bins contained 24 geophone pairs per bin, spanning an offset between 2 and 48 m. Dispersion plots were generated from the CMPcc bins for waves

that were travelling from ‘left-to-right’ as well as for ‘right-to-left’ travelling waves. The best quality dispersion plot was selected for analysis.

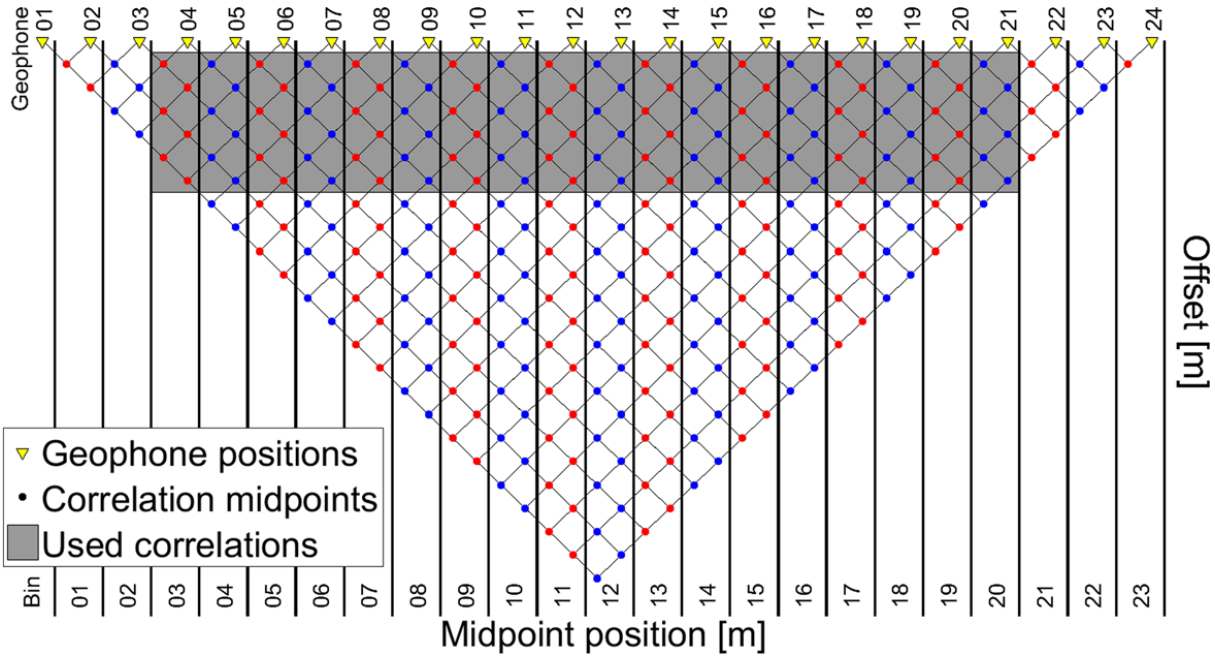


Figure 4.7: Schematic representation of CMPcc binning. Geophones are represented by yellow triangles, and the correlation midpoints are indicated by dots. The correlations within the grey zone are used for analysis. Only bins with a sufficient number of midpoints are used (bins 3 to 20 in this example) and fixed offset range (6 geophones in this example).

The dispersion plots found by the classic MASW and the CMPcc approach were inverted to derive V_S models and investigate the V_S variation along the profile. The inversion algorithm searches the model space to find the V_S profile with the minimum misfit between the modelled dispersion curve and the measured energy on the dispersion plot. The most likely V_S model for each data set was determined with in-house software by manual optimisation and by applying an automated genetic algorithm. The full array was processed both manually and automatically. The CPMcc gathers were processed automatically. For the manual optimisation, the SCPT V_S model was used as a starting model. The emphasis of this exercise was to obtain the V_S model that fits all modes and the particular shapes of the modes, such as curvatures at certain frequencies. The genetic algorithm automatically generates numerous V_S model realisations, each associated with a modelled dispersion curve. The best V_S model from the manual optimisation was used to define the search space of the automatic algorithm. The goodness of fit was defined by the energy of the dispersion plot along the modelled dispersion curve. After a number of iterations, the genetic algorithm converges to a group of likely models. The best V_S model is chosen from this group based on the best goodness of fit. Figure 4.8 shows an example of a dispersion plot of the full line array of 96 geophones and resulting V_S profiles obtained with the two inversion approaches. Generally, the two approaches result in the same pattern of V_S, but the transition

depths and V_S values of the individual layers vary between the methods. The theoretical fundamental and the higher modes corresponding to the V_S profile for both methods are shown in the dispersion plot. Only the fundamental mode is used in the goodness of fit definition in the genetic algorithm. All modes are considered in the visual inspection of the fit between the model and the data in the manual approach. The maximum depth of reliable V_S information was determined by a sensitivity analysis of the deeper layers to changes in depth and V_S during the manual procedure. The maximum reliable depth for V_S varied between 10 m for a site with a very thick layer of low V_S to ~50 m for sites with stiffer soils.

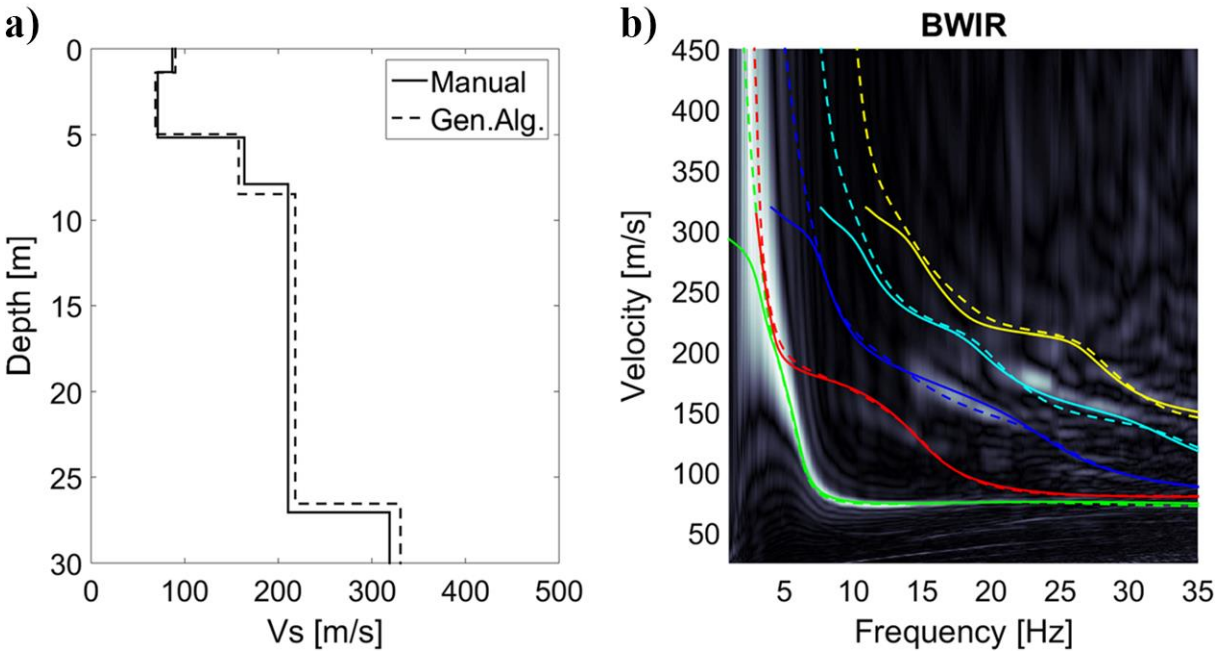


Figure 4.8: MASW result for station BWIR. V_S profiles from the manual optimisation (solid line) and the genetic algorithm (dashed line) are shown in (a). Dispersion plot showing the energy in the velocity-frequency domain in grey scale and the theoretical dispersion curves for the V_S profiles of the left panel for the manual optimisation (solid line) and the genetic algorithm (dashed line), shown in (b). The fundamental mode is shown in green; the higher modes in red, blue, cyan and yellow.

The CMPcc result for station BWIR is shown in Figure 4.9. Figure 4.9a shows the best V_S model for each of the 72 CMPcc gathers as determined using the genetic algorithm. The V_S profile resulting from each CMPcc gather is represented by a colour-coded column. The panel of 72 columns does not represent a 2D V_S profile, because of the large overlap in data between in the CMPcc models (Figure 4.7). However, the plot is indicative of variation in thickness and V_S values of the individual layers along the full array of ~200 m length. The transition between Holocene and Pleistocene deposits at ~8 – 9 m (in SCPT) varies between ~4 and 9 m. Figure 4.9b shows the standard deviation of the group of best models for each CMPcc gather. The standard deviation varies laterally as well and is generally higher for deeper layers. This means that V_S for deeper layers is less well constrained. The aggregated results

of the CMPcc analysis are shown Figure 4.9c. The transitions between the model layers appear to be smeared relative to the standard MASW interpretation which shows sharp transitions (Figure 4.8).

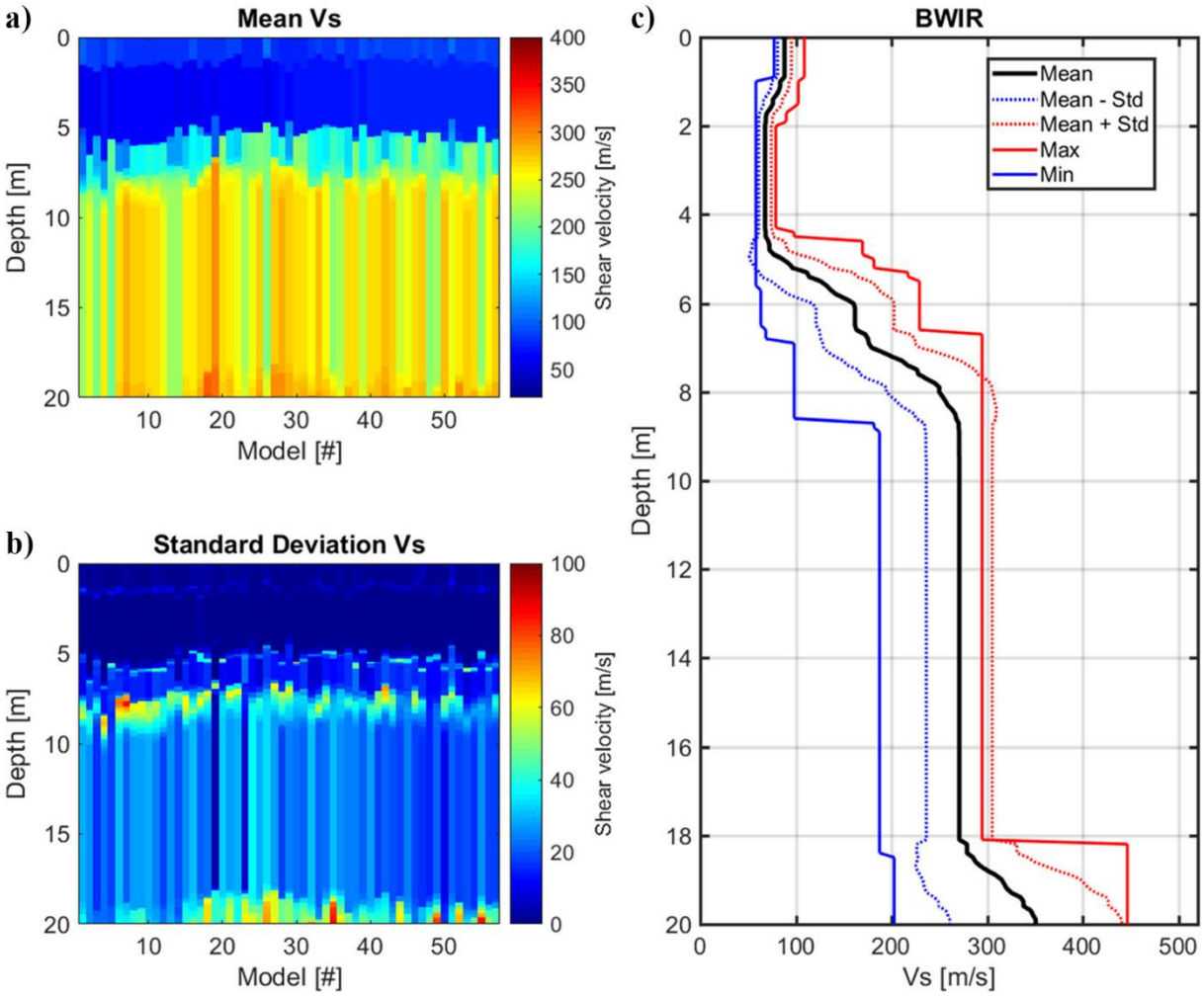


Figure 4.9: CMPcc result for station BWIR. Mean of best V_S models for the 72 CMPcc gathers along the line (a). Standard deviation of best V_S models for the 72 CMPcc gathers along the line (b). Best fit curve of the 72 models with the maximum and minimum value observed in the whole CMPcc and the standard deviation from all models (c).

Passive or ambient-vibration-based surface wave methods record background vibrations emanating from ocean wave activity, atmospheric conditions, wind effects, traffic, industrial, construction activities, etc., which collectively are referred to as microseisms. Examples of application of microseism techniques can be found in Yong et al. (2013). Typically, microseisms with frequencies below 1 Hz have natural origins, whereas those above 1 Hz are largely due to human activities (Okada, 2003). As frequencies below 1 Hz are difficult to generate by active sources, microseisms can help increasing the bandwidth at the low end and therefore the microtremor array technique will usually extend the depth of investigation of MASW.

The microtremor array experiment was conducted to test whether the MASW data could be enhanced by including ambient noise data. The microtremor array data were acquired using the same planted geophone arrays as the MASW with a source (Table 4.1). However, this time ambient noise was recorded. At each site, between 70 and 80 recordings were made, each with a duration of 32 s at a sample interval of 2 ms. The microtremor array data were processed using the extended spatial autocorrelation (ESAC) technique (e.g. Mulargia and Castellaro, 2013). ESAC is based on the spatial autocorrelation (SPAC) method of Aki (1957). A drawback of the ESAC method is that only a single dispersion curve is determined, most likely the fundamental mode, but the method is considered more suitable for microtremor array measurements than frequency-wavenumber spectrum (fk) methods (Ohori et al., 2002). Figure 4.10 shows the dispersion information obtained from the microtremor array and active source data acquired at station BGAR. The dispersion curve from the microtremor array measurements (red dots in Figure 4.10) agrees well with the fundamental mode in the dispersion plot of the MASW data (greyscale dispersion plot of Figure 4.10). However, the microtremor array data do not significantly extend the bandwidth of the dispersion data.

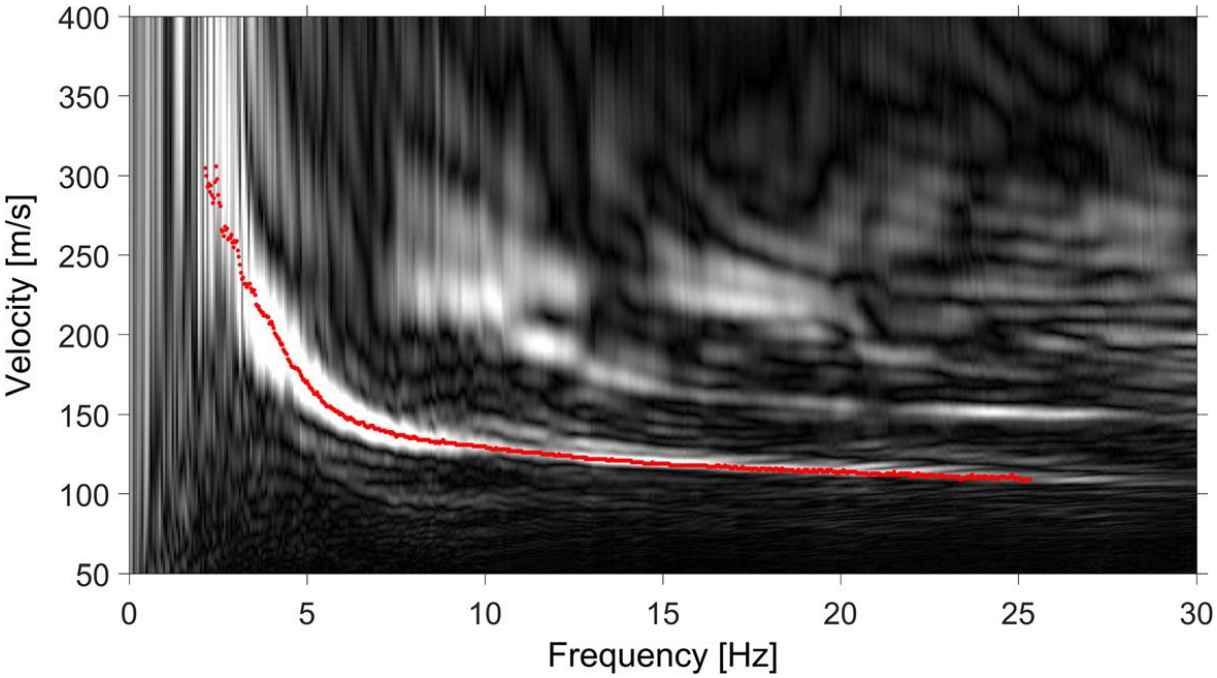


Figure 4.10: Dispersion curves determined with the ESAC method applied on the passive data at BGAR (red dots) plotted on top of the (black and white) dispersion plot determined for the active data using the MASW method.

During the processing of the microtremor array dataset, it was not possible to extract surface wave dispersion data from the ambient noise acquired at sites BAPP and BHKS. The MASW results indicate the presence of a thin, low-velocity (V_S ~50 m/s) surface layer at these sites. Lateral variations in

thickness and V_S of top layers have a relatively large influence on the dispersion in the EPAC procedure and can affect the whole V_S model. The dispersion energy in the dispersion plot therefore becomes less reliable or impossible to define on the dispersion curve. The MASW data for these two stations showed good quality dispersion plots. The maximum resolved depth of stations BAPP and BHKS was limited to ~10 – 20 m (instead of 30 m) due to the presence of the very low-velocity layer at the top.

Another means to extend the low-frequency range of the MASW is to use low-frequency geophones. We installed 1 Hz geophones which partially coincided with the 4.5 Hz array (Figure 4.5). Because of the high costs of these geophones, only 12 were available, which creates a very short array. Nonetheless, the dispersion plots of the 1 Hz array and the 4.5 Hz array are compared in Figure 4.11. The effect from the number of geophones in the array is clear from the top and middle panel, both for the 4.5 Hz geophones. Reduction of the number of geophones results in smeared dispersion energy. The 1 Hz array shows more low-frequency energy than the corresponding 4.5 Hz array (bottom versus middle panel). In the current setup, however, the quality is insufficient to be able to extend the dispersion curve to lower frequencies. The quality could be improved by using a low-frequency source such as a low-frequency shear wave vibrator and by deploying more 1 Hz geophones at larger distances between the geophones. Ambient noise recording using the extended 1 Hz array might also increase the low energy content of the dispersion plot.

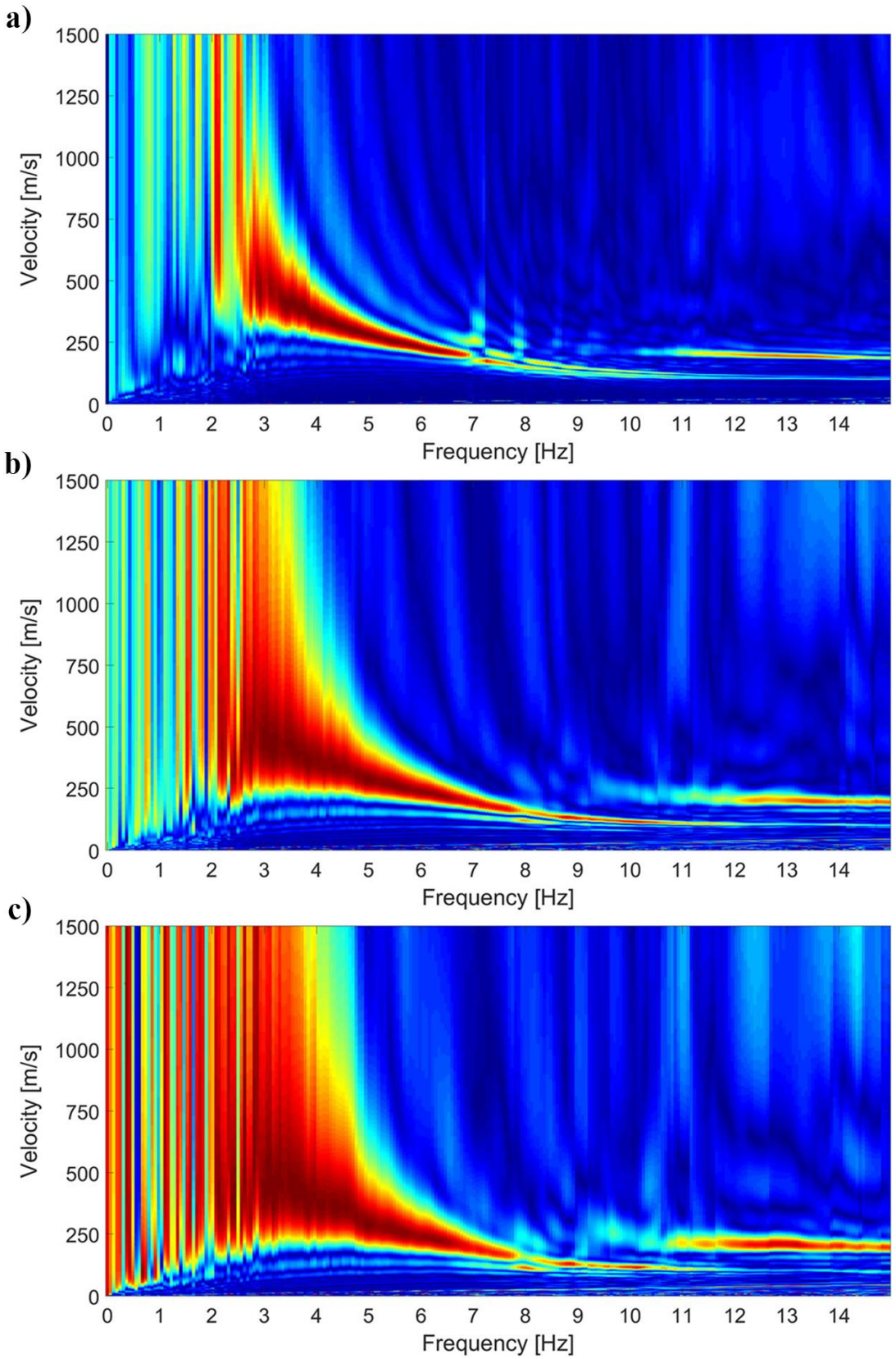


Figure 4.11: Comparison of dispersion plots for station BKAN. 4.5 Hz array of all 96 geophones are shown in (a).4.5 Hz array of 12 geophones at corresponding locations of 1 Hz array are shown in (b).1 Hz array of 12 geophones are shown in (c).

4.2.4 Cross-hole tomography

The cross-hole tomography data were acquired using three boreholes in an L-shaped configuration. The shear wave source was located in the corner of the L, while the receiver string was located either at 10 m at the end of the short leg of the L or at 25 – 26 m at the end of the long leg of the L. Thus, the shots were performed twice: once recorded by the receiver array in the borehole of the short leg and once recorded by the receiver array in the borehole of the long leg. This geometry was chosen to generate tomographic images at two different scales and in two directions. The borehole source is coupled to the borehole wall by a pneumatic clamping system (inflatable bladder). The orientation of the source is controlled from the surface by a torsional stiff hose. The seismic blow direction was aligned perpendicular to the receiver borehole in order to generate SH-waves. To obtain the opposite blow direction the source was rotated by 180°, thus generating S waves with opposite polarities. For each shot direction a separate seismic record was acquired. The source also generated P-waves.

The cross-hole seismic data processing included several steps. First, the travel times were determined manually by picking the arrivals of both the P- and S-waves. Next, the subsurface was numerically divided into cells. Vertical and horizontal cell sizes of approximately 1 m were selected. Seismic waves are assumed to propagate along curved ray paths. The simultaneous iterative reconstructive technique (SIRT; Gilbert, 1972) algorithm was used for travel time inversion. This algorithm is iterative and minimises the residual of the observed and calculated seismic travel times by a correction of the seismic slowness, i.e. the reciprocal of the seismic velocity in each cell. The tomograms for each borehole set were processed separately. An example of a V_S and a V_P tomogram is shown in Figure 4.12. The heterogeneity of the sediment at short distance scales is apparent. The transition from relatively low (~ 180 m/s) to relatively higher V_S (250 – 300 m/s) at the Pleistocene surface occurs at ~14 and ~18 m depth in the two SCPTs at the location. The transition is present in the tomograms at a depth varying between 12 and 25 m, showing that the stratigraphy is variable even over distances as short as a couple of metres. Comparing the V_P and V_S tomograms shows that the V_S/V_P or Poisson ratio is also highly variable over short distances and varies with depth.

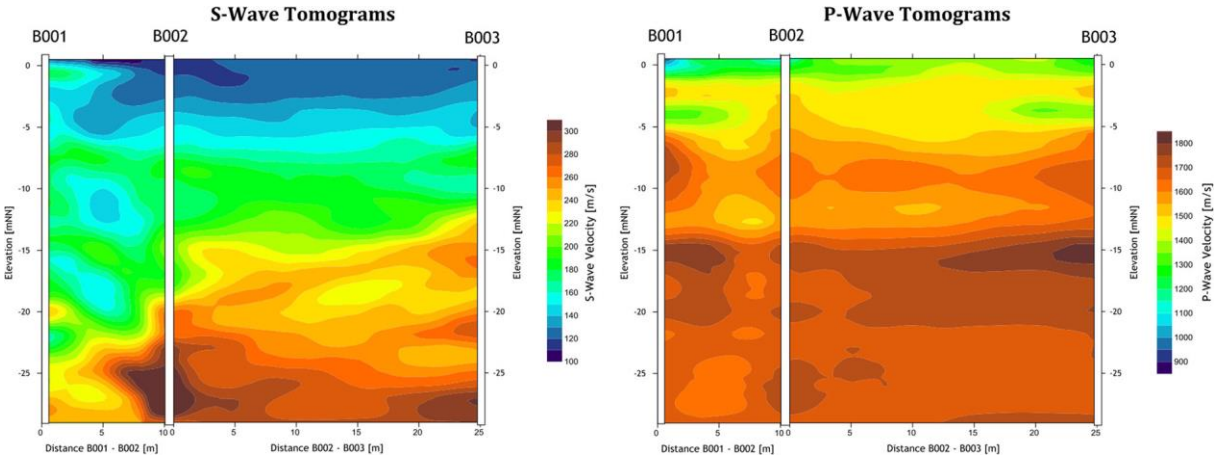


Figure 4.12: V_S and V_P images from cross-hole tomography for station BUHZ.

4.2.5 Seismic interferometry at vertical seismic arrays

In addition to the determination of detailed V_S profiles at the surface recording stations, interval V_S have been derived at ~70 near-surface vertical seismic arrays that cover the Groningen region (Figure 4.1). The seismic arrays consist of geophones at 200, 150, 100 and 50 m depth and an accelerometer at the surface. Local events are recorded over this near-surface borehole network. Shear-wave velocities at depth levels where seismicity occurs are an order of 10 times larger than near the surface. Consequently, shear waves bend towards vertical propagation in the near surface and are largely recorded on the horizontal components. This illumination is suitable to estimate seismic interval velocities between the receiver levels in the boreholes. Two methods were considered to determine the interval velocities. The first method uses the time differences of single phases after correction for the angle of incidence. These single phases exhibit large uncertainties, both on the timing and on the angle of incidence. The second method, which is applied here, is seismic interferometry on a catalogue of local events with sufficient signal-to-noise ratio (Hofman et al., 2017). Horizontal-component seismograms are rotated towards the transverse component and cross-correlated over different depth levels of single boreholes. By cross-correlating entire waveforms and stacking in cross-correlations of many different events, a precise estimate is obtained of the local seismic response: the waveforms are obtained as if there were a seismic source at one of the receiver levels and all the other receivers measured its response. The obtained response is dominated by a direct up-going and down-going wave. From these waves, the timing is picked and converted to interval velocities along the boreholes.

4.3 Integration of Various Methods

The various methods are based on different properties and behaviour of seismic waves and sample different kinds of soil volumes. All the results for one location are gathered and compared in Figure 4.13. The sample volume of the methods and thus level of detail decreases from left to right. The SCPTs result in very detailed V_S profiles. However, they represent local V_S variations. The two SCPTs with 80 m offset near station BWSE are similar, but individual layers occur at slightly different depths and with varying V_S values. The V_S is low (~130 – 140 m/s) between the surface and ~8 – 9 m depth, next there is a faster layer of ~2 m (225 – 460 m/s) below which there is an increase in V_S from ~170 m/s to 350 m/s apart from a local high V_S layer at 18 m depth in SCPT04.

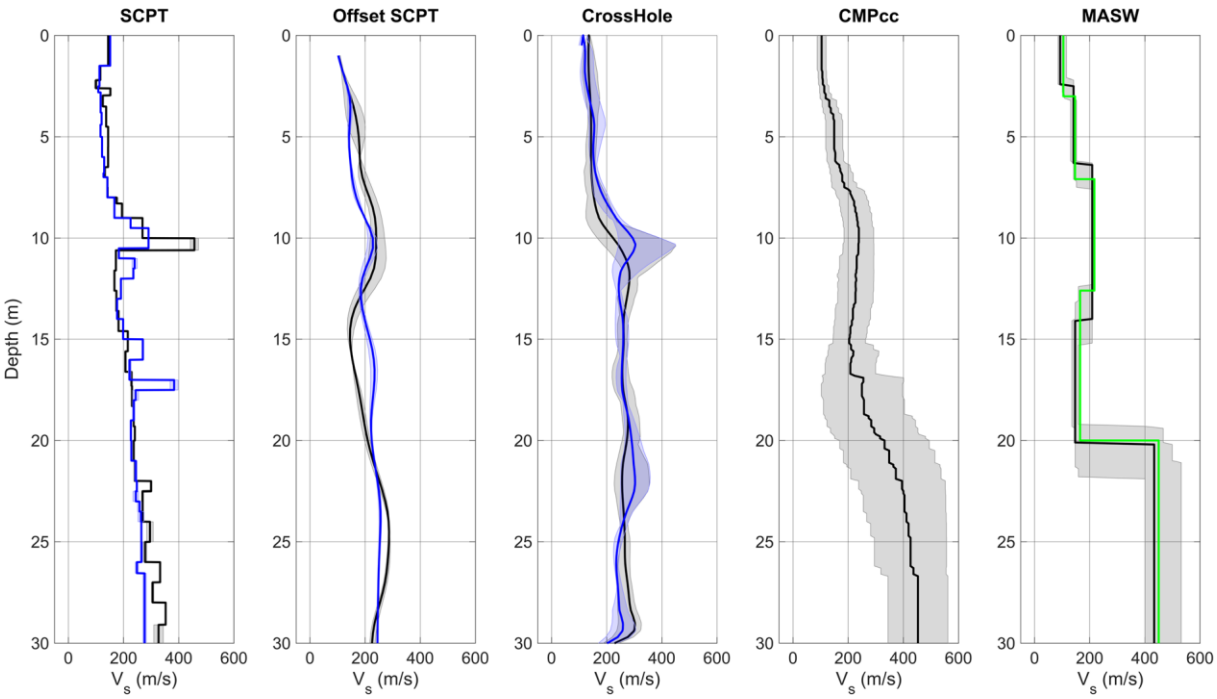


Figure 4.13: V_S profiles for station BWSE from different measurement techniques, including uncertainty bands. From left to right: SCPT03 (grey) and SCPT04 (blue) with band indicating variation between left and right blow; average profile for offset SCPTs between 1 and 5 m offset with shaded band indicating the minimum and the maximum V_S ; cross-hole average profiles for long leg (blue) and short leg (grey) with shaded band indicating the minimum and the maximum V_S ; CMPcc based on MASW array, shaded band indicates standard deviation of the 72 best models; MASW with manual fit in green and automatic inversion using the genetic algorithm in black with grey shaded band indicating the minimum and the maximum V_S.

The original tomographic images of OSCPT and cross-hole V_S show the local variations in V_S. In order to compare them to the other 1D profiles, they have been simplified by averaging V_S over depth slices. The 2D details, which are advantages of these methods, are lost in this way. The 1D OSCPT and 1D cross-hole profiles generally follow the SCPT profiles, but with less detail. The CMPcc and the MASW profile show a shallow V_S layer of ~90 m/s of 2 m at the top, followed by a 4 m thick layer of ~150 m/s, a 9 m thick layer of ~210 m/s and a 4 m thick layer of ~160 m/s. The very low V_S top layer in the MASW V_S profile is missed in the SCPT. Shear wave velocity results from the top 2 – 3 m in the SCPT cannot always be reliably determined due to the noisy record and the short distance of the waves travelled. This results in overlapping P- and S-waves in the record and the difficulty in reliably picking the S-arrival. The gradual increase in V_S below ~11 m that is apparent in the SCPT was not resolved in the MASW V_S profile. The most representative V_S profile is a combination of the SCPT, cross-hole and the MASW V_S profiles with some weighing. For the present study, we adopted a pragmatic choice: the SCPT was combined with the top layer of MASW only if the SCPT results were unreliable for the top few metres. When two SCPTs were available, the station representative SCPT was chosen based on the distance

between the SCPT and the station, the geology at the site and quality of the SCPT. To check the validity of the choice of SCPT, the theoretical dispersion curves of the SCPT were plotted on top of the MASW dispersion plot (Figure 4.14). Because of the aforementioned possible unreliability of the top metres of the V_S from SCPT, the minimum V_S value of the top three layers was assumed for these layers. Generally, the fit is very good.

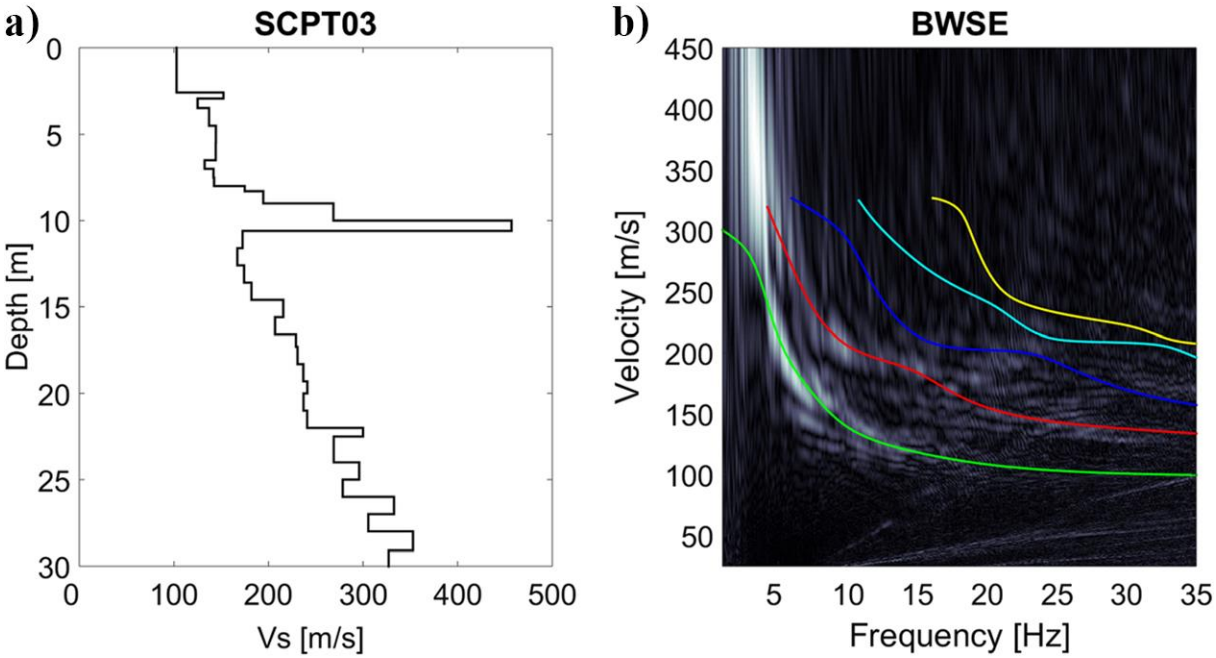


Figure 4.14: Example of SCPT profile on MASW for station BWSE. SCPT03 V_S profile with the top 3 layers replaced by the minimum value (a). Theoretical dispersion curves of the V_S profile for fundamental (green) and higher modes (red, blue, cyan and yellow) plotted on top of the MASW dispersion plot (grey scale) for station BWSE (b).

The 18 stations sample a variety of geological settings, but most stations are situated in areas with a Holocene cover on top of Pleistocene sediments. The average V_S is linked to the age of the deposits (Holocene or Pleistocene) and the lithology (peat, clay, sand). The transition between Holocene deposits (relatively low V_S) and Pleistocene deposits (relatively high V_S) is often easily recognised in the profiles by a jump from low V_S in the shallow layers to higher V_S values in the deeper layers (Figure 4.15). This occurs at 11 m depth for station BMD2, at 9 m for BWIR, at 8 m at BAPP and at 9.5 m for BLOP. Individual peat layers can be recognised from their low V_S, e.g. between 4.5 and 7 m at station BAPP. Between stations, the variation in V_S of the stratigraphic and lithological units is consistent. The general ranges of V_S for the Groningen deposits are < 100 m/s for Holocene peat, 100 – 200 m/s for Holocene clay and Pleistocene peat, 200–250 m/s for Pleistocene clay and fine sand and > 250 m/s for Pleistocene medium and coarse sand.

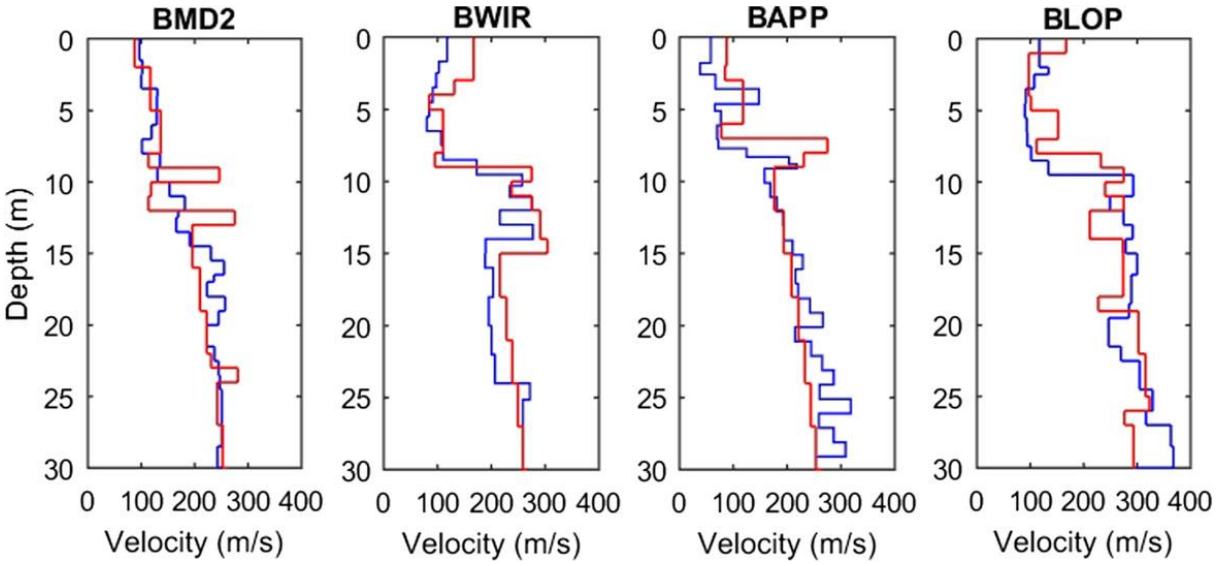


Figure 4.15: V_S profiles at selected B stations. Measured V_S in blue and modelled mean V_S (Kruiver et al., 2017a) in red.

4.4 Discussion

4.4.1 Performance of techniques and sampling scales

The various techniques to determine V_S in the field generally perform well in the Groningen setting. The depth of penetration of SCPT is in most cases possible to the target depth of 30 m. In some cases, this maximum was not achieved because of a combination of high friction due to stiff clay, high tip resistance or high friction in the Pleistocene sands. The MASW suffered from limited depth of penetration in some cases as well. The most apparent case is station BAPP where the top 7 to 8 m consists of very low V_S (< 100 m/s) material. In this location, the dispersion could be determined down to approximately 1 Hz, but the modelling shows that it only contains information from the top 15 m.

The SCPT and cross-hole techniques are based on picking shear-wave arrivals. The source-receiver distance needs to be sufficiently large to be able to reliably distinguish between the arrivals of different waves. For the cross-hole setup, the distance between source and receiver was always sufficiently large for reliable first arrival picking. For the SCPT, on the other hand, the distance between the source and receiver varies with depth, because the source stays at the surface while the receiver penetrates the soil. As a consequence, the quality of the data from the SCPT varies with depth: the top part might be unreliable when wave forms overlap. The unreliable top part (2 – 3 m) of the SCPT V_S profile was replaced by the more reliable MASW results for three of the 18 stations.

We demonstrated that the resolution and scale at which the different methods obtain the V_S profile is quite different. The surface-wave method ‘averages’ the V_S information over the whole array length of approximately 200 m and therefore is only sensing V_S structures if they have a significant contrast,

thickness and lateral extent. On the other hand, the SCPT method samples the velocity on a scale of a few metres at most. The OSCPT and cross-hole methods sample the data at intermediate scale. It is clear from the OSCPT, cross-hole and CMPcc results and the locations with two SCPT profiles that changes in velocities can be significant over small distances. Therefore, it is important to consider the relation between the scale of the V_S profile from a certain method and scale at which earthquake amplification occurs. The primary goal of the V_S measurements was to calibrate the transfer functions. A pragmatic choice was made to use the SCPT close to the accelerometer station (with MASW for the uppermost few metres when needed) for calculation, because it is both most detailed and contains extra information on lithology and shallow stratigraphy.

4.4.2 Comparison to other types of V_S estimates and derived analyses

Additional to providing V_S profiles for the ground motion model, the SCPT V_S values were used to derive a V_S model for Groningen. For this, SCPT V_S from this fieldwork and from archive data were classified in terms of stratigraphy and lithology to derive V_S distributions (Kruiver et al., 2017a). These V_S distributions were used to model V_S in the entire Groningen field in the top 50 m using the detailed 3D voxel model of geology GeoTOP of TNO Geological Survey of the Netherlands (Stafleu et al., 2011; Maljers et al., 2015; Stafleu and Dubelaar, 2016). The modelled V_S profiles at the stations are shown in Figure 4.15 for comparison with the in situ measured V_S. There is generally good agreement between the measured V_S at the site and the modelled values, especially considering the regional character of the GeoTOP model.

Theoretical 1D SH-wave site transfer functions (TFs) were calculated for each of the measured V_S profiles at the B stations. These transfer functions were used to deconvolve Fourier amplitude spectra (FAS) of surface recordings to a reference horizon, at some 800 m depth, for the purpose of determining seismological parameters for modelling earthquake ground motions (Bommer et al., 2017). The simulated ground motions were then used in a non-linear soil response analysis using a field-wide velocity model (Kruiver et al., 2017a) to determine zone-specific spectral acceleration amplification functions (AFs) for use in hazard and risk analyses (Rodriguez-Marek et al., 2017). As such, it is important to verify both the consistency of the V_S models and the accuracy and applicability of the site TFs. At the G-stations from the KNMI monitoring network, no in-situ measured V_S data are available. The V_S profiles inferred from seismic interferometry at selected G-stations and the modelled V_S profiles are compared in Figure 4.16. The modelled V_S data have been converted to interval velocities corresponding to the geophone intervals by determination of the harmonic means. These compare very well to the interval velocities estimated from seismic interferometry. The main uncertainty in the velocities estimated with seismic interferometry is related to interference between the direct waves and the reflected phases and noise. In Hofman et al. (2017), confidence ranges are added to all estimated profiles. For V_S, the confidence regions are generally very small and only exceed 20 m/s for a limited

number of very noisy stations. Differences in the estimated and modelled V_S in the top 50 m can be attributed to local variations in geology at the station sites relative to the GeoTOP model.

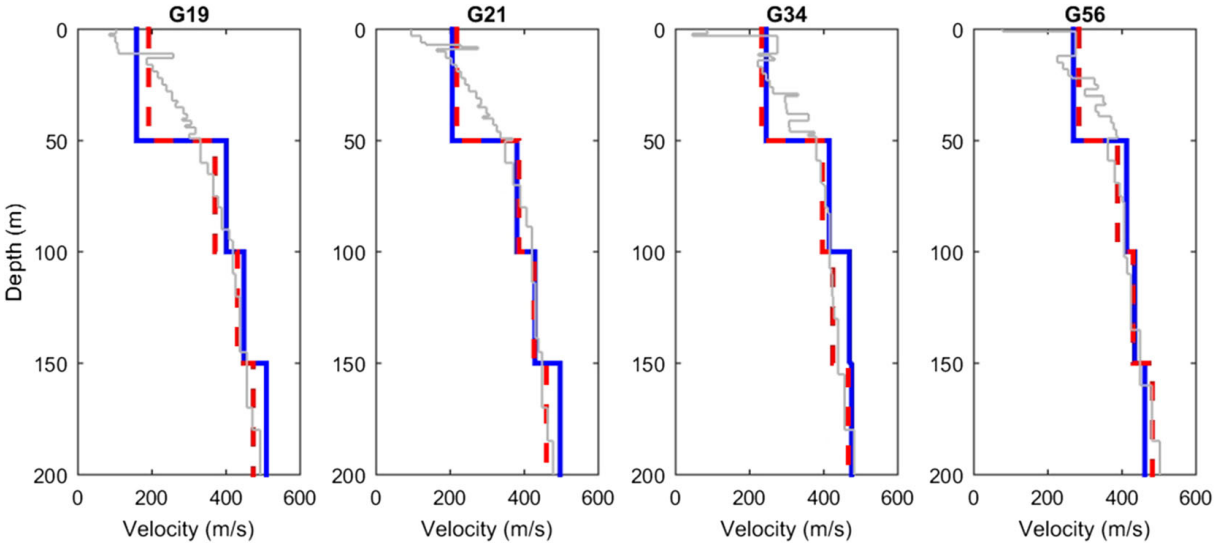


Figure 4.16: V_S profiles at selected G stations. Interval V_S from seismic interferometry in blue, modelled mean V_S (Kruiver et al., 2017a) in grey and harmonic means of modelled V_S in dashed red.

Independent calculation of site transfer functions is typically performed using site-to-reference spectral ratios, or in the absence of a reference site (as in Groningen), by calculating empirical transfer functions from spectral modelling (Edwards et al., 2013). This approach has been successfully used in guiding the development of V_S models in Alpine and urban regions of Switzerland (Michel et al., 2014, 2016). The principal of empirical transfer functions is to isolate site effects. The approach of Edwards et al. (2013) uses a simple seismological point-source model (Brune, 1970; Anderson and Hough, 1984) to account for source and path effects in recordings of small earthquakes. Consistent site effects are then extracted from the intra-event FAS residuals over numerous events. By averaging over numerous events, distances and azimuths and extracting only the intra-event residuals, the non-uniqueness of spectral analysis approaches is largely removed (Goertz-Allmann and Edwards, 2013; Michel et al., 2014, 2016). The result is that site TFs are — over a broad frequency band — independent from the inverted source and path effects. Furthermore, in this analysis, we take advantage of the availability of the measured V_S as a priori information for the inversions and reduce possible trade-offs further. The 1D SH TF with vertical incidence from measured V_S profile is used as a starting model, with the inversion completely free to modify the TFs.

Figure 4.17 shows a comparison of the TFs for four sites with measured V_S profiles. The overall shape of the empirical TFs (determined from earthquake recordings following Edwards et al., 2013) and theoretical 1D SH TFs (determined from numerical linear site response analysis) is very similar, with only small differences in minor peaks and troughs. For the borehole (G) stations there are no measured

V_S profiles. However, in this case, we can take advantage of the surface-to-borehole-at 200 m depth (S/B) spectral ratio to calculate the effect of the soil column on the wavefield. Figure 4.18 shows S/B spectral ratios calculated using small earthquakes ($1.5 > M_L > 3.1$). In order to compare S/B spectral ratios with theoretical transfer functions, the TF between the borehole at 200 m depth (within-rock: i.e. accounting for both up- and down-going waves) and the outcropping surface must be calculated. This is equivalent to taking the ratio of the TFs between the reference horizon and both the outcropping surface and the 200 m depth 'within-rock' borehole levels. Generally, the amplification from the recordings and theoretical transfer functions agree well.

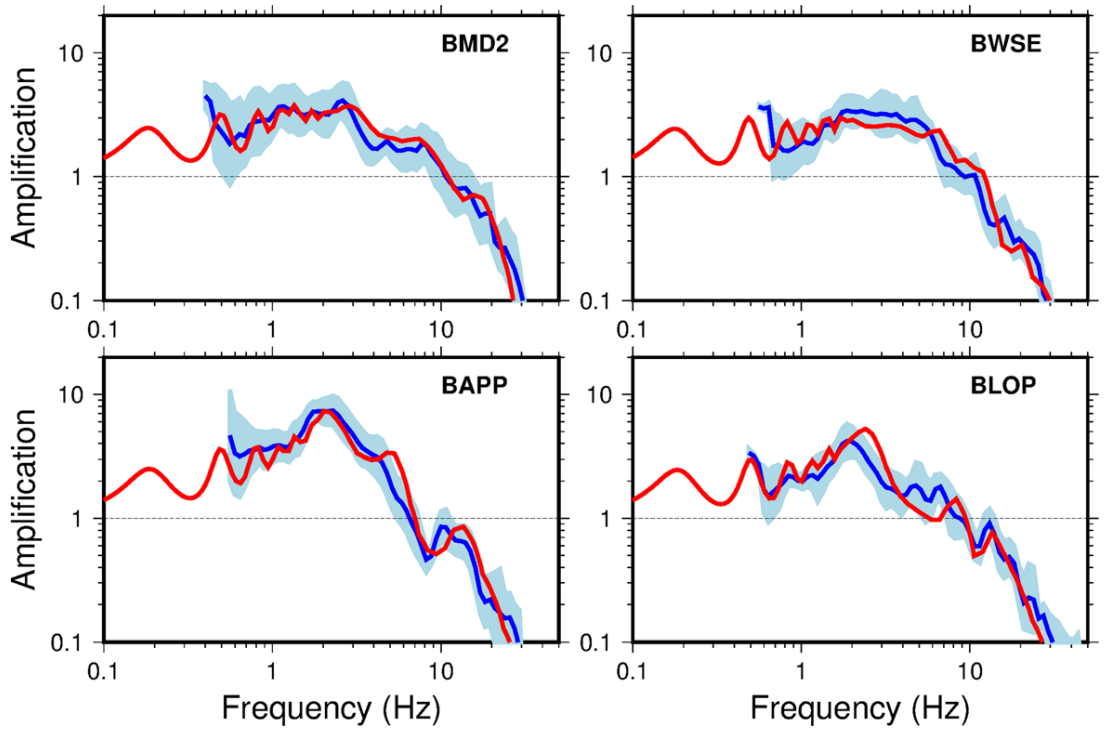


Figure 4.17: Comparison for selected B stations of empirical amplification (reservoir to surface amplification) from the Groningen earthquake recordings database (blue) and standard deviation (pale blue) along with the theoretical vertical 1D SH amplification between the reference and surface (red) based on numerical linear site response analyses.

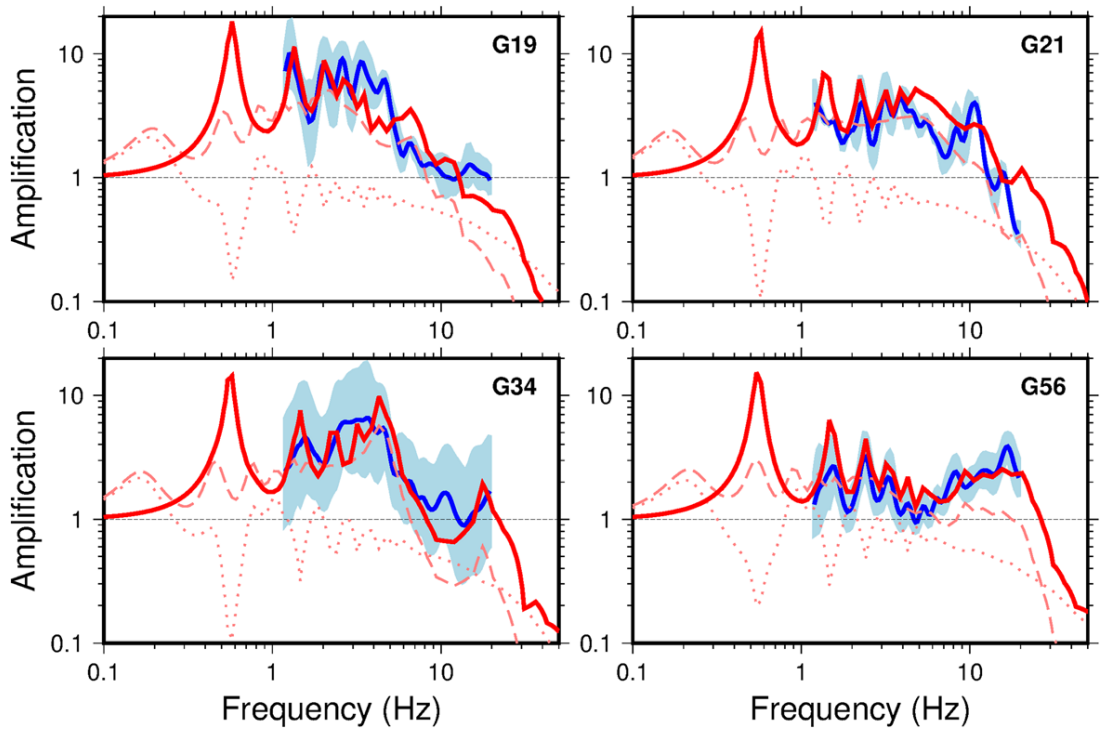


Figure 4.18: Comparison for selected G stations of FAS spectral ratio of surface to 200 m depth from the Groningen earthquake recordings database (blue) and standard deviation (pale blue) along with the spectral ratio of surface to 200 m depth from theoretical 1D SH linear site response analyses (solid red). The dashed red line indicates the 1D SH TF at the surface and dotted red line at 200 m depth.

The good agreement between measured/inferred V_S and modelled V_S from Figure 4.17 and Figure 4.18 indicates that the use of vertical 1D SH TFs is appropriate over the 800 m from reference rock horizon to surface. The velocity models determined for the reference to surface produce remarkably similar TFs to those empirically observed in earthquake signals.

4.5 Conclusions

A fieldwork campaign was conducted in the Groningen gas field to determine in-situ V_S to approximately 30 m depth for the purpose of reducing uncertainty in the ground motion model for induced earthquakes. A suite of field techniques was used and existing techniques were extended. For example, the SCPT procedure was adjusted to take measurements at stratigraphy boundaries in order to sample each layer (especially peat) in sufficient detail and to avoid contamination of the measured V_S by the under- or overlying soil layer. We added source offsets to the SCPT (OSCPT) at 1 to 20 m from the cone location to be able to perform tomography of V_S. This provided insights regarding spatial variations of V_S and representativeness of any individual SCPT.

The cross-hole tomography also showed that there is heterogeneity on spatial scales of one to several metres. For example, the jump in V_S associated with the transition between Holocene and Pleistocene

deposits varies in depth by several metres over a horizontal distance of 25 m. The cross-hole tomography is very suitable to investigate spatial variation of V_P and V_S properties.

The MASW analysis consisted of both active and ambient noise data acquisition and various methods of processing. The classic MASW processing of the offset gather of the array resulted in the large scale V S structures at the station sites. The passive and the MASW dispersion characteristics matched well. However, the microtremor array data did not significantly extend the bandwidth of the dispersion data relative to the MASW at our sites. This could be improved by including lower frequency geophones and ambient noise data collection for a longer period of time. The CMPcc approach on the MASW data indicated the lateral variability of V_S along the full array.

We made a pragmatic choice to achieve the final V_S profile at each station, using the SCPT, only substituting by the MASW value when the SCPT was unreliable. The comparison between the measured V_S and the modelled V_S that was used for site response analysis shows an excellent match. The correspondence between the V_S from seismic interferometry and the modelled V_S agrees very well. The measured V_S profiles significantly enhanced the ground motion model derivation by using them to deconvolve the recorded motions from the Groningen earthquake database to the reference baserock horizon.

5. PUBLICATION III: JOINT-INVERSION OF CROSS-BOREHOLE P-WAVES, HORIZONTALLY AND VERTICALLY POLARISED S-WAVES: TOMOGRAPHIC DATA FOR HYDROGEOPHYSICAL SITE CHARACTERISATION

P-wave, as well as horizontally and vertically polarized S-wave tomographic data were collected between two borehole pairs. This enabled the joint-inversion of the three datasets. By employing structural constraints, the S-wave traveltimes were coupled to the more accurate P-wave traveltimes during the inversion. Thereby, the traveltime and anisotropic artefacts, initially observed in the individually inverted S-wave tomograms, were significantly reduced and the correlation with the borehole logs improved, while the resolution of the jointly inverted P-wave tomogram was only marginally affected. The joint-inversion proves successful in determining the S-wave velocity distribution more accurately than individual inversions. In addition, the jointly inverted tomograms were used to detect aquifer heterogeneities, caused by differences in clay content, and to distinguish areas of relatively high effective pressure. By comparing the jointly inverted S-wave tomograms, suggests the effect of S-wave anisotropy, which showed substantial velocity differences of approximately -10% to +10%. The anisotropy may have been caused by the presence water-filled pores, microcracks and preferred mineral alignment (mainly clay) in the media.

5.1 Introduction

Cross-borehole tomographic investigations are routinely applied for high resolution lithological structure delineation (Yamamoto et al., 1994; Angioni et al., 2003; Daley et al., 2004; Dietrich and Tronicke, 2009). Applications range from exploring development sites considered for larger building projects, such as power stations, dams and high-rise buildings, to natural resource exploration and ground water aquifer studies. Currently, P wave tomography is employed more frequently than S-wave borehole tomographic surveys (Paasche et al., 2011). Examples of S-wave borehole tomography include a survey to (1) derive geotechnical elastic properties (Angioni et al., 2003), (2) constrain a hydro-geological model (Daley et al., 2004) and (3) perform a joint interpretation of co-located P- and S-wave tomograms by means of an integrated analysis (Dietrich and Tronicke, 2009). The velocity structures and the elastic parameters, i.e. Young's modulus, Bulk modulus, Shear modulus, Poisson's ratio and the P-wave to S-wave velocity ratio (v_P/v_S), were used for a joint interpretation. These S-wave tomographic surveys were conducted with a single S-wave polarisation, using either vertically polarised (SV-waves) or horizontally polarised S-waves (SH-waves).

Cross-borehole surveys employing both horizontally and vertically polarising S-wave sources have been used previously for anisotropic S-wave measurements (e.g. Sully and Campanella, 1995; Ku and Mayne, 2014). These were conventional crosshole testing surveys and were restricted by gathering only 1D measurements with depth. However, using both vertically and horizontally polarised S-waves in

conjunction with P-waves in a tomographic survey enables the determination of three 2D velocity tomograms which can be jointly interpreted.

The co-located datasets also enable joint tomographic inversions using a cross-gradient constraint (Gallardo and Meju, 2003; Gallardo and Meju, 2004). The cross-gradient constraint enforces structural similarity of the resulting models and has been used for jointly inverting different geophysical datasets. For example, Gallardo and Meju (2004) jointly inverted DC-resistivity and refraction seismic data, Tryggvason and Linde (2006) jointly inverted local earthquake tomographic data consisting of P- and S-waves traveltimes, and Moorkamp et al. (2011) provide a framework for jointly inverting magnetotelluric, gravity and refraction seismic data. Jointly inverted P-, SH- and SV-wave traveltime data enable the structural coupling of the less accurate S-wave to the more accurate P-wave traveltimes. Thereby, the S-wave velocities are estimated better, as erroneous traveltimes will not cause artefacts in the tomogram. In addition, the two differently polarised S-wave tomograms will enable to estimate the presence of anisotropy.

We chose the SAFIRA (SAnierungs-Forschung In Regional kontaminierten Aquiferen, i.e. research on remedial measures in regionally contaminated aquifers) research facility in Zeitz, Germany (Weiß et al., 2001; Weiß et al., 2002), as the test site exhibited an overconsolidated clay layer of approximately 15 m thickness (Dietze, 2007, pp. 24-28). Theoretical considerations and bender element testing have shown that the S-wave velocity changes with increased external stresses (Fratta et al., 2004; Lee et al., 2005). Therefore, the SAFIRA site exhibiting the overconsolidated clay layer was sought to test with the two different S-wave sources.

5.2 Geology of the SAFIRA Site

The geology of the SAFIRA research facility is composed of Tertiary and Quaternary sedimentary deposits of the river Weiße Elster, which slightly dip to the North and North-East. Two groundwater aquifers are present, consisting of medium to coarse grained sand. The two aquifers are separated by clay and interbedded lignite seams (Dietze, 2007, p. 25). For two reasons, the tomographic measurements target the layers below Aquifer 1, i.e. the layers of clay and lignite seams, and Aquifer 2. Firstly, all layers below Aquifer 1 are saturated, which would limit refraction effects along the water table boundary. Secondly, the sediments of Aquifer 1 and the layers below were overconsolidated during the glaciation period of the Elster-Saale. Therefore, some form of anisotropy is expected, which would result in different S-wave velocities between horizontally and vertically polarised S-waves.

5.3 Data Acquisition

Tomographic measurements were conducted between two borehole pairs, with all four boreholes being near-vertical with depths of more than 40 m. The two borehole pairs are separated by a distance of approximately 14 m and 9 m on surface, with the borehole locations shown in Figure 5.1.

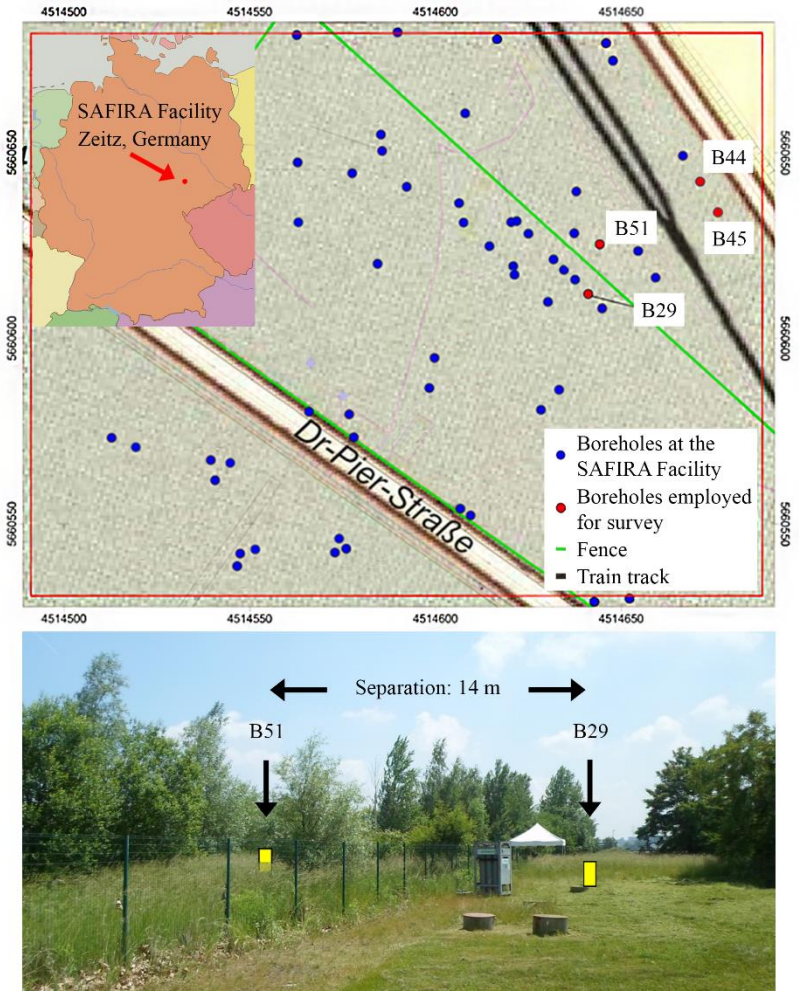


Figure 5.1: Overview of the borehole locations at the SAFIRA research facility in Germany with the highlighted borehole pairs B29 - B51; and B45 - B44.

Two different sources were employed, thereby generating three different types of waves. These were P-waves, SH-waves and SV-waves. The sources were successively lowered into one borehole (B51 or B44) and a ten-station three-component receiver array recorded the signals in the adjacent borehole (B29 or B45). Alignment of the sources and receivers was performed from surface and enabled by rotationally stiff hoses attached to the borehole devices. The horizontally polarising source was aligned to either shoot in a 90° or 270° angle to the receiver borehole and the vertically polarising source was shooting either up or down. This reversal in shooting direction generated S-waves with opposing polarity, comparable to the Crossover method in S-wave crosshole testing surveys (Tanimoto and Kurzeme, 1973). Once aligned, the sources and receivers were pneumatically clamped to the borehole wall. For

each layout, care was taken to keep the receiver string in place and at the same pneumatic clamping pressure of 10 bar, while the sources were exchanged.

Data were collected between the depths of 5 and 49 m (B29-B51) and between 12 and 42 m (B44-B45) with a source and receiver spacing of 1 m respectively, and with a high signal-to-noise ratio. The temporal sampling rate was 16 kHz for both sources. Examples of raw receiver gathers at a depth of 18 m are shown in Figure 5.2 for the horizontally and vertically polarised sources respectively. It can be observed that the horizontally-polarising S-wave source produces SH-waves and P-waves (Figure 5.2a), while the vertically-polarising source predominantly produces SV waves (Figure 5.2b).

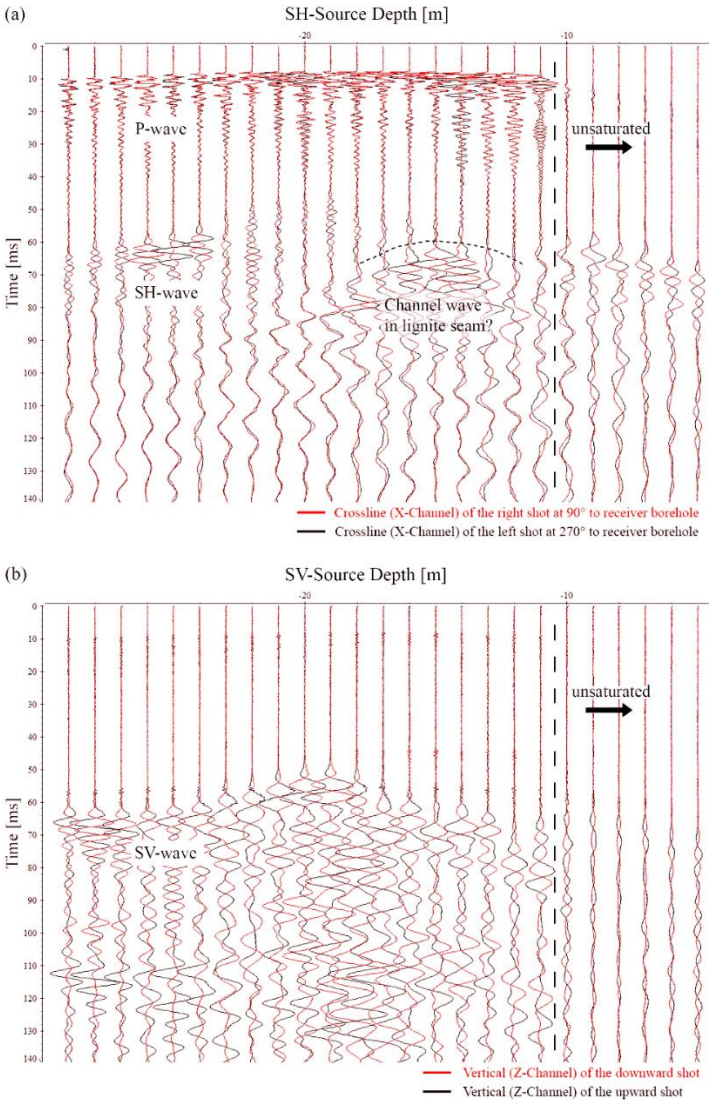


Figure 5.2: Example of a raw receiver gather for tomographic slice plane B29-B51 at 18 m depth of the horizontally-polarising S-wave source (a) and the vertically-polarising S-wave source (b) at the SAFIRA site. For the SH-wave source (a), the horizontal channel perpendicular (90°) to the source borehole is shown for the two opposing strike directions (90° and 270° to the receiver borehole). Both SH-wave and P-wave are clearly visible. For the SV-wave source (b), the vertical channel is shown for the two opposing strike directions up and down. The SV-wave is clearly distinguishable.

The three-component receivers allowed the computation of hodograms, whereby the seismic wave motion is visualised by plotting the amplitudes of the different components (x, y and z) relative to each other. Shear wave splitting into orthogonal S-waves is commonly recognised by the use of such hodograms (e.g. Crampin and Chastin, 2003). The hodogram analysis indicates that the vertically polarising source produces SV-waves, while the main S-wave polarisation of the horizontally polarising source is horizontal. Therefore, we concluded that the SV-waves and SH-waves are in fact vertically and horizontally polarised, respectively. The dominant frequency for the P-wave is approximately 1200 to 1400 Hz and for the two S-waves in the range of about 100 to 400 Hz.

Data processing included the re-sorting of traces, adjusting for trigger delays and independent picking of P wave and S-wave traveltimes. The SH-traveltimes were picked by analysing the horizontal channels perpendicular to the source borehole, while the SV traveltimes were picked on the vertical channel. The P-traveltimes, on the other hand, were determined on the in-line receivers. Subsequently, the traveltimes were analysed for their plausibility and erroneous traveltimes were re-picked. In total, approximately 950 and 710 P-wave, 960 and 708 SH-wave and 880 and 710 SV-wave traveltimes were picked for the tomographic planes B29-B51 and B44-B45 respectively (Figure 5.3). The traveltime accuracies are estimated at 0.1 ms for the P wave and approximately 1.0 ms for the S-wave. This is a rough estimate, based on the visual analysis of the raw shot gathers and on the traveltimes sorted by both shot and receiver gathers. The borehole deviation was measured on-site and incorporated in the subsequent inversion process.

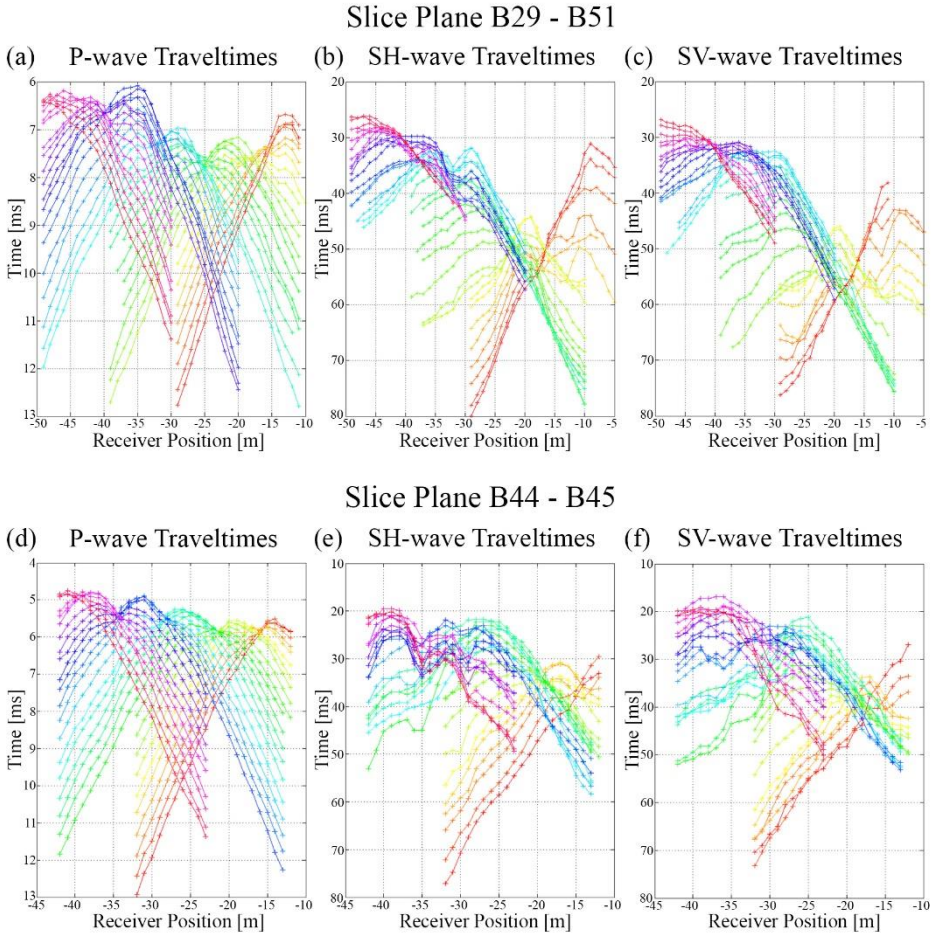


Figure 5.3: SV-, SH- and P-wave traveltimes of the SAFIRA research site sorted by receiver depth for the two slice planes B29-B51 (a-c) and B44-B45 (d-f). SH-wave and P-wave traveltimes were determined from a horizontally polarising S-wave source and the SV-waves were determined from a vertically polarising S-wave source.

5.4 Tomographic Inversion

5.4.1 Separate inversion

The seismic velocity models were determined on a 2D grid consisting of cells of roughly 1 m by 1 m, by inverting the 1D seismic traveltimes. Mathematically, the relationship

$$\mathbf{Jm} = \boldsymbol{\tau} \tag{5.1}$$

has to be solved, with the seismic slowness vector (**m**), the measured traveltime vector (**τ**) and the Jacobian matrix (**J**), which connects the two relationships. In this particular case of seismic tomography, the Jacobian corresponds to the lengths of rays in each model cell. In the first iteration, a straight raypath is assumed. Numerically, a sequence of approximations are made in a linear-least-squares sense, so that the $\ell 2$ norm of the residual (**r**) decreases monotonically for every iteration k, giving the objective function

$$\| \mathbf{r}_k \|_2 = \| \boldsymbol{\tau} - \mathbf{J}_k \mathbf{m}_k \|_2. \tag{5.2}$$

A challenge is that the traveltime measurements ($\boldsymbol{\tau}$) always have a level of inaccuracy, which leads to an amplification of noise in the resulting model slowness ($\mathbf{m}$). Therefore, a Tikhonov regularisation term is added to Equation 2

$$\| \mathbf{r}_k \|_2 = \| \boldsymbol{\tau} - \mathbf{J}_k \mathbf{m}_k \|_2 + \alpha \| \mathbf{R}\mathbf{m}_k \|_2, \tag{5.3}$$

with the spatial second-order derivative, i.e. Laplacian matrix, ($\mathbf{R}$) and the scalar Lagrange multiplier (α) (Menke, 1989, p. 58). The Laplacian smoothing serves as a low-pass filter and reduces the noise effects during the inversion. The system of equations is then solved using a conjugate gradient solver of the LSQR type, i.e. least-squares QR-factorisation (Paige and Saunders, 1982), which is based on the bi-diagonalisation procedure by Golub and Kahan (1965). For each LSQR iteration (k), the model ($\mathbf{m}$) is perturbed to fit the residual traveltimes of the previous iteration ($\mathbf{r}_k$)

$$\begin{pmatrix} \mathbf{J}_k \\ \alpha\mathbf{R} \end{pmatrix} \Delta\mathbf{m}_{k+1} = \begin{pmatrix} \mathbf{r}_k \\ \mathbf{0} \end{pmatrix}. \tag{5.4}$$

The slowness model ($\mathbf{m}$) is subsequently updated with

$$\mathbf{m}_{k+1} = \mathbf{m}_k + \Delta\mathbf{m}_{k+1}. \tag{5.5}$$

A number of LSQR iterations were determined, with the stopping criteria taking effect, when successive models correlated by more than 99.9%. Subsequently, the Jacobian travelpath matrix ($\mathbf{J}$) can then be re-computed. This time, the new model ($\mathbf{m}_{k+1}$) is used to perform a curved ray tracing, based on the algorithm by Gruber and Greenhalgh (1998), which is based on subdividing the individual model cells into primary and secondary nodes. A new traveltime residual ($\mathbf{r}$) is determined and subsequently, the process is repeated, by solving the new system of equations.

The entire inversion sequence consisted of (1) estimating a homogenous starting model, by determining the average velocity of all straight raypaths; (2) selecting only the horizontal rays to perform a straight-ray inversion; (3) inverting for the final velocity model using all determined traveltimes and performing 10 curved-ray iterations. Since, the geology suggests a layered sedimentary environment, the obtained layered model served as a new, improved starting model. The programmatic implementation builds on the borehole tomographic software *bh_tomo* (Giroux et al., 2007).

5.4.2 Joint-inversion

Joint-inversions of the co-located traveltime datasets (P-, SH- and SV-wave) were performed, by adding cross-gradient constraints (Gallardo and Meju, 2004). The purpose of the cross-gradient constraint is to ensure structural similarity between the tomograms. Thus, changes in velocity should occur along the same boundaries, i.e. in the same direction, in the opposite direction, or only in one of the models.

Mathematically, the cross-product, termed the cross-gradient function (**t**), of two velocity models ($\mathbf{m}^1$, $\mathbf{m}^2$) should thus be zero, i.e.

$$\mathbf{t}_k = \nabla\mathbf{m}_k^1 \times \nabla\mathbf{m}_k^2, \tag{5.6}$$

for the k^{th} inversion iteration. Usually the cross-gradient function has three components. However, since the inversion was performed on a 2D plane, only one of the three components, i.e. the y-component, of the cross-gradient function (**t**) is non-zero. This non-zero component is discretised using a forward difference scheme and given by

$$\mathrm{t}_k^y = t_k = \frac{1}{\Delta x \Delta z}\left(m_c^1\left(m_b^2 - m_r^2\right) + m_r^1\left(m_c^2 - m_b^2\right) + m_b^1(m_r^2 - m_c^2)\right). \tag{5.7}$$

The subscripts *c*, *b* and *r* denote the centre, bottom and right cell of the discretised model. A visualisation of the discretisation and of the subscripts is given by Gallardo and Meju (2003). The cross-gradient function is non-linear in that it can only be computed for the previously determined velocity models ($\mathbf{m}^1$, $\mathbf{m}^2$), i.e. iteration *k*. However, the cross-gradient constraint shall apply to the current iteration (*k*+1). To implement the cross-gradient function effectively in the inversion, a first-order Taylor expansion is used to approximate the cross-gradient function for the current iteration (*k*+1)

$$\mathbf{t}_{k+1} \cong \mathbf{t}_k + \begin{pmatrix}\mathbf{B}^1 & \mathbf{B}^2\end{pmatrix}\begin{pmatrix}\Delta\mathbf{m}^1 \\ \Delta\mathbf{m}^2\end{pmatrix}, \tag{5.8}$$

with every row of the matrix $\mathbf{B}^1$ and $\mathbf{B}^2$ then consisting of 3 non-zero components. These components are derived from the discretised cross-gradient function (c.f. eq. 9 of Gallardo and Meju, 2004), where the two matrices $\mathbf{B}^1$ and $\mathbf{B}^2$ are combined, i.e. horizontally concatenated, to give 6 non-zero components for a matrix $\mathbf{B} = \begin{pmatrix}\mathbf{B}^1 & \mathbf{B}^2\end{pmatrix}$. For a joint inversion of all three datasets, the system of equations that is subsequently solved with the LSQR algorithm then becomes

$$\begin{pmatrix}\mathbf{J}_k \\ \alpha\mathbf{R} \\ \lambda\mathbf{B}_k\end{pmatrix}\Delta m_{k+1} = \begin{pmatrix}\mathbf{r}_k \\ 0 \\ -\lambda\mathbf{t}_k\end{pmatrix}, \tag{5.9}$$

(c.f. eq. 4 and 5 in Tryggvason and Linde, 2006) and is therefore, similar to Equation 4 of the individual inversion, where the matrices and vectors are now given by

$$\mathbf{J} = \begin{pmatrix} \beta\mathbf{J}_P & \mathbf{0} & \mathbf{0} \\ \mathbf{0} & \mathbf{J}_{SH} & \mathbf{0} \\ \mathbf{0} & \mathbf{0} & \mathbf{J}_{SV} \end{pmatrix}, \tag{5.10}$$

$$\mathbf{R} = \begin{pmatrix} \beta\mathbf{R} & \mathbf{0} & \mathbf{0} \\ \mathbf{0} & \mathbf{R} & \mathbf{0} \\ \mathbf{0} & \mathbf{0} & \mathbf{R} \end{pmatrix}, \tag{5.11}$$

$$\mathbf{B} = \begin{pmatrix} \mathbf{B}_{k,P\times SH} & \mathbf{B}_{k,P\times SH} & \mathbf{0} \\ \mathbf{B}_{k,P\times SV} & \mathbf{0} & \mathbf{B}_{k,P\times SV} \\ \mathbf{0} & \mathbf{B}_{k,SH\times SV} & \mathbf{B}_{k,SH\times SV} \end{pmatrix}. \tag{5.12}$$

It is noteworthy to mention that, by definition, the cross-gradient function is computed only for two models. Therefore, a total of three cross-gradient constraints; P- and SH-wave, P- and SV-wave, SH- and SV-wave, were emplaced to ensure structural similarity for all three velocity models. Therefore, the matrices B and t are composed of these three components. This procedure is similar to the one proposed by Gallardo (2007), who generalised joint-inversions to more than two models.

The model perturbation of iteration $k + 1$ is now given by

$$\Delta\mathbf{m}_{k+1} = \begin{pmatrix} \Delta\mathbf{m}_{k+1,P} \\ \Delta\mathbf{m}_{k+1,SH} \\ \Delta\mathbf{m}_{k+1,SV} \end{pmatrix}, \tag{5.13}$$

the measured traveltime residuals of the previous iteration k given by

$$\mathbf{r}_k = \begin{pmatrix} \beta\mathbf{r}_{k,P} \\ \mathbf{r}_{k,SH} \\ \mathbf{r}_{k,SV} \end{pmatrix}, \tag{5.14}$$

and the cross-gradient function of the previous iteration k given by

$$\mathbf{t}_k = \begin{pmatrix} \mathbf{t}_{k,P\times SH} \\ \mathbf{t}_{k,P\times SV} \\ \mathbf{t}_{k,SH\times SV} \end{pmatrix}. \tag{5.15}$$

The parameter β serves as a weighting parameter to account for the differences in traveltimes between the P- and S-waves and was set to the difference in standard deviation, which is approximately $\beta \approx 8.2$ and $\beta \approx 5.6$ for the two tomographic slice planes B29-B51 and B44-B45 respectively. Differences in standard deviation between the two S-wave datasets (SH- and SV-wave) were small and the two stated

values for β are the averages. If these differences in traveltimes are not accounted for, then predominantly the S-wave residuals, since they are larger than the P-wave residuals, are adjusted in the inversion process. This would then defeat the benefit of incorporating the accurate P-wave traveltimes.

The parameter λ describes the weighting of the cross-gradient constraint. By setting $\lambda = 0$ results in jointly inverting the datasets without a structural constraint. Depending on the P-wave weight, the results then look similar to the individually inverted tomograms, i.e. the artefacts remain visible in the S-wave tomograms and the structural similarity between the P- and S-wave tomograms is low. If on the other hand λ is very large, then the cross-gradient constraint is almost zero everywhere, resulting in high structural similarity between the tomograms. This however, results in the picked traveltimes playing a negligible role and the resulting tomograms appearing very smooth, up to the extent that the resulting tomograms are of entirely homogenous velocities. Thus, care was taken to adjust in that the general velocity trends remained intact, while at the same time achieving a high structural similarity.

The general joint-inversion procedure was analogous to the individual inversion sequence. Three homogenous starting models were estimated based on the average P-, SH- and SV-wave velocities. These homogenous starting models were then improved by conducting three individual inversions based only on the horizontal rays. Finally, the three datasets were jointly inverted, by conducting 10 curved-ray iterations, to receive three velocity models with a high structural similarity.

5.5 Results

5.5.1 Separate inversion

The individually inverted P-wave and S-wave tomograms between boreholes B29 and B51, and between B44 and B45 are shown in Figure 5.4. The tomograms show distinct horizontal layering which can be well correlated to the borehole data. This layering is best visible in the P-wave tomograms (Figure 5.4a and d) with layers of clay, lignite, silt, coarse and medium grained sand.

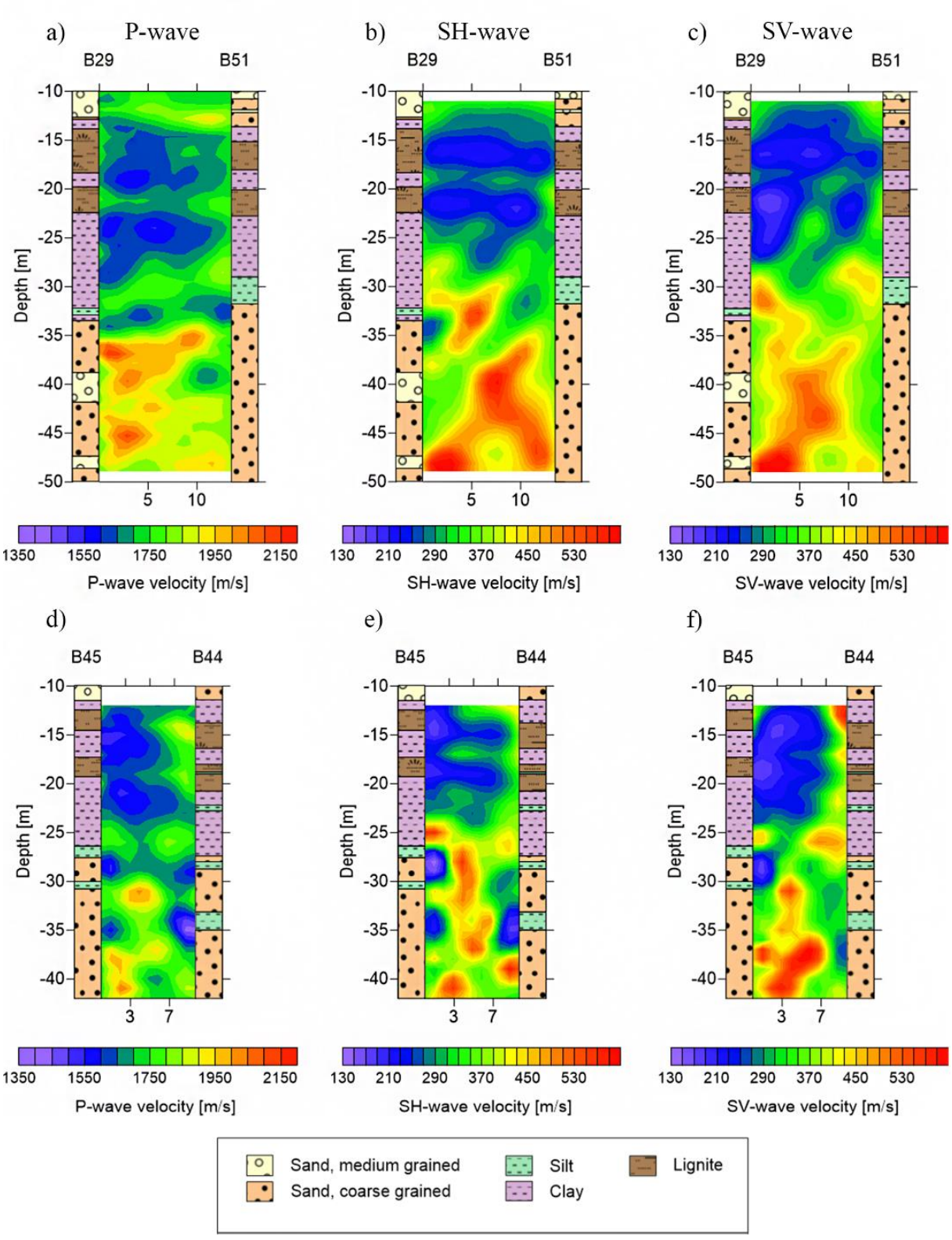


Figure 5.4: Individually inverted P-, SH- and SV-wave tomograms between boreholes B29 and B51 (a-c) and between boreholes B44 and B45 (d-f) at the SAFIRA research site. The SH- and SV-wave tomograms (b, c, e, f) exhibit artefacts and correlate less with the borehole logs than the more accurate P-wave tomograms (a, d).

The tomograms and associated velocity distributions show two distinct features. Firstly, the P-wave velocity distributions (Figure 5.4a) do not correspond with the distribution of the S-wave velocities (Figure 5.4b, c). While the P-wave velocity is higher (1650 to 1750 m/s) in the lignite seams than in the surrounding clay (approximately 1550 m/s), the opposite is true for the horizontally and vertically polarised S-waves with velocities of 200 to 250 m/s in the lignite seams and 280 to 320 m/s in the surrounding clay (Figure 5.4b, c). However, these differences in velocity could be due to the non-unique nature of individually inverting different traveltime datasets.

Secondly, the S-wave tomograms (see Figure 5.4 b, c, e and f) generally correlate less with the borehole logs compared to the P-wave tomograms, due to the presence of X-shaped distortions. These distortions are interpreted as artefacts, which could either stem from traveltime picking inaccuracies or unaccounted S-wave anisotropy. Since the P-wave tomograms do not show these distortions, acquisition artefacts are ruled out. The two S-wave velocities are in general similar. However, due to the artefacts, the differences cannot be entirely attributed to geological origin, but rather due to the non-unique nature of the inversion process.

5.5.2 Joint-inversion

To reduce the multi-solutions of the inversion problem and artefacts in the S-wave tomograms, the datasets were jointly inverted, with the results shown in Figure 5.5. The advantages in the joint-inversion are most apparent when analysing the S-wave tomograms. They correlate better with the borehole logs and are in general geologically more plausible than the individually inverted tomograms (see Figure 5.4). For example, the highly variable lower zones of the S-wave tomograms are now less variable (e.g. from a range of approximately 300 - 550 m/s, to 450 - 550 m/s for slice plane B29-B51) and the boundaries correlate well with lithological changes which are also observed in the borehole logs. The artefacts present in the individually inverted tomograms are now reduced and the S-wave models are smoothed. At the same time the P-wave resolution only marginally decreased.

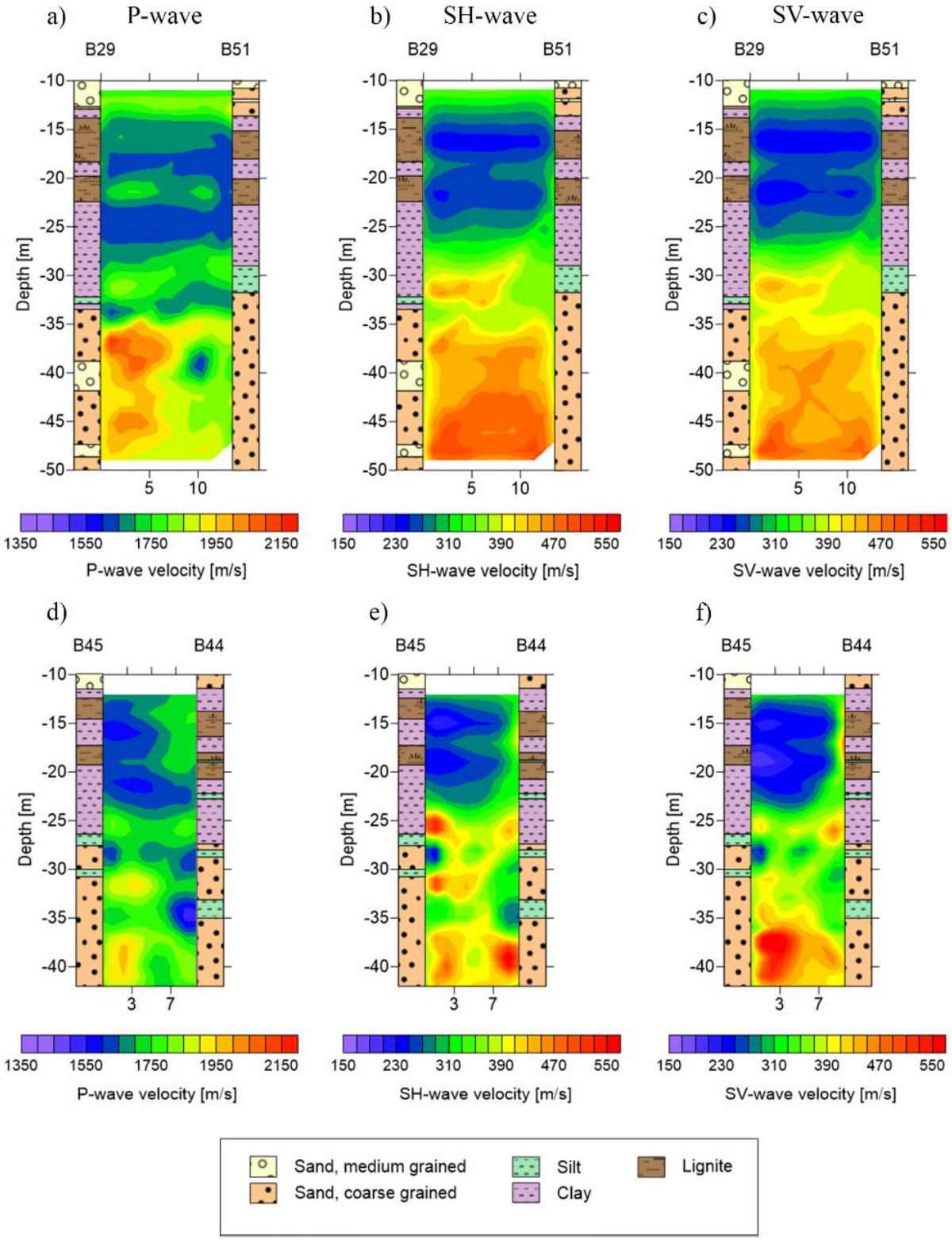


Figure 5.5: Jointly inverted P-, SH- and SV-wave tomograms between boreholes B29 and B51 (a-c) and between boreholes B44 and B45 (d-f) at the SAFIRA research site. The joint-inversion couples the S-wave tomograms (b, c, e, f) to the more accurate P-wave tomograms (a,d) and thereby reduces the artefacts in the S-wave tomograms.

5.5.3 Resolution and data accuracy

The dominant frequency estimates show that the P-wave has significantly higher frequency content (1200 to 1400 Hz) than the S-waves (100 to 400 Hz). With P-wave velocities in the range of 1400 to 2100 m/s and S-wave velocities in the range of 200 to 550 m/s, this results in P-wavelengths of approximately 1 to 1.75 m and S-wavelengths of approximately 0.5 to 5.5 m. However, in the faster S-wave layers, the frequency content is above average (200 to 400 Hz) and in the slow S-wave layers, the frequency content is below average (100 to 200 Hz). For this reason, we interpret that the S-wavelengths are in the same range as the P-wavelengths. In addition, the ray coverage of all wave modes is very similar. Therefore, the resolution of the different wave modes is expected to be in the same range.

The picking accuracy is estimated at a factor of about ten times higher for the P-wave compared to the S-wave (0.1 ms compared to 1.0 ms). However, the traveltimes show that on average the S-wave arrives about five times later compared to the P-wave. In relative terms, this equates to the P-wave picks being about two times more accurate than the S-wave picks and may, in part, explain the presence of artefacts in the S-wave tomograms. Therefore, the less accurate S-wave traveltimes were structurally coupled to the more accurate P-wave traveltimes in the joint inversion.

5.6 Discussion

It seems that the initially observed artefacts of the individually inverted S-wave tomograms are largely removed, due to the structural coupling. Despite the lack in traveltime picking accuracy of the S-waves, this seems to be an effective solution to estimate the S-wave velocity distribution better, while retaining the geological and structural plausibility. Otherwise, without the cross-gradient constraint, the S-wave inversion minimises the error of some inaccurate traveltimes causing artefacts. Gaining confidence in the geological plausibility of the jointly inverted P- and S-wave tomograms enables the analysis of petrophysical and anisotropic effects.

5.6.1 Elastic properties

From the jointly inverted tomograms we can now determine the v_P/v_S ratio, with the average S-wave velocity (Figure 5.6). The individually inverted tomograms show a variable v_P/v_S ratio from the lignite seams to the surrounding clay. These differences in velocity persist when jointly inverting the tomographic datasets. The v_P/v_S ratio is consistent for the two tomographic slice planes and varies by a factor of approximately two from top (ratio of 6 - 7.5) to bottom (ratio of 3.5 - 4.5) of the tomograms. It is therefore likely that these differences in velocity distribution are geologically induced and could for example be due to differences in effective pressure, clay content or porosity.

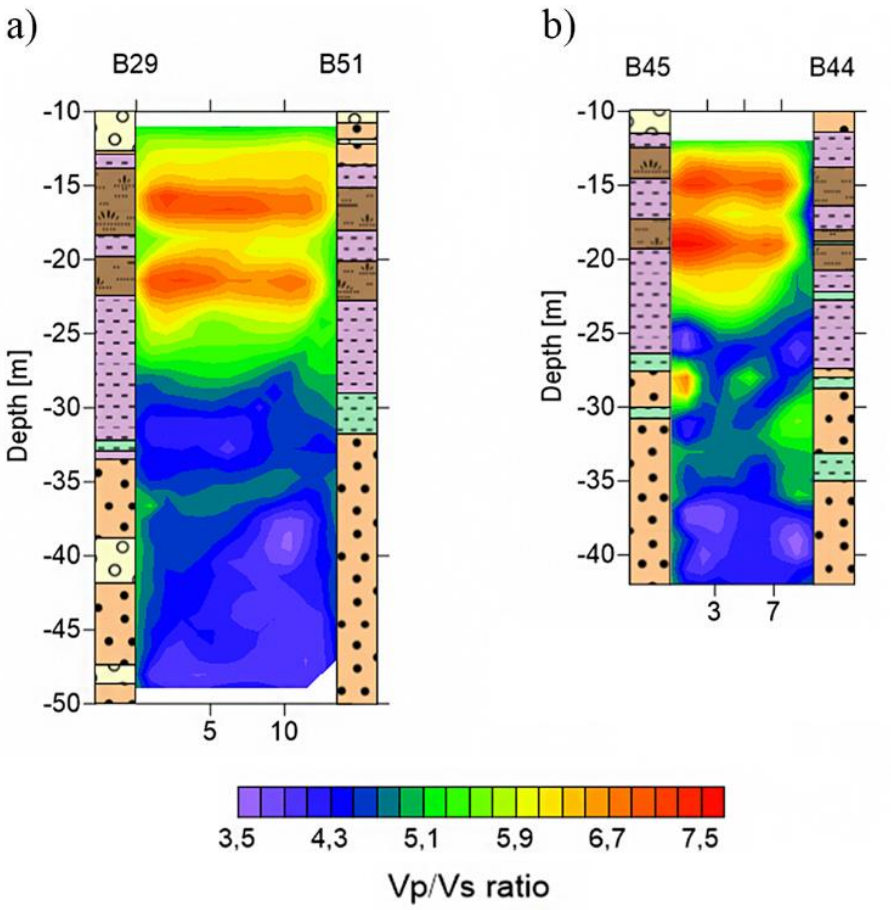


Figure 5.6: Ratio of the jointly inverted P-wave to S-wave velocities for boreholes B29-B51 (a) and B44-B45 (b).

In all tomograms it seems that the lower part of the clay layer, is characterised by substantially higher velocities than the upper part. The v_P/v_S ratio also shows this division across the two tomographic planes, with the ratio sharply decreasing (from a ratio of 5.5 to approximately 4) for the lower part of the clay layer. Generally, a decrease in clay content and porosity and an increase in effective pressure would cause such velocity increases and the v_P/v_S ratio decreases (Eberhart-Phillips et al., 1989). Therefore, these effects could be caused by high effective pressures that the water of Aquifer 2 exerts on the overlying constraining clay.

Aquifer 2 has a substantial velocity heterogeneity that is most pronounced between boreholes B44-B45. The borehole logs of B44 and B45 show the presence of silt layers, which correspond well to lower seismic velocities in the tomograms and increased v_P/v_S ratios. Laboratory measurements of seismic velocities in sandstones support these correlations (Eberhart-Phillips et al., 1989). Silt layers in Aquifer 2 are absent in the borehole logs of B29 and B51, and the corresponding tomograms and v_P/v_S ratios show less variation. The joint-inversion of P- and S-wave data thus contributes to effectively detecting aquifer heterogeneities, by detecting areas of increased silt content.

5.6.2 Estimation of anisotropic effects

Inaccuracies in traveltime picking that would usually lead to artefacts in a tomogram have been considered. For example, the borehole deviation was measured in-situ and incorporated in the inversion. In addition, possible source delays, i.e. differences between trigger responses for the two employed sources, were measured in the laboratory and accounted for. These small differences (approx. 0.1 ms) in delay were also observable when comparing the P-wave arrivals of the two sources. If unaccounted for, then these systematic errors lead to distortions (e.g. Maurer, 1996). Another explanation for the artefacts that are visible in the individually inverted S-wave tomograms is the presence of anisotropy. Laboratory experiments (Carrion et al., 1992) and field measurements (Pratt and Chapman, 1992) have shown that even weak anisotropy can produce significant tomographic artefacts if unaccounted for.

It is unlikely that differences in S-wave velocities are primarily due to incorrectly determined traveltime picks. For example, Figure 5.7 shows the picked traveltimes for the SH-wave (a) and the SV-wave (b) for the same raw receiver gather at a depth of 22 m for tomographic plane B44-B45. The two traveltime sets show a clear difference, which is unlikely due to an error in interpretation. The P-wave arrival in both gathers is equivalent, which supports the notion that S-wave anisotropy is present.

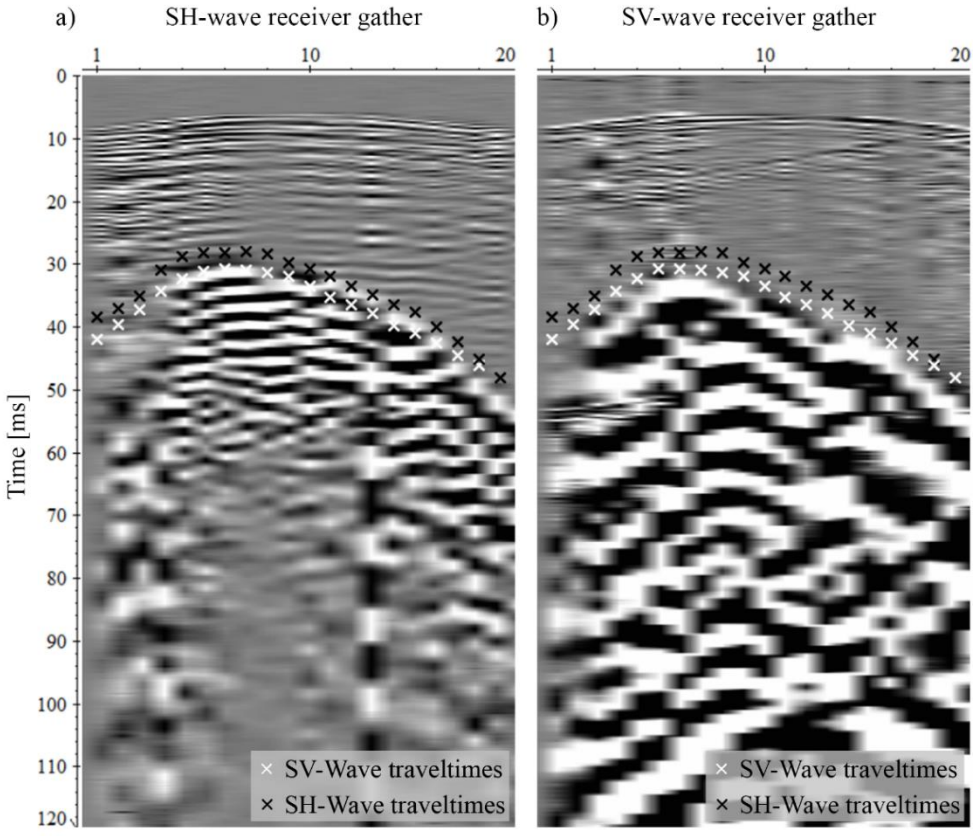


Figure 5.7: Receiver gathers at a depth of 22 m in variable density visualisation for the SH-wave source (a) and the SV-wave source (b). There is a considerable difference from SH-wave traveltimes (black crosses) to SV-wave traveltimes (white crosses). The presence of anisotropy is unlikely due to a deficient picking accuracy.

To estimate the level of S-wave anisotropy, we divide the jointly inverted S-wave tomograms. This is then similar to the conventional procedure for estimating differences in SV- to SH-wave velocities in the geotechnical field, whereby the traveltimes are determined from 1D measurements in the so-called Crosshole Test (e.g. Sully and Campanella, 1995; Ku and Mayne, 2014). Figure 5.8 shows the ratios of the SV- to SH-wave tomograms, as well as the ratio in horizontal straight-ray velocities, i.e. the Crosshole Test data subset. Both S-wave anisotropy estimates show a similar trend, with substantial S-wave anisotropy (-5% to +5% for B29-B51; and -15% to +10% for B44-B45).

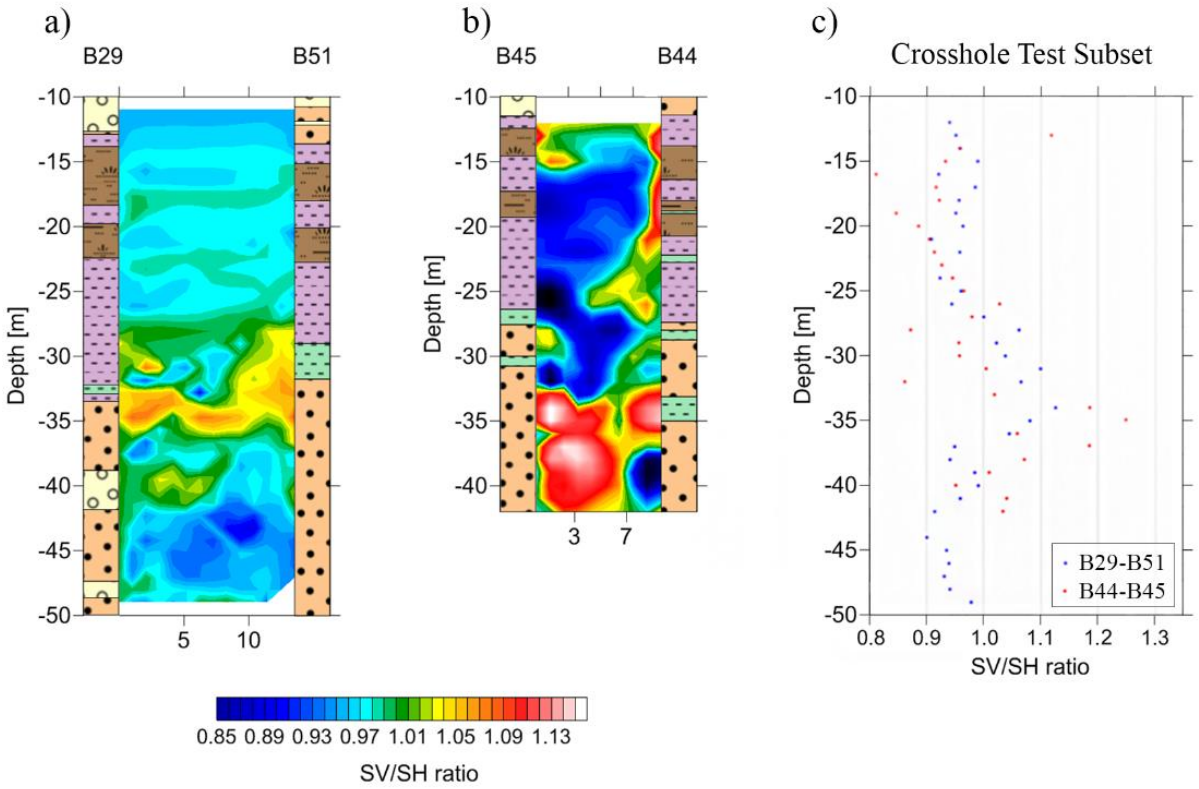


Figure 5.8: Ratio of the jointly inverted SV- and SH-wave tomograms for tomographic plane B29-B51 (a) and B44-B45 (b). The general trend is similar to the one suggested by the velocities of the horizontal raypaths (c).

The SV- to SH-wave velocity ratios show different zones which are consistent for the two tomographic planes. These different anisotropic zones may indicate different types of deposition or differences in effective pressure (e.g. Clayton, 2011). Due to the overconsolidation that took place during the glaciation periods and the presence of aquifers, variations in effective pressure may play the primary role.

The S-wave anisotropy is more pronounced between boreholes B44-B45 (factor 2 to 3 compared to tomographic plane B29-B51). This could either indicate that the anisotropy varies locally, or that azimuthal anisotropy is present, since the azimuth of the two tomographic planes differs by 45°. It is

also possible that the observed anisotropy is caused by the orientation of macro-and micro-cracks (if present), foliation and preferred mineral orientation. However, laboratory physical property measurements would be necessary to constrain these interpretations.

Contrarily, plotting the P-wave velocities as a function of the raypath angle suggests that no angle dependency, and thus no P-wave anisotropy, is present. The level of anisotropy may therefore explain the absence of artefacts in the individually inverted P-wave tomograms and the artefacts in the S-wave tomograms.

5.7 Conclusion

Co-located P-, SH- and SV-wave tomography data were acquired for two borehole pairs separated by approximately 14 m and 9 m on surface. The resulting P-wave tomograms correlate well with the borehole logs. However, the S-wave tomograms showed the presence of distortions, which could be either attributed to traveltime picking artefacts or to unaccounted S-wave anisotropy. To increase the reliability of the S-wave tomograms, joint-inversions were performed, whereby a cross-gradient constraint was emplaced to structurally couple the S-waves to the more accurate P-wave traveltimes. The resulting jointly inverted S-wave tomograms show a better correlation with the borehole logs than the individually inverted tomograms, while the loss in resolution for the P-wave was marginal.

The jointly inverted tomograms proved useful in detecting (1) aquifer heterogeneities, which are likely due to differences in clay content; (2) differences in effective pressure in the overlying clay layer; and (3) estimating the extent of S-wave anisotropy, by comparing the SV- and SH-wave velocities. Across both tomographic planes substantial S-wave anisotropy is present, with similar trends observable. The anisotropy likely contributed to the artefacts in the individually inverted S-wave tomograms.

6. PUBLICATION IV: SEISMIC VTI PARAMETER INVERSION FROM P- AND S-WAVE CROSS-BOREHOLE MEASUREMENTS IN AN AQUIFER ENVIRONMENT

6.1 Abstract

Joint P- and S-wave measurements for tomographic cross-borehole analysis can offer more reliable interpretational insight concerning lithological and geotechnical parameter variations compared to P-wave measurements on their own. However, anisotropy can have a large influence on S-wave measurements, with the S-wave splitting into two modes. We present an inversion for parameters of VTI (transversely isotropic with a vertical symmetry axis) media. Our inversion is based on the traveltime perturbation equation, using cross-gradient constraints to ensure structural similarity for the resulting VTI parameters. We first demonstrate the inversion on a synthetic dataset consisting of P-waves, vertically and horizontally polarized S-waves. Subsequently, we present inversion results for a dataset comprising jointly measured P-waves, vertically and horizontally polarized S-waves that was acquired in a near-surface (< 50 m) aquifer environment (SAFIRA research site, Germany). The inverted models show that the anisotropy parameters ε and δ are close to zero, with no P-wave anisotropy present. A high Vp/Vs ratio of up to nine causes considerable SV-wave anisotropy despite the low magnitudes for ε and δ. The SH-wave anisotropy parameter γ is estimated to be between 0.05 and 0.15 in the clay and lignite seams. The S-wave splitting is confirmed by polarization analysis prior to the inversion. The results suggest that S-wave anisotropy may be more severe than P-wave anisotropy in near-surface environments and should be taken into account when interpreting cross-borehole S-wave data.

6.2 Introduction

Seismic traveltime tomography is routinely used in a cross-borehole setup to reconstruct elastic parameters and has evolved to a commonly applied high-resolution method, with applications that range from geotechnical site characterization (Yamamoto et al., 1994; Rumpf and Tronicke 2014), hydrogeological investigations (Fechner 1998; Moret et al., 2006; Paasche et al., 2006; Doetsch et al., 2010), mineral exploration (Seebold et al., 1999) and nuclear waste storage (Wong et al., 1983; Marelli et al., 2010), to reservoir characterization (Macrides et al., 1988; Zhang et al., 2012).

Tomographic studies are often performed under the assumption that the subsurface medium is isotropic with respect to the seismic velocity. However, real materials are often anisotropic, with the seismic velocity dependent on the azimuthal or polar angle (Thomsen, 2002). Anisotropy can be caused by aligned cracks (Crampin, 1981) or minerals (Brocher and Christensen, 1990), sedimentary layering (Helbig, 1981; Thomsen, 1986) and stress anisotropy (Nur and Simmons, 1969; Clayton, 2011). Carrion et al., 1992) have shown that even weak anisotropy can produce visible artifacts in borehole tomograms, if unaccounted for. For the lowest anisotropic symmetry (triclinic) up to 21 independent parameters have to be derived to fully describe the seismic velocity in an anisotropic elastic medium.

An overview of anisotropic models and methods in seismic exploration can be found in (Helbig and Thomsen, 2005) and (Tsvankin et al., 2010). Fortunately, the material can often be described by simpler forms of anisotropy where symmetries exist, which significantly limit the number of independent variables. Usually the material is interpreted as being transversely isotropic with an axis of symmetry that is either vertial or tilted, designated VTI or TTI, respectively. For a VTI medium the number of independent variables is reduced to five, which are best described by the Thomsen parameters (1986); these are the vertical P- and S-wave velocity (Vp0, Vs0) and the anisotropy parameters ε, δ and γ. In case of a TTI medium the tilt angle (θ) and the azimuth (φ) of the axis of symmetry have to be given as well. A detailed analysis of notation and seismic inversion methods for different anisotropic symmetries is given by (Tsvankin and Grechka, 2011) and (Tsvankin, 2012, pp. 1-13).

The seismic kinematic equation was first extended to heterogeneous and anisotropic environments by Červený (1972). He applied a Hamiltonian form of the eikonal equation (Vidale, 1988) to a general anisotropic medium and expressed a first-order traveltime perturbation equation in terms of the polarization vectors of the P- and S-waves. Chapman and Pratt (1992) proposed a similar approach to Červený (1972) in a cross-borehole tomographic setting and presented an inversion for TTI parameters in a near-surface (< 60 m) clay environment Pratt and Chapman (1992). This inversion procedure of Chapman and Pratt (1992) was further used by Pratt et al. (1993), who acquired seismic data in the crown pillar of a sulfide ore mine and inverted the P-wave traveltimes for TTI parameters. Their anisotropic inversion approach successfully removed distortions that had previously affected the velocity distributions derived from an isotropic assumption and provided further analysis of the overall bulk properties of the rock mass.

These previous borehole tomographic studies, which focused on the inversion for the anisotropy parameters, only used P-wave traveltimes. Thus, only the TTI parameters Vp0, ε, δ and θ were derived (φ was inferred), while the S-wave velocity (Vs0) and the SH-wave anisotropy parameter γ were ignored. Several studies have been conducted using jointly measured P- and S-wave traveltimes and assuming an isotropic seismic velocity wavefield. For example, Angioni et al. (2003) derived elastic properties in a geotechnical context, Daley et al. (2004) constrained a hydro-geological model, while Dietrich and Tronicke (2009) used a geostatistical inversion of P- and S-wave data to delineate the detailed structure of an aquifer and to derive elastic parameters, such as Young's modulus, bulk modulus, shear modulus and Poisson's ratio. Further, von Ketelhodt et al. (2018) used both a vertically and horizontally polarized shear source to generate a jointly measured P-, SV- and SH-wave dataset at the SAFIRA test site in Zeitz, Germany. The P- and S-wave traveltimes were jointly inverted using a structural constraint. This meant that the two models (P- and S-wave velocity fields) were coupled by assuming that the cross-gradient (cross product of the gradients of the two models) was zero. The S-

wave tomograms, obtained by joint inversion, no longer showed distortions and were easier to interpret than S-wave tomograms obtained by independent inversions of the S-wave traveltime datasets.

The inversion procedures of Červený (1972) and Chapman and Pratt (1992) suffer from a singularity problem for the two S-waves. Zhou et al. (2008) suggested an altered version of the traveltime-perturbation-based inversion, which does not suffer from the S-wave singularity problem. In this paper, we first introduce our anisotropic inversion, which is based on the inversion procedure of Zhou et al. (2008). We extend the inversion procedure by adding cross-gradient constraints (Gallardo and Meju, 2003, 2004) to ensure structural similarity for the resulting VTI parameters and test the capabilities of the inversion algorithm on a synthetic model. Finally, we apply the inversion to cross-borehole data consisting of P-, SV- and SH-wave traveltimes, acquired at the SAFIRA site in Germany (von Ketelhodt et al., 2018), to estimate the full suite of VTI parameters.

6.3 Tomographic Inversion Theory

6.3.1 VTI model

We invert for a transversely isotropic model with a vertical symmetry axis (VTI medium), which is best described by the five Thomsen parameters (Thomsen, 1986) defined in terms of the density normalized elasticity tensor elements a_{11}, a_{13}, a_{33}, a_{44}, a_{66} as

$$Vp0 = \sqrt{a_{33}}, \tag{6.1}$$

$$Vs0 = \sqrt{a_{44}}, \tag{6.2}$$

$$\varepsilon = \frac{a_{11} - a_{33}}{2a_{33}}, \tag{6.3}$$

$$\delta^* = \frac{1}{2a_{33}^2}[2(a_{13} - a_{44})^2 - (a_{33} - a_{44})(a_{11} + a_{33} - 2a_{44})], \tag{6.4}$$

$$\gamma = \frac{a_{66} - a_{44}}{2a_{44}}. \tag{6.5}$$

Here, Vp0 is the vertical P-wave velocity and Vs0 is the vertical S-wave velocity. The parameters ε, δ and γ are dimensionless and describe the magnitude of the anisotropy. In the case of isotropy, all three parameters are equal to zero. The parameters ε and δ influence the P- and SV-wave velocities, while the SH-wave velocity depends on the parameter γ. The parameter ε describes the fractional difference between the vertical and horizontal P-wave velocity, and predominantly governs the magnitude of the P-wave anisotropy. The SV-wave velocity mostly depends on the squared P- to S-wave velocity ratio and the difference between ε and δ, which is summarized by the SV-wave anisotropy parameter $\sigma = (\mathrm{Vp0/Vs0})^2(\varepsilon - \delta)$ (Tsvankin and Thomsen, 1994; Tsvankin, 2012). The parameter γ describes the

ellipticity of the SH-wave traveltime surface and is subsequently described as the SH-wave anisotropy parameter.

6.3.2 First order traveltime perturbation equation

We utilize the first-order traveltime perturbation equation by Zhou et al. (2008). Thereby, the traveltime τ for an anisotropic medium is expressed as the integral of the phase-slowness vector $\mathbf{p}$ along the raypath R

$$\tau_R = \int_R \mathbf{p} \cdot d\mathbf{x}, \tag{6.6}$$

where $\cdot$ represents the dot product of the 3D vectors. This formulation is extended for the case that the model m_v undergoes a perturbation from m_v to $m_v + \delta m_v$, whereby the model is comprised of the five (i.e. $v = 1,2,\ldots,5$) VTI-model parameters Vp0, Vs0, ε, δ, γ. The raypath also undergoes a perturbation from R: $\mathbf{x}$ to $R + \delta R$: $\mathbf{x} + \delta\mathbf{x}$, with the 3D position vector $\mathbf{x}$. Equation 6.6 can then be re-formulated to

$$\tau_{R+\delta R} = \int_{R+\delta R} (\mathbf{p} + \delta\mathbf{p}) \cdot d(\mathbf{x} + \delta\mathbf{x}). \tag{6.7}$$

After some simplifications, and by ignoring higher-order terms, the first-order traveltime perturbation equation is given by Zhou et al. (2008) as

$$\delta\tau_R = \int_R (\delta\mathbf{p} \cdot d\mathbf{x} - d\mathbf{p} \cdot \delta\mathbf{x}). \tag{6.8}$$

Both the changes to the phase-slowness vector perturbation ($\delta\mathbf{p}$) and to the raypath coordinate perturbation ($\delta\mathbf{x}$) are caused by a model perturbation (δm). Subsequently, the phase-slowness perturbation ($\delta\mathbf{p}$) in the anisotropic medium is approximated by two contributions. The first contribution comes from the model changes (δm) with a fixed raypath (R) and the second contribution from the raypath perturbation (δR), while the model (m) remains unchanged, i.e.

$$\delta\mathbf{p} \approx \frac{\partial\mathbf{p}}{\partial m_v}\delta m_v + \frac{\partial\mathbf{p}}{\partial x_i}\delta x_i. \tag{6.9}$$

This phase-slowness disturbance approximation ($\delta\mathbf{p}$) is incorporated into equation 6.8 giving

$$\delta\tau = \int_R \left(\frac{\partial\mathbf{p}}{\partial m_v}\delta m_v\right) \cdot d\mathbf{x} + \int_R \left[\left(\frac{\partial\mathbf{p}}{\partial x_i} \cdot \delta x_i\right) d\mathbf{x} + d\mathbf{p} \cdot \delta\mathbf{x}\right],$$

$$= \int_R \left(\frac{d\mathbf{x}}{d\tau} \cdot \frac{\partial\mathbf{p}}{\partial m_v}\right) dm_v\, d\tau + \int_R \left(\frac{d\mathbf{x}}{d\tau} \cdot \frac{\partial\mathbf{p}}{\partial x_i} - \frac{dp_i}{d\tau}\right) \delta x_i\, d\tau,$$

$$= \int_R \left(\mathbf{U} \cdot \frac{\partial\mathbf{p}}{\partial m_v}\right) dm_v\, d\tau + \int_R \left(\mathbf{U} \cdot \frac{\partial\mathbf{p}}{\partial x_i} - \frac{dp_i}{d\tau}\right) \delta x_i\, d\tau,$$

$$= \int_R \left(\mathbf{U} \cdot \frac{\partial \mathbf{p}}{\partial m_v} \right) dm_v \, d\tau, \tag{6.10}$$

which introduces the group velocity ($\mathbf{U} = \mathrm{d}\mathbf{x}/\mathrm{d}\tau$). In the above formulation (equation 6.10), we use the relation

$$\mathbf{U} \cdot \frac{\partial \mathbf{p}}{\partial x_i} = \mathbf{U} \cdot \frac{\partial p_i}{\partial x_i} = \frac{\partial x_i}{d\tau} \frac{dp_i}{dx_i} = \frac{dp_i}{d\tau}.$$

The identity

$$\mathbf{U} \cdot \frac{\partial \mathbf{p}}{\partial m_v} = -\mathbf{p} \cdot \frac{\partial \mathbf{U}}{\partial m_v} \tag{6.11}$$

allows equation (6.10) to be expressed in the two forms

$$\delta\tau = \int_R \left(\hat{\mathbf{r}} \cdot \frac{\partial \mathbf{p}}{\partial m_v} \right) \delta m_v \, ds, \tag{6.12}$$

$$\delta\tau = -\int_R \frac{1}{cU} \left(\mathbf{n} \cdot \frac{\partial \mathbf{U}}{\partial m_v} \right) \delta m_v \, ds, \tag{6.13}$$

where c is the phase velocity and $\hat{\mathbf{r}} = d\mathbf{x}/ds$ and $ds = |d\mathbf{x}|$. Zhou and Greenhalgh (2005) show the calculation of the integrands in equation (6.12) and (6.13), which Zhou et al. (2008) use, together with the first-order traveltime perturbation formula of Červený (1972) to simplify equation (6.10) to

$$\delta\tau = -\int_R \frac{\partial m_v}{cU} \cdot \frac{\partial c}{\partial m_v} \, ds. \tag{6.14}$$

Thus, the traveltime perturbation equation for a VTI medium is simplified to only include the phase velocity (c), the group velocity (U) and the phase velocity derivatives ($\partial c/\partial m_v$), which are derived explicitly in Zhou et al. (2008). Since the traveltimes determined from tomographic data are related to the phase velocity (c), we use Crampin's formula (1981) to determine the group velocity (U) for a 2D medium with

$$U = \sqrt{c^2 + \left(\frac{\partial c}{\partial \theta} \right)^2}. \tag{6.15}$$

The phase velocity (c) for a VTI medium is angle dependent (polar angle θ) and derived by Daley and Hron (1977), whereby

$$c = \begin{cases} \sqrt{P \pm \sqrt{P^2 - Q}}, & P, SV \\ \sqrt{a_{66} + (a_{44} - a_{66}) \cos^2 \theta}, & SH \end{cases} \tag{6.16}$$

with

$$P = \frac{1}{2}(Q_1 + Q_2),$$

$$Q = Q_1 Q_2 - Q_3,$$

$$Q_1 = a_{11} + (a_{44} - a_{11})\cos^2\theta,$$

$$Q_2 = a_{44} + (a_{33} - a_{44})\cos^2\theta,$$

$$Q_3 = \frac{1}{4}(a_{13} - a_{44})^2 \sin^2(2\theta).$$

The variables a_{11}, a_{13}, a_{33}, a_{44} and a_{66} are the density normalised matrix elements of the elastic modulus matrix which Thomsen (1986) related to his parameters that are defined in equations (6.1) to (6.5).

6.3.3 Joint-inversion for anisotropy parameters

To apply the perturbation equation practically and reconstruct the anisotropic model from a tomographic dataset, we discretise the inter-borehole space two-dimensionally into N cells. Therefore, the perturbation formula (equation 6.14) has to be expressed in a discrete form, which is given by

$$\delta\tau = -\sum_{k=1}^{N} \int_{R_k} \frac{\partial m_v}{cU} \cdot \frac{\partial c}{\partial m_v}\, ds. \tag{6.17}$$

The traveltime perturbation for a specific ray is determined by summing the individual components related to the ray segments (R_k).

In the simplest form, the tomographic problem that is iteratively solved, is expressed as

$$\mathbf{m}_{(l)} = \mathbf{m}_{(l-1)} + \boldsymbol{J}_{(l)}^{-g} \delta\boldsymbol{\tau}_{(l-1)} \tag{6.18}$$

for iteration $l = 1,2,\ldots$, with the anisotropic model (**m**) consisting of the five model parameters (Vp0, Vs0, ε, δ, γ), the traveltime residuals ($\delta\boldsymbol{\tau}$) and the Jacobian matrix (**J**), which connects the traveltime residuals ($\delta\boldsymbol{\tau}$) with the model parameters (**m**). The superscript $-g$ denotes the generalized inverse. With the first-order traveltime perturbation equation, the Jacobian (**J**) is given by the partial derivatives of the traveltime ($\boldsymbol{\tau}$) with respect to the model parameters ($\boldsymbol{m}$). In discrete form, Zhou et al. (2008) express the Jacobian as

$$J_{(l)} = \frac{\partial \tau_j}{\partial m_i} = -\sum_{k=1}^{N} \frac{R_{jk}}{2} \left\{ \left[\frac{1}{cU} \frac{\partial c}{\partial m_i} \right]_{m_l, x_{A_j}^k} + \left[\frac{1}{cU} \frac{\partial c}{\partial m_i} \right]_{m_l, x_{B_j}^k} \right\}, \tag{6.19}$$

whereby, the parameters c, U and $\frac{\partial c}{\partial m_i}$ are determined by means of Lagrangian interpolation (Kreyszig, 2011, pp. 809-811) at the cell edges, with position x_A (left edge) and position x_B (right edge) of the ray segment R_k of ray j.

This, of course, requires an anisotropic curved raytracing to determine the raypath with its segments (R_k). To achieve this, we are using a modified version of the raytracing algorithm of Giroux and Gloaguen (2012), which is available through the *bh_tomo* tomographic software package (Giroux et al., 2007). The algorithm is based on the algorithm of Gruber and Greenhalgh (1998) and uses a grid of primary nodes, located at the corner of the model cells, and secondary nodes populated in between. Originally, the traveltimes at the nodes were determined based on an elliptical anisotropic velocity model. We modified the code and determined the traveltimes according to a VTI velocity model instead.

6.3.4 Constraints

To regularize our solution, we applied cross-gradient constraints (Gallardo and Meju, 2003, 2004) to ensure structural similarity among the five resulting VTI-model parameters. This meant that the VTI-model parameters were coupled by assuming that the cross-gradient, which is the cross product of the gradients, is zero. Changes in the model should then occur along the same boundaries. The 3D cross-gradient function ($\mathbf{t}$) for two models, model 1 ($\mathbf{m}^{\{1\}}$) and model 2 ($\mathbf{m}^{\{2\}}$), is defined as

$$\mathbf{t}_{(l)}(x,y,z) = \nabla\mathbf{m}^{\{1\}}_{(l)}(x,y,z) \times \nabla\mathbf{m}^{\{2\}}_{(l)}(x,y,z) \tag{6.20}$$

for iteration (l). The 3D cross-gradient function has three components (x, y, and z), given by

$$\mathbf{t}_{(l)}(x,y,z) = \begin{pmatrix} \mathbf{t}_{x,(l)} \\ \mathbf{t}_{y,(l)} \\ \mathbf{t}_{z,(l)} \end{pmatrix} = \begin{pmatrix} \nabla\mathbf{m}^{\{1\}}_{y,(l)}\nabla\mathbf{m}^{\{2\}}_{z,(l)} - \nabla\mathbf{m}^{\{1\}}_{z,(l)}\nabla\mathbf{m}^{\{2\}}_{y,(l)} \\ \nabla\mathbf{m}^{\{1\}}_{z,(l)}\nabla\mathbf{m}^{\{2\}}_{x,(l)} - \nabla\mathbf{m}^{\{1\}}_{x,(l)}\nabla\mathbf{m}^{\{2\}}_{z,(l)} \\ \nabla\mathbf{m}^{\{1\}}_{x,(l)}\nabla\mathbf{m}^{\{2\}}_{y,(l)} - \nabla\mathbf{m}^{\{1\}}_{y,(l)}\nabla\mathbf{m}^{\{2\}}_{x,(l)} \end{pmatrix}. \tag{6.21}$$

However, on a 2D plane, the models only vary with distance (x) and depth (z). Perpendicular to that plane (y-direction) the model is assumed to be constant and therefore the model derivatives ($\nabla\mathbf{m}_y$) are zero. Thus, only the y-component of the cross-gradient function is non-zero (i.e. $\mathbf{t} = \mathbf{t}_y(x,z)$), which we discretized using a forward difference scheme (Gallardo and Meju, 2004; von Ketelhodt et al., 2018). The individual components of $\mathbf{t}$ are then given by

$$t_{c,(l-1)} = \frac{1}{\Delta x \Delta z}\left[m_c^{\{1\}}\left(m_b^{\{2\}} - m_r^{\{2\}}\right) + m_r^{\{1\}}\left(m_c^{\{2\}} - m_b^{\{2\}}\right) + m_b^{\{1\}}\left(m_r^{\{2\}} - m_c^{\{2\}}\right)\right], \tag{6.22}$$

with the subscripts c, b and r denoting the centre, bottom and right cell of the discretized model (c.f. Figure 1 in Gallardo and Meju, 2003). In the above formulation, it is only possible to determine the

cross-gradient function ($\mathbf{t}$) of a known model, i.e. the previous iteration ($l-1$). To determine ($\mathbf{t}$) for the current iteration (l), and to incorporate the constraint into equation (6.18), we use a first-order Taylor expansion

$$\mathbf{t}_{(l)} \approx \mathbf{t}_{(l-1)} + \begin{pmatrix}\mathbf{B}^{\{1\}} & \mathbf{B}^{\{2\}}\end{pmatrix}\begin{pmatrix}\Delta\mathbf{m}^{\{1\}} \\ \Delta\mathbf{m}^{\{2\}}\end{pmatrix}, \tag{6.23}$$

with the gradient of the cross-gradient function ($\nabla\mathbf{t} = \mathbf{B} = \begin{pmatrix}\mathbf{B}^{\{1\}} & \mathbf{B}^{\{2\}}\end{pmatrix}$) for models $\mathbf{m}^{\{1\}}$ and $\mathbf{m}^{\{2\}}$.

By definition, the cross-gradient function is determined only between two models. Therefore, we apply the constraints a total of four times, in that we couple Vs0, ε, δ and γ to Vp0.

We incorporate these constraints into our inverse problem (equation 6.18), which we now state as

$$\begin{pmatrix}\mathbf{J}_{(l)} \\ \lambda\mathbf{B}_{(l)}\end{pmatrix}\Delta\mathbf{m}_{(l)} = \begin{pmatrix}\delta\boldsymbol{\tau}_{(l)} \\ -\lambda\mathbf{t}_{(l)}\end{pmatrix}, \tag{6.24}$$

with the matrices **J** and **B** composed of

$$\mathbf{J} = \begin{pmatrix}\beta\mathbf{J}_{P,Vp0} & 0 & \beta\mathbf{J}_{P,\varepsilon} & \beta\mathbf{J}_{P,\delta} & 0 \\ 0 & \mathbf{J}_{SV,Vs0} & \mathbf{J}_{SV,\varepsilon} & \mathbf{J}_{SV,\delta} & 0 \\ 0 & \mathbf{J}_{SH,Vs0} & 0 & 0 & \mathbf{J}_{SH,\gamma}\end{pmatrix}, \tag{6.25}$$

$$\mathbf{B} = \begin{pmatrix}\mathbf{B}_{Vp0\times Vs0} & \mathbf{B}_{Vp0\times Vs0} & 0 & 0 & 0 \\ \mathbf{B}_{Vp0\times\varepsilon} & 0 & \mathbf{B}_{Vp0\times\varepsilon} & 0 & 0 \\ \mathbf{B}_{Vp0\times\delta} & 0 & 0 & \mathbf{B}_{Vp0\times\delta} & 0 \\ \mathbf{B}_{Vp0\times\gamma} & 0 & 0 & 0 & \mathbf{B}_{Vp0\times\gamma}\end{pmatrix}. \tag{6.26}$$

Two weighting parameters are employed: β and λ. The parameter β controls the difference in traveltime accuracy between the P- and S-waves. We define β as the ratio of the standard deviation between the S- and P-wave traveltimes (S-wave traveltime is the average between SV- and SH-wave traveltimes). Since we acquired data in the near-surface environment (< 50 m), the P- to S-wave velocity ratio ranged from 5 to 8, and therefore our factor β reflected this and was also between 5 and 8. If we were to omit β, i.e. $\beta = 1$, then the inversion would primarily fit the model to the less accurate S-wave traveltimes. The parameter λ controls the weighting of the cross-gradient constraint. By setting λ to zero means having no cross-gradient constraint and setting λ to a very large value ensures a high degree of structural similarity, but also acts as a damping filter to the starting model.

We solve equation (6.24) in a least-squares-sense by using an LSQR algorithm (Paige and Saunders, 1982). We perform a maximum of twenty-five LSQR iterations with a stopping criterion taking effect

when two subsequent models correlate by more than 99.99%. The number of LSQR iterations corresponds approximately to the number of singular values (Yao et al., 1999). By conducting twenty-five iterations we ensured that contributions from the anisotropy parameters ε, δ and γ could be resolved while disregarding small singular values that only insignificantly contributed to the model.

To constrain the inversion further, we threshold the model parameters separately after each iteration (l), e.g. if $Vp0_i \leq a$, then $Vp0_i = a$ for a lower bound (a), or if $Vp0_i \geq b$, then $Vp0_i = b$ for an upper bound (b), for a model cell i.

6.3.5 Iterative inversion scheme

The iterative inversion scheme is made up of three parts. First, a homogeneous starting model is chosen, based on the average P- and S-wave velocities and initial anisotropy parameter estimates. Secondly, the homogeneous starting models for Vp0 and Vs0 are improved by conducting separate inversions only with traveltimes corresponding to the horizontal P- and S-wave raypaths. Since we operate in a horizontally layered sedimentary environment, this improves the starting model. Finally, the three datasets (P-, SV- and SH-wave) are jointly inverted, by conducting ten anisotropic curved-ray iterations, to invert for the VTI-model parameters, consisting of the two velocity fields (Vp0, Vs0) and three anisotropy parameters (ε, δ, γ). After each curved-ray iteration, equation (6.24) is solved with a twenty-five iteration LSQR algorithm.

The cross-gradient weighting parameter λ is chosen to minimise the traveltime residual, i.e. $\min\|\mathbf{Jm} - \tau\|_{\ell 2}$, while ensuring a maximum smooth model $\mathbf{m}$, with the model smoothness defined as $\|\mathbf{m}\|_{\ell 2}$. This procedure of finding an optimal cross-gradient constraint parameter (λ) is similar to finding an optimal damping parameter in linear inversion problems (Aster et al., 2013, p. 94).

6.4 Synthetic Verification

To verify the inversion procedure, we performed a reconstruction test with synthetic data. The source-receiver geometry is identical to the geometry of the SAFIRA dataset. Furthermore, the synthetic model has similar velocities and anisotropy magnitudes as estimated for the SAFIRA dataset (Figure 6.1). We used the anisotropic raytracing algorithm to determine synthetic P-, SV- and SH-wave traveltimes and reconstructed the synthetic models by using the inversion sequence described above, using homogeneous starting models (phase velocities of Vp0 = 1000 m/s and Vs0 = 100 m/s; anisotropy parameters of $\varepsilon = 0$, $\delta = 0$, $\gamma = 0$). The P- and S-wave starting models were improved by performing an inversion only with traveltimes corresponding to horizontal raypaths. Subsequently, we performed ten curved ray anisotropic inversions to reconstruct the model (Figure 6.1b). The choice of the cross-gradient weighting parameter λ is shown in Figure 6.1d, where the inversion is performed with several

different cross-gradient weights. We choose λ by minimizing the model smoothness, while ensuring a minimal traveltime residual, which occurs for $\lambda = 7500$ (Figure 6.1d).

The joint inversion for VTI parameters (Figure 6.1) demonstrates that the P- and S-wave velocities are reconstructed well, with all subtle features (e.g. the undulation at a depth of 35 m and the thin layer at a depth of 27 m) accurately resolved. The resolution of the reconstructed anisotropy parameters is slightly lower compared to Vp0 and Vs0, and is dependent on their magnitude. Our synthetic distribution of γ has the highest dynamic range with magnitudes from $\gamma = 0$ to $\gamma = 0.15$. The reconstruction of γ shows that all subtle features are well resolved, with a similar quality to Vp0 and Vs0. The reconstruction of the parameters ε and δ shows that not all subtle features (undulation and thin layer) are resolvable, which is due to the lower dynamic range of the synthetic ε and δ values ($\varepsilon = 0.01$ to $\varepsilon = 0.06$ and $\delta = 0.01$ to $\delta = 0.05$, Figure 6.1a). Nonetheless, the bigger geological features (e.g. the thicker layer at depths of 15 to 20 m) are resolved with the correct magnitudes.

In addition, we were able to compare the traveltime residuals of the anisotropic models, obtained by jointly inverting the P-, SV- and SH-wave traveltimes, to the residuals of the isotropic models, obtained by separately inverting the P-, SV- or SH-wave traveltimes for the three tomograms Vp, Vsv and Vsh (Figure 6.1c). The root-mean-square (rms) errors are reduced for the anisotropic inversions, with the rms error defined as the $\ell 2$ norm of the residual traveltimes. For the P-wave the rms error reduces from 1.16 ms to 0.32 ms, for the SV-wave residuals from 9.62 ms to 6.28 ms, and for the SH-wave the residuals significantly reduce from 10.14 ms to 1.54 ms when inverting for anisotropy. The large improvement for the SH-wave errors is due to the large values of $\gamma = 0.15$ in the synthetic model. Thus, the synthetic reconstruction shows that our inversion for anisotropy parameters improves the imaging of geological features and reduces the rms error of the residual traveltimes.

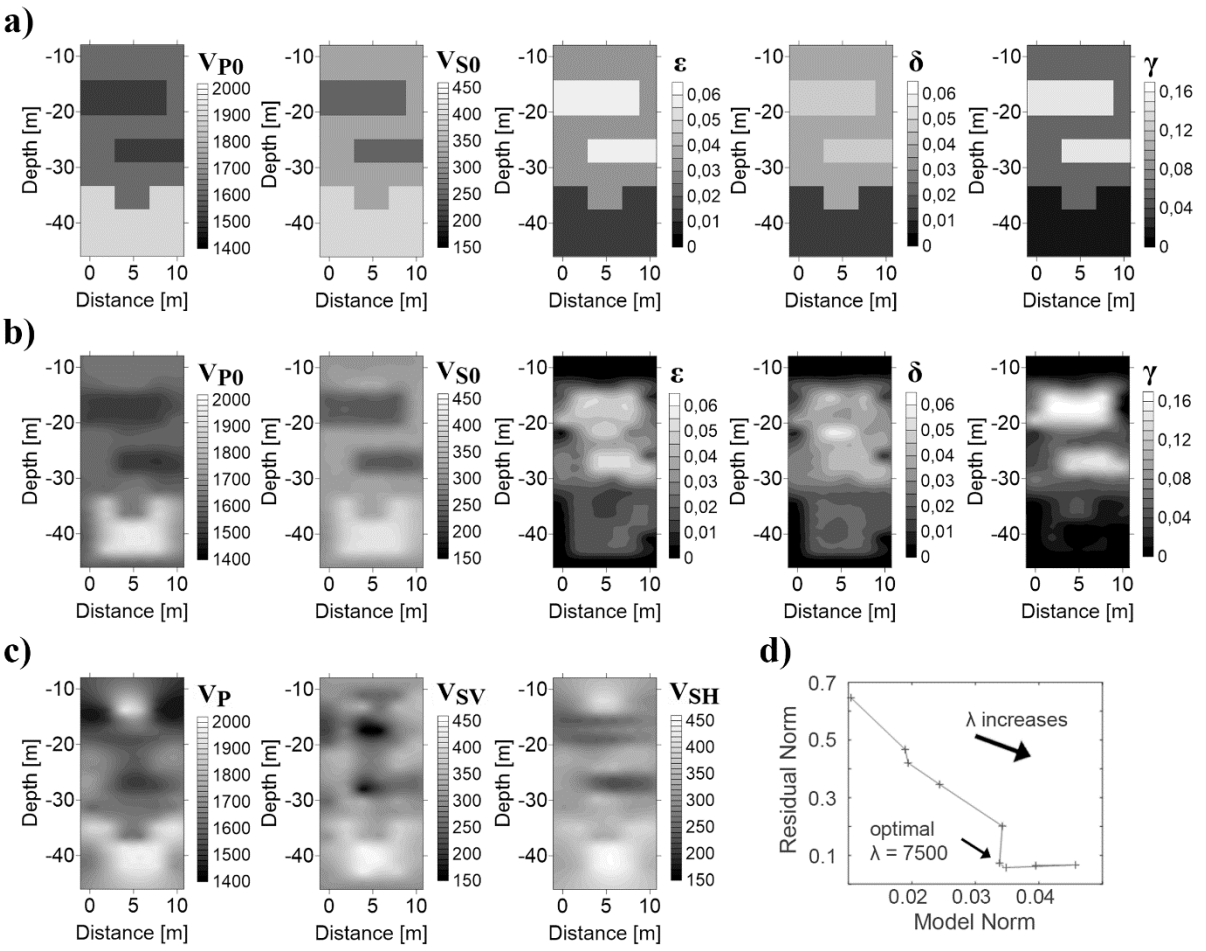


Figure 6.1: Synthetic anisotropic models (a) are reconstructed using the joint-inversion approach (b), whereby the optimal cross-gradient parameter was chosen with λ = 7500 (d). Separate isotropic inversions of the P-, SV- and SH-wave data are shown in (c).

6.5 Application to the SAFIRA Site

6.5.1 The SAFIRA dataset

The SAFIRA (Sanierungs-Forschung In Regional kontaminierten Aquiferen, i.e. research on remedial measures in regionally contaminated aquifers) research facility is located at the southern border of the Elster sedimentary basin, approximately 40 km south of Leipzig and 5 km east of Zeitz in Germany (Dietze, 2007, pp. 24-28). The research area is located on an old hydrogenation plant which was constructed in 1939 to produce fuels, lubricants, benzene and paraffin. During World War Two the plant was mostly destroyed by bombing, but reconstructed during the subsequent Soviet occupation. The operations ceased after the German reunification in 1990 due to high production costs. However, as a consequence of the destruction in World War Two and frequent leaks that occurred up to 1990, large amounts of benzene and by-products contaminated the ground water. A research facility was established in 1999 in the area of the contamination plume and the SAFIRA project started. The main objective of

the research activities was to test new ground water treatment methods (Weiß et al., 2002) and many boreholes were subsequently drilled.

The geology at SAFIRA consists of two aquifers, with layered clay and interbedded lignite seams. The overconsolidation of the clay and the lignite seams during the glaciation period of the Elster-Saale provide the theoretical conditions for a velocity difference between differently polarized S-waves. In such an environment, anisotropy is likely to occur since theoretical considerations and laboratory transducer measurements have shown that the S-wave velocity changes with increased external stresses and stress anisotropy (Fratta et al., 2004; Lee et al., 2005; Ku and Mayne, 2014).

Seismic data for tomographic analysis were acquired between two borehole pairs in the depth range of 10 to 50 m (Figure 6.2). The two acquisition planes are specified as Plane 1 (between boreholes B29 and B51) and Plane 2 (between boreholes B44 and B45). Plane 1 is orientated north-northwest to south-southeast, while Plane 2 is orientated north-northeast to south-southwest. The azimuths of the two planes differ by approximately 50°. The boreholes in each pair are separated by approximately 10 m (Plane 1) and 14 m (Plane 2).

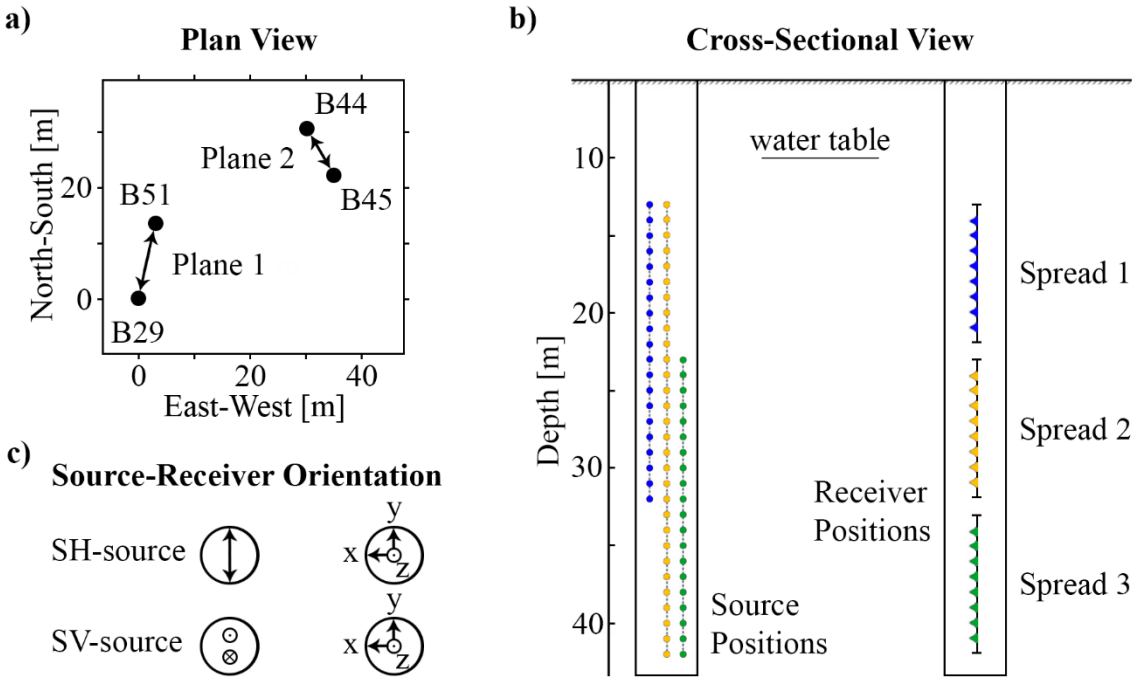


Figure 6.2: Overview of boreholes employed for the seismic acquisition (a) for Plane 1 (14 m between boreholes B29 and B51) and Plane 2 (10 m between boreholes B44 and B45). A cross-sectional view is shown in (b) with example source and receiver positions for different ten-level receiver spreads. The horizontally and vertically polarized source striking directions and three-component receiver orientations are shown in plan view in (c).

For both acquisition planes (Plane 1 and Plane 2), we employed two different sources: a horizontally and a vertically polarized source. Both sources were pneumatically clamped to the borehole. Internally, the sources use a number of electromagnetic coils that are placed adjacent to a copper plate. The copper plate and the coils are repulsed when an electrical current flow is triggered. For the horizontally polarized source, this causes the plate to mechanically strike the side of the borehole wall. In the case of the vertically polarized source, the electromagnetic coils are repulsed vertically, which produces a vertical shearing motion on the side of the borehole. Both sources were fired twice per position: up and down for the vertically polarized source, and left and right with respect to the receiver borehole for the horizontally polarized source. This enabled vertical stacking of the data to increase the signal-to-noise ratio. We recorded the data with a ten-level three-component receiver array (10 Hz resonant frequency) and temporally sampled at 16 kHz.

The sources and receivers were spaced at 1 m intervals and the source excitation was performed at the same position as the receivers and at ten positions above and ten positions below the receiver spread. This ensured an adequate overlap between adjacent receiver spreads, good angular coverage and a completion of the acquisition in the allocated six days' time. We measured the inclination of each borehole at site and found that the deviation from vertical did not exceed 1 m over a depth of 50 m. We used the surveyed borehole geometry in our inversions. Further, we determined the P- and S-wave traveltimes manually and corrected them for trigger delays, which we measured by comparing the P-wave arrival for both sources.

Before inverting for the anisotropy parameters at the SAFIRA site, we investigated whether the environment is anisotropic. We first conducted polarization analyses of the S-wave arrivals from the vertically- and horizontally polarized sources, which indicated the presence of S-wave splitting, and secondly, we estimated the magnitude of the anisotropy by analysing the straight-ray velocities as a function of the raypath angle.

6.5.2 Polarization analysis

To support a subsequent inversion for anisotropy parameters, we first determine the presence of S-wave splitting with polarization analyses. Recording the seismic data with three-component geophone sensors enabled the construction of hodograms (Jurkevics, 1988; Micheals, 2001), where the direction of particle motion of the incoming seismic wave is determined. The seismic wave motion is visualized in 3D, by plotting the amplitudes of the three different components (x, y, z) relative to each other. We use a covariance matrix (Flinn, 1965) to determine the linearity, azimuth and dip of the motion. A linearity of unity describes particle motion in a single linear direction, whereas a linearity of zero corresponds to spherical particle motion. An example of such a polarization analysis is shown in Figure 6.3.

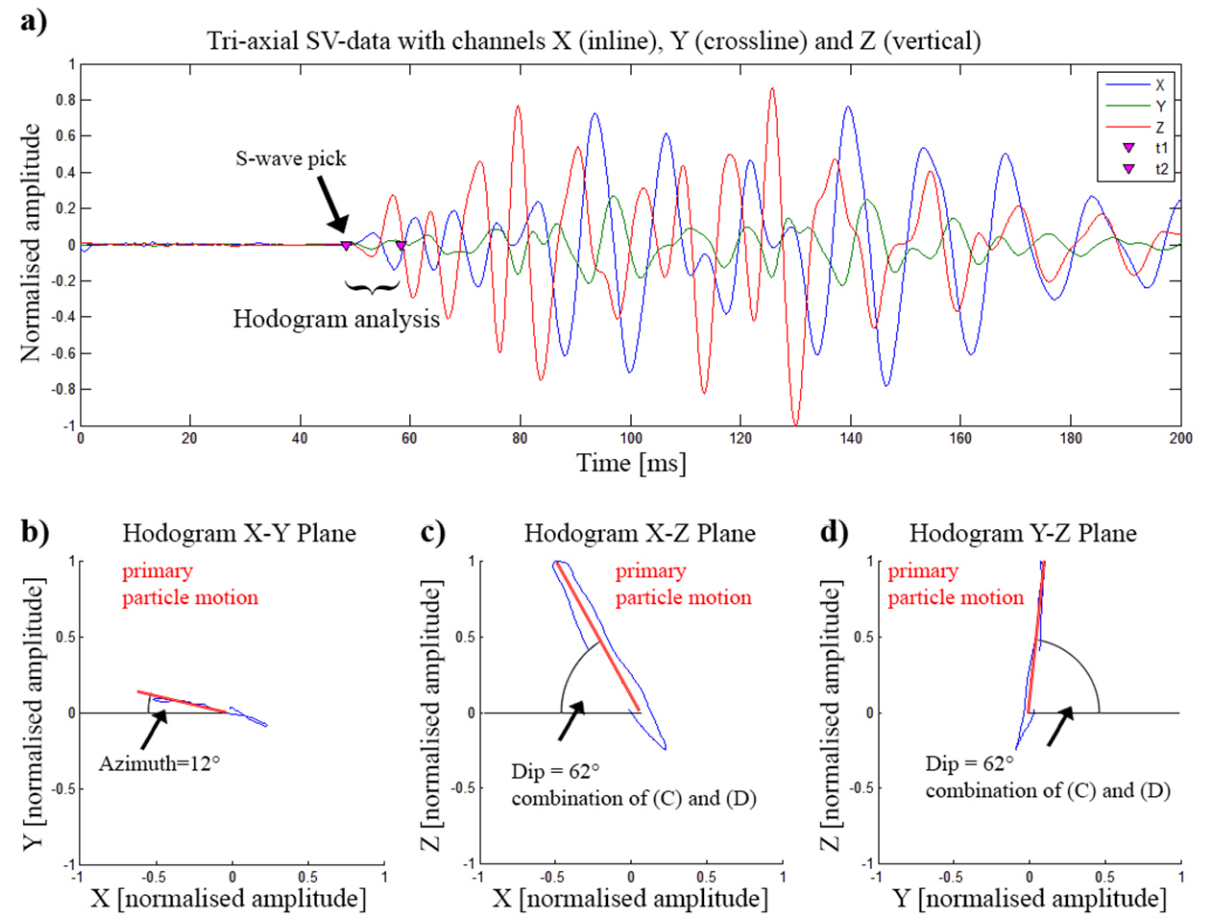


Figure 6.3: Example hodogram analysis with the primary particle motion indicated by the red line in the bottom three hodograms. The hodograms with calculated primary particle motion (b) to (d) depict particle motion for different 2D planes and are determined for a 10 ms window, starting with the S-wave traveltime pick from the vertically polarized source data.

P-wave Polarisation

We determine the P-wave polarization of the crosshole data subset (only horizontal rays), prior to analysing the polarization of the S-waves. In general, the P-wave traveltimes are determined with a high precision (with errors below 0.1 ms) and the polarization is therefore easier to interpret than an S-wave that splits into a fast and slow S-wave in an anisotropic environment. We determine the three polarization parameters, i.e. linearity, azimuth and dip, as a function of depth for the crosshole data subset of both sources (Figure 6.4a, b), by analysing the P-wave particle motion within a 1 ms time window. Even though the vertically polarized source produces low amplitude P-wave data for this source-receiver geometry, the polarization analysis (Figure 6.4b) still yields a very similar result to the polarization analysis of the horizontally polarized source (Figure 6.4a), where the P-wave coda has a significantly higher signal-to-noise ratio.

The polarization analysis shows that the P-wave is close to linearly polarized and the calculated dip is slightly positive for both sources and fluctuates around zero (in the range of -30° to +30°). A small positive dip is expected, as the velocity generally increases with depth and therefore the P-wave is refracted upwards and reaches the receiver from below, causing a slightly positive, upwards motion on the vertical channel.

We expected that 3D effects would be small in the layered environment and consequently that the P-wave raypath would lie in the 2D plane between the two boreholes and hence the azimuth to be approximately zero. However, the P-wave polarization analysis shows that the azimuth follows a pattern that is controlled by the acquisition design, with the data recorded with receiver spreads consisting of ten levels. We interpret this systematic rotation in measured azimuth to be caused by an axial rotation of the receivers at depth. Ideally, the horizontal receivers should be aligned perpendicular to the source-borehole plane to optimally record a horizontally polarized S-wave. Thus, we used the measured azimuth to axially rotate the data (Jackson et al., 1991) and correct for this effect.

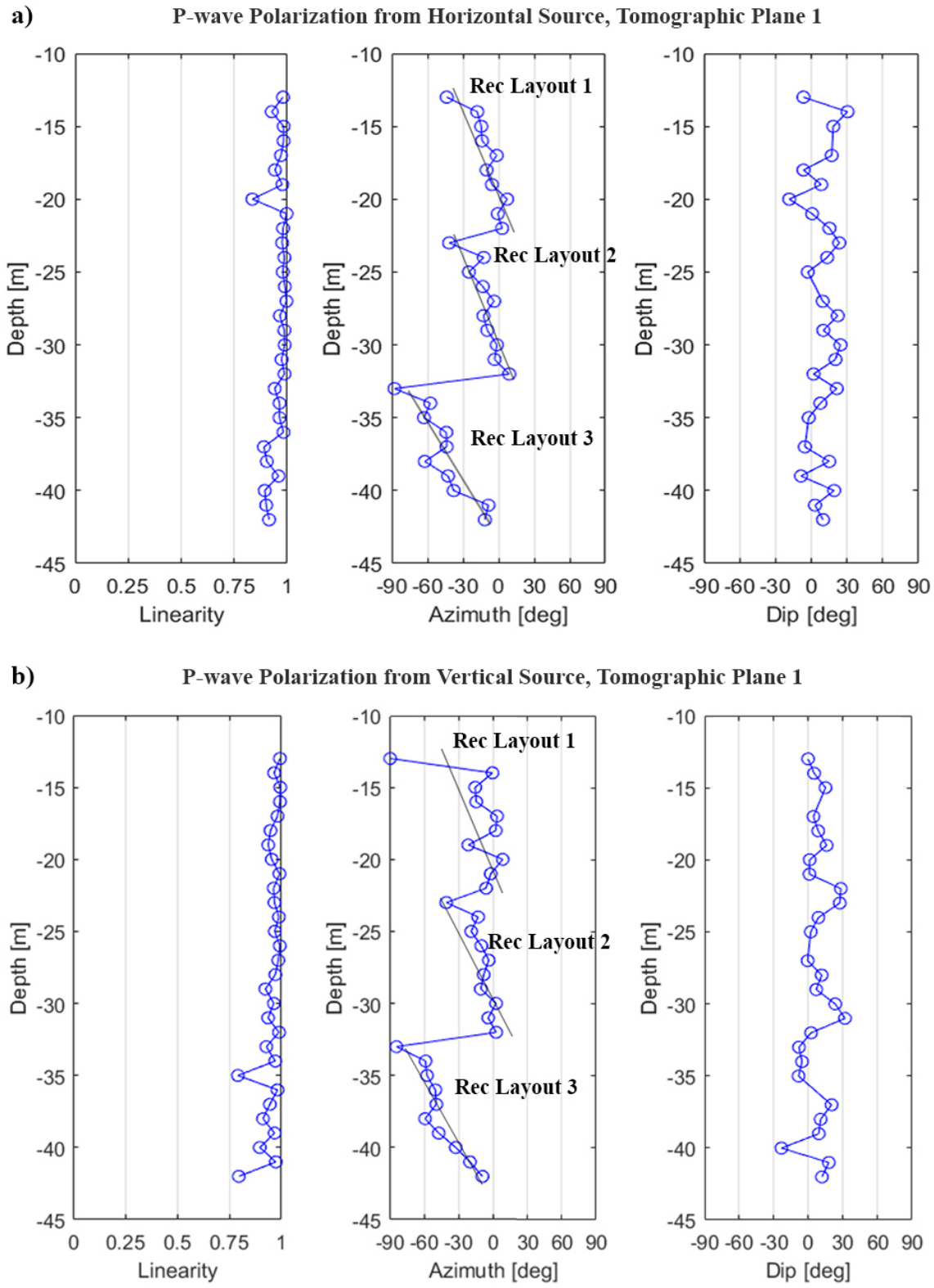


Figure 6.4: P-wave polarization of the crosshole data subset for tomographic Plane 1 (boreholes B44 and B45). The linearity, azimuth and dip is determined from the hodograms as a function of depth. The polarization is determined for both sources: the horizontally polarized source (a) and the vertically polarized source (b). The azimuth of the P-wave is a function of the ten-level receiver spreads.

S-wave Polarisation

After correcting the receiver orientation by rotating the data according to the P-wave azimuth, the rotated crossline channels are now ideally orientated to record a horizontally polarized S-wave. We now examine the S-wave polarization for both sources and acquisition planes, i.e. Plane 1 (Figure 6.5) and Plane 2 (Figure 6.6). Similar to the P-wave polarization analysis, the S-wave polarization analysis operates on a time window of about one period (t = 7.5 ms). Thereby, the analysis focuses only on the very first S-wave motions. The advantage of choosing a small analysis time window is that the polarization analysis only takes the first S-wave arrival into consideration, with no other later arriving S-waves, e.g. refracted, and reflected S-waves, or the slow S-wave mode due to S-wave splitting, influencing the results. The disadvantage is that the analysis is dependent on an accurate S-wave traveltime pick. Nonetheless, the traveltime picking accuracy is determined at about 1 ms and is therefore, within the time window range.

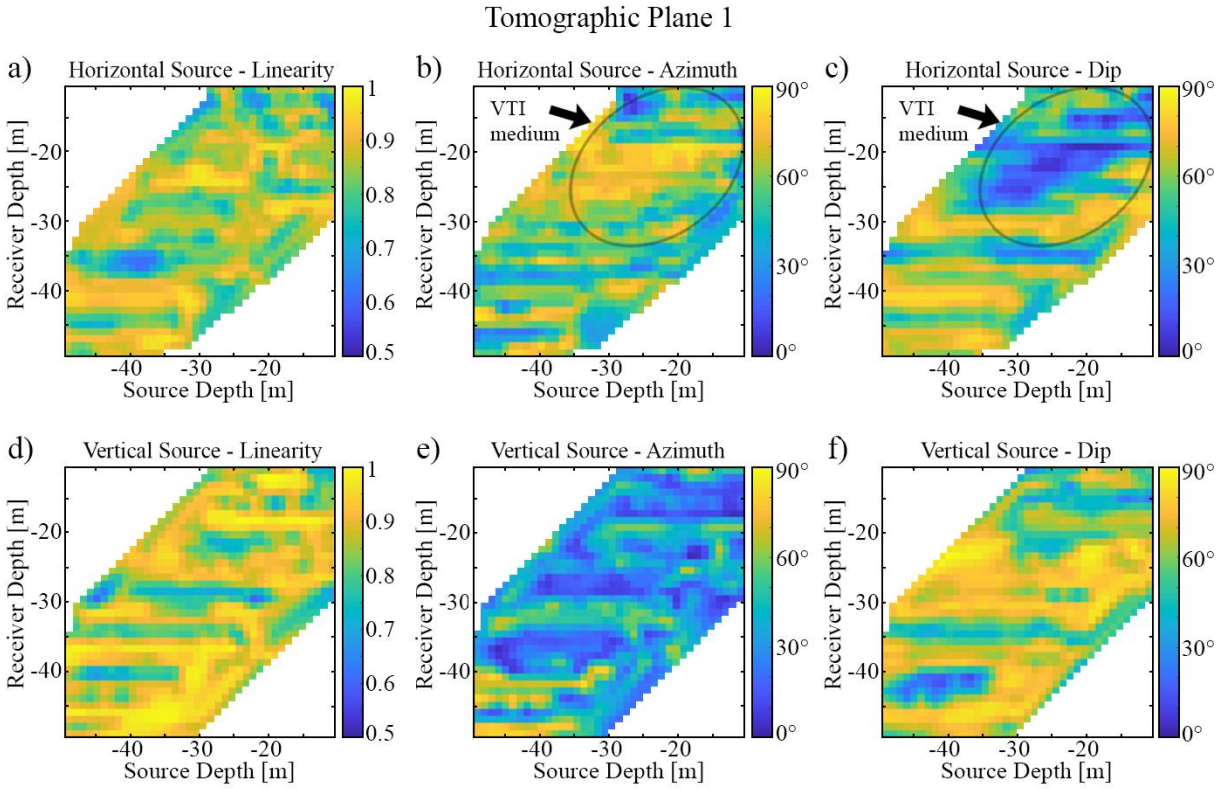


Figure 6.5: S-wave polarization is shown for the horizontally (a-c) and vertically polarized source (d-f). The linearity, azimuth and dip is shown as a function of the receiver and source depth for tomographic Plane 1, between boreholes B29 and B51.

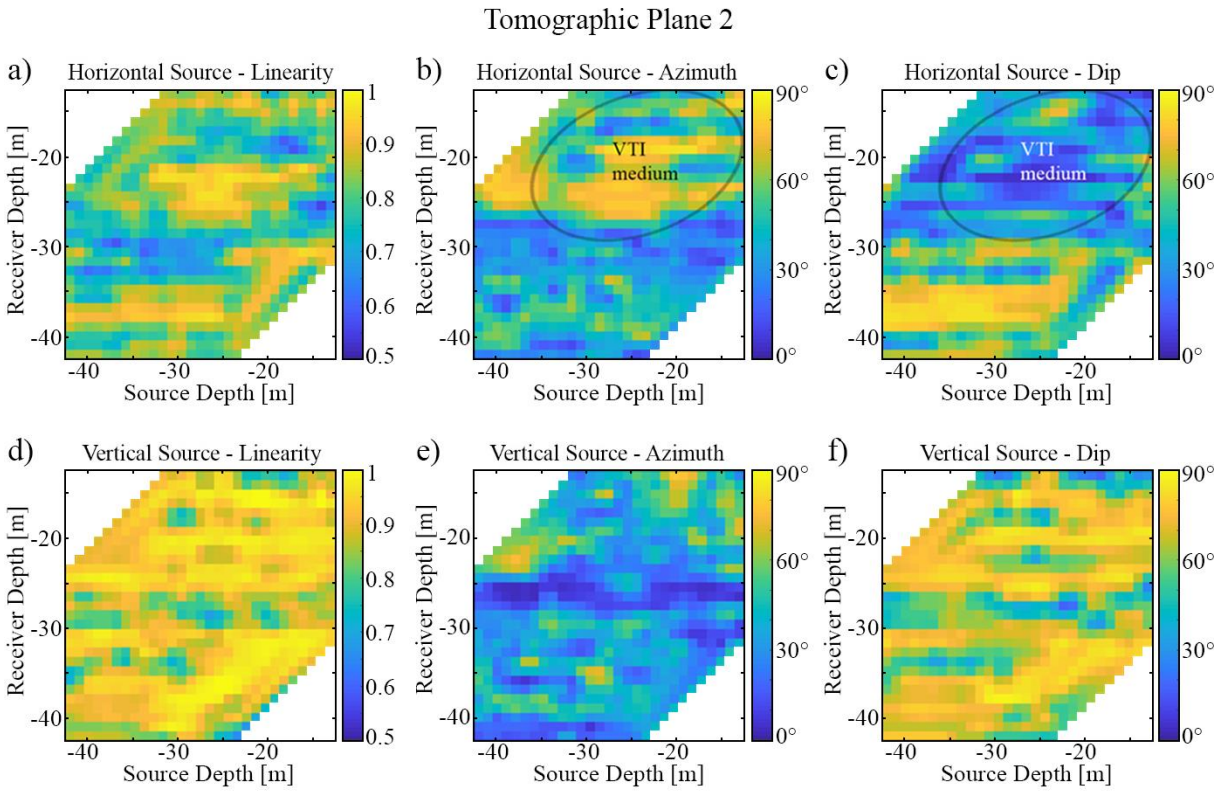


Figure 6.6: S-wave polarization is shown for the horizontally (a-c) and vertically polarized source (d-f). The linearity, azimuth and dip is shown as a function of the receiver and source depth for tomographic Plane 2, between boreholes B44 and B45.

The S-wave polarization analysis (Figure 6.5 and 6.6) shows that the vertically polarized source produces S-waves that are in general very linearly polarized (linearity > 0.8, Figure 6.5d and Figure 6.6d), with the polarization azimuth tending towards a range of 0° to 30° (Figure 6.5e and Figure 6.6e). The polarization dip of the vertically polarized source is generally in the 60° to 90° range (Figure 6.5f and Figure 6.6f). Thus, the vertically polarized source produces S-waves that are generally vertically polarized.

The horizontally polarized source, on the other hand, generates S-wave polarizations that are dependent on the receiver depth. In the upper 30 m, the azimuth is in the 60° to 90° range (Figure 6.5b and Figure 6.6b). This was intentional as we shot in a direction perpendicular to the tomographic plane. In addition, the dip (0° to 30° range, Figure 6.5c and Figure 6.6c) suggests that a horizontally polarized S-wave (SH-mode with transverse polarization, orthogonal to the propagation plane) is recorded. However, when we analyse the polarization below a depth of 30 m to the bottom of the borehole at 50 m, then we see that the azimuth (Figure 6.5b and Figure 6.6b) and dip (Figure 6.5c, Figure 6.6c) changes abruptly and resembles the polarization characteristics of a vertically polarized S-wave (azimuth < 30° and dip > 60°).

The S-wave polarization analysis (e.g. Figure 6.5c) shows that the measured polarization is often consistent for a particular receiver, which is visible as horizontal striping in the images. We therefore speculate that either source and receiver coupling or the near-receiver material play a non-negligible role. Nonetheless, the general trend is not influenced by this filter effect.

Thus, we identify two different elastic zones; an upper zone from a depth of 10 m to 30 m and a lower zone below 30 m to the bottom of the boreholes at 42 m and 50 m. The upper zone suggests a VTI medium, induced by the overconsolidated clay and lignite seams. In the upper zone, the horizontally polarized source generates predominantly SH-waves (Figure 6.5b, c, and Figure 6.6b, c) and the vertically polarized source generates predominantly waves that are polarized in the vertical plane (Figure 6.5e, f, and Figure 6.6e, f). We suspect that these predominantly vertical polarizations can be attributed to SV-waves, which are polarized perpendicular to the raypath propagation in the near-vertical plane.

In the lower zone, below a depth of approximately 30 m, the polarization of the S-wave changes. There, predominantly vertically polarized S-waves are recorded (Figure 6.5b, c, and Figure 6.6b, c). Thus, the VTI approximation cannot be applied here, as no SH-wave traveltimes are recorded in this lower zone. We think it is possible that a different elastic zone is present with a different symmetry, such as a TTI medium. In that case, the vertically- and horizontally polarized source would then have a nonzero projection onto the propagation plane and each source would generate both the fast and slow S-wave mode. If the SV-wave anisotropy parameter exceeds the SH-wave anisotropy parameter ($\sigma > \gamma$) then the SV-wave would travel at a higher velocity than the SH-wave. A polarization analysis of the (fast) S-wave would then show a primarily vertically polarized S-wave for both sources. Consequently, we disregard the data from the lower zone and concentrate on the data of the upper zone, where we assume a VTI medium.

6.5.3 Estimation of anisotropy

Prior to inverting for VTI parameters in the upper zone, we estimate the magnitude of anisotropy by first comparing SH- and SV-wave traveltime picks on the raw data. Figure 6.7 shows the S-wave traveltimes picked from the vertical channel data of the vertically polarized source (Figure 6.7a) and the S-wave traveltimes picked from the transverse channel of the horizontally polarized source (Figure 6.7b). The two sets of S-wave traveltimes suggest that anisotropy is present, having a bigger influence than traveltime picking uncertainties. Possible trigger delays are ruled out due to the P-wave arriving at the same time for both sources. The frequency content differs for the two sources, with a dominant S-wave frequency of approximately 150 Hz for the vertically polarized source and 300 Hz for the horizontally polarized source. However, we suspect that this does not influence the traveltime picking uncertainty. The traveltimes were picked on all three channels (radial, transverse and vertical). An

example of such three component data is shown (in Figure 6.7c and d) for a source depth of 25 m and receiver depth of 22 m with the picked SV- and SH-wave traveltimes.

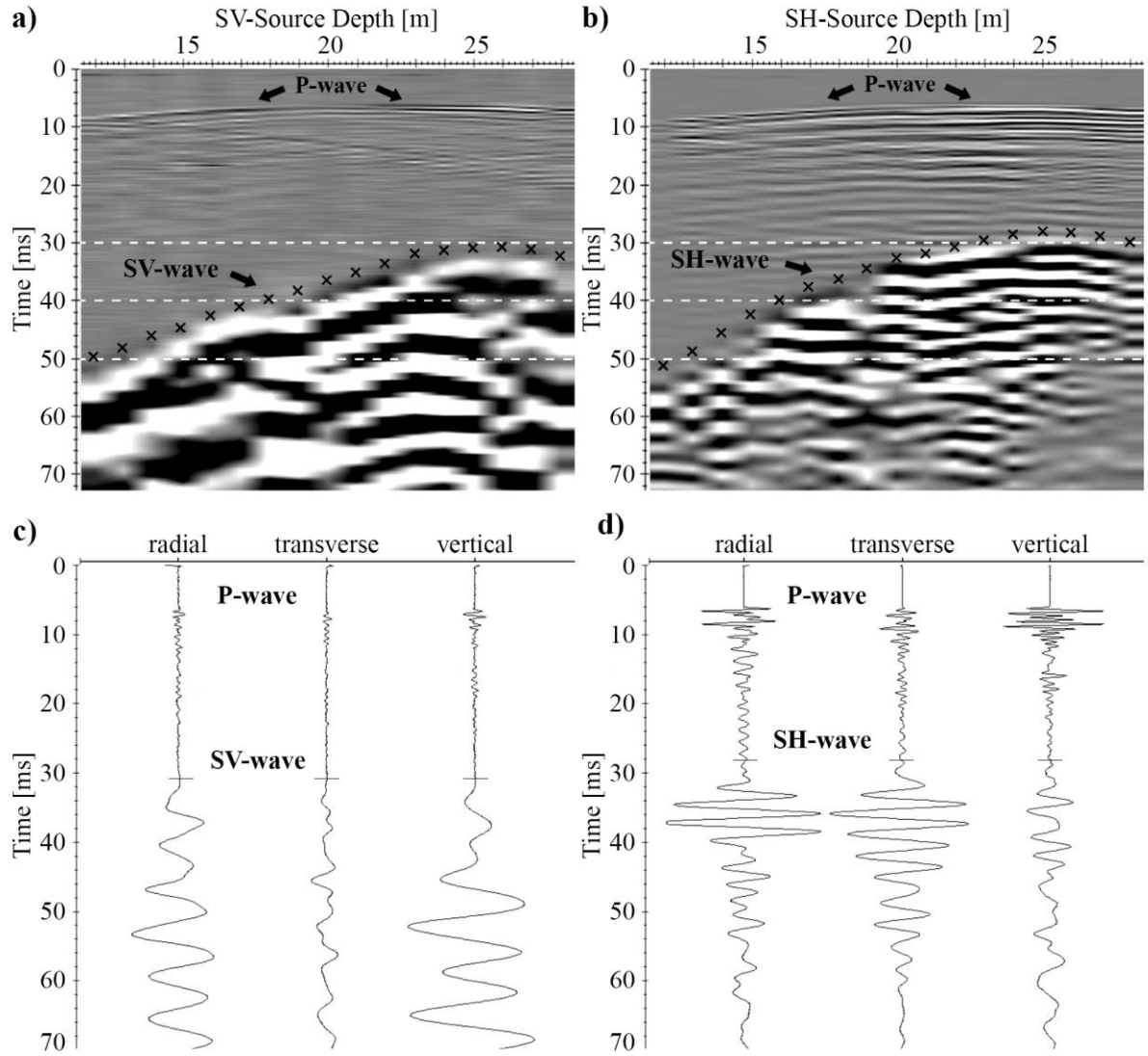


Figure 6.7: Receiver gather at a depth of 22 m, generated with the vertically (a) and horizontally polarized source (b) in borehole B44. The data are shown in variable density visualization. Vertical component data is shown for the vertically polarized source (a) and transverse component data is shown for the horizontally polarized source (b). The S-wave traveltime picks are indicated by the crosses (SV-wave traveltimes (a), SH-wave traveltimes (b)). An example of three component data is shown in (c) and (d) for a source depth of 25 m and a receiver depth of 22 m (vertically polarized source (c) and horizontally polarized source (d)).

Secondly, we estimate the magnitude of anisotropy by plotting the velocity as a function of the raypath angle (Figure 6.8). We compare the mean velocities associated with a raypath angle (blue curves in Figure 6.8) to the isotropic case (black curves in Figure 6.8). Subsequently, we use our inversion code

to determine VTI parameters which fit angle dependent velocities (red dashed curves in Figure 6.8) to the mean velocities. In this preliminary inversion, we assume a straight raypath and discretize using a minimum amount of model cells. The estimated VTI parameters are determined as $\varepsilon = 0.028$, $\delta = 0.032$ and $\gamma = 0.045$ for tomographic Plane 1 and $\varepsilon = 0.011$, $\delta = 0.009$ and $\gamma = 0.086$ for tomographic Plane 2. This initial estimate of the VTI parameters helps constrain the anisotropy parameters during the inversion. For example, we constrain the parameters $\varepsilon < 0.05$ and $\delta < 0.05$ since the minimal variation of the P-wave velocities as a function of the raypath angle suggests that little P-wave anisotropy is present.

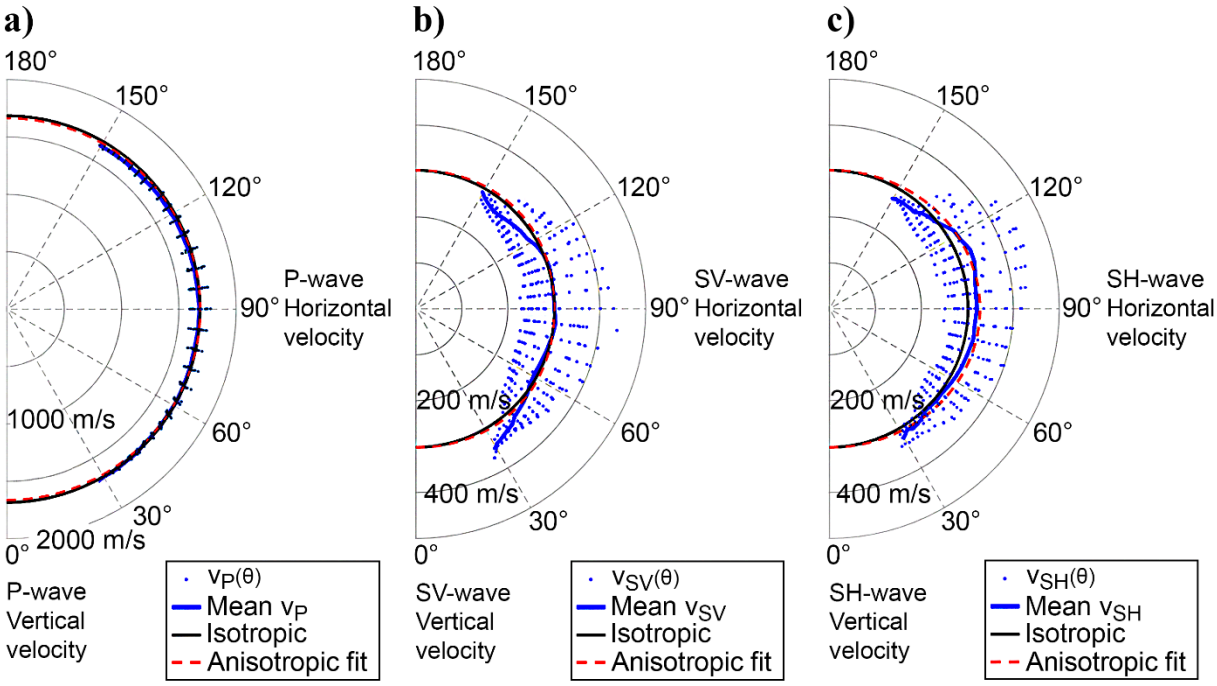


Figure 6.8: Straight ray velocities are shown which are plotted as a function of the ray path angle for P-waves (a), SV-waves (b) and SH-waves (c) in the VTI zone of Plane 2 of the SAFIRA dataset. The mean velocities for a ray path angle are shown by the blue curve. The velocities in a homogeneous isotropic medium would lie on the black curve. The mean velocities and the black isotropic curve deviate marginally for the P-waves and up to about 10% for the S-waves. We invert for VTI parameters which fit angle dependent velocities (red dashed curves) to the mean velocities.

6.5.4 Inversion for anisotropy parameters

We perform joint inversions for the anisotropy parameters in the VTI zone (upper zone for depths of 10 to 30 m) for Plane 1 (Figure 6.9) and Plane 2 (Figure 6.10). We discretize the medium between the boreholes into 7×16 and 6× 16 model cells with approximately 1040 traveltimes (380 P, 310 SV, 350 SH) and 930 traveltimes (330 P, 300 SV, 300 SH) for tomographic Plane 1 and Plane 2, respectively. For both tomographic inversions, we chose homogeneous starting models for the anisotropy parameters ($\varepsilon = 0$, $\delta = 0$, $\gamma = 0$). The starting P- and S-wave velocities (Vp0 and Vs0) were determined by

inverting only with traveltimes along horizontal raypaths. Subsequently, we inverted for the VTI parameters by performing 10 iterations with different values for the cross-gradient weighting parameter (λ). We chose λ to minimize both the residual and model norm (Figure 6.9c and Figure 6.10c).

The inversion results show the layered stratigraphy, which is supported by borehole logs (Weiß et al., 2002). The estimated anisotropy parameters ε and δ have low values and are in the range of 0 to 0.04. The estimated anisotropy parameter γ, on the other hand, is significantly higher and is between 0 and 0.10 (Plane 1) and between 0 and 0.15 (Plane 2).

We compare the anisotropic tomograms, obtained by jointly inverting the P-, SV- and SH-wave traveltimes for VTI parameters, to isotropic tomograms, obtained by separately inverting the P-, SV- or SH-wave traveltimes (Figure 6.9b and Figure 6.10b). Subsequently, we compare the rms errors of the isotropic inversions to the rms errors of the joint-inversions for VTI parameters. While the SV- and SH-wave traveltime residuals are significantly reduced (from 38 to 23 ms and 60 to 37 ms for the SV-waves, and from 38 to 19 ms and 26 to 20 ms for the SH-waves for Plane 1 and Plane 2 respectively), the residuals associated with the P-wave traveltimes increase (from 1.10 to 1.45 ms and from 0.8 to 1.3 ms for Plane 1 and Plane 2) when we perform the joint-inversion for anisotropy parameters. Nonetheless, the isotropic and anisotropic tomographic P-wave velocities have similar velocity distributions.

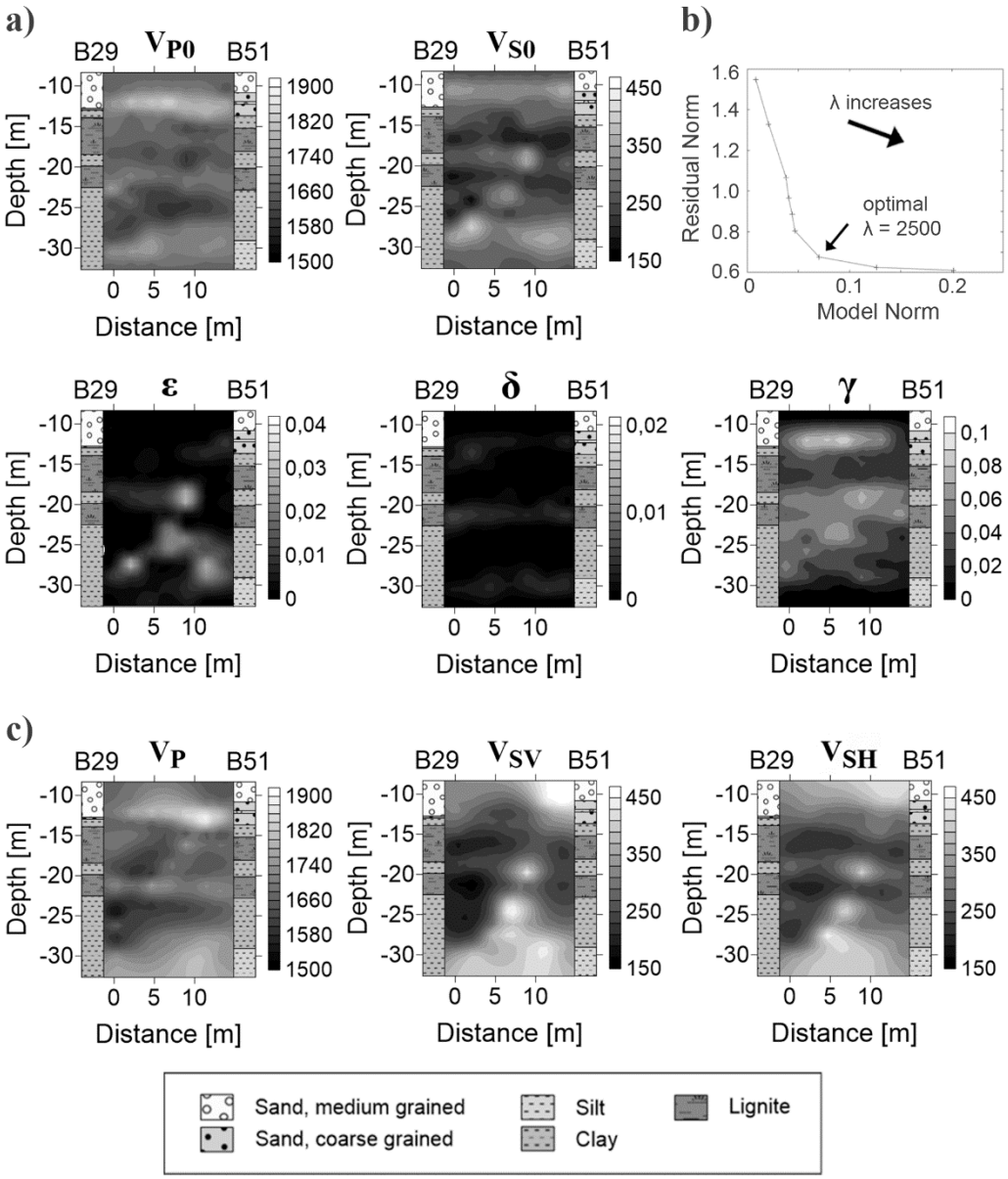


Figure 6.9: Joint-inversion for VTI parameters for tomographic Plane 1 (between boreholes B29 and B51) is shown in (a). We chose the cross-gradient parameter (λ = 2500) by trading off between the model norm and the residual norm for inversions with different values for λ (b). Separate isotropic inversions of the P-, SV- and SH-wave data is shown in (c).

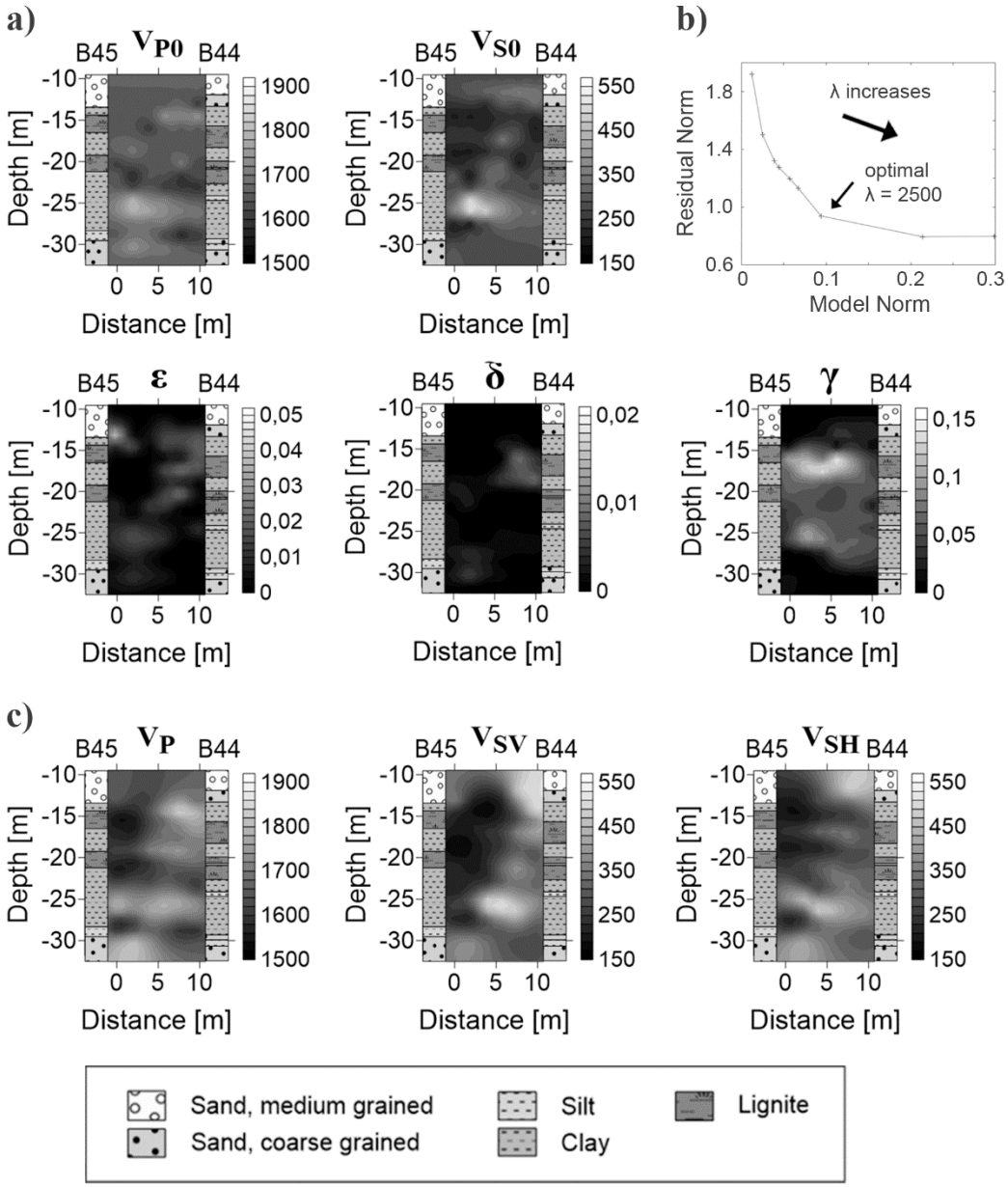


Figure 6.10: Joint-inversion for VTI parameters for tomographic Plane 2 (between boreholes B44 and B45) is shown in (a). We chose the cross-gradient parameter (λ = 2500) by trading off between the model norm and the residual norm for inversions with different values for λ (b). Separate isotropic inversions of the P-, SV- and SH-wave data is shown in (c).

6.6 Resolution

We determine the resolution of our VTI inversions by first conducting a checkerboard test (Spakman and Nolet, 1988; Rawlinson et al., 2014). We define two checkerboard models with the same acquisition geometry as Plane 2 of the SAFIRA dataset, consisting of the five VTI parameters Vp0, Vs0, ε, δ and γ. The first model is a coarse checkerboard with checker dimensions of approximately 3×3 m (Figure 6.11a) and the second model is a fine checkerboard with checker dimensions of approximately 1.5×1.5 m (Figure 6.12a). In both checkerboard models the P- and S-wave velocities vary by ±10% from the

average velocities. The anisotropy parameters vary in the same direction as the P- and S-wave velocities with ε and δ varying from 0.02 to 0.04 and γ varying from 0.08 to 0.12, which are similar to the anisotropy magnitudes we determined with the inversions (see Figure 6.9 and Figure 6.10). We use our forward raytracing algorithm to compute synthetic traveltimes and add normally distributed noise with a standard deviation equal to our measurement uncertainty estimates of 0.1 ms for the P-wave traveltimes and 1.0 ms for the S-wave traveltimes. We then reconstruct the checkerboard models with the same inversion algorithm that we used for the SAFIRA dataset. The reconstruction of the coarse checkerboard model (Figure 6.11b) shows that the structures are well resolved for the velocity fields Vp0 and Vs0. The resolution of the anisotropy parameters is lower, yet the general structures are still detectable. The recovered velocities and anisotropy parameters have a similar magnitude as the synthetic checkers (Figure 6.11a). The reconstruction of the fine checkerboard model (Figure 6.12b) shows that the structures are only partly resolved. In addition, the recovered S-wave velocities and the magnitudes of the recovered anisotropy parameters ε, δ and γ are inaccurate, with the recovered values either too high or too low. Thus, we estimate that our resolution is in the range of 3×3 m for the velocity fields Vp0 and Vs0 and slightly higher for the anisotropy parameters ε, δ and γ.

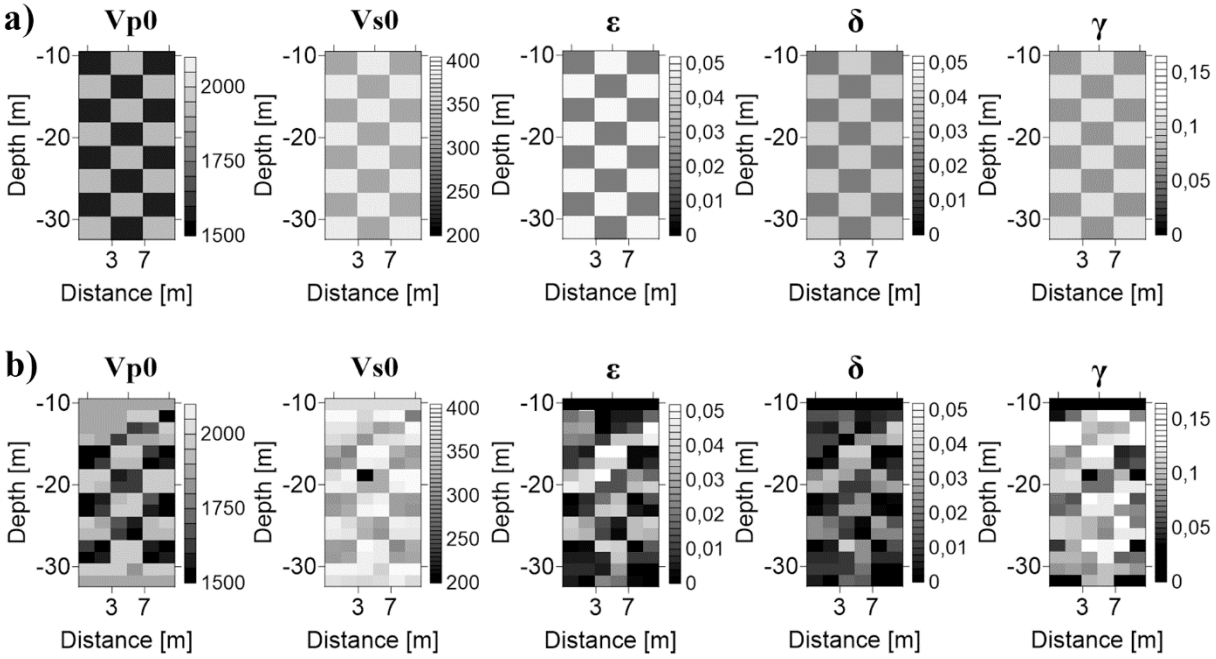


Figure 6.11: Coarse checkerboard VTI-model with approximately 3×3 m cell sizes (a) and the reconstructed model (b).

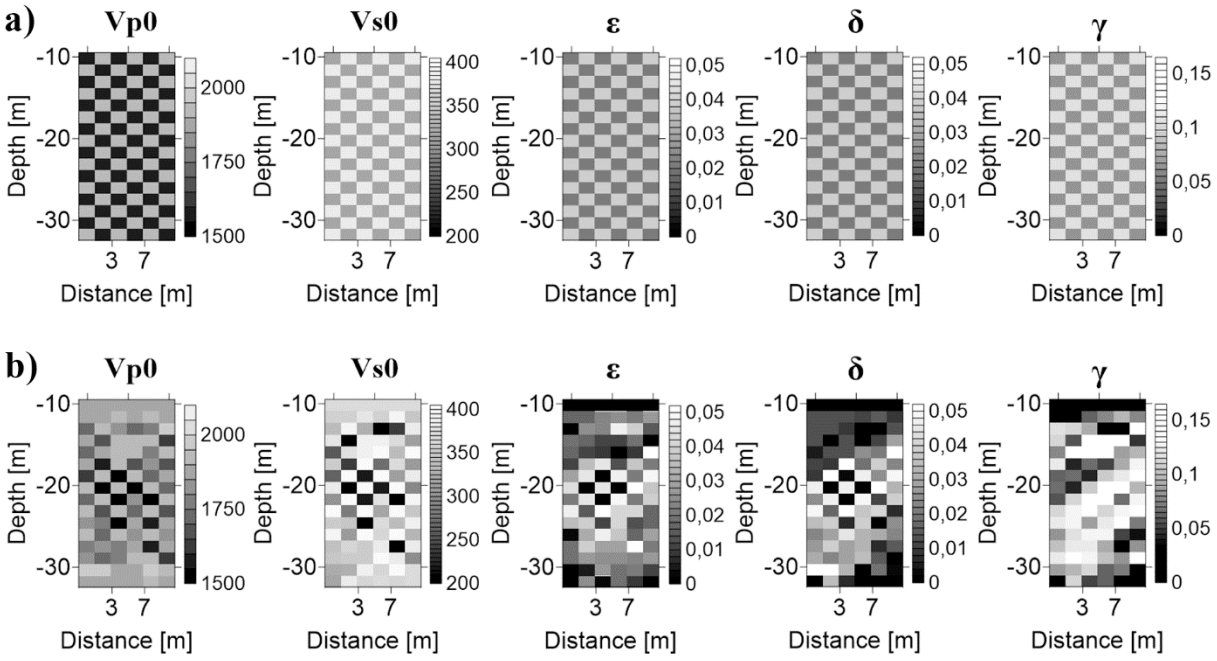


Figure 6.12: Fine checkerboard VTI-model with approximately 1.5×1.5 m cell sizes (a) and the reconstructed model (b).

Secondly, we infer the error of the inverted VTI parameters. To achieve this we randomly perturb the measured traveltimes, by adding normally distributed random noise with a standard deviation equal to our estimated measurement uncertainties (0.1 ms for the P-wave traveltimes and 1.0 ms for the S-wave traveltimes). Subsequently, we invert for the VTI parameters, using the same inversion parameters (number of iterations, magnitude of weighting parameters β and λ). Then we determine the error of the inversion by subtracting the result from the original inversion result (see Figure 6.9 and Figure 6.10). This procedure of adding random noise, inverting and determining the error is repeated 100 times for both tomographic Plane 1 and Plane 2. Finally, we determine a maximum absolute error as determined by two standard deviations, from the error distributions of the 100 different inversions (Figure 6.13). The maximum errors for the P- and S-wave velocities have maxima of approximately 80 m/s (maximum error of 5% for the P-wave and 40% for the S-wave). The maximum errors associated with the anisotropy parameter ε are approximately 0.02 for Plane 1 and 0.04 for Plane 2, while the errors associated with δ are close to zero. We suspect that the P-wave traveltimes, which are not affected by the anisotropy, constrain these errors for ε and δ. The SH-wave anisotropy parameter γ has the most amount of uncertainty, with maximum errors in the range of 0.03 and 0.06 for Plane 1 and Plane 2.

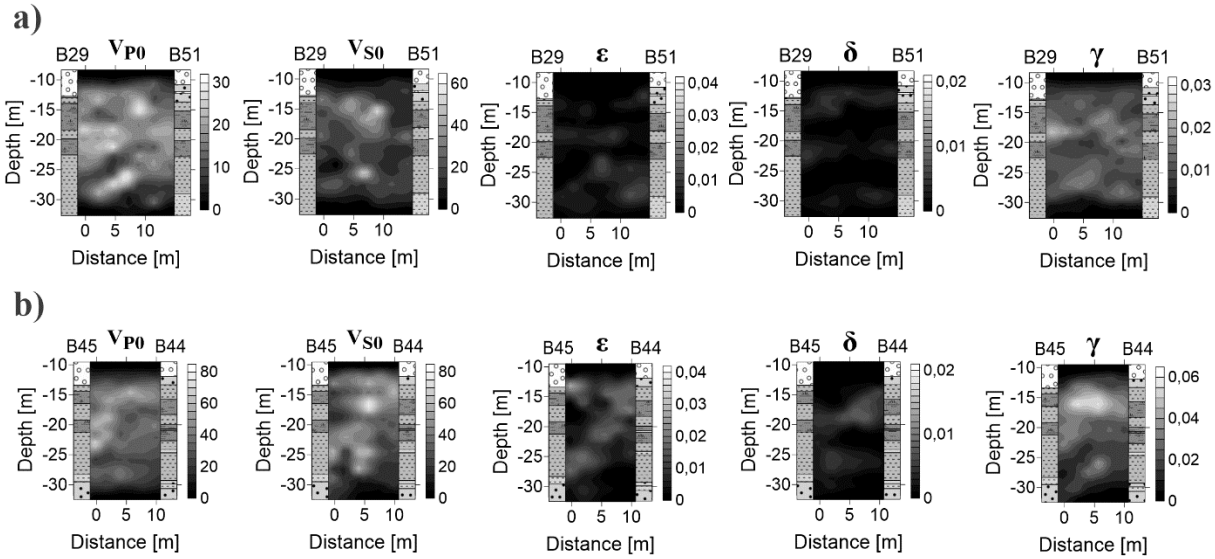


Figure 6.13: The absolute error estimated for the VTI parameters for Plane 1 (a) and Plane 2 (b). First, inversions were performed with perturbed traveltimes, i.e. normally distributed noise was added. Subsequently, an error was determined from the original inversion results (see Figure 6.9 and Figure 6.10). This procedure was repeated 100 times, i.e. 100 inversions with random errors. Finally, the absolute error is determined as two standard deviations from the error distributions.

6.7 Discussion

The goal of our study was to increase the information derived from cross-borehole seismic data for tomographic analysis by implementing directional energy sources that generate SV- and SH-waves, as well as analysis techniques that jointly invert P-, SV- and SH-wave data to estimate the anisotropy parameters. The estimates of resolution and error may be slightly understated, since Tsvankin and Grechka (2011) have shown that anisotropy parameters are generally not estimated with an accuracy higher than 0.04 to 0.05. Specifically, our estimated error for ε and δ may be higher. Nonetheless, the inversion suggests that the magnitudes of the anisotropy parameters ε and δ are generally close to zero with ε reaching magnitudes of 0.04 in a few isolated model cells (see Figure 6.9 and Figure 6.10). The checkerboard model reconstructions (see Figure 6.12) suggest that these isolated higher ε magnitudes are likely below the resolution limit and attributed to compensations of traveltime picking errors. In addition, there is no plausible geological explanation of such local ε maxima. It is thus probable that ε and δ are close to zero.

Such small ε and δ magnitudes indicate that the P-wave anisotropy is very weak and negligible. This is supported by the fact that the P-wave inversions with an isotropic assumption have a slightly lower error compared to the error associated with the P-wave inversions with an anisotropic assumption. The SV-wave anisotropy is also dependent on the magnitudes of ε and δ, which implies that the SV-wave anisotropy is weak as well. However, SV-wave anisotropy is controlled by $\sigma = (\mathrm{Vp0}/\mathrm{Vs0})^2(\varepsilon - \delta)$,

with the squared P- to S-wave velocity ratio playing an important role. In our near-surface environment the Vp/Vs ratio ranges from approximately 4 to 9. Even with very small ε and δ magnitudes, these high velocity ratios cause considerable SV-wave anisotropy. This effect is shown in Figure 6.14, where the angle dependent SV-wave velocity is shown in a homogeneously anisotropic medium for different Vp/Vs ratios. The P-wave velocity and the difference between ε and δ were kept constant at 1800 m/s and 0.01 respectively. For a Vp/Vs ratio of nine, the SV-wave velocity ranges from 200 to 240 m/s (20% difference), while for a Vp/Vs ratio of three, the SV-wave velocity ranges only from 600 to 613 (2% difference). Thus, at the SAFIRA site the SV-wave anisotropy is substantial, despite a negligible P-wave anisotropy.

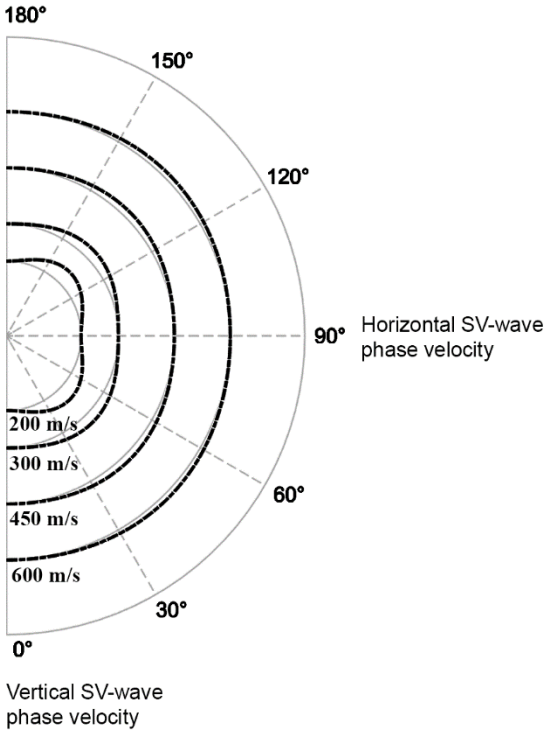


Figure 6.14: SV-wave velocity as a function of the raypath angle for different Vp/Vs ratios is shown. The P-wave velocity and the difference between ε and δ were kept constant at 1800 m/s and 0.01. High Vp/Vs ratios amplify SV-wave anisotropy severely, even if the anisotropy parameters ε and δ are small in magnitude.

The inversions for the SH-wave anisotropy parameter γ is in the range of 0.05 to 0.10 and 0.05 to 0.15 in the clay and lignite seams, with errors in the range of ± 0.03 and ± 0.06 for Plane 1 and Plane 2 respectively. The polarization analysis (see Figure 6.5 and Figure 6.6) and the initial anisotropy estimates (see Figure 6.8) confirmed such S-wave splitting. The differences in γ for the two tomographic planes could be due to the structural complexity or due to an azimuthal dependency of γ. In the latter case a VTI-model would no longer be applicable for the SAFIRA site, but rather an orthorhombic or lower symmetry model. However, the errors associated with the tomographic inversions do not make it

possible to determine whether γ is dependent on the azimuthal angle. Since the two tomographic planes have different azimuthal alignments (difference in 50°), an azimuthal dependence may be possible. However, more cross-borehole measurements with varying acquisition plane azimuths would be needed to determine such a dependence.

The accuracy of our inversions for anisotropy parameters may also be influenced by other factors such as slightly dipping geological layers, foliation or fractures. Nonetheless, we generated anisotropic tomograms with significantly lower S-wave residuals compared to their corresponding isotropic tomograms. This occurrence of S-wave splitting requires an anisotropic material. Therefore, it was sensible to invert for all VTI parameters and not only for the SH-wave anisotropy parameter γ. The advantage of inverting for all VTI parameters is a higher certainty that ε and δ are close to zero and that the material is in fact isotropic with respect to the P-wave, yet anisotropic with respect to the S-wave.

For consolidated rocks (depths > 3000 m), there is a linear relationship, with a correlation coefficient of approximately 0.75, between the P-wave anisotropy parameter ε and the SH-wave anisotropy parameter γ (Wang, 2002). However, in our anisotropic models, there is a significant difference between the two parameters, with $\varepsilon \approx 0$ and $\gamma \approx 0.5$ to 0.15, which may be explained by the soft sedimentary (sand and clay) material. Performing laboratory tests of anisotropy parameters for saturated sands and clays in the near-surface environment is challenging, since the same stress environment needs to be re-created or preserved (Clayton, 2011). While S-wave velocity measurements are frequently carried out to determine the shear stiffness because of its geotechnical importance (Mayne, 2001), a joint-measurement of P-, SV- and SH-wave velocities is conducted less often (e.g. Mackens et al., 2017). We are not aware of published work addressing P- and S-wave anisotropy in a saturated near-surface (depth < 50 m) environment.

We suspect that the anisotropy is primarily caused by the clay minerals and the anisotropic stress environment (differences in vertical to horizontal stress). Due to the high Vp/Vs ratio, we believe that the stress-induced anisotropy could have a much larger effect on the S-wave compared to the P-wave. This arises from the consideration that the S-wave amplitude is inversely proportional to the material stiffness. Thus, in a low-stiffness near-surface environment, the high S-wave amplitudes could facilitate such a higher sensitivity to the stress environment, compared to a low amplitude P-wave. The dynamic range of the P-wave velocities (velocity range of 1600 to 1800 m/s or a difference of $\pm$5% from the average) compared to the dynamic range of the S-wave velocities (velocity range of 140 to 420 m/s, or a difference of $\pm$50% from the average) support this.

6.8 Conclusions

We performed a joint-inversion for anisotropy parameters for both a synthetic and a real dataset consisting of jointly measured P-, SV- and SH-wave traveltimes for two tomographic planes at the SAFIRA site. The inversion algorithm we used in this study is based on the traveltime perturbation equation and utilizes cross-gradient constraints to ensure structural similarity of the resulting VTI parameters. The inversion and error analysis shows that ε and δ are likely close to zero, indicating that the P-wave anisotropy is negligible. Despite the low estimated magnitudes for ε and δ, the high Vp/Vs ratio of up to nine causes considerable SV-wave anisotropy. The SH-wave anisotropy parameter γ suggests magnitudes of 0.05 to 0.15 in the lignite and clay zones. This S-wave splitting into an SV- and SH-wave was confirmed with a polarization analysis. In addition, the S-wave residuals are lower for the jointly inverted VTI-model compared to separate inversions using only SV- or SH-waves. The high magnitudes of the SH-wave anisotropy parameter γ compared to very low magnitudes of the P-wave anisotropy parameter ε are unusual but may be common in near-surface environments, where the S-wave may be much more sensitive to stress-induced anisotropy than the P-wave. S-wave measurements may thus be well suited for 4D monitoring of remediation sites in near-surface environments.

7. PUBLICATION V: POST-STACK DENOISING OF LEGACY REFLECTION SEISMIC DATA: IMPLICATIONS FOR COALBED METHANE EXPLORATION, KALAHARI KAROO BASIN, BOTSWANA

7.1 Abstract

We have recovered legacy 2D seismic data from the Kalahari Karoo Basin, Botswana, which show signatures associated with the coalbed-methane-bearing seams of the Mmamabula and Morupule Formations. These deeply buried coal seams (~ 500 m below surface) may represent a new alternative source of energy for the region. Prior to interpreting the seismic data, we have improved the imaging of the coal seams by attenuating noise with the curvelet transform. The data were transformed to the curvelet domain, and scale and angular direction thresholds were selected and applied, thereby removing previous processing artefacts and noise. The resulting denoised seismic data are characterized by high signal-to-noise ratio, showing a clear continuity of the seismic reflections associated with the coal seams. We constrained the seismic interpretation with borehole logs, which confirmed the locations of the coal sequence at the top of the Mmamabula and Morupule Formations. The curvelet-denoised seismic sections enable a more reliable mapping of the coal zone, which is displaced by major faults with throws of up to ~ 500 m. Following these encouraging results, we emphasized the value of enhancing and reinterpreting legacy data, as it is a cost-effective and environmentally-friendly method for deep coal seam and mineral exploration.

7.2 Introduction

The Central Kalahari Karoo Basin of Botswana has been estimated to contain about 5.6 trillion cubic meters (Tcm) of coalbed methane (CBM) reserves (Advanced Resources International, 2003). Recoverable reserves are estimated at 1.7 Tcm with some of the most prospective areas found in the eastern portions of the basin (Advanced Resources International, 2008). These estimates came from a number of boreholes drilled into the coalbeds of the basin (Hildebrand et al., 2009; Milkov et al., 2017). The natural gas resource is envisaged to offer great potential as an alternative fuel for future power generation, transport and industry. During the 1970s, a reconnaissance aeromagnetic survey and geological mapping of Botswana was undertaken to outline the depth and structure of the basement rocks (Figure 1) (Reeves, 1978). The purpose of the survey and interpretation was also to determine the nature and thickness of the overlying Kalahari Group and Karoo Supergroup. Shell Coal Botswana carried out a reconnaissance drilling program in the Ncojane area, southwest Botswana during the late 1970s with the purpose of investigating the possible coal potential of this relatively unknown part of the Karoo sequence (Clark et al., 1986). This was followed by "The Kalahari Drilling Project" (1981-1982) in western and northern Botswana, where several boreholes were drilled, most of which penetrated the Karoo sequence and confirmed the existence of a relatively continuous coal-bearing Karoo sequence throughout western Botswana (Meixner and Peart, 1984). In addition, Advanced Resources International

in association with Scales Associates and the Department of Geological Survey of Botswana undertook preliminary CBM studies between 2001 and 2003. The main study investigated the availability and potential for development of natural gas resources associated with the coal-bearing sequences of the Kalahari Karoo Basin (Advanced Resources International, 2003). The major findings of these studies indicated considerable coalbed methane and shale gas resources in the eastern and northern part of the Kalahari Karoo Basin.

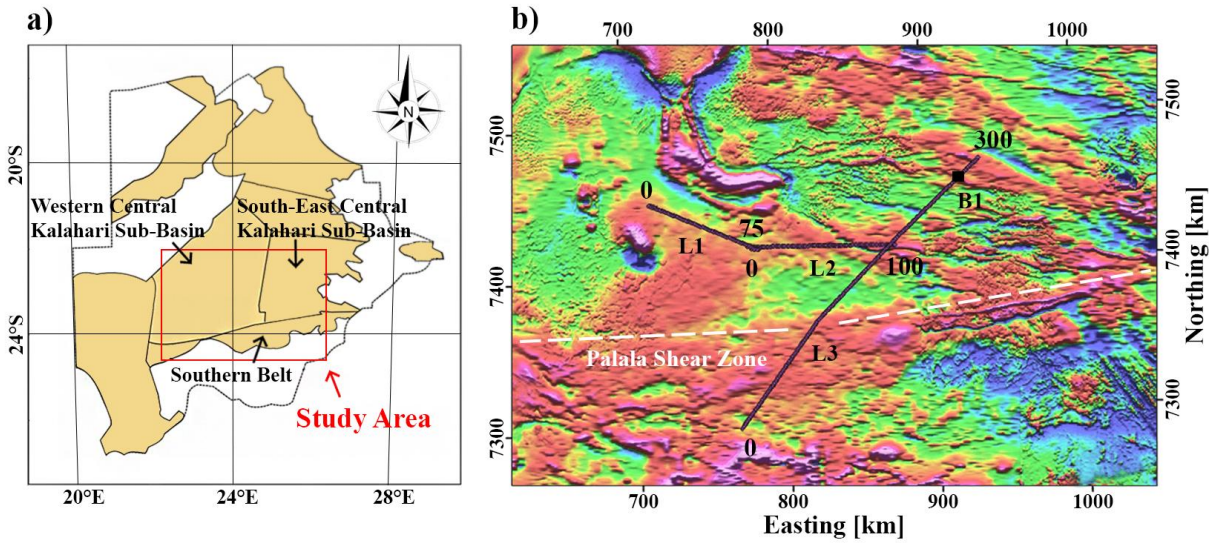


Figure 7.1: The distribution of the Kalahari Karoo Basin in Botswana (a) is shown in light yellow (modified from Smith, 1984). The location of the seismic lines (L1, L2, L3) and borehole B1 are superimposed on the regional total intensity magnetic map (b), Courtesy of the Council for Geosciences of South Africa. The distances along the lines are indicated in kilometres, e.g. line L1 ends at 75 km.

Although magnetic surveys and drilling were effective in the delineation of subsurface structures such as dikes and major faults, they were unable to map the structure of deeply buried strata in detail, which is critical for coalbed methane exploration. It was envisaged that an integrated exploration approach involving geological mapping, magnetic survey, drilling and high-resolution seismic surveys, will likely yield the best results. The reflection seismic method, in particular, has become an important tool to help unravel structures hosting coal deposits at great depth. This study demonstrates how legacy reflection seismic data, initially acquired for gold exploration, have been successfully used to explore for some of the world's largest, deeply buried coal deposits in Botswana and map the gross structural architecture that controlled these deposits.

The reflection seismic method had its origin in the oil industry in the 1960s, where it was used to locate oil and gas reservoirs in sedimentary rocks. Over the past few decades, the method has been actively used for coal exploration, mine planning and safety (Krey et al., 1982; Goossens and Buchanan, 1984; Gochioco, 1991; Tselentis and Paraskevopoulos, 2002; Prasad et al., 2015). For example, in the last 40

years numerous 2D and 3D seismic data have been acquired in Australia and the United State of America for coal mining operations and safety (Henson and Sexton, 1991; Urosevic et al., 1992; Gochioco, 2000; Walton et al., 2000; Gochioco et al., 2012).

The major advantage of using seismic data is its ability to produce a more continuous image of a target coal seam, which cannot be achieved via borehole drilling. Previous studies on seismic coal exploration demonstrated that coal seams typically show strong contrasts in acoustic impedance with respect to surrounding strata. These impedance contrasts are typically controlled by the low density and low velocity of the coal compared to surrounding strata (Gochioco et al., 2012). For young coals where the surrounding strata is poorly consolidated, the comparatively low velocity of the coal is responsible for the acoustic impedance contrast.

High-resolution 2D seismic data were acquired by AngloGold in the 1980s in the same area that is now known to host the CBM reserves. Figure 1 shows the location of three lines (L1, L2, and L3) in our study area, underlain by the regional magnetic map. The primary goal of these seismic surveys was to search for gold-bearing strata at depths below 2 to 4.5 km from surface, since gold-bearing units of the Witwatersrand Supergroup were expected to extend northwards underneath the Kalahari sedimentary cover. However, no gold-bearing conglomerate units were found beneath the Kalahari Karoo Basin. With the discovery of coalbed methane reserves, these legacy seismic data have been revisited to map and study the zones of coal seams in detail.

Unfortunately, the original seismic data were not optimally stored in the last four decades. With company mergers and frequent changes of personnel a lot of critical information has been lost. For example, the observer reports and headers of the raw data often omit crucial information such as the accurate location, which is common for legacy seismic data of Southern Africa (Terracin and Manzi, 2017). Often no information is provided at all, making the re-processing unfeasible. Nonetheless, the stacked seismic sections are available and can be used for a geological interpretation to complement the present boreholes. Since part of the study area now has become a National Park, acquisition of new data is difficult. This highlights the importance of enhancing and improving the quality of the legacy data. Since the early 2000s, global developments in the re-processing and interpretation of the legacy seismic data have made the technique increasingly effective to the point that it has become fundamental and a well-established method in the oil, gas and mineral exploration.

A multitude of post-stack processing procedures are available to improve the signal-to-noise ratio, from gain balancing and structurally conformal filtering (Khan et al., 2017) to random noise suppression via Wiener filtering (e.g. Canales, 1984; Jeng et al., 2008). One relatively new and promising development is the application of a multi-scale transform, called the curvelet transform, to seismic data (Hennenfent

and Herrmann, 2006). Application of the transform to the post-stack seismic data improves the data quality by attenuating both random and coherent noise. The developments of these denoising techniques make it worthwhile to reprocess and reinterpret legacy data to enhance the detection of economic resources, which is not possible with old conventional interpretation tools (e.g., amplitude display analysis, manual and autopicking of horizons). However, despite these developments, denoising techniques are underutilized in the coal environments and remains an unfamiliar technique to many geoscientists in coal exploration and mining. The latest development of curvelet transform is particularly interesting to Botswana's CBM exploration mining industry because it supports the quest to locate deeper CBM reservoirs, as well as any subtle geological structures that compartmentalize these targets, ahead of exploration planning and drilling.

In this case study, the curvelet-filtered seismic sections offer new insights into the seismic stratigraphy, the seismic reflectivity of the thin coal seams, and the timing of fault activity in the Kalahari Karoo Basin, with significant implications for exploration for CBM resources. We first introduce the geologic setting of the coalbed methane reserves in the Kalahari Karoo Basin and the aspects of the legacy seismic dataset. We then describe the curvelet denoising procedure and show the results of such a denoising application to our dataset.

7.3 Geological Setting

The Kalahari Karoo Basin is known to host substantial CBM resources, many of which are currently located at great depths. These may become attractive to exploit in the future, depending on the oil price, technological developments and environmental limitations. The basin (Figure 1a) contains rocks that belong to the Late Carboniferous to Early Jurassic Karoo Supergroup, a predominantly clastic succession that is sub-divided into local formations in the various sub-regions and delineated mainly by basement topography and sedimentary facies changes (Brett et al., 2000; Bordy et al., 2010). The Karoo Supergroup is mainly covered by sediments of the Cenozoic Kalahari Group. The detailed stratigraphy of the Kalahari Karoo Basin is largely unknown and extensive sedimentological studies, to our knowledge, have not been published (Singletary et al., 2003). The Karoo Supergroup in the Kalahari Karoo Basin was deposited in relatively shallow depressions that resulted from the pre-existing relief of the rigid cratonic basement and syn-Karoo faulting (Brett et al., 2000). The Karoo Supergroup is sub-divided into several groups, namely the lower Dwyka, Ecca and Beaufort Groups and the upper Lebung and Stormberg Groups (Figure 2).

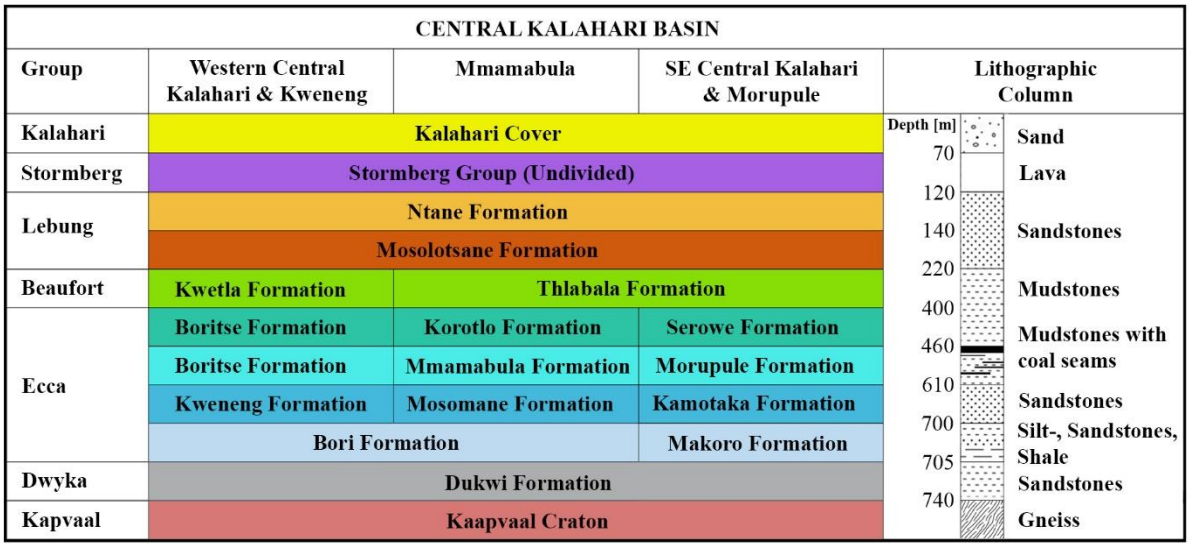


Figure 7.2: Stratigraphy of the Central Kalahari Karoo Basin, showing the lithographic depth column derived from borehole B1 (after Bordy et al., 2010).

The Permo-Carboniferous lower part of the Karoo Supergroup generally hosts glacial deposits of the Dwyka Group (diamictite and sandstone) followed by the marine to fluvio-deltaic rocks of the Ecca Group (Brett et al., 2000). The Ecca Group is coal-bearing in an otherwise carbonaceous mudstone and white, poorly-cemented arkosic sandstone environment (Cairncross, 2001). The succeeding Permo-Triassic succession is entirely non-marine, non-carbonaceous in nature (Beaufort Group, Tlhabala and Kwetla Formations: varicoloured to pale grey, non-carbonaceous mudstone, thin limestone and rare claystone). The Late Triassic–Early Jurassic upper Karoo contains the fluvial and aeolian strata of the Lebung Group (red mudstones, sandstones and medium- and coarse-grained, orange to white sandstones) and igneous units of the Stormberg Group (continental flood basalts and associated subvolcanic complexes) (Bordy et al., 2010).

Regional magnetic data (see Figure 7.1b) show the presence of many linear features, which are due to faulting, and deeper crustal structures. The most prominent of these lineaments is the Palala–Zoetfontein shear zone, which separates two Archean provinces, viz. the Kaapvaal and the Zimbabwe Province (Schaller et al., 1999). The faulting affects the vertical position of the coal seams and thus prior imaging is critical before planning exploration wells for CBM resources.

7.4 Legacy Seismic Data

The legacy seismic data covering the area of interest were acquired and processed by AngloGold in the 1980s and 1990s, producing final post-stack migrated seismic profiles that exhibit strong seismic reflectivity for shallow (< 1000 m) and deep targets (> 1000 m). The seismic data encompasses three 2D lines (L1, L2, and L3) and span a length of approximately 80 km for L1, 100 km for L2, and 300 km

for L3. Lines 1 and 2 are orientated approximately East-West, while line L3 runs North-South. Key acquisition parameters are listed in Table 7.1.

Table 7.1: Data acquisition parameters of the 2D CBM Botswana dataset

Survey parameters	**Line 1**	**Line 2**	**Line 3**
Type of survey	2D	2D	2D
Year	1989	1988	1989
Total survey length	75 km	100 km	300 km
Line direction	NW-SE	E-W	SW-NE
Spread type	Symmetrical split spread in the middle	Asymmetrical split spread at the ends of the lines	Symmetrical split spread in the middle
Offset range	-	-	End on: near offset = 150 m, far offset = 2500 m
Nominal fold	40	50	60
Recording system			
Recording device	SN 338	SN 338	SN 338
Sampling rate	4 ms	4 ms	4 ms
Recording length	6 s	6 s	6 s
Sweep length	24 s	24 s	24 s
Sweep	10 – 90 Hz	10 – 68.5 Hz	10 – 48 Hz
Source information			
Source spacing	50 m	50 m	50 m
Energy source	1 vibrator (Pelton Mk II)	3 vibrators (Pelton Mk II) in a line	1 vibrator (Pelton Mk II)
Receiver information			
Receiver spacing	25 m	25 m	25 m
Receiver/trace	6	6	6
Geophone type	10 Hz (GSC 20D)	10 Hz (GSC 20D)	10 Hz (GSC 20D)

Aspects of the seismic design that were appropriate for assessing the resolution at primary target depths include the source and receiver station intervals (SI, RI) along acquisition lines, source type and dominant frequency of the data. The following parameters are relevant to the resolution of the legacy data and are summarised in Table 7.2: The acquisition (SI: 50 m; RI: 25 m; sweep frequency: 24 s; 10-90 Hz (L1), 10-68.5 Hz (L2), 10-48 Hz (L3)) using the Sercel SN 388 24-bit system (recorder) at a sampling rate of 4 ms and a 40,000 pound peak force of one or three vibrators ensured good signal strength and high quality of the seismic data.

The seismic data were passed through the standard workflow including field pre-processing and full processing. Field pre-processing, which provides brute stacks with elevation corrections, was done to

evaluate the quality of the data, estimate the signal-to-noise ratio (S/N), and to detect and remove erroneous and noisy traces. Full processing improved the S/N ratio through various pre-stack operations such as trace editing, gain recovery, linear noise removal, surface-consistent "spiking" deconvolution, zero-phase spectral whitening, trace balancing, velocity picking and a 70% stretch mute. Subsequent processing steps included the application of refraction statics, normal move-out correction, stacking, fx-deconvolution, amplitude equalization, finite-difference migration and time-to-depth conversion (Table 7.2). Post-stack, the seismic data are characterized by a seismic zero-phase wavelet with a dominant peak frequency of approximately 25 Hz for the three lines, an average velocity of 3300 m/s, and wavelength (λ) of approximately 132 m. According to the Widess (1973) criteria, the vertical resolvability limit (R) for these data is approximately equal to $R = \lambda /4 \approx 33$ m. The low frequency of the data is not surprising since the objective of the survey was to image deeply buried strata (2 to 4.5 km depths) to explore for gold-bearing horizons.

Other side effects of the original objective to image deeper in the crust are artefacts in the area of the coal reflector. These could be the result of a non-optimal choice in migration velocity, as well as intrinsic artefacts resulting from the migration algorithm itself. In addition, the stacked seismic data may suffer from pre-stack (i.e., filtering on shot gathers) processing artefacts. Thus the data had to be enhanced, prior to the interpretation of the coal-bearing upper 1.5 km. In this structurally-complex environment, we show that the curvelet transform proved exceptionally useful.

Table 7.2: Processing steps applied to L1-L3 reflection seismic legacy data prior to curvelet denoising

1	Data reformat (convert SEGD to SEG Y)
2	Geometry application (CDP bin 25 m)
3	Trace editing
4	First-break picking and statics
5	1st RMS velocity analysis (iterative)
6	NMO mute
7	Minimum phase conversion
8	Noise attenuation (Band pass filtering and Spectral whitening)
9	Amplitude recovery: spherical divergence correction
19	Amplitude versus offset gain correction
11	Surface consistent gain correction
12	Frequency/Amplitude dependent noise attenuation
13	Zero-phase surface consistent spiking deconvolution
14	1st pass residual static corrections (iterative)
15	2nd pass RMS velocity analysis (iterative)
16	2nd pass residual static corrections (iterative)
17	NMO correction, 70% stretch mute
18	Stack
19	fx-deconvolution
20	Amplitude equalization using data window
21	Migration (Finite Difference algorithms)
22	Curvelet denoising
23	Time-to-depth conversion (using constant velocity of 3300 m/s)

7.5 Curvelet Denoising

Curvelets, like wavelets, belong to the family of multi-resolution transforms, also referred to as multi-scale transforms, and have their origins in image denoising applications (Candès and Guo, 2002; Starck et al., 2002; Candès and Donoho, 2004). Similar to curvelets, seismic wavefronts are oscillatory in the direction of propagation and smooth along the front. Thus, curvelets resemble the seismic wavefronts locally (Hennenfent and Herrmann, 2006) and provide a useful transformation to sparsely represent seismic data with their continuous wavefronts and discontinuous edges. This sparsity characteristic can be exploited to denoise seismic data. Shan et al. (2009), in a study using synthetic data, showed that the denoising capability of curvelets is superior to 2D wavelets. The curvelet transform has proven very useful when applied to real data, especially in structurally-complex environments. For example, Neelamani et al. (2008) showed how curvelet denoising improved the quality of a post-stack 3D reflection seismic cube, which was acquired in a carbonate environment.

Mathematically, the curvelet transform is an approximation of n-dimensional data, with $n \geq 2$. The signal can then be represented by using a linear, weighted combination of curvelets (Neelamani et al., 2008)

$$f(x_1, \dots, x_n) = \sum_l \lambda_{l,f} C\,(x_1, \dots, x_n), \tag{6.30}$$

with the n-dimensional seismic data (f), the curvelet coefficients ($\lambda_{l,f}$) and the curvelet functions (C). For the simplest, 2D case, the curvelet functions (C) are oscillatory in one direction and smooth in the other. In the oscillatory direction, the curvelet function resembles a wavelet (usually the Meyer wavelet); and in the smooth direction, the curvelet is spatially defined by a Gaussian function. The relationship between their length and width is governed by the parabolic scaling relationship of length $\propto$ 2×width. They are thus anisotropic in their design, making them not only multi-scale, but also multi-directional. The spatial Gaussian constraint ensures a good localisation, in terms of the uncertainty theorem (e.g. Donoho and Stark, 1989), in both spatial- and frequency-space, i.e. the phase-space. An example of a single 2D curvelet in the spatial domain is shown in Figure 7.3a and b, and in the frequency domain in Figure 7.3c, which comes in the form of two angular wedges around the origin. This particular curvelet is of scale 3 (third inner square frame in the frequency domain) with an angular direction of approximately -45° (controlled by the angular wedges). Other scales are indicated by the Roman numerals, in this example from scale 1 to scale 5 (Figure 7.3c).

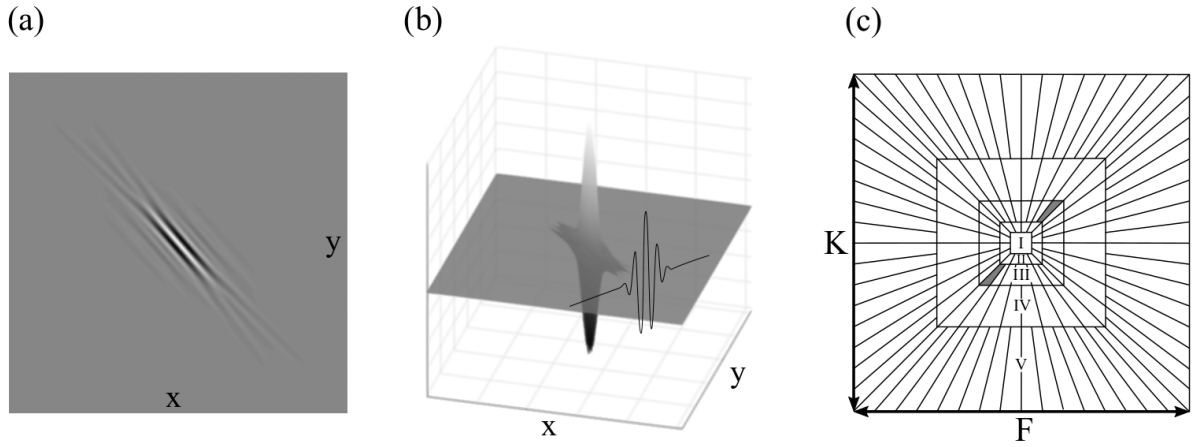


Figure 7.3: A curvelet is shown in the spatial domain (a). A different visualisation in the spatial domain is shown in (b), where a Gaussian function constrains the curvelet in the smooth direction and a wavelet constrains the curvelet in the oscillatory direction. The rapidly decaying amplitude of the curvelet in the spatial domain makes its localisation possible. The frequency domain of the curvelet has the form of two wedges around the origin (c). This curvelet is of scale 3, with the other scales indicated by Roman numerals, in this example from scale I to scale V. For every other scale, the number of angular wedges doubles (second dyadic coronae structure).

The number of angular wedges doubles for every other scale, which partitions the frequency domain into second dyadic coronae. Curvelets of higher scales are thus characterised by higher frequency or wavenumber components than lower scale curvelets. With the characteristic of different scales and

angular directions, a parallel can be drawn to an F-K filter, whereby different scales (curvelet domain) correspond to different frequencies (F-K domain) and different angular directions (curvelet domain) correspond to different wavenumbers (F-K domain). However, filtering in the curvelet domain has been more successful compared to filtering in the F-K domain (Naghizadeh and Sacchi, 2018), largely because of a better sparse approximation to the seismic data.

A seismic image can be represented by a combination of curvelets of different scales and angular directions. Figure 7.4 illustrates this principle of how the sum of different curvelet scales comprises a simple seismic image. To decompose the seismic image into the different scale contributions, a forward curvelet transform is applied to the data. Subsequently, the curvelet coefficients of all scales, except one, are thresholded, i.e. set to zero. Finally, the inverse curvelet transform is applied. The forward and inverse curvelet transform is based on the fast discrete curvelet transform code provided by the curvelab project (Candès et al., 2005).

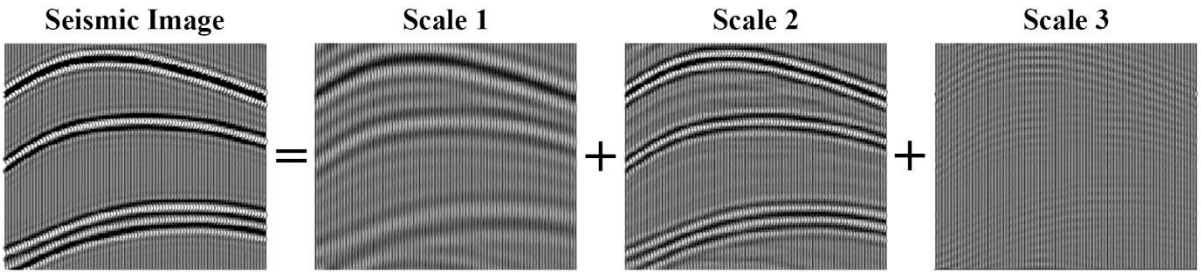


Figure 7.4: Example of a seismic image and its deconstruction into multi-scale curvelets.

We follow a similar approach to denoise our seismic data. We firstly perform a forward curvelet transform, secondly modify the curvelet coefficients by thresholding, and finally perform the inverse curvelet transform to obtain a denoised image. There are several methods to determine the thresholds and to decide which curvelet coefficients to keep (Górszczyk et al., 2014). In the simplest case, one would choose to keep a certain percentage of the highest amplitude curvelets and discard all others, i.e. set them to zero.

We used three criteria to perform denoising. Firstly, we threshold based on the highest curvelet coefficient amplitudes, in that we remove all coefficients that are below that threshold. For example, we rank the coefficients according to their amplitude and then keep a certain percentage, e.g. keep 10% of the highest amplitude coefficients. All other coefficients are set to zero. Since uncorrelated noise is usually lower in amplitude compared to reflection signal, this serves to denoise the data.

Secondly, we apply varying thresholds at different scales, as we have found that the reflections in a seismic section are usually represented very well by only a few curvelet scales. All other scales, e.g.

curvelets at the highest scale and with the highest frequency components, again predominantly represent uncorrelated noise. Thus, thresholding the higher scale curvelets more aggressively than the lower scale curvelets achieves a clearer image.

Lastly, we threshold based on angular direction to reduce coherent noise. The legacy seismic data we worked with was processed in the late 1980s, with the assumption that reflectors are near-horizontal. Thus, the post-stack finite-difference migration algorithm used does not faithfully image features with dips exceeding approximately 35° to 45° (Yilmaz, 1986, p. 277). Thus, setting curvelet coefficients with angular wedges in the range of 45° to 90° to zero, we can effectively remove steeply dipping artefacts and coherent noise, without compromising the quality of reflectors.

We test our denoising scheme on a subset of the Marmousi2 synthetic dataset (Martin et al., 2006) (Figure 7.5). We add different magnitudes (20%, 50% and 100%) of broadband white noise (Figure 7.6a-c) to the data subset and subsequently denoise using the curvelet transform (Figure 7.6d-f). The differences between the noisy and the denoised sections are shown in Figure 7.6g-i. We repeat this procedure for the Marmousi2 subset with added self-similar noise (Figure 7.7). In this context, self-similar means that the noise content has the same frequency response as the reflection seismic data. The frequency-wavenumber domains for the denoising of the Marmousi2 subset are shown in (Figure 7.8) and (Figure 7.9). The difference between the noisy data and the denoised data (Figure 7.6g-i and Figure 7.7g-i) shows that only uncorrelated noise is removed from the image, while the reflections are preserved.

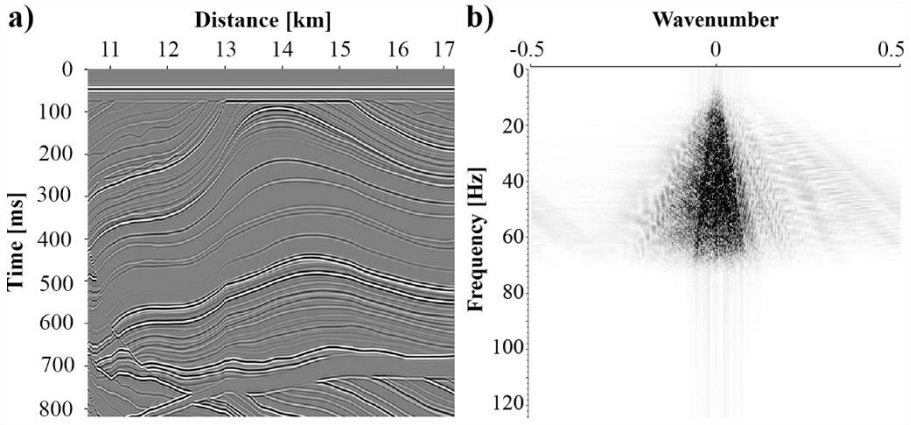


Figure 7.5: We use a subset of the Marmousi2 model (Martin et al., 2006) (a) with the frequency-wavenumber domain (b) is used to illustrate our curvelet denoising scheme.

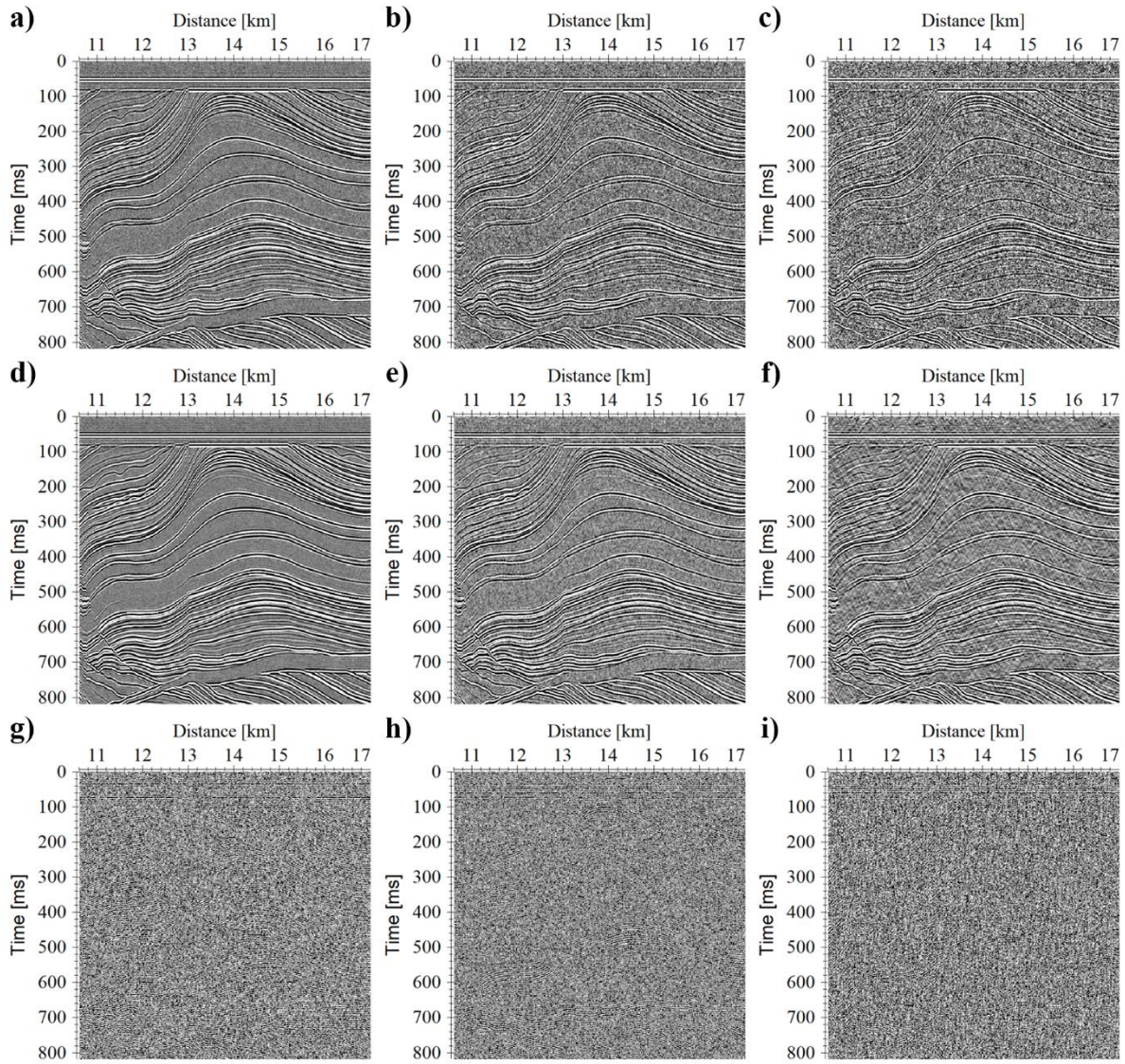


Figure 7.6: We add 20% (a), 50% (b) and 100% (c) broadband white noise to the Marmousi2 data subset (Fig. 7.5) and denoise using the curvelet transform, with 20% noise: (d), 50% noise: (e), 100% noise (f). The difference of the noisy datasets and the denoised datasets are shown in (g) to (i). The corresponding frequency-wavenumber domains are shown in Fig. 7.8.

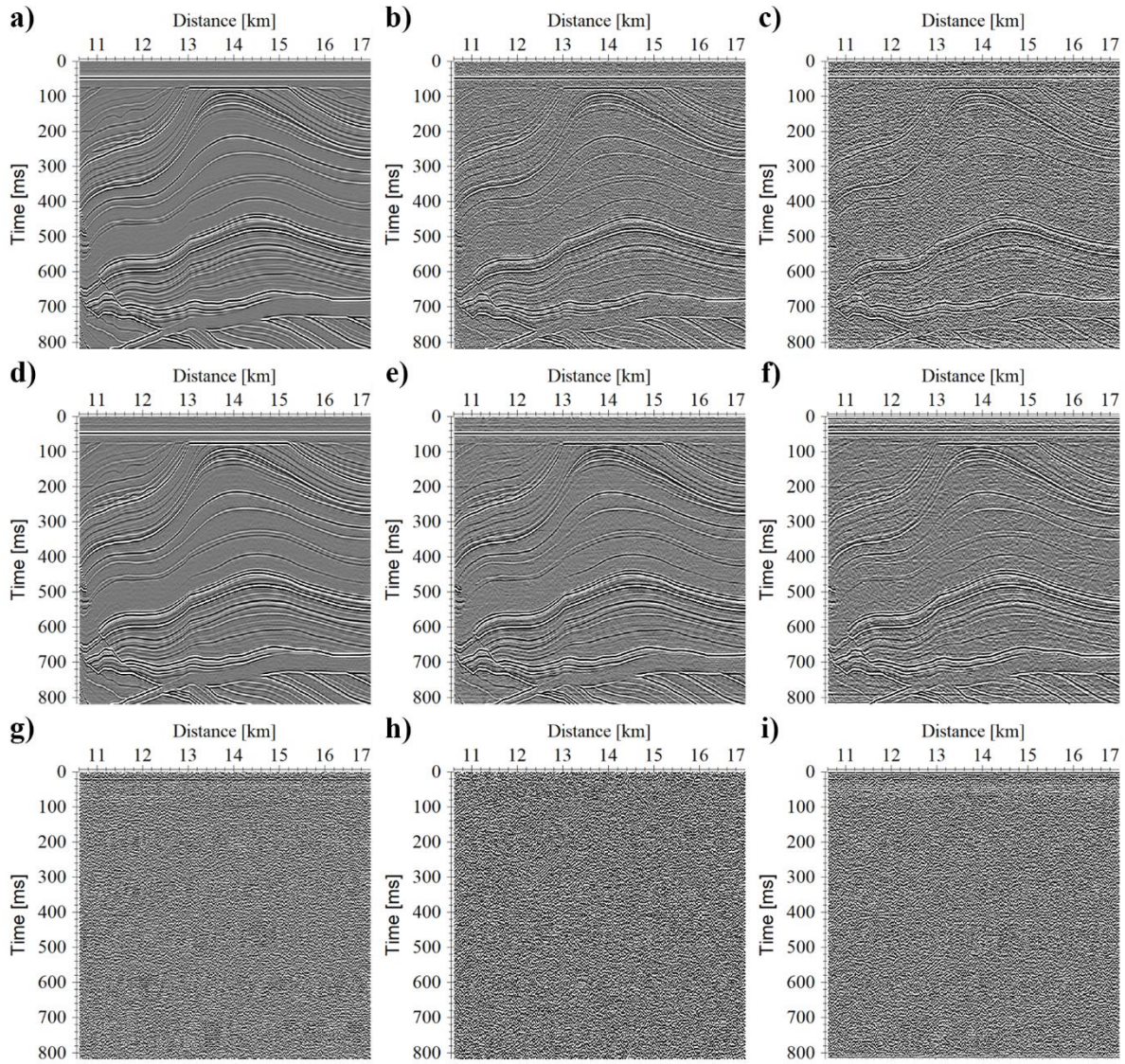


Figure 7.7: We add 20% (a), 50% (b) and 100% (c) self-similar noise to the Marmousi2 data subset (Fig. 7.5) and denoise using the curvelet transform, with 20% noise: (d), 50% noise: (e), 100% noise (f). The difference of the noisy datasets and the denoised datasets are shown in (g) to (i). The corresponding frequency-wavenumber domains are shown in Fig. 7.9.

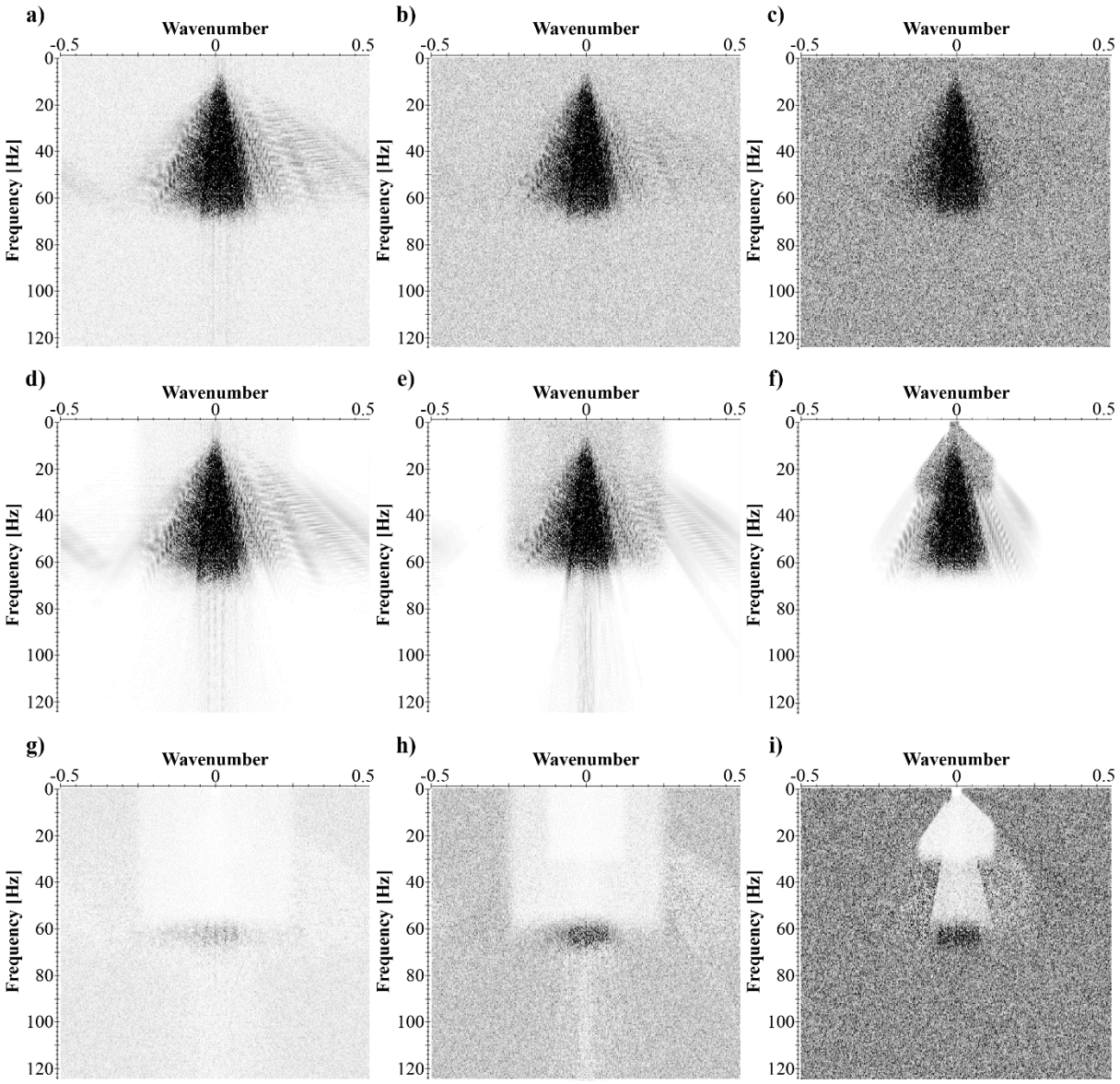


Figure 7.8: The frequency-wavenumber domains corresponding to the curvelet denoising applied to the Marmousi2 subset with added broadband white noise (Fig. 7.6).

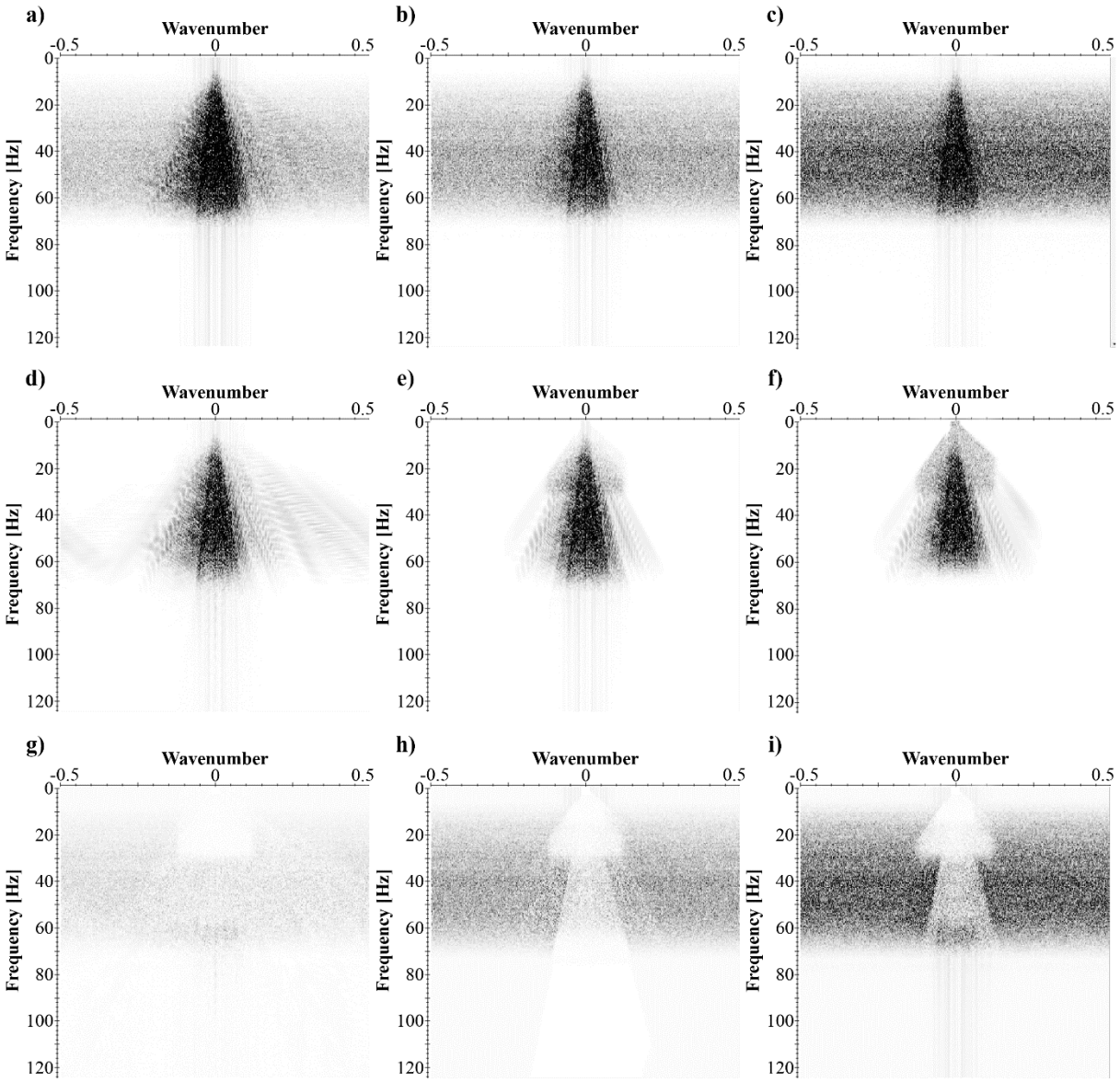


Figure 7.9: The frequency-wavenumber domains corresponding to the curvelet denoising applied to the Marmousi2 subset with added self-similar noise (Fig. 7.7).

The details of the denoising procedure are demonstrated in Figure 7.10, where the different curvelet scale and angular wedge contributions are shown. For visualisation purposes, we are using only four scales for the curvelet transform in this example. We see that the reflections can be represented using only curvelets of scale 2 (angular wedges from -45° to 45°) and scale 3 (angular wedges from -22.5° to 22.5°), highlighted in green. Less reflection energy is represented by curvelet domains highlighted by yellow (scale 1; scale 3 with angular wedges between -45° to -22.5° and 22.5° to 45°; and scale 4 with angular wedges between -22.5° to 22.5°). Thus, denoising would focus on removing curvelet coefficients of all the non-highlighted curvelet domains. The green and yellow highlighted curvelet domains would also be thresholded, e.g. keep 10% of the highest amplitude curvelets coefficients in the green domain and keep 5% of the highest amplitude coefficients in the yellow domain, prior to applying

the inverse transform and obtaining the final denoised image. Practically, we used more scales (6) and angular subdivisions (16 angular wedges for scale 2) in the denoising example (Figure 7.6). However, the principal denoising scheme and analysis remained the same.

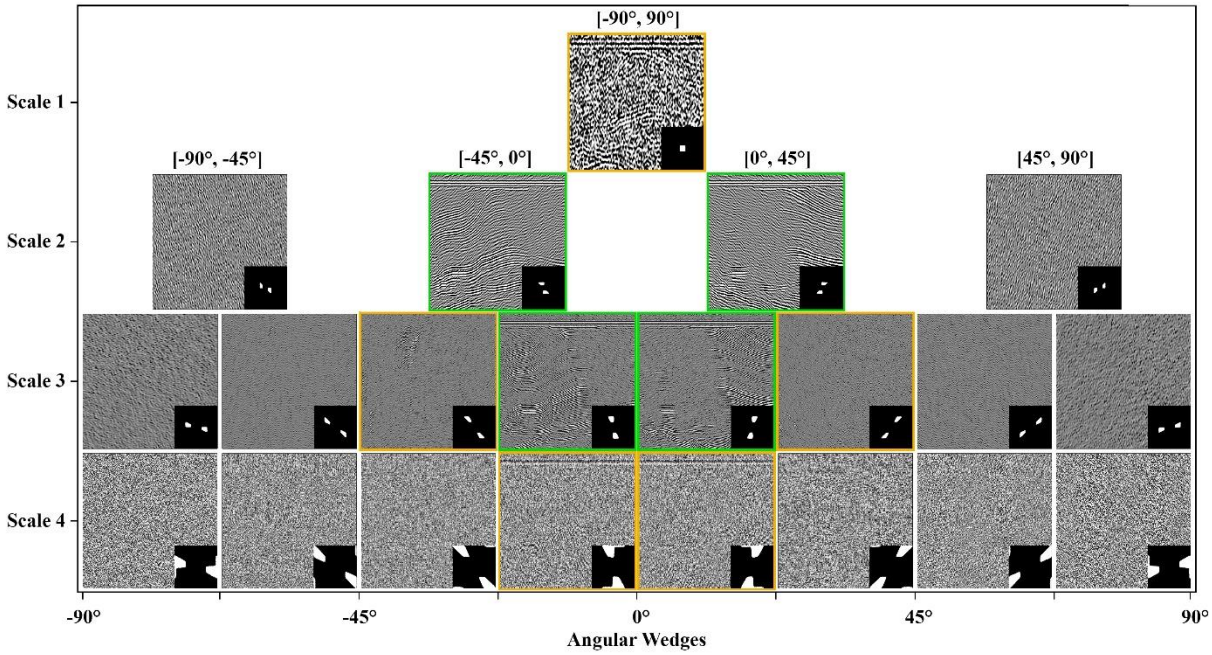


Figure 7.10: Example of the inverse curvelet transform applied to different scales and angular wedges. The reflection horizons of the Marmousi2 data subset can be best represented by scale 2 (angular wedges from -45° to 45°) and scale 3 (angular wedges from -22.5° to 22.5°), highlighted in green. Curvelets domains highlighted by yellow also have some reflection data. The f-k spectrum is shown in the bottom right corner of each inverse transform, where black is equal to zero, i.e. no energy content at these frequencies and wavenumbers.

7.6 Application to Legacy Coalbed Methane Dataset

In a similar fashion to the synthetic data (see Figure 7.6 and 7.7), we applied the curvelet transform to the 2D reflection seismic data from Botswana. We threshold the curvelet coefficients by keeping approximately 10% of the highest amplitude curvelets and removing steeply-dipping coherent noise, with a detailed area of a denoised migrated section shown in Figure 7.11. The denoised section (Figure 11b) shows that the potential migration artefacts, the effects of undermigrated data and the possible stacking of non-reflection events above the main coal reflector (Figure 7.11a) are effectively removed. This is also evident when viewing the difference between the denoised and original section (Figure 7.11c), which shows that both high-frequency incoherent noise, and steeply-dipping coherent noise are removed from the curvelet denoised section. We show the influence on the interpretation in Figures 7.12, 7.13 and 7.14. Reflections are more continuous after denoising, which is indicated by the white boxes and arrows in (Figures 7.12b and 7.13b).

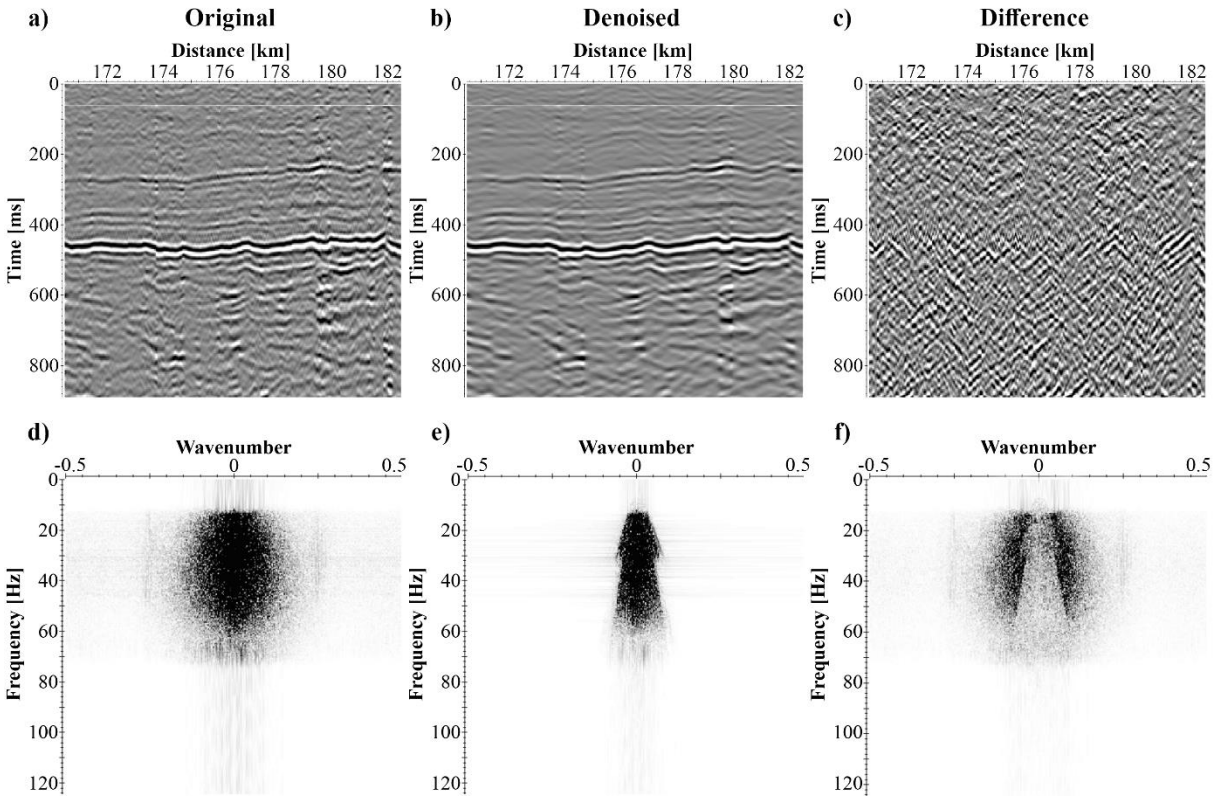


Figure 7.11: Curvelet denoising applied to the CBM Botswana dataset. The original data (a) is enhanced by curvelet denoising (b). The difference between the original and denoised data is shown in (c), which mainly consists of dipping events that interfere with the horizontal reflection horizons. The corresponding frequency-wavenumber domains are shown in (d) to (f).

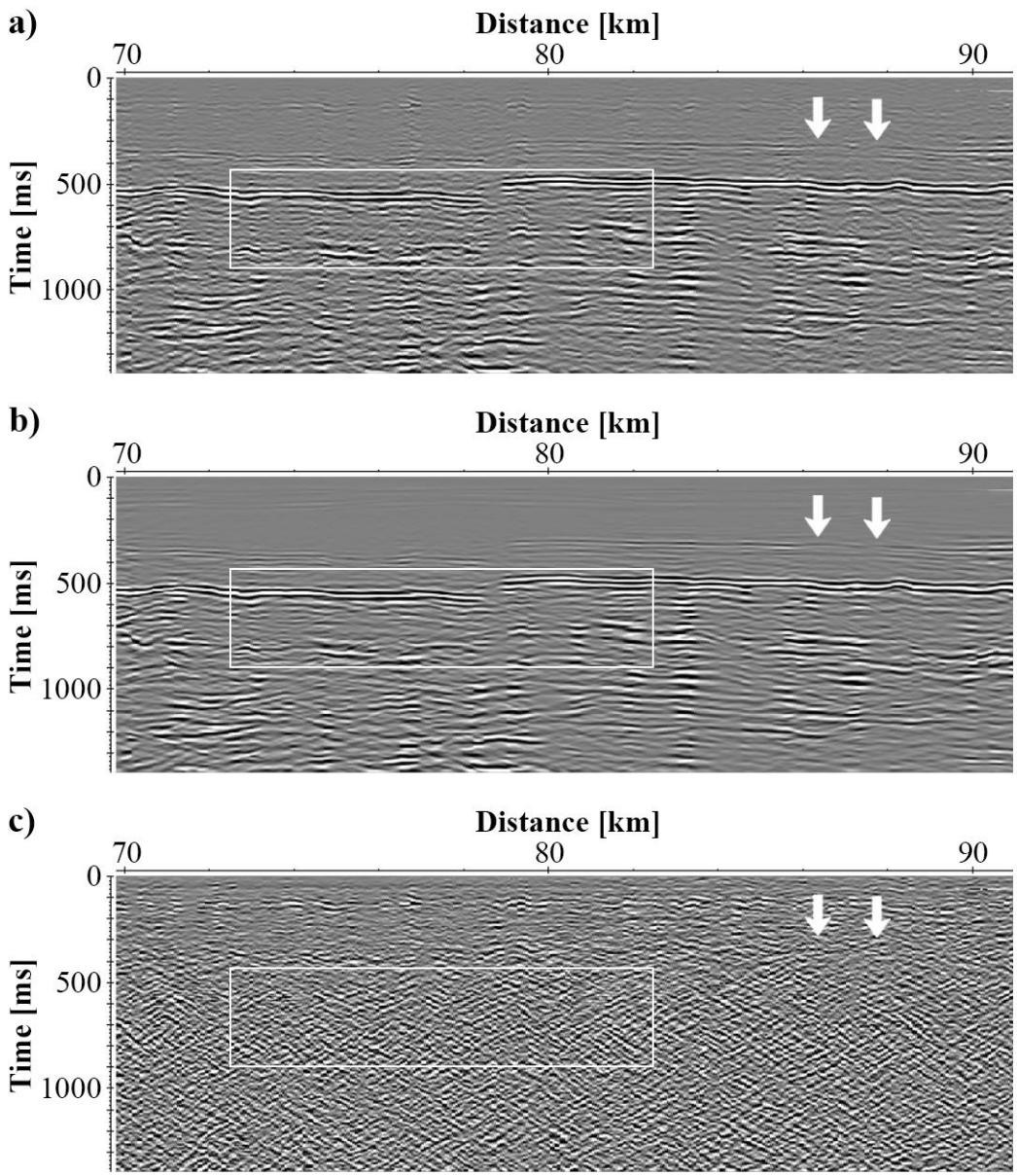


Figure 7.12: Improvements to interpretation after curvelet denoising applied to Line 2. The continuity of the reflections is enhanced after curvelet denoising (b), compared to the original stacked data (a). The difference between the original data and the denoised data is shown in (c). Attribute analysis of the data in the white box is shown in Fig. 7.14 (a) and (b).

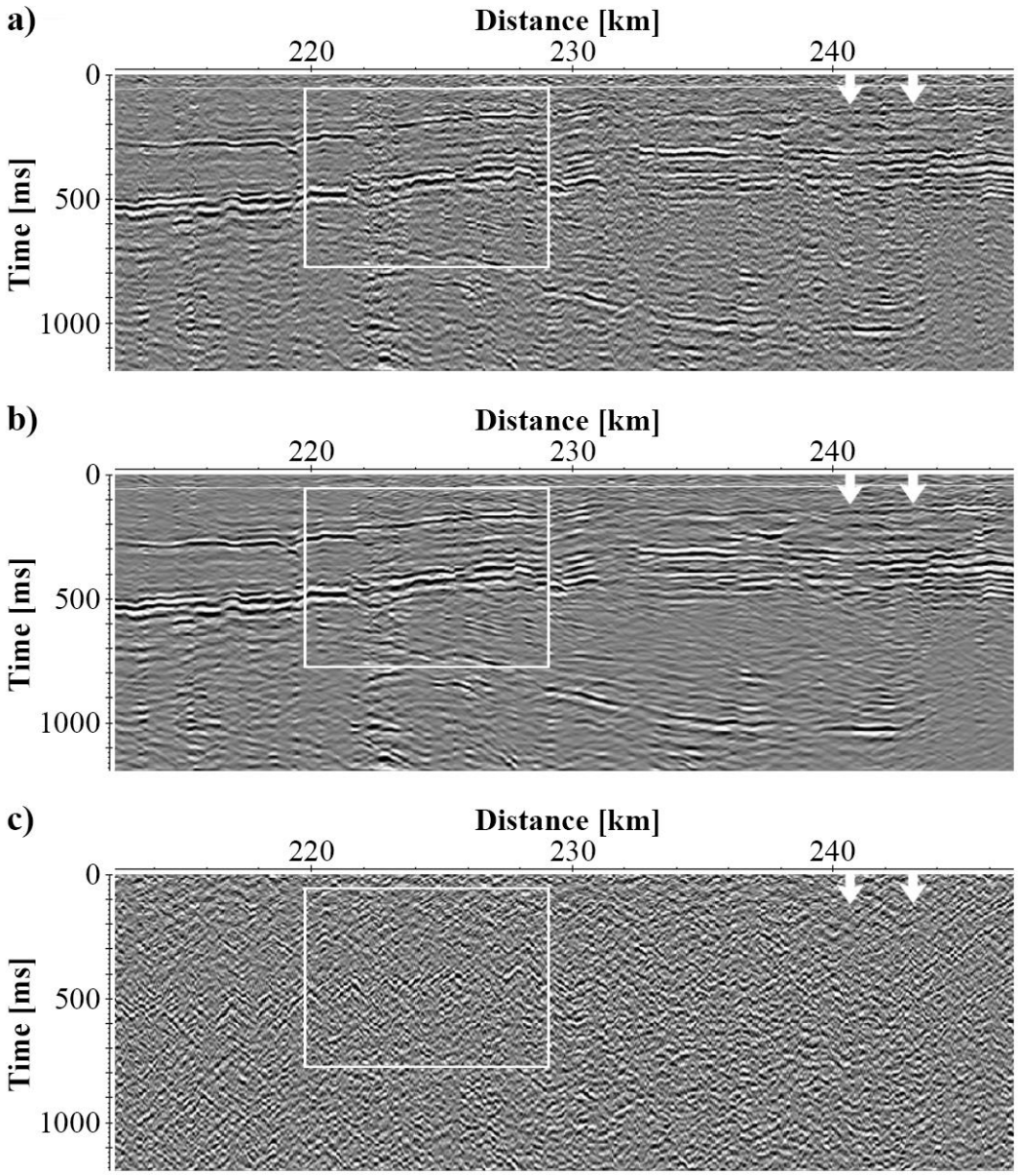


Figure 7.13: Curvelet denoising applied to the original data of Line 3 (a), with improvements shown after the denoising in (b). The difference between the original data and the denoised data is shown in (c). Both continuity (white arrows) can be enhanced and high frequency noise (white box) can be removed by applying the transform to the data, without compromising the quality of the reflection horizons. Attribute analysis of the data in the white box is shown in Fig. 7.14 (c) and (d).

To show the effectiveness of the curvelet denoising and the improved continuity of the reflection events, we computed the instantaneous phase, available in the Seismic Micro-Technology Kingdom Suite package, (Figure 7.14) of both the original and the denoised data in the white boxes (see Figure 7.12 and 13). Instantaneous phase is one of the instantaneous attributes (post-stack attributes), described by Taner (2001), which have been successfully used to enhance the quality of the seismic interpretations for both hard- and soft-rock reflection seismic data (Manzi et al., 2013). The instantaneous phase

attribute is measured from −180° to +180° and is derived from the complex seismic trace consisting of a real and an imaginary trace component (Taner and Sheriff, 1977). Firstly, we chose the instantaneous phase attribute because of its sensitivity to noise present in the seismic data. The computation of the instantaneous phase is independent of the trace reflection magnitude, which explains this sensitivity to noise. Secondly, we used the instantaneous phase to enhance the lateral continuity of reflections. Figure 7.14a-d shows some portions of the instantaneous phase displays of the original and denoised seismic sections for L2 and L3 (indicated as white boxes in Figures 7.12 and 7.13). It is evident that the instantaneous phase computed for the original data is contaminated by high noise spikes (indicated by black boxes) resulting from the low signal-to-noise ratio of the original data (Figures 7.14a, c). In contrast, the instantaneous phase displays for the denoised sections (Figure 7.14b, d) provide an improved resolution with less chaotic seismic events at both shallow and deeper parts of the sections (shown by black boxes). Furthermore, phase attributes computed for the original seismic sections (Figures 7.14a, c) exhibit more chaotic and less continuous reflection events (indicated by black arrows) than those observed in the phase displays computed for the denoised sections (Figure 7.14b, d). In addition, further inspection of the instantaneous phase displays for the denoised sections suggest that the attribute is able to highlight areas that are characterized by seismic wavelet interference due to stratigraphic terminations and complex faulting (see black arrows).

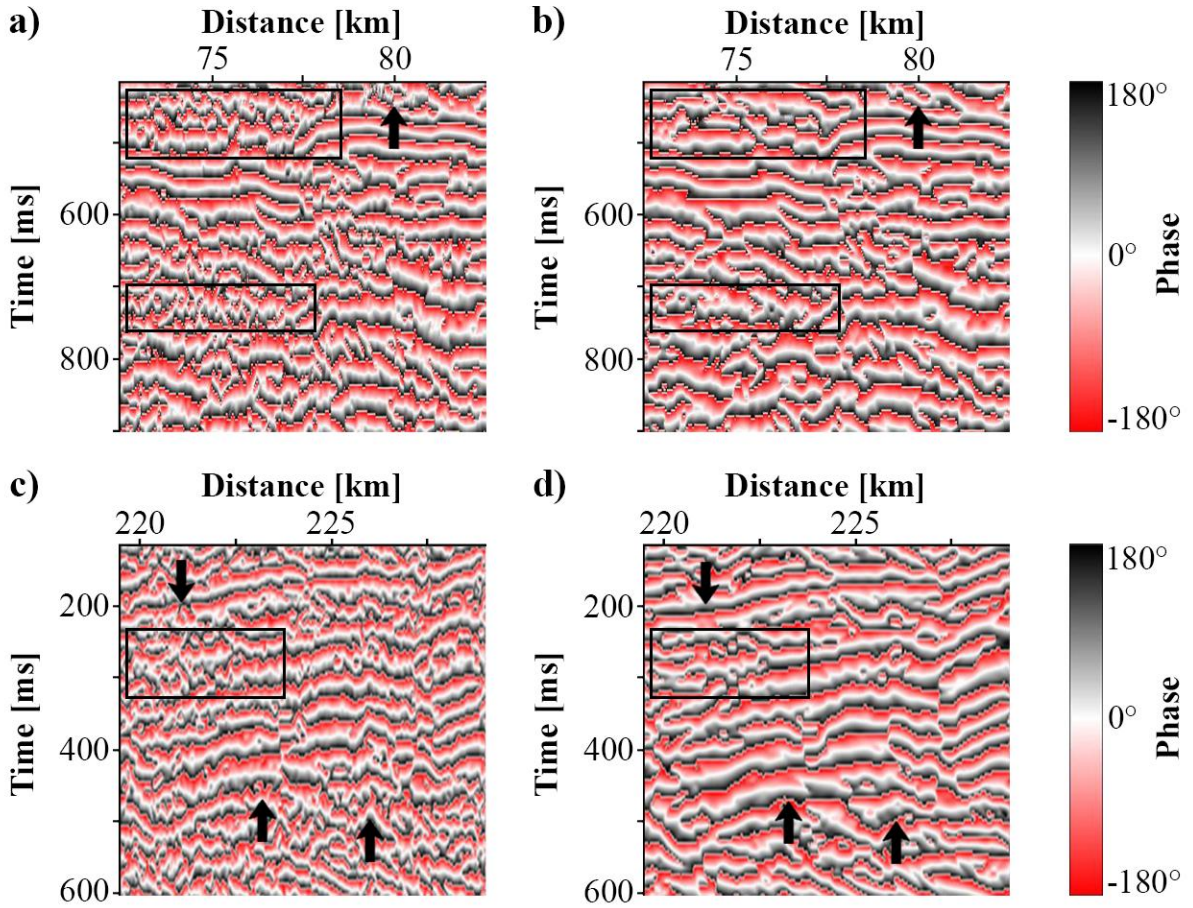


Figure 7.14: Instantaneous phase computed for a selection of Line 2 (a, b) and for a selection of Line 3. The selections are indicated by the white boxes in Fig. 7.12 (Line 2) and Fig. 7.13 (Line 3). The curvelet denoised sections (b, d) show better instantaneous phase continuities compared to the original data sections (a, c).

In the original data, shown in Figures 7.12a, 7.13a, 7.14a, c, it is not easy to verify whether or not these discontinuities represent real faults, and this may lead to misinterpretations. On the other hand, our results show that the application of the curvelet transform to legacy data can attenuate noise and preserve the continuity of the seismic events.

The interpretation of the denoised sections is shown in Figure 7.15. The interpreted seismic sections (Figure 7.15b, d, f) are based on the data of borehole B1, using a constant time-depth conversion with a velocity of 3300 m/s. Seismic reflectors correlating with the coal sequence and host stratigraphy were then interpreted on the 2D seismic profiles. In total, we interpret three distinct reflection horizons, which correspond to different sedimentological packages. The upper reflection corresponds to package P1, consisting of the Kalahari cover and the Stormberg Group. The impedance contrast between the overlying basalts of the Stormberg Group and the sandstones of the Ntane Formation cause the reflection horizon, which is not entirely continuous. For example, line L1, the western half of line L2 and the

southern half of line L3 do not show a reflection horizon from sedimentological package P1, which is likely caused by a thin Kalahari cover and basalt layer in those areas.

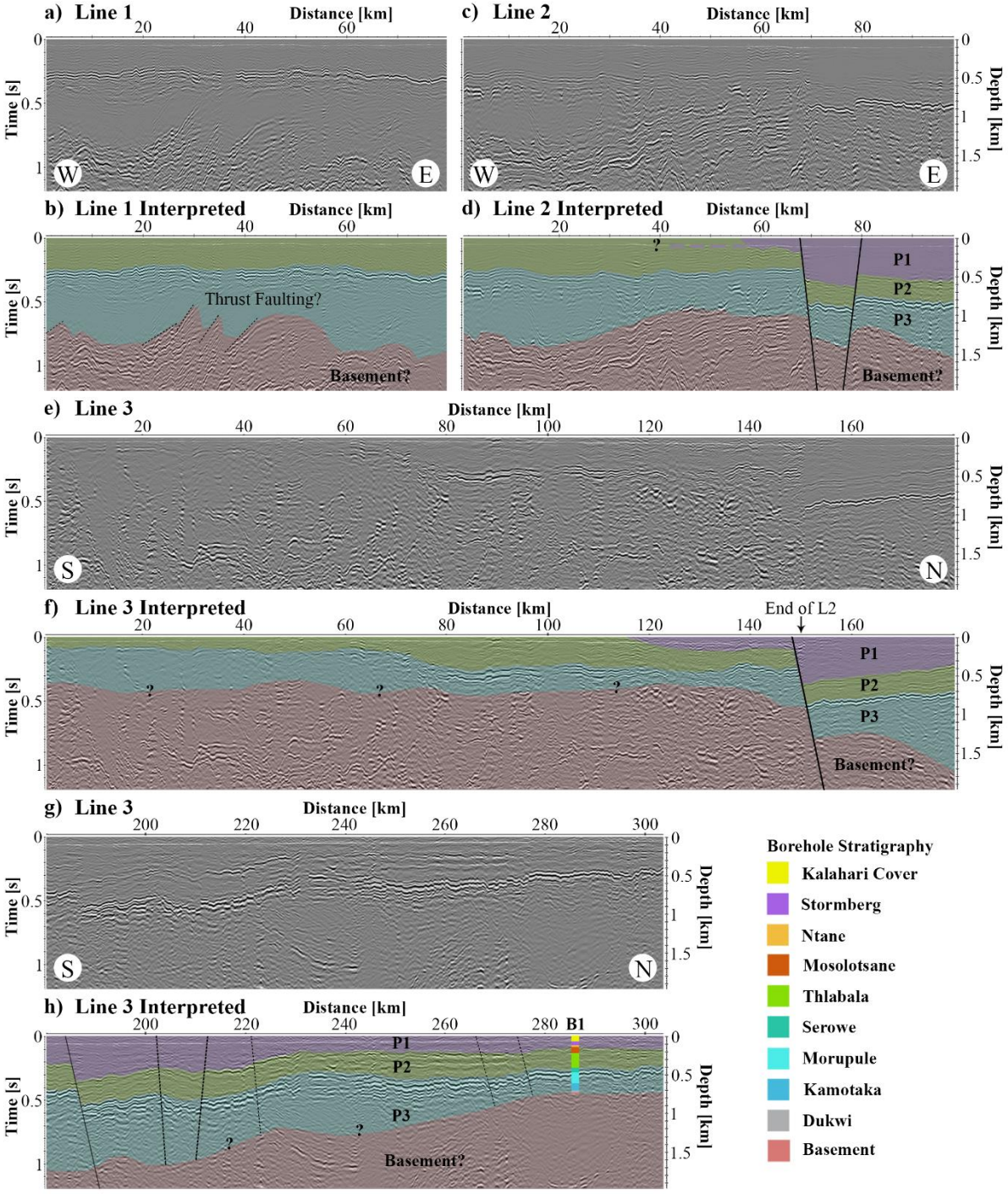


Figure 7.15: Stacked and denoised seismic sections for Lines 1 (a), 2 (c), and 3 (e, g) are shown, as well as the corresponding interpretations (b, d, f, h). The interpreted seismic sections comprise three distinct reflections, thereby enabling the division of the sections into three different sedimentological packages (P1, P2, P3) and underlying basement. Verified faults are indicated by a bold line and non-verified faults by a dotted line.

The second, and primary, reflector is due to the coal zone occurring in the top of the Mmamabula / Morupule Formations. A distinct change on the variable density display marks the strong seismic reflector. The reflector was traced as peaks on the seismic section, since we expected a decrease in acoustic impedance from the overlying high velocity sediments of the Mosolotsane Formation, to the relatively low velocity and density of the coal seams of the Mmamabula / Morupule Formations. We interpret the area between the upper reflector and the coal zone reflector as sedimentological package P2, consisting of the Ntane, Mosolotsane, Thlabala / Kwetla Formations and extending until the Serowe Formation.

Below, we see discontinuous reflections which could be caused by the cratonic basement. The very bottom of borehole B1 extends to the basement on line L3 (Figure 7.15h). However, due to the discontinuous, and partly low amplitude nature of the basement reflections, more boreholes are needed to constrain the position accurately on line L3. For lines L1 (Figure 7.15a, b) and line L2 (Figure 7.15c, d) the basement reflector is more identifiable, with possible thrust faulting occurring on line L1 (Figure 7.15a, b). However, the interpretation is only based on the single borehole B1 and we would need more boreholes to confirm the interpretation.

The interpreted sedimentological packages P1 to P3 show significant faulting in a post-coal depositional phase on lines L2 and L3, which crosscut and displace the coal sequence, with vertical displacements in the range of 20 m to 475 m. For example, the Palala-Zoetfontein fault is clearly visible on line L3 (bold black line on Figure 7.15f) at around 145 km along the profile with a throw of approximately 475 m. Another significant, yet different, normal fault with a throw of approximately 450 m is visible between 67 km to 80 km along the profile on line L2 (Figure 7.15d). Further non-verified normal faults are visible with smaller throws on line L3 (dotted lines. Line L1 does not show any significant faulting.

All the identified faulting affects the coal zone and could therefore be factored into the future CBM exploration and development. The seismic data show the benefit of delineating the faults and different CBM depths before commencement of further exploration drilling.

7.7 Discussion

Seismic methods have been used for coal and coalbed methane exploration for more than 20 years. Many case studies have demonstrated the ability of the method for imaging deep thin coal seams and structures that crosscut them. In particular, Eaton et al. (2010) and Malehmir et al. (2012) provide a comprehensive overview of key accomplishments from various mineral exploration projects, including coal, in Australia and around the world. Many examples provided clear images of coal seams at the subsurface despite varying geological conditions and different acquisition and processing parameters. All environments have their challenges but in the end, a successful utilisation of the method is dependent

on the quality of the final seismic images, from which a geological interpretation is then derived to direct drilling.

Denoising techniques using the curvelet transform, like many image-based filters, are sensitive to noise in the seismic data from which they are derived. The noise in data may be coherent or incoherent and have different sources. The noise tends to interfere with the thin coal reflections and complicate the seismic interpretations. For example, the dipping coherent noise can cause linear features on seismic sections, which are not easily distinguishable from real geological features. These interferences can be so strong that they make it almost impossible to clearly identify the actual geological structures. The cause for dipping coherent noise in the data is not known, but it is very likely that much of this noise is related to processing artefacts (such as velocity errors related to statics, NMO and migration, as well as possible remainders of surface waves and refracted waves prior to stacking) and acquisition footprints (such as those due to geometry, fold, azimuths and offsets). Migration velocity errors, in particular, can cause overlapping signals in the data.

We note that the denoising technique was applied on the image in the post-stack and post-migrated domain. It is thus important to realize that this technique is image-driven and is therefore sensitive to artefacts due to inadequate processing steps. More importantly, its computation is not based on the physics of wave propagation. We therefore envisage that the application of the curvelet transform to the shot gathers (if become available in the future) may provide much better images of the subsurface in our data. Nevertheless, our results suggest that curvelet transform denoising technique can be of great help to an interpreter of legacy data.

7.8 Conclusion

In this study, we have demonstrated that improving seismic images of the legacy seismic data acquired in complex geological setting covered by thick sediments is possible through the application of the latest post-stack processing algorithms. The existing 2D high-resolution legacy seismic data, initially acquired for gold exploration over the Kalahari Karoo Basin, has been re-examined and interpreted for CBM resources and reservoirs. We applied a curvelet denoising algorithm to the dataset to improve the post-stack imaging of shallow coal reflectors, located up to a depth of 1000 m. Initially these reflectors were poorly imaged due to a poor choice in migration velocity, migration artefacts, as well as incoherent noise. The subsequent interpretation has shown to be important in determining coal geometry and depth location, as well as the presence of faulting. Normal faults with throws of up to approximately 475 m have been identified. Since only very limited borehole data exists, this information will likely be factored into future CBM exploration and development for the security of Botswana's energy.

Although the acquisition and processing steps undertaken for Botswana 2D seismic data offered great advantages for accurate coal interpretation, the conventional interpretation techniques did not allow for exploitation of the data to its full potential. For example, coal continuity and subtle faults could not be easily recognized on the migrated seismic sections. To effectively characterise the coal seams in detail, new seismic data acquisition would be needed, employing modern technology such as high-resolution 3D acquisition, and broadband sweeps. However, denoising procedures using the curvelet transform proved to be an effective method for reducing noise and enhancing the detection of these features in the available legacy data. The depth position of the coal seams and orientation of structures (faults) that offset the coal seams were mapped with a high level of confidence.

8. CONCLUSIONS AND OUTLOOK

8.1 Conclusions

The main research goal of this thesis was to evaluate S-wave tomography in different geological settings and to find optimal processing parameters. The first two publications (Chapters 3 and 4) showed the general benefits of interpreting S-wave, in addition to P-wave, tomography data. In Publication I, different mechanical properties were derived, which aided the interpretation of a large weak zone prior to the construction of a large infrastructural project in Kuala Lumpur, Malaysia. Publication II, showed different measurement techniques to improve the quality of a regional S-wave velocity model in the Groningen gas field, the Netherlands, to improve the modelling of surface wave amplification factors, which are relevant for the regional reservoir-related seismicity. Particularly, S-wave tomography showed that the S-wave velocity is laterally highly variable, which was not obvious from the P-wave measurements on their own. To test the effects of S-wave polarisation and anisotropy, further tomography measurements were conducted at the SAFIRA research facility in Zeitz, Germany, where different directional seismic sources were employed. This lead to the generation of horizontally and vertically polarised S-waves, as well as P-waves. Thus three traveltime datasets with the same acquisition geometry had to be interpreted. In Publication III, I proposed a joint-inversion procedure that structurally coupled the S-wave traveltimes to the more accurate P-wave traveltimes. This produced better S-wave tomograms that were devoid of previous X-shaped artefacts, aided the interpretation in the hydrogeological near-surface environment, and could become a standard technique to more reliable estimate S-wave velocities. In Publication IV, I showed that the tri-axial recordings of the tomography data enables the detection of seismic anisotropy. I proposed an inversion procedure that estimated VTI parameters (Vp0, Vs0, ε, δ, γ) by jointly inverting for the P-, SV- and SH-wave traveltimes, while again ensuring structural similarity through the use of cross-gradient constraints. The results showed that anisotropy plays an important role in near-surface S-wave tomography data and, if disregarded, can severely distort the results. Publication V addressed a secondary research goal of this thesis, where the curvelet transform was applied to denoise reflection seismic data from the Kalahari-Karoo Basin, Botswana. The discovery of CBM resources lead to an increased interest in these legacy reflection seismic data and I showed that curvelet denoising is a valuable signal processing tool to increase the signal-to-noise ratio prior to the interpretation.

8.2 Outlook

Even though several advantages of S-wave tomography and curvelet denoising were discussed, there are still many possibilities for further research and improvements. Firstly, it would have been beneficial to estimate the P- and S-wave velocity by a joint-inversion approach in Publication I, instead of the individual inversions that were performed and then jointly interpreting these. By collecting data with an additional, vertical, source would have perhaps also enabled the direct inversion for the elastic

parameters. Further, discrete joint-inversions could have been performed, which were originally proposed for cavity detection (Musil et al., 2003) and may have been more suitable than smoothness constrained first-onset traveltime inversion as used in Publication I. Also hybrid joint inversion approaches using fuzzy clustering for linking inverse problems (e.g. Linder et al., 2010; Sun and Li, 2016), could have offered the possibility of discretely and jointly inverting the datasets with petrophysical constraints. In geological settings such as the one encountered in the Kuala Lumpur Limestone, with high-contrast anomalies and cavities, such petrophysically constrained fuzzy clustering approaches might be more promising than smoothness-constrained inversion or purely discrete inversions.

The inversion for anisotropy parameters discussed in Publication IV, suffered from a lack of resolution. Due to the increase in parameters the number of model cells had to be reduced. Otherwise the tomographic inversion problem would not have been overdetermined as required for a least-squares inversion. Adaptive or staggered grids (Vesnaver and Böhm, 2000) could provide a solution to this dilemma, by performing multiple inversions, every time with a slightly shifted grid. These different tomograms would then be combined to yield a tomogram of higher resolution. A different method to increase the resolution would be the use of a full waveform inversion (FWI) (Köhn, 2011, pp. 54-55; Lüth et al., 2014). This method uses the entire wavetrain, opposed to only the traveltimes. The IFOS2D project (Bohlen et al., 2016), from the University of Karlsruhe, offers such an inversion package and could be used in the future.

One of the main challenges I see with anisotropy parameter estimations is their uncertainty, since inaccuracies in traveltime picking will always be compensated by the anisotropy parameter estimates. In Publication IV, the uncertainty estimate was produced with the help of checkerboard tests, which have their limitations due to the use of the same parametrisation and the same forward solver to generate the synthetic dataset and to subsequently invert the data (Rawlinson et al., 2014). Using a Bayesian inversion approach (Giroux and Gloaguen, 2012) would be beneficial in determining the uncertainty, since the variance is a directly determined parameter in such a statistical inversion process. A Bayesian inversion approach could also be compared to a local-search smoothness constrained inversion to determine the variation in result and uncertainty.

Further, it would be interesting to compare the estimated anisotropy parameters with seismic laboratory measurements (e.g. Lee and Santamarina, 2004) of core logs. Unfortunately, no longer such core logs exist at the SAFIRA site. Thus, similar tomography measurements would have to be performed at a different test site. A different verification of anisotropy parameters could come from vertical seismic profiling measurements (VSP), since Tsvankin and Grechka (2011) showed that anisotropy parameters

can be estimated from such VSP surveys. These measurements could also be extended three-dimensionally and perhaps offer even more insight into additional anisotropy parameters.

S-wave tomography was performed in near-surface environments, with the geology consisting of mainly soft sediments (sands and clay) and to a lesser degree weathered rock (limestone). To further develop S-wave tomography it would be beneficial to test in hard-rock environments such as the deep Witwatersrand gold mines. Such a highly pressurized environment would likely produce wavefield effects related to anisotropy, scattering and dispersion that could possibly be used in imaging. Perhaps, even triplication points in SV-wavefields could be detected and utilised.

The curvelet transform was applied to post-stack reflection seismic images. However, ground-roll usually represents the biggest noise contribution for onshore reflection seismic surveys on land. Naghizadeh and Sacchi (2018) proposed a technique based on the curvelet transform to remove such ground-roll. Thus, the curvelet code of Publication V could be extended to handle pre-stack seismic data as well. This could provide very useful for future seismic surveys and the subsequent processing. Finally, different multi-resolution transforms, such as the shearlet transform (Easley et al., 2008), could be used for seismic noise reduction and compared to the employed curvelet transform.

9. REFERENCES

Advanced Resources International. 2003. Results of the central Kalahari Karoo Basin coalbed methane feasibility study, prepared for the Department of Geologic Survey, Botswana, Lobatse. Advanced Resources International, Arlington, Virginia, USA.

Advanced Resources International. 2008. Technical and economic feasibility study for coalbed methane development in eastern Botswana, prepared for Botswana Development Corporation and U.S. Trade and Development Agency. Advanced Resources International, Arlington, Virginia, USA.

Aki, K. 1957. Space and time spectra of stationary stochastic waves, with special reference to microtremors. Bulletin Earthquake Research Institute, University of Tokyo, 35, 415–457.

Al-Yahya, K. 1985. An iterative solution to seismic tomography. In: *Stanford Exploration Project: Report Number 42*: Stanford University, CA, USA.

Anderson, J.G., and Hough, S.E. 1984. A model for the shape of the Fourier amplitude spectrum of acceleration at high-frequencies. Bulletin Seismological Society America, 74, 1969–1993.

Andrus, R.D., and Stokoe, K.H. 2000. Liquefaction resistance of soils from shear-wave velocity. Journal of Geotechnical and Geoenvironmental Engineering, 126(11), 1015-1025.

Angioni, T., Rechtien, R.D., Cardimona, S.J., and Luna, R. 2003. Crosshole seismic tomography and borehole logging for engineering site characterization in Sikeston, MO, USA. Tectonophysics, 368, 119–137.

Aster, R.C., Borchers, B., and Thurber, C.H. 2013. *Parameter Estimation and Inverse Problems*, (second edition): Elsevier.

ASTM D4428. 2000. Standard test methods for crosshole seismic testing. Annual Book of ASTM Standards, 04.08, American Society of the International Association for Testing and Materials (ASTM), West Conshohocken, PA, USA.

Birch, F. 1966. Compressibility; elastic constants. In: *Handbook of Physical Constants*: Schairer, J.F., and Spicer, H.C. (eds), Geological Society of America, Memoir 97.

Brocher, T.M., and Christensen, N.I. 1990. Seismic anisotropy due to preferred mineral orientation observed in shallow crustal rocks in southern Alaska: Geology, 18, 737–740.

Bohlen, T., Nil, D.D., Groos,L., Heider, S., Köhn, D., Kurzmann, A., Schaefer, M., Gassner, L., Metz, T., Thiel, N., and Wittkamp, F. 2016. IFOS2D, Version 2.0.3, https://git.scc.kit.edu/GPIAG-Software/IFOS2D.

Bois, P., La Porte, M., Lavergne, M., and Thomas, G. 1972. Well-to-well seismic measurements. Geophysics, 37(3), 471–480.

Bommer, J.J., Stafford, P.J., Edwards, B., Dost, B., van Dedem, E., Rodriguez-Marek, A., Kruiver, P.P., van Elk, J., and Doornhof, D. 2017. Framework for a ground-motion model for induced seismic hazard and risk analysis in the Groningen gas field. Earthquake Spectra, 33(2), 481–498.

Boon, C.W., Ooi, C.E., and Ooi, L.H. 2017. Retaining a soil connectivity from an overhang feature in karstic limestone: Expanded Abstracts, Southeast Asian Conference and Exhibition in Tunnelling and Underground Space 2017, Subang Jaya, Malaysia.

Bordy, E.M., Segwabe, T., and Makuke, B. 2010. Sedimentology of the upper Triassic–lower Jurassic (?) Mosolotsane Formation (Karoo Supergroup), Kalahari Karoo Basin, Botswana. Journal of African Earth Sciences, 58, 127–140.

Bourbie, T., Coussy, O., and Zinszner, B. 1987. *Acoustics of Porous Media*: Gulf Publishing Company, Paris, France. Translated by Marshall, N. from French, Acoustique des Milieux Poreu.

Brett, J.S., Mason, R., and Smith, P.H. 2000. Geophysical exploration of the Kalahari Suture Zone. Journal of African Earth Sciences, 30, 489–497.

Brune, J.N. 1970. Tectonic stress and spectra of seismic shear waves from earthquakes. Journal of Geophysical Research, 75(26), 4997–5009.

Butcher, A.P., Campanella, R.G., Kaynia, A.M., and Massarsch, K.R. 2005. Seismic cone downhole procedure to measure shear wave velocity – A guideline prepared by ISSMGE TC10: Geophysical Testing in Geotechnical Engineering. *Proceedings of the XVIth International Conference on Soil Mechanics and Geotechnical Engineering*, Osaka, Japan.

Cairncross, B. 2001. An overview of the Permian (Karoo) coal deposits of southern Africa. African Earth Sciences, 33, 529–562.

Canales, L.L. 1984. Random noise reduction. Presented at the *54th SEG Conference* and published in the *SEG Technical Program Expanded Abstracts*, 3(1), 525–572.

Candès, E.J., and Guo, F. 2002. New multiscale transforms, minimum total variation synthesis: applications to edge-preserving image reconstruction. Signal Processing, 82, 1519–1543.

Candès, E.J., and Donoho, D.L. 2004. New tight frames of curvelets and optimal representations of objects with piecewise C 2 singularities. Communications on Pure and Applied Mathematics, 57, 219–266.

Candès, E.J., Demanet, L., Donoho, D.L., and Ying, L. 2005. Fast discrete curvelet transforms, technical report, California Institute of Technology; www.curvelet.org.

Carrion, P., Costa, J., Pinheiro, J. E., and Schoenberg, M. 1992. Cross-borehole tomography in anisotropic media. Geophysics 57(9), 1194–1198.

Červený, V. 1972. Seismic rays and ray intensities in inhomogeneous anisotropic media. Geophysical Journal of the Royal Astronomical Society, 29, 1–13.

Chapman, C.H., and Pratt R.G. 1992. Traveltime tomography in anisotropic media - I. theory: Geophysical Journal International, 109, 1–19.

Clark, G.C., Lock, N.P. and Smith, R.A. 1986. Coal resources of Botswana. In: Anhaeusser, C.R., and Maske, S. (eds.), *Mineral Deposits of Southern Africa*, 2071–2085: Geological Society of South Africa, Johannesburg, South Africa.

Clayton, C.R.I. 2011. Stiffness at small strain: research and practice. Geotechnique, 61(1), 5–37.

Clayton, C.R., Heymann, G., and Matthews, M.C. 2012. The value of stiffness measured in field seismic surveys. International Journal of Geo-Engineering, 4(2), 17–36.

Cox, H. 1856. The deflection of imperfectly elastic beams and the hyperbolic law of elasticity. Transactions of the Cambridge Philosophical Society, 9(2), 177–190.

Crampin, S. 1981. A review of wave motion in anisotropic and cracked elastic media. Wave Motion, 3, 343–391.

Crampin, S., and Chastin, S. 2003. A review of shear wave splitting in the crack-critical crust. Geophysical Journal International, 155, 221–240.

Daley, P.F., and Hron, F. 1977. Reflection and transmission coefficients for transversely isotropic media. Bulletin of the Seismological Society of America, 67(3), 661–675.

Daley, T.M., Majer, E.L., and Peterson, J.E. 2004. Crosswell seismic imaging in a contaminated basalt aquifer. Geophysics, 69(1), 16–24.

Day, M. 2004. Karstic problems in the construction of Milwaukee's deep tunnels. Environmental Geology, 45, 859–863.

Dietrich, P., and Tronicke, J. 2009. Integrated analysis and interpretation of cross-hole P- and S-wave tomograms: a case study. Near Surface Geophysics, 7(2), 101–109.

Dietze, M. 2007. *Evaluierung von Feldmethoden zur Quantifizierung von Schadstoffminderungen im Fahnenbereich am Beispiel eines BTEX-Schadens*. Tübingen, Germany: PhD thesis at the Institut für Geowissenschaften der Universität Tübingen.

Dines, K.A., and Lytle, R.J. 1979. Computerized geophysical tomography. *Proceedings of the IEEE*, 67(7), 1065–1073.

Doetsch, J., Linde, N., Coscia, I., Greenhalgh, S.A., and Green, A.G. 2010. Zonation for 3D aquifer characterization based on joint inversions of multimethod crosshole geophysical data. Geophysics, 75(6), G53–G64.

Donoho, D.L., and Stark, P.B. 1989. Uncertainty principles and signal recovery. Society for Industrial and Applied Mathematics Journal of Applied Mathematics, 49(3), 906–931.

Dubois, C., Quinif, Y., Baele, J.-M., Dagrain, F., Deceuster, J., and Kaufmann, O. 2014. The evolution of the mineralogical and petrophysical properties of a weathered limestone in southern Belgium. Geologica Belgica, 17, 1–8.

Easley, G., Labate, D., and Lim, W.Q. 2008. Sparse directional image representations using the discrete shearlet transform. Applied and Computational Harmonic Analysis, 25(1), 25–46.

Eaton, D.W., Adam, E., Milkereit, B., Salisbury, M., Roberts, B., White, D., and Wright, J. 2010. Enhancing base-metal exploration with seismic imaging. Canadian Journal of Earth Sciences, 47(5), 741–760.

Eberhart-Phillips, D., Han, D-H., and Zoback, M.D. 1989. Empirical relationships among seismic velocity, effective pressure, porosity, and clay content in sandstone. Geophysics, 54(1), 82–89.

Edwards, B., Michel, C., Poggi, V., and Fäh, D. 2013. Determination of site amplification from regional seismicity: application to the Swiss National Seismic Networks. Seismological Research Letters, 84(4), 611–621.

Fechner, T. 1998. *Seismische Tomographie zur Beschreibung Heterogener Grundwasserleiter*. PhD thesis at the University of Tübingen, Germany.

Fechner, T., Ehosioke, S.I., Mackens, S., Karl, L., and Tweeton, D. 2015. Reliability maps for seismic tomography: *Expanded Abstracts of the International Conference on Engineering Geophysics*, Al Ain, United Arab Emirates.

Flinn, E.A. 1965. Signal analysis using rectilinearity and direction of particle motion. *Proceedings of the IEEE*, 53(12), 1874–1876.

Fratta, D., Tanner, W.M., and Damasceno, V.M. 2004. Using elastic waves for the tomographic imaging of stresses in soils. FastTIMES, 9(4), 37–45.

Gallardo, L.A., and Meju, M.A. 2003. Characterization of heterogeneous near-surface materials by joint 2D inversion of dc resistivity and seismic data. Geophysical Research Letters, 30(13), 1–4.

Gallardo, L.A., and Meju, M.A. 2004. Joint two-dimensional DC resistivity and seismic travel time inversion with cross-gradients constraints. Journal of Geophysical Research, 109(B3), B03311.

Gallardo, L.A. 2007. Multiple cross-gradient joint inversion for geospectral imaging. Geophysical Research Letters, 34(L19301), 1–5.

Garofalo, F., Foti, S., Hollender, F., Bard, P.Y., Cornou, C., Cox, B.R., Ohrnberger, M., Sicilia, D., Asten, M., Di Giulio, G., Forbiger, T., Guillier, B., Hayashi, K., Martin, A., Matsushima, S., Mercerat, D., Poggi, V., and Yamanaka, H. 2016. InterPACIFIC project: comparison of invasive and non-invasive methods for seismic site characterization. Part I: intra-comparison of surface wave methods. Soil Dynamic Earthquake Engineering, 82, 222–240.

Garofalo, F., Foti, S., Hollender, F., Bard, P.Y., Cornou, C., Cox, B.R., Dechamp, A., Ohrnberger, M., Perron, V., Sicilia, D., Teague, D., and Verniault, C. 2016. InterPACIFIC project: comparison of invasive and non-invasive methods for seismic site characterization. Part II: inter-comparison between surface-wave and borehole methods. Soil Dynamic Earthquake Engineering, 82, 241–254.

Ghasemi, E., Yagiz, S., and Ataei, M. 2014. Predicting penetration rate of hard rock tunnel boring machine using fuzzy logic. Bulletin of Engineering Geology and the Environment, 73, 23–35.

Gilbert, P. 1972. Iterative methods for the three dimensional re-construction of an object from projections. Journal of Theoretical Biology, 36(1), 105–117.

Giroux, B., Gloaguen, E., and Chouteau, M. 2007. bh_tomo – A Matlab borehole georadar 2D tomography package. Computers and Geosciences, 33(1), 126–137.

Giroux, B., and Gloaguen, E. 2012. Geostatistical traveltime tomography in elliptically anisotropic media. Geophysical Prospecting, 60, 1–17.

Gochioco, L.M. 1991. Advances in seismic reflection profiling for US coal exploration. The Leading Edge, 10(12), 24–29.

Gochioco, L.M. 2000. High-resolution 3-D seismic survey over a coal mine reserve area in the U.S. – A case study. Geophysics, 65, 712–718.

Gochioco, L.M., Gochioco, J.R. and Ruev Jr, F. 2012. Coal geophysics expands with growing global demands for mine safety and productivity. The Leading Edge, 31(3), 308–314.

Goertz-Allmann, B.P., and Edwards, B. 2013. Constraints on crustal attenuation and three-dimensional spatial distribution of stress drop in Switzerland. Geophysical Journal International, 196(1), 493–509.

Golub, G., and Kahan, W. 1965. Calculating the singular values and pseudo-inverse of a matrix. Journal of the Society for Industrial and Applied Mathematics, Numerical Analysis Series B, 2(2), 205–224.

Goossens, R.F., and Buchanan, D.J. 1984. The role of seismic surveying in coal mining exploration. Mining Science and Technology, 1(4), 253–267.

Górszczyk, A., Adamczyk, A., and Malinowski, M. 2014. Application of curvelet denoising to 2D and 3D seismic data — Practical considerations. Journal of Applied Geophysics, 105, 78–94.

Gruber, T., and Greenhalgh, S.A. 1998. Precision analysis of first-break times in grid models. Geophysics, 63(3), 1062–1065.

Hayashi, K., and Suzuki, H. 2004. CMP cross-correlation analysis of multi-channel surface-wave data. Exploration Geophysics, 35(1), 7–13.

Helbig, K. 1981. Systematic classification of layered-induced transverse isotropy. Geophysical Prospecting, 29, 550–577.

Helbig, K., and Thomsen, L. 2005. 75-plus years of anisotropy in exploration and reservoir seismics: a historical review of concepts and methods. Geophysics, 70(5), 9ND–23ND.

Hennenfent, G., and Herrmann, F.J. 2006. Seismic denoising with nonuniformly sampled curvelets. IEEE Computing in Science and Engineering, 8(3), 16–25.

Henson Jr, H. and Sexton, J.L. 1991. Premine study of shallow coal seams using high-resolution seismic reflection methods. Geophysics, 56(9), 1494–1503.

Hildebrand, R., Bishop, M., and Cronshaw, M. 2009. Evaluating coalbed methane plays in frontier areas – an example from Southern Africa. *AAPG Annual Convention and Exhibition*, Denver, Colorado, USA.

Hofman, L.J., Ruigrok, E., Dost, B., and Paulssen, H. 2017. A shallow velocity model for the Groningen area in the Netherlands, Journal of Geophysical Research of the Solid Earth, 122, 8035–8050.

Jackson, G.M., Mason, I.M., and Greenhalgh, S.A. 1991. Principal component transforms of triaxial recordings by singular value decomposition. Geophysics, 56(4), 528–533.

Jackson, M.J., and Tweeton, D. 1996. 3DTOM: Three-dimensional geophysical tomography, US Department of the Interior, Bureau of Mines: Report of Investigation, 9617, 84.

Jeng, Y., Li, Y.-W., Chen, C.-S., and Chien, H.-Y. 2008. Adaptive filtering of random noise in near-surface seismic and ground-penetrating radar data. Journal of Applied Geophysics, 68(1), 36–46.

Jurkevics, A. 1988. Polarization analysis of three-component array data. Bulletin of the Seismological Society of America, 78(5), 1725–1743.

Kaczmarz, S. 1937. Angenäherte Auflösung von Systemen linearer Gleichungen. Acad. Polon. Sci. Lett. A, 355–357.

Kak, A.C. 1979. Computerized tomography with X-ray, emission, and ultrasound sources. *Proceedings of the IEEE*, 67(9), 1245–1272.

Khan, O., Spaak, M., and Vial-Aussavy, A. 2017. Realizing the potential of legacy seismic – getting more value from vintage data. *Abu Dhabi International Petroleum Exhibition and Conference, Extended Abstracts*, SPE-188678-MS.

Köhn, D. 2011. *Time Domain 2D Elastic Full Waveform Tomography*. PhD thesis, Kiel University, Germany.

Krey, T., Arnetzl, H., and Knecht, M. 1982. Theoretical and practical aspects of absorption in the application of in-seam seismic coal exploration. Geophysics, 47(12), 1645–1656.

Kreyszig, E. 2011. *Advanced Engineering Mathematics*: John Wiley and Sons, Boston, MA, USA.

Kruiver, P.P., van Dedem, E., Romijn, R., de Lange, G., Korff, M., Stafleu, J., Rodriguez-Marek, A., van Elk, J., and Doornhof, D. 2017a. An integrated shear-wave velocity model for the Groningen gas field. Bulletin of Earthquake Engineering, 15(9), 3555–3580.

Kruiver, P.P., Wiersema, A., Kloosteman, F.H., de Lange, G., Korff, M., Stafleu, J., Busschers, F.S., Harting, R., Gunnink, J.L., van Elk, J., and Doornhof, D. 2017b. Characterisation of the Groningen sub-surface for seismic hazard and risk modelling. Netherlands Journal of Geosciences, 96(5), s215–s233.

Ku, T., and Mayne, P.W. 2014. Stress history profiling in soils using OCD-G0 anisotropy relationship. Geotechnical Engineering, 167(GE5), 476–490.

Lee, J.-S., and Santamarina, J.C. 2004. Bender elements: performance and signal interpretation. Journal of Geotechnical and Geoenvironmental Engineering, 131(9), 1063–1070.

Lee, J.-S., Fernandez, A.L., and Santamarina, J.C. 2005. S-wave velocity tomography: small-scale laboratory application. Geotechnical Testing Journal, 28(4), 1–9.

Linder, S., Paasche, H., Tronicke, J., Niederleithinger, E., and Vienken, T. 2010. Zonal cooperative inversion of crosshole P-wave, S-wave, and georadar traveltime data sets. Journal of Applied Geophysics, 72(4), 254–262.

Lüth, S., Bohlen, T., Giese, R., Heider, S., Hock, S., Jetschny, S., Polom, U., Wadas, S., and Rechlin, A. 2014. Seismic tomography and monitoring in underground structures: developments in the Freiberg Reiche Zeche underground lab (Freiberg, Germany) and their application in underground construction (SOUND). In: Weber, M., and Münch, U. (eds), *Tomography of the Earth's Crust: From Geophysical Sounding to Real-Time Monitoring*, 115–133. Springer, Cham, Switzerland.

Lytle, R.J., Dines K.A., Laine, E.F., and Lager, P.L. 1978. Electromagnetic cross-borehole survey of a site proposed for an urban transit station: Report UCLR-52484, Lawrence Livermore Laboratory, University of California.

Mackens, S., Karl, L., Fechner, T., and Tweeton, D. 2014. Interpretation of seismic tomography results using data quality and residual error maps. *Extended Abstracts of the SAGEEP 2014*, Boston, MA, USA.

Mackens, S., Hocine, Y., and Werban, U. 2017. Direct-push based seismic crosshole testing for geotechnical engineering applications. Journal of Environmental and Engineering Geophysics, 22(3), 291–297.

Macrides, C.G., Kanasewich, E.R., and Bharatha, S. 1988. Multiborehole seismic imaging in steam injection heavy oil recovery projects. Geophysics, 53, 65–75.

Malehmir, A., Durrheim, R., Bellefleur, G., Urosevic, M., Juhlin, C., White, D.J., Milkereit, B., and Campbell, G. 2012. Seismic methods in mineral exploration and mine planning: A general overview of past and present case histories and a look into the future. Geophysics, 77(5), WC173–WC190.

Maljers, D., Stafleu, J., van der Meulen, M.J., and Dambrink, R.M. 2015. Advances in constructing regional geological voxel models, illustrated by their application in aggregate resource assessments. Netherlands Journal of Geosciences, 94, 257–270.

Manzi, M.S.D., Hein, K.A.A., Durrheim, R.J., and King, N. 2013. Seismic attribute analysis to enhance detection of thin gold-bearing reefs: South Deep gold mine, Witwatersrand basin, South Africa. Journal of Applied Geophysics, 98, 212–228.

Marelli, S., Manukyan, E., Maurer, H., Greenhalgh, S.A., and Green, A.G. 2010. Appraisal of waveform repeatability for crosshole and hole-to-tunnel seismic monitoring of radioactive waste repositories. Geophysics, 75(5), Q21–Q34.

Martin, G.S., Wiley, R., and Marfurt, K.J. 2006. Marmousi2: An elastic upgrade for Marmousi. The Leading Edge, 25(2), 156–166.

Maurer, H. 1996. Systematic errors in seismic crosshole data: Application to the coupled inverse technique. Geophysical Research Letters, 23(19), 2681–2684.

Mayne, P.W. 2001. Stress-strain-strength-flow parameters from enhanced in-situ tests. *International Conference on In-Situ Measurement of Soil Properties and Case Histories*, Bali, Indonesia, 27–48.

Meixner, H.M., and Peart, R.J. 1984. The Kalahari Drilling Project: a report on the geophysical and geological results of follow-up drilling to the aeromagnetic Survey of Botswana, Vol. 27. Geological Survey Department.

Menke, W. 1989. *Geophysical Data Analysis: Discrete Inverse Theory*: Academic Press.

Micheals, P. 2001. Use of principal component analysis to determine down-hole tool orientation and enhance SH-waves. Journal of Environmental and Engineering Geophysics, 6(4), 175–183.

Michel, C., Edwards, B., Poggi, V., Burjanek, J., Roten, D., Cauzzi, C., and Fäh, D. 2014. Assessment of site effects in alpine regions through systematic site characterization of seismic stations. Bulletin of the Seismological Society of America, 104(6), 2809–2826.

Michel, C., Fäh, D., Edwards, B., and Cauzzi, C. 2016. Site amplification at the city scale in Basel (Switzerland) from geophysical site characterization and spectral modelling of recorded earthquakes. Phys Chem Earth, Parts A/B/C, 98, 27–40.

Milkov, A.V., Potgieter, J., Faiz M., Mayers, A., and Parker, I. 2017. Evaluation of coal bed methane play in the eastern part of the central Kalahari Karoo Basin (Botswana). *Abstract, AAPG Annual Convention and Exhibition*, Houston, Texas, USA.

Moorkamp, M., Heincke, B., Jegen, M., Roberts, A.W., and Hobbs, R.W. 2011. A framework for 3-D joint inversion of MT, gravity and seismic refraction data. Geophysical Journal International, 184, 477–493.

Moret, G.J.M., Knoll, M.D., Barrash, W., and Clement, W.P. 2006. Investigating the stratigraphy of an alluvial aquifer using crosswell seismic traveltime tomography. Geophysics, 71(3), B63–B73.

Mufti, I.R. 1995. Pitfalls in crosshole seismic interpretation as a result of 3-D effects. Geophysics, 60, 821–833.

Musil, M., Maurer, H.R., and Green, A.G. 2003. Discrete tomography and joint inversion for loosely connected or unconnected physical properties: Application to crosshole seismic and georadar data sets. Geophysical Journal International, 153(2), 389–402.

Mulargia, F., and Castellaro, S. 2013. A seismic passive imaging step beyond SPAC and ReMi. Geophysics, 78(5), KS63–KS72.

Naghizadeh, M., and Sacchi, M. 2018. Ground-roll attenuation using curvelet downscaling. Geophysics, 83(3), V185–V195.

Natterer, F. 1986. Computerized tomography. In: *The Mathematics of Computerized Tomography*, 1–8: Vieweg+ Teubner Verlag, Wiesbaden, Germany.

Neelamani, R., Baumstein, A.I., Gillard, D.G., Hadidi, M.T., and Soroka, W.L. 2008. Coherent and random noise attenuation using the curvelet transform. The Leading Edge, 27(2), 240–248.

Nolet, G. 1984. Damped least squares methods to solve large tomographic systems and determine the resolving power. Terra Cognita, 4, 285.

Nolet, G. 1985. Solving or resolving inadequate and noisy tomographic systems. Journal of Computational Physics. 61, 463–482.

Nolet, G. 1987. *Seismic Tomography with Applications in Global Seismology and Exploration Geophysics*: Springer, Dordrecht, the Netherlands.

Nur, A., and Simmons, G. 1969. Stressinduced velocity anisotropy in rock: An experimental study. Journal of Geophysical Research, 74, 6667–6674.

Ogura, K., Uchiyama, S., Ohhashi, T., and Saito, H. 1989. Study of continuous measurement of suspension P-S logging. *SEG Technical Program Expanded Abstracts*, 43–46.

Ohori, M., Nobata, A., and Wakamatsu, K. 2002. A comparison of ESAC and FK methods of estimating phase velocity using arbitrarily shaped microtremor arrays. Bulletin of the Seismological Society of America, 92(6), 2323–2332.

Ohya, S., Ogura, K., and Imai, T. 1984. The suspension PS velocity logging system. *Expanded Abstracts, Offshore Technology Conference*, Houston, Texas.

Okada, H. 2003. The microtremor survey method, In: *Geophysical Monograph Series, Number 12*: Society of Exploration Geophysicists, Tulsa, OK, USA.

Paasche, H., Ohrnberger, M., Werban, U., and Fechner, T. 2011. Multi-scale S-wave tomography for exploration and risk assessment of development sites (MuSaWa). Geotechnologien, 24–34.

Paasche, H., Rumpf, M., Lontsi, A.M., Hausmann, J., Hannemann, K., Fechner, T., Ohrnberger, M., Werban, U., Tronicke, J., Krüger, F., and Dietrich, P. 2014. MuSaWa: Multi-scale S-wave tomography for exploration and risk assessment of development sites. In: *Tomography of the Earth's Crust: From Geophysical Sounding to Real-Time Monitoring*, 95–114: Springer, Cham, Switzerland.

Paasche, H., Tronicke, J., Holliger, K., Green, A.G., and Maurer, H. 2006. Integration of diverse physical-property models: Subsurface zonation and petrophysical parameter estimation based on fuzzy c-means cluster analyses. Geophysics, 71(3), H33–H44.

Paige, C.C., and Saunders, M.A. 1982. LSQR: An algorithm for sparse linear equations and sparse least squares. ACM Transactions on Mathematical Software, 8(1), 43–71.

Park, C.B., Miller, R.D., and Xia, J. 1999. Multichannel analysis of surface waves. Geophysics, 64(3), 800–808.

Pavlis, G.L., Sigloch, K., Burdick, S., Fouch, M.J., and Vernon, F.L. 2012. Unraveling the geometry of the Farallon plate: synthesis of three-dimensional imaging results from USArray. Tectonophysics, 532, 82–102.

Peterson, J.E., Paulson, B.N.P., and McEvilly, T.V. 1985. Applications of algebraic reconstruction techniques to crosshole seismic data. Geophysics, 50(10), 1566–1580.

Polymenakos, L., and Tweeton, D. 2015. Reevaluating a seismic traveltime tomography survey at Kastas tumulus (Amphipolis, Greece). Journal of Archaeological Science: Reports, 4, 434–446.

Prasad, P.P., Dhanam, K., Kishore, P.P., Mysaiah, D., and Seshunarayana, T. 2015. High resolution seismic reflection studies in Godavari coal fields: Mapping of coal seams and associated structural features. Journal of the Geological Society of India, 86(3), 317–323.

Pratt, R.G., and Chapman, C.H. 1992. Traveltime tomography in anisotropic media – II. Application. Geophysical Journal International, 109, 20–37.

Pratt, R.G., McGaughey, W.J., and Chapman, C.H. 1993, Anisotropic velocity tomography: A case study in a near-surface rock mass: Geophysics, 58, 1748–1763.

Quan, Y., and Harris, J.M. 1997. Seismic attenuation tomography using the frequency shift method. Geophysics, 62(3), 895–905.

Rawlinson, N., Fichtner, A., Sambridge, M., and Young, M.K. 2014, Seismic tomography and the assessment of uncertainty: Advances in Geophysics, 55, 1–76.

Reeves, C.V. 1978. The reconnaissance aeromagnetic survey of Botswana, 1975-1977. Final interpretation report. Terra Surveys Ltd, Botswana Geological Survey Department, p. 315.

Robertson, J.D., and Corrigan, D. 1983. Radiation patterns of a shear-wave vibrator in near-surface shale. Geophysics, 48, 19–26.

Rodriguez-Marek, A., Kruiver, P.P., Meijers, P., Bommer, J.J., Dost, B., van Elk, J., and Doornhof, D. 2017. A regional site-response model for the Groningen gas field. Bulletin of the Seismological Society of America, 108(5), 2067–2077.

Rumpf, M., and Tronicke, J. 2014. Predicting 2D geotechnical parameter fields in near-surface sedimentary environments. Journal of Applied Geophysics, 101, 95–107.

Scales, J.A., Gersztenkorn, A., and Treitel, S. 1988. Fast lp solution of large, sparse, linear systems: application to seismic travel time tomography. Journal of Computational Physics, 75(2), 314–333.

Schaller, M., Steiner, O., Studer, I., Holzer, L., Herwegh, M., and Kramers, J.D. 1999. Exhumation of Limpopo Central Zone granulites and dextral continent-scale transcurrent movement at 2.0 Ga along the Palala Shear Zone, Northern Province, South Africa. Precambrian Research, 96, 263–288.

Seebold, I., Lehmann, B., Arribas, A., Ruíz, C., Shephard, T.J., and Ashworth, K.L. 1999. Development of tomographic systems for mining, mineral exploration and environmental purposes. Transactions-Institution of Mining and Metallurgy. Section B. Applied Earth Science, 108, 105–118.

Sethian, J.A. 1999. Fast marching methods. SIAM Rev, 41(2), 199–235.

Shan, H., Ma, J., and Yang, H. 2009. Comparisons of wavelets, contourlets and curvelets in seismic denoising. Journal of Applied Geophysics, 69, 103–115.

Sheriff, R.E., and Geldart, L.P. 1995. *Exploration Seismology*, (second edition): Cambridge University Press, Cambridge, United Kingdom.

Singletary, S.J., Hanson, R.E., Martin, M.W., and Crowley, J.L. 2003. Geochronology of basement rocks in the Kalahari Desert, Botswana, and implications for regional Proterozoic tectonics. Precambrian Research, 121, 47–71.

Smith, R. 1984. The Lithostratigraphy of the Karoo Supergroup in Botswana. Botswana Geological Survey Department. Bulletin 26, 239.

Spakman, W., and Nolet, G. 1988, Imaging algorithms, accuracy and resolution in delay time tomography, In: *Mathematical Geophysics*, *Modern Approaches in Geophysics*, 155–187: Springer, Dordrecht, the Netherlands.

Stafleu, J., Maljers, D., Gunnink, J.L., Menkovic, A., and Busschers, F.S. 2011. 3D modeling of the shallow subsurface of Zeeland, the Netherlands. Netherlands Journal of Geosciences, 90, 293–310.

Stafleu, J., and Dubelaar, C.W. 2016. Product specification subsurface model GeoTOP. TNO Report 2016-R10133 v1.3, 53 pp. Available at: www.dinoloket.nl/en/want-know-more.

Starck, J.-L., Candès, E.J., and Donoho, D. 2002. The curvelet transform for image denoising. IEEE Transactions on Image Processing, 11(6), 670–684.

Stewart, R.R. 1991. Exploration Seismic Tomography: Fundamentals. *SEG Continuing Education short course, Vol. 3*: Society of Exploration Geophysicists, Tulsa, OK, USA.

Sully, J.P., and Campanella, R.G. 1995. Evaluation of in situ anisotropy from crosshole and downhole shear wave velocity measurements. Géotechnique, 45(2), 267–282.

Sun, J., and Li, Y. 2016. Joint inversion of multiple geophysical data using guided fuzzy c-means clustering. Geophysics, 81(3), ID37–ID57.

Tan, B. 2006. Urban geology of Kuala Lumpur and Ipoh, Malaysia. P*roceedings of the 10th IAEG International Congress*, The Geological Society of London, Nottingham, United Kingdom.

Taner, M.T. 2001. Seismic attributes. CSEG recorder, 26(7), 49–56.

Taner, M.T., and Sheriff, R.E. 1977. Application of amplitude, frequency, and other attributes to stratigraphic and hydrocarbon exploration. In: Payton, C.E. (ed), *Seismic Stratigraphy - Applications to Hydrocarbon Exploration*, 301–327: Am. Ass. Petr. Geol. Memoir 26.

Tanimoto, K., and Kurzeme, M. 1973. In situ shear wave velocity by cross-hole method. Journal of Soil Mechanics and Foundations, 99(4), 351–353.

Terracin, M., and Manzi, M. 2017. Spatial corrections for post-stack time migrated legacy 2D seismic data: a case study from the Witwatersrand Basin, South Africa. *South African Geophysical Association Biennial Conference*, Sommerset West, Cape Town.

Thomsen, L. 1986. Weak elastic anisotropy. Geophysics, 51(10), 1954–1966.

Thomsen, L. 2002. Understanding Seismic Anisotropy in Exploration and Exploitation. *SEG Distinguished Instructor Short Course, No. 5*: Society of Exploration Geophysicists, Tulsa, OK, USA.

Tokimatsu, K., and Uchida, A. 1990. Correlation between liquefaction resistance and shear wave velocity. Soils and Foundations, 30(2), 33–42.

Tryggvason, A., and Linde, N. 2006. Local earthquake (LE) tomography with joint inversion for P- and S-wave velocities using structural constraints. Geophysical Research Letters, 33(7), L07303.

Tryggvason, A., Rögnvaldsson, S.T., and Flóvenz, O.G. 2002. Three-dimensional imaging of the P- and S-wave velocity structure and earthquake locations beneath Southwest Iceland. Geophysical Journal International, 151, 848–866.

Tselentis, G.A., and Paraskevopoulos, P. 2002. Application of a high-resolution seismic investigation in a Greek coal mine. Geophysics, 67(1), 50–59.

Tsvankin, I. 2012. *Seismic Signatures and Analysis of Reflection Data in Anisotropic Media* (third edition): Society of Exploration Geophysicists, Tulsa, OK, USA.

Tsvankin, I., Gaiser, J., Grechka, V., van der Baan, M., and Thomsen, L. 2010. Seismic anisotropy in exploration and reservoir characterization: An overview: Geophysics, 75, 75A15–75A29.

Tsvankin, I., and Grechka, V. 2011. *Seismology of Azimuthally Anisotropic Media and Seismic Fracture Characterization*: Society of Exploration Geophysicists, Tulsa, OK, USA.

Tsvankin, I., and Thomsen, L. 1994. Nonhyperbolic reflection moveout in anisotropic media: Geophysics, 59, 1290–1304.

Um, J., and Thurber, C. 1987. A fast algorithm for two-point ray tracing. Bulletin of the Seismological Society of America, 77, 972–986.

Urosevic, M., Evans, B.J., and Hatherly, P.J. 1992. The improvement in seismic resolution by map and trace attribute analysis. Exploration Geophysics, 23(2), 387–392.

van der Hilst, R., Engdahl, R., Spakman, W., and Nolet, G. 1991. Tomographic imaging of subducted lithosphere below northwest Pacific island arcs. Nature, 353, 37–43.

van der Hilst, R., Widiyantoro, S., and Engdahl, R. 1997. Evidence for deep mantle circulation from global tomography. Nature, 386, 578–584.

Vesnaver, A., and Böhm, G. 2000. Staggered or adapted grids for seismic tomography. The Leading Edge, 19(9), 944–950.

Vidale, J.E. 1988. Finite-difference calculation of traveltimes: Bulletin of the Seismological Society of America, 78, 2062–2076.

Voigt, W. 1910. *Lehrbuch der Kristallphysik*: Teubner, Leipzig, Germany.

von Ketelhodt, J.K., Fechner, T., Manzi, M.S.D., and Durrheim, R.J. 2018. Joint-inversion of cross-borehole P-waves, horizontally and vertically polarised S-waves: tomographic data for hydrogeophysical site characterization. Near Surface Geophysics, 16, 529–542.

Walton, C., Evans, B., and Urosevic, M. 2000. Imaging coal seam structure using 3-D seismic methods. Exploration Geophysics, 31(3), 509–514.

Wang, J.-N., and Munfakh, G. 2001. Seismic design of tunnels. Transactions on the Built Environment, 57, 589–598.

Wang, Z. 2002. Seismic anisotropy in sedimentary rocks, part 2: Laboratory data. Geophysics, 67(5), 1423–1440.

Watanabe, T., Matsuoka, T., and Ashida, Y. 1999. Seismic traveltime tomography using Fresnel volume approach. *SEG Technical Program Expanded Abstracts 18*, 1402–1405.

Weiß, H., Schirmer, M., Teutsch, G., and Merkel, P. 2001. Sanierungsforschung in regional kontaminierten Aquiferen (SAFIRA) – 1. Information zum Forschungsschwerpunkt am Standort Bitterfeld. Grundwasser, 6(3), 113-122.

———— 2002. Sanierungsforschung in regional kontaminierten Aquiferen (SAFIRA) – 2. Projektüberblick und Pilotanlage. Grundwasser, 7(3), 135-139.

Widess, M. B. 1973. How thin is a thin bed? Geophysics, 38(6), 1176–1180.

Wong, J., Hurley, P., and West, G.F. 1983. Crosswell seismology and seismic imaging in crystalline rocks. Geophysical Research Letters, 10(8), 686–689.

Yamamoto, T., Nye, T., and Kuru, M. 1994. Porosity, permeability, shear strength: Crosswell tomography below an iron foundry. Geophysics, 59(10), 1530–1541.

Yao, Z.S., Roberts, R.G., and Tryggvason, A. 1999. Calculating resolution and covariance matrices for seismic tomography with the lsqr method: Geophysical Journal International, 138, 886–894.

Yilmaz, Ö. 1986. *Seismic Data Processing*: Society of Exploration Geophysicists, Tulsa, OK, USA.

Yong, A., Martin, A., Stokoe, K., and Diehl, J. 2013. ARRA-funded VS30 measurements using multi-technique approach at strong-motion stations in California and central-eastern United States (Open-File Report 2013–1102). US Geological Survey, 59.

Zhang, F., Juhlin, C., Cosma, C., Tryggvason, A., and Pratt, R.G. 2012. Cross-well seismic waveform tomography for monitoring CO2 injection: a case study from the Ketzin Site, Germany. Geophysical Journal International, 189(1), 629–646.

Zhao, D. 2004. Global tomographic images of mantle plumes and subducting slabs: insight into deep Earth dynamics. Physics of the Earth and Planetary Interiors, 146, 3–34

Zhou, B., and Greenhalgh, S.A. 2005. Analytic expressions for the velocity sensitivity to the elastic moduli for the most general anisotropic media. Geophysical Prospecting, 52, 619–641.

Zhou, B., Greenhalgh, S.A., and Green, A. 2008. Nonlinear traveltime inversion scheme for crosshole seismic tomography in tilted transversely isotropic media. Geophysics, 73(4), D17–D33.

10. APPENDIX

The appendix consists of instructions for the three Matlab programs that I wrote and implemented for data analysis of Chapters 5, 6 and 7. The code is available in the digital copy of this thesis.

10.1 Joint-Inversion – Matlab Code Instructions

The joint-inversion program is a 2D code for the estimation of seismic velocities (P- and S-wave mode) in between near-vertical borehole pairs and was used for the inversions presented in Chapter 5. The program requires a set of co-measured (same acquisition geometry) traveltimes. These traveltimes are then used to estimate seismic velocities.

The "heart" of the program can be found in *Main_inversion.m* (single dataset inversion), *Main_inversion_joint.m* (inversion of two datasets, e.g. P- and S-wave), and *Main_inversion_joint_3sets.m* (inversion of three datasets, e.g. P-, SH- and SV-wave). These programs have the primary objective of (1) loading the traveltime datasets, (2) defining the inversion parameters, such as the number of iterations, (3) calling the inversion subroutine, and (4) displaying and saving the results.

The inversion subroutine differs slightly depending on the number of datasets that are inverted (i.e. different subroutines for *Main_inversion.m*, *Main_inversion_joint.m*, etc.). In these subroutines (the file names start with *inv_lsqr2D*) (1) further inversion parameters are defined, (2) the forward raytracing executed to determine an rms-error and (3) the matrix inverted with an LSQR subroutine.

10.2 Inversion for Anisotropy Parameters – Matlab Code Instructions

The anisotropy parameter estimation program is based on the FORTRAN program by Zhou et al. (2008). Therefore, parts of the program were ported to the Matlab environment. The main use of the program is similar to the joint-inversion program, in that the main inversion program file has to be run (denoted *Main_Safira1_top.m* and *Main_Safira2_top.m*). In this file the inversion parameters are defined and subroutines called. In addition forward modelling studies can be tested. These program files start with *forward* (e.g. checker board reconstruction tests).

10.3 Curvelet Denoising – Matlab Code Instructions

The SeiCurve program was written to easily denoise reflection seismic data using the curvelet transform. The user can read in (noisy) seismic data in segy or seg2 format, interactively choose the best curvelet denoising parameters and save the result to segy or seg2 file.

The program was written using the object-orientated capabilities of the Matlab environment and a Model-Controller-Viewer architecture was chosen. This means that the graphical user interfaces (GUIs) are defined in the program files denoted with *View* (e.g. *View_Main.m* controls the GUI of the main program when it starts). All the data storage and manipulation (e.g. segy seismic data and curvelet transform) is performed in *Model.m*. Further seismic data storage is perfomed in the Matlab files *Curve.m* and *Scale.m* (strictly these are also of the "model" category in the Model-Controller-Viewer architecture). Lastly, the program files denoted with *Controller* serve to communicate between the viewer and the model. In these files, the subroutines are called and different viewing options set. The main program can be started by calling the program file *Controller.m* from the main Matlab environment.